

MAY 2023

**AJNR**

VOLUME 44 • PP 497-623

# AJNR

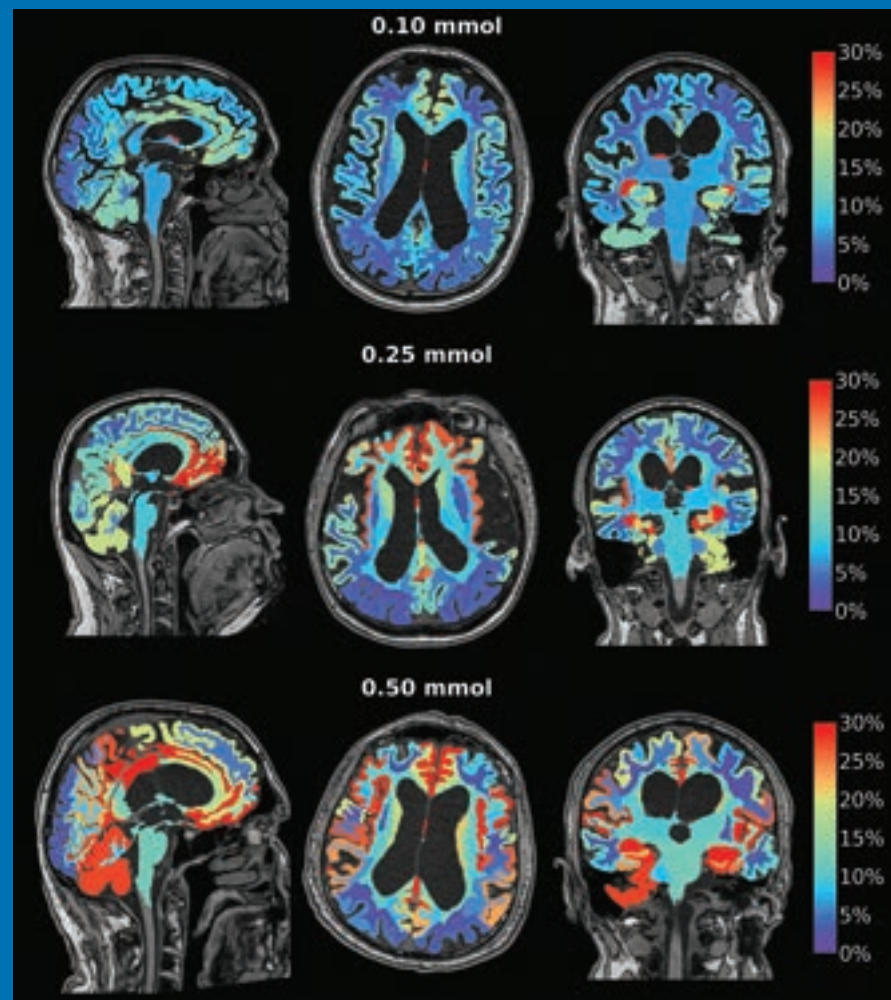
## AMERICAN JOURNAL OF NEURORADIOLOGY

MAY 2023  
VOLUME 44  
NUMBER 5  
WWW.AJNR.ORG

THE JOURNAL OF DIAGNOSTIC AND  
INTERVENTIONAL NEURORADIOLOGY

Safety study of intrathecal gadobutrol  
Dual-layer detector cone-beam CT angiography for stroke assessment  
Endolymphatic hydrops detection in patients with Ménière disease  
MELAS: Classic-versus-atypical presentations

Official Journal ASNR • ASFNR • ASHNR • ASPNR • ASSR



# FRED™ X™

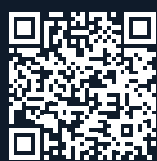
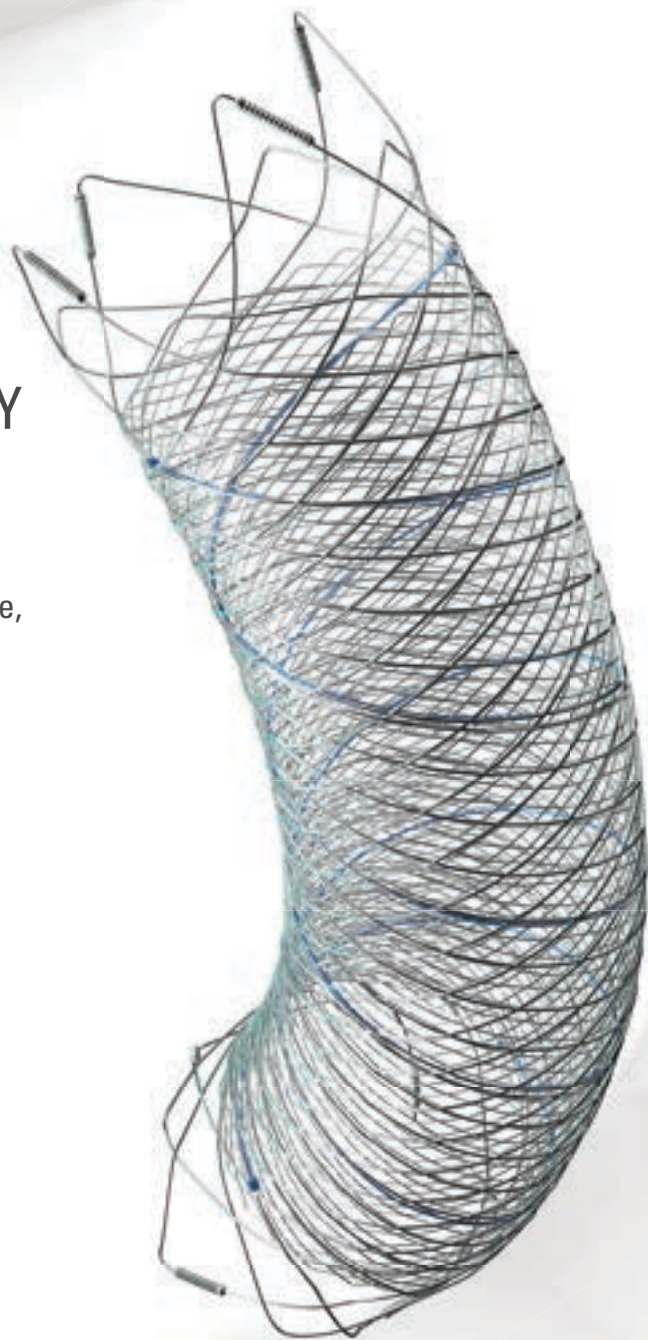
## Flow Diverter Stent

### THE NEXT ADVANCEMENT IN FLOW DIVERSION TECHNOLOGY

The FRED™ X Flow Diverter features the same precise placement and immediate opening of the FRED™ Device, now with X Technology. X Technology is a covalently bonded, nanoscale surface treatment, designed to:

- **REDUCE MATERIAL THROMBOGENICITY<sup>1</sup>**
- **MAINTAIN NATURAL VESSEL HEALING RESPONSE<sup>2,3,4</sup>**
- **IMPROVE DEVICE DELIVERABILITY AND RESHEATHING<sup>1</sup>**

The only FDA PMA approved portfolio with a 0.021" delivery system for smaller device sizes, and no distal lead wire.



For more information, contact your local MicroVention sales representative or visit our website. [www.microvention.com](http://www.microvention.com)



<sup>\*</sup> Data is derived from in vivo and ex vitro testing and may not be representative of clinical performance.

<sup>1</sup> Data on file

<sup>2</sup> Tanaka M et al. Design of biocompatible and biodegradable polymers based on intermediate water concept. Polymer Journal. 2015;47:114-121.

<sup>3</sup> Tanaka M et al. Blood compatible aspects of poly(2-methoxyethylacrylate) (PMEA) – relationship between protein adsorption and platelet adhesion on PMEAs surface. Biomaterials. 2000;21:1471-1481.

<sup>4</sup> Schiel L et al. X Coating™: A new biopassive polymer coating. Canadian Perfusion Canadienne. June 2001;11(2):9.

**Indications for Use:** The FRED X System is indicated for use in the internal carotid artery from the petrous segment to the terminus for the endovascular treatment of adult patients (22 years of age or older) with wide-necked (neck width 4 mm or dome-to-neck ratio < 2) saccular or fusiform intracranial aneurysms arising from a parent vessel with a diameter 2.0 mm and 5.0 mm.

**Rx Only:** Federal (United States) law restricts this device to sale by or on the order of a physician. For Healthcare professionals intended use only.

MICROVENTION, FRED and HEADWAY are registered trademarks of MicroVention, Inc. in the United States and other jurisdictions. Stylized X is a trademark of MicroVention, Inc. © 2022 MicroVention, Inc. MM1222 US 03/22

# WEB™ 17

Aneurysm Embolization System

# LOWER PROFILE



## NEW SIZES



## MORE ACCESS OPTIONS



#### INDICATIONS FOR USE:

The WEB Aneurysm Embolization System is intended for the endovascular embolization of ruptured and unruptured intracranial aneurysms and other neurovascular abnormalities such as arteriovenous fistulae (AVF). The WEB Aneurysm Embolization System is also intended for vascular occlusion of blood vessels within the neurovascular system to permanently obstruct blood flow to an aneurysm or other vascular malformation.

#### POTENTIAL COMPLICATIONS:

Potential complications include but are not limited to the following: hematoma at the site of entry, aneurysm rupture, emboli, vessel perforation, parent artery occlusion, hemorrhage, ischemia, vasospasm, clot formation, device migration or misplacement, premature or difficult device detachment, non-detachment, incomplete aneurysm filling, revascularization, post-embolization syndrome, and neurological deficits including stroke and death. For complete indications, potential complications, warnings, precautions, and instructions, see instructions for use (IFU provided with the device).

VIA 21, 27, 33 - The VIA Microcatheter is intended for the introduction of interventional devices (such as the WEB device/stents/flow diverters) and infusion of diagnostic agents (such as contrast media) into the neuro, peripheral, and coronary vasculature.

VIA 17,17 Preshaped - The VIA Microcatheter is intended for the introduction of interventional devices (such as the WEB device/stents/flow diverters) and infusion of diagnostic agents (such as contrast media) into the neuro, peripheral, and coronary vasculature.

The VIA Microcatheter is contraindicated for use with liquid embolic materials, such as n-butyl 2-cyanoacrylate or ethylene vinyl alcohol & DMSO (dimethyl sulfoxide).

The device should only be used by physicians who have undergone training in all aspects of the WEB Aneurysm Embolization System procedure as prescribed by the manufacturer.

RX Only: Federal law restricts this device to sale by or on the order of a physician.

For healthcare professional intended use only.



MicroVention Worldwide  
Innovation Center PH +1.714.247.8000

35 Enterprise  
Aliso Viejo, CA 92656 USA  
MicroVention UK Limited PH +44 (0) 191 258 6777  
MicroVention Europe, S.A.R.L. PH +33 (1) 39 21 77 46  
MicroVention Deutschland GmbH PH +49 211 210 798-0  
Website microvention.com



WEB™ and VIA™ are registered trademarks  
of Sequent Medical, Inc. in the United States.

©2021 MicroVention, Inc. MM1184 WW 11/2021





# The ASNR Career Center

**The Go-To Job Site for Neuroradiology Employers and Job Seekers**

## *For Job Seekers*

- Access to an expanded network of jobs via the National Healthcare Career Network
- Confidential resume posting
- Professional online profile

## *For Employers*

- Employer resources to help you recruit top talent
- Multiple pricing options, including free Fellowship listings
- Resume search

**Start here: [careers.asnr.org](https://careers.asnr.org)**

## Announcement: The New Editor-in-Chief of AJNR



### Max Wintermark, MD, MAS, MBA

On behalf of the Search Committee for Editor-in-Chief of the *American Journal of Neuroradiology*, I am pleased to announce that the new Editor-in-Chief will be Max Wintermark, MD, MAS, MBA.

First, I would like to thank the members of the Search Committee, including Mauricio Castillo, MD, FACR, Pina Sanelli, MD, MPH, FACR, Carolyn Meltzer, MD, FACR, Erin Simon Schwartz, MD, FACR, Joshua Nickerson, MD, Courtney Tomlinson, MD, Harry Cloft, MD, PhD, Peter D. Chang, MD, Lubdha Shah, MD, Gregory Zaharchuk MD, PhD, C. Douglas Phillips, MD, Yvonne Lui, MD, and Bryan Comstock as well as Karen Halm and Mary Beth Hepp, from ASNR's Headquarters for their service, hard work, and dedication. There were several qualified applicants for the position and the committee members devoted many hours to make a decision.

Second, we especially wish to thank Dr. Jeffrey Ross for his extraordinary dedication and exceptional contributions to the *AJNR*. In June 2023, Jeffrey S. Ross, MD, will complete an 8-year term as the sixth Editor-in-Chief of the *AJNR*. He was preceded by a number of distinguished Editors including our first *AJNR* EIC, Juan M. Taveras, MD (1980–1989), followed by Michael S. Huckman, MD (1990–1997), Robert M. Quencer, MD (1997–2005), Robert I. Grossman, MD (2006–2007), and Mauricio Castillo, MD (2007–2015).

Under Dr. Ross' strong leadership, the *AJNR* remains the premier clinical neuroimaging journal with high-quality, peer-reviewed articles that serve as a beacon for achieving excellence in patient care, research, and teaching. Dr. Ross assembled a talented international editorial board during his tenure. With 1700+ papers, the number of submissions to the journal was record-breaking in 2020. Over 90 COVID-19 papers have received expedited publication to date, and almost 1100 original submissions are projected for 2022. Dr. Ross championed the migration to a new, improved website platform in 2017, enhancing the journal's online presence. The *AJNR* website had an incredible 11.7 million visits in 2021. Dr. Ross established the Statistical Senior Editor and Artificial Intelligence Deputy Editor positions, elevating the quality of *AJNR*'s peer review process. In addition, during Dr. Ross' tenure, the Impact Factor and h-index for the journal steadily increased and contributed to *AJNR*'s international recognition as the leading journal for all aspects of neuroimaging research, education, and best practice.

Finally, I would like to take this opportunity to highlight Max Wintermark's illustrious career. His academic, research, and

administrative leadership skill sets are well-suited for this new role. Max is a nationally and internationally renowned neuroradiologist, who is Professor of Radiology and the Chair of Neuroradiology at the University of Texas MD Anderson Center in Houston.

Max received his medical degree from the University of Lausanne in Switzerland. He completed his radiology residency training at the University Hospital in Lausanne and his clinical fellowship in Neuroradiology at the University of California at San Francisco (UCSF). He is board-certified in Diagnostic Radiology with a Certificate of Added Qualification in Neuroradiology. He completed a master's degree in clinical research with a focus on study design, biostatistics, and epidemiology at UCSF. In addition, he holds an MBA with a focus in medical management from the University of Massachusetts at Amherst.

Max's previous faculty appointments include UCSF, the University of Virginia, and Stanford University. Max has served as a peer-reviewer for the *AJNR* and was a member of the Editorial Board of *AJNR* for many years. He also serves as the Senior Editor for Neuroradiology for the *American Journal of Roentgenology*, and he is a Past President of the American Society of Functional Neuroradiology. He served as the chair of the Research Committee of the American Society of Neuroradiology; he is currently Vice-President of the American Society of Neuroradiology. He was a recent recipient of the ASNR Outstanding Contributions in Research Award in 2021.

Dr. Wintermark is an expert in advanced neuroimaging techniques and has had a very active research program over the past two decades. His research program focuses on both clinical and preclinical research and includes diverse conditions such as stroke, TBI, brain tumors, psychiatric diseases, advanced neuroimaging, novel imaging techniques, and AI. He has published a total of 556 peer-reviewed articles, including 60 in *AJNR* and his articles have been cited almost 110,000 times with an h-index of 92. He has authored four books and more than 100 book chapters, and holds 10 patents.

Please join me in welcoming Max Wintermark, MD, MAS, MBA to the position of Editor-in-Chief of the *AJNR* starting July 2023. We are fortunate to have such an accomplished leader in neuroradiology in this position to build on the tradition of excellence of our past editors and to provide pivotal leadership and strategic vision for our journal.

### Tina Young Poussaint, MD, FACR

Chair, *AJNR* Editor-in-Chief Search Committee  
1st Past President, American Society of Neuroradiology  
Past President, American Society of Pediatric Neuroradiology

# AJNR *go green*

***AJNR* urges American Society of Neuroradiology members to reduce their environmental footprint by voluntarily suspending their print subscription.**

The savings in paper, printing, transportation, and postage directly fund new electronic enhancements and expanded content.

The digital edition of *AJNR* presents the print version in its entirety, along with extra features including:

- Publication Preview
- Case Collection
- Podcasts
- The *AJNR* News Digest
- The *AJNR* Blog

It also reaches subscribers much faster than print. An electronic table of contents will be sent directly to your mailbox to notify you as soon as it publishes.

Readers can search, reference, and bookmark current and archived content 24 hours a day on [www.ajnr.org](http://www.ajnr.org).

ASNR members who wish to opt out of print can do so by using the *AJNR* Go Green link on the *AJNR* Website (<http://www.ajnr.org/content/subscriber-help-and-services>). Just type your name in the email form to stop print and spare our ecosystem.



**I am a global citizen.**

**I am patient-centered care.**

**I am committed to health equity.**

**I am a teacher.**

**I am a life-long learner.**

**I am determined.**

**I am curious.**

**I am a collaborative team player.**

**I am a volunteer.**

**I am ASNR.**

**Don't miss out on the tools, resources and relationships you've come to rely on. Log in and renew your ASNR membership today! [www.asnr.org](http://www.asnr.org)**

**ASNR**  
American Society of Neuroradiology





# Simplify the MOC Process



# Manage your CME Credits Online

## CMEgateway.org

### Available to Members of Participating Societies

American Board of Radiology (ABR)  
American College of Radiology (ACR)  
American Roentgen Ray Society (ARRS)  
American Society of Neuroradiology (ASNR)  
Commission on Accreditation of Medical  
Physics Educational Programs, Inc. (CAMPEP)  
Radiological Society of North America (RSNA)  
Society of Interventional Radiology (SIR)  
SNM  
The Society for Pediatric Radiology (SPR)

### It's Easy and Free!

Log on to CME Gateway to:

- View or print reports of your CME credits from multiple societies from a single access point.
- Print an aggregated report or certificate from each participating organization.
- Link to SAMs and other tools to help with maintenance of certification.

### American Board of Radiology (ABR) participation!

By activating ABR in your organizational profile, your MOC-fulfilling CME and SAM credits can be transferred to your own personalized database on the ABR Web site.

### Sign Up Today!

go to [CMEgateway.org](http://CMEgateway.org)

Announcing a New Funding Partnership Between the Alzheimer's Association and  
the Foundation of the American Society of Neuroradiology

## Imaging Research in Alzheimer's and Other Neurodegenerative Diseases Program

Up to three grants funded each year  
Up to \$200,000 available for each grant

### *This New Grant Program Is Designed To:*

Support the development of new novel imaging tools

Advance imaging-based research

Provide funding for novel and innovative imaging data analysis as  
relates to Alzheimer's and related dementias

### *Letter of Intent Deadline*

To be considered for an Imaging Research Grant, you must submit a Letter of Intent  
by Monday, June 5, 2023, at 5:00 pm ET online via **proposalcentral.com**.  
*No exceptions.*

For complete details and additional deadlines, please visit **foundation.asnr.org**.







# The next generation GBCA from Guerbet is here

---



To learn more,  
scan QR code or visit  
[www.guerbet-us.com](http://www.guerbet-us.com)



# AJNR


## AMERICAN JOURNAL OF NEURORADIOLOGY

MAY 2023  
VOLUME 44  
NUMBER 5  
WWW.AJNR.ORG

Publication Preview at [www.ajnr.org](http://www.ajnr.org) features articles released in advance of print. Visit [www.ajnrblog.org](http://www.ajnrblog.org) to comment on AJNR content and chat with colleagues and AJNR's News Digest at <http://ajnrndigest.org> to read the stories behind the latest research in neuroimaging.

497 **PERSPECTIVES** *J.S. Ross*




















### REVIEW ARTICLE

-  498 **Symptomatic Developmental Venous Anomaly: State-of-the-Art Review on Genetics, Pathophysiology, and Imaging Approach to Diagnosis** *C.C.-T. Hsu, et al.* **ADULT BRAIN**








### RADIOLOGY-PATHOLOGY CORRELATION

- 505 **Erdheim-Chester Disease** *J.C. Benson, et al.* **ADULT BRAIN**

### GENERAL CONTENTS

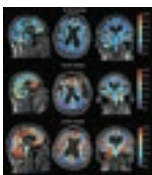
-  511 **Prospective Safety Study of Intrathecal Gadobutrol in Different Doses** *A. Sperre, et al.* **PATIENT SAFETY**
-   517 **Post-COVID-19 Brain [<sup>18</sup>F] FDG-PET Findings: A Retrospective Single-Center Study in the United States** *P. Debs, et al.* **ADULT BRAIN**
-    523 **Dual-Layer Detector Cone-Beam CT Angiography for Stroke Assessment: First-in-Human Results (the Next Generation X-ray Imaging System Trial)** *F. Ståhl, et al.* **ADULT BRAIN INTERVENTIONAL**
-   530 **Clinical Relevance of Plaque Distribution for Basilar Artery Stenosis** *J. Luo, et al.* **ADULT BRAIN INTERVENTIONAL**
-   536 **DWI-Based Radiomics Predicts the Functional Outcome of Endovascular Treatment in Acute Basilar Artery Occlusion** *X. Zhang, et al.* **ADULT BRAIN FUNCTIONAL**
-    543 **Deep Learning of Time-Signal Intensity Curves from Dynamic Susceptibility Contrast Imaging Enables Tissue Labeling and Prediction of Survival in Glioblastoma** *J. Yun, et al.* **ADULT BRAIN FUNCTIONAL**
-   553 **Associating IDH and TERT Mutations in Glioma with Diffusion Anisotropy in Normal-Appearing White Matter** *H. Halilbrahimoglu, et al.* **ADULT BRAIN FUNCTIONAL**
-   562 **3D Capsule Networks for Brain Image Segmentation** *A. Avesta, et al.* **ADULT BRAIN**
-   569 **Assessing the Equivalence of Brain-Derived Measures from Two 3D T1-Weighted Acquisitions: One Covering the Brain and One Covering the Brain and Spinal Cord** *D. Pareto, et al.* **ADULT BRAIN**

AJNR (Am J Neuroradiol ISSN 0195-6108) is a journal published monthly, owned and published by the American Society of Neuroradiology (ASNR), 820 Jorie Boulevard, Oak Brook, IL 60523. Annual dues for the ASNR include approximately 19% for a journal subscription. The journal is printed by Intellicor Communications, 330 Eden Road, Lancaster, PA 17601; Periodicals postage paid at Oak Brook, IL and additional mailing offices. Printed in the U.S.A. POSTMASTER: Please send address changes to American Journal of Neuroradiology, P.O. Box 3000, Denville, NJ 07834, U.S.A. Subscription rates: nonmember \$452 (\$530 foreign) print and online, \$320 online only; institutions \$520 (\$594 foreign) print and basic online, \$1029 (\$1103 foreign) print and extended online, \$380 online only (basic), \$825 online only (extended); single copies are \$35 each (\$40 foreign). Indexed by PubMed/MEDLINE, BIOSIS Previews, Current Contents (Clinical Medicine and Life Sciences), EMBASE, Google Scholar, HighWire Press, Q-Sensei, RefSeek, Science Citation Index, SCI Expanded, ReadCube, and Semantic Scholar. Copyright © American Society of Neuroradiology.


-  574 **Higher Incidence of Unruptured Intracranial Aneurysms among Black and Hispanic Women on Screening MRA in Large Urban Populations** *K. Javed, et al.* **ADULT BRAIN**
- 580 **Commentary**  
**Prevalence of Intracranial Aneurysms with Emphasis on Ethnicity and Race** *G. Ben-Arie*
-  582 **Intensive Blood Pressure Management Preserves Functional Connectivity in Patients with Hypertension from the Systolic Blood Pressure Intervention Randomized Trial** *C. Shah, et al.* **FUNCTIONAL**
-  589 **Imaging the Tight Orbit: Radiologic Manifestations of Orbital Compartment Syndrome** *C. Maier, et al.* **HEAD & NECK**
-  595 **A Novel MR Imaging Sequence of 3D-ZOOMit Real Inversion-Recovery Imaging Improves Endolymphatic Hydrops Detection in Patients with Ménière Disease** *J. Li, et al.* **HEAD & NECK**
-  602 **MELAS: Phenotype Classification into Classic-versus-Atypical Presentations** *C.A.P.F. Alves, et al.* **PEDIATRICS**
-   611 **Brain Activation Evoked by Motor Imagery in Pediatric Patients with Complete Spinal Cord Injury** *L. Wang, et al.* **PEDIATRICS**
- 618 **Fluoroscopy- and CT-Guided Gold Fiducial Marker Placement for Intraoperative Localization during Spinal Surgery: Review of 179 Cases at a Single Institution—Technique and Safety Profile** *C.P. Siminski, et al.* **SPINE INTERVENTIONAL**
- 623 **35 YEARS AGO**
- ONLINE FEATURES**
- WHITE PAPER**
- E21 **Critical Appraisal of Artificial Intelligence–Enabled Imaging Tools Using the Levels of Evidence System** *N. Pham, et al.*
- LETTER**
- E29 **Pituitary MRI to Evaluate Extraocular Muscles: Is That Possible with a Routine Scanning Protocol?** *B. Kocak*
- E30 **Reply** *M. White, et al.*

**BOOK REVIEWS** *R.M. Quencer, Section Editor*

Please visit [www.ajnrblog.org](http://www.ajnrblog.org) to read and comment on Book Reviews.



Enrichment in the brain by gadobutrol, used as a CSF tracer, in patients with iNPH from the article by A. Sperre et al, in this issue.

 Indicates Editor's Choices selection



Indicates Fellows' Journal Club selection



Indicates open access to non-subscribers at [www.ajnr.org](http://www.ajnr.org)



Indicates article with supplemental online data



Indicates article with supplemental online video



Evidence-Based Medicine Level 1



Evidence-Based Medicine Level 2

### EDITOR-IN-CHIEF

#### Jeffrey S. Ross, MD

Professor of Radiology, Department of Radiology,  
Mayo Clinic College of Medicine, Phoenix, AZ

### SENIOR EDITORS

#### Harry J. Cloft, MD, PhD

Professor of Radiology and Neurosurgery,  
Department of Radiology, Mayo Clinic College of  
Medicine, Rochester, MN

#### Christopher G. Filippi, MD

Professor and Alice Ettinger-Jack R. Dreyfuss  
Chair of Radiology,  
Tufts University School of Medicine,  
Radiologist-in-Chief  
Tufts University Medical Center, Boston, MA

#### Thierry A.G.M. Huisman, MD, PD, FICIS, FACR

Radiologist-in-Chief and Chair of Radiology, Texas  
Children's Hospital,  
Professor of Radiology, Pediatrics, Neurosurgery,  
and OBGYN, Baylor College of Medicine,  
Houston, TX

#### Yvonne W. Lui, MD

Associate Professor of Radiology,  
Chief of Neuroradiology,  
New York University School of Medicine,  
New York, NY

#### C.D. Phillips, MD, FACR

Professor of Radiology, Weill Cornell Medical  
College, Director of Head and Neck Imaging,  
New York-Presbyterian Hospital, New York, NY

#### Lubdha M. Shah, MD, MS

Professor of Radiology and Director of Spine  
Imaging, University of Utah Department of  
Radiology and Imaging Sciences, Salt Lake City, UT

### STATISTICAL SENIOR EDITOR

#### Bryan A. Comstock, MS

Senior Biostatistician,  
Department of Biostatistics,  
University of Washington, Seattle, WA

### ARTIFICIAL INTELLIGENCE DEPUTY EDITOR

#### Peter D. Chang, MD

Assistant Professor-in-Residence,  
Departments of Radiological Sciences,  
Computer Sciences, and Pathology,  
Director, Center for Artificial Intelligence in  
Diagnostic Medicine (CAIDM),  
University of California, Irvine, Irvine, CA

### EDITORIAL BOARD

Ashley H. Aiken, Atlanta, GA

Matthew D. Alexander, Salt Lake City, UT

Lea M. Alhilali, Phoenix, AZ

Jason W. Allen, Atlanta, GA

Mohammed A. Almekhlafi, Calgary, Alberta,  
Canada

Niranjan Balu, Seattle, WA

Matthew J. Barkovich, San Francisco, CA

Joachim Berkefeld, Frankfurt, Germany

Karen Buch, Boston, MA

Judah Burns, New York, NY

Danielle Byrne, Dublin, Ireland

Federico Cagnazzo, Montpellier, France

Gloria C. Chiang, New York, NY

Daniel Chow, Irvine, CA

Kars C.J. Compagne, Rotterdam, The Netherlands

Yonghong Ding, Rochester, MN

Birgit Ertl-Wagner, Toronto, Ontario, Canada

Aaron Field, Madison, WI

Nils D. Forkert, Calgary, Alberta, Canada

Frank Gaillard, Melbourne, Australia

Joseph J. Gemmete, Ann Arbor, Michigan

Brent Griffith, Detroit, MI

Michael J. Hoch, Philadelphia, PA

Joseph M. Hoxworth, Phoenix, AZ

Raymond Y. Huang, Boston, MA

Susie Y. Huang, Boston, MA

Ferdinand K. Hui, Honolulu, HI

Christof Karmonik, Houston, TX

Gregor Kasprian, Vienna, Austria

Timothy J. Kaufmann, Rochester, MN

Hillary R. Kelly, Boston, MA

Toshibumi Kinoshita, Akita, Japan

Ioannis Koktzoglou, Evanston, IL

Stephen F. Kralik, Houston, TX

Luke Ledbetter, Los Angeles, CA

Franklin A. Marden, Chicago, IL

Markus A. Möhlenbruch, Heidelberg, Germany

Mahmud Mossa-Basha, Morrisville, NC

Renato Hoffmann Nunes, Sao Paulo, Brazil

Sam Payabvash, New Haven, CT

Johannes A.R. Pfaff, Salzburg, Austria

Eike I. Piechowiak, Bern, Switzerland

Laurent Pierot, Reims, France

Alexander R. Podgorsak, Chicago, IL

Eytan Raz, New York, NY

Jeff Rudie, San Diego, CA

Paul M. Ruggieri, Cleveland, OH

Fatih Seker, Heidelberg, Germany

Maksim Shapiro, New York, NY

Timothy Shepherd, New York, NY

Mark S. Shiroishi, Los Angeles, CA

Neetu Soni, Rochester, NY

Ashok Srinivasan, Ann Arbor, MI

Jason F. Talbott, San Francisco, CA

Anderanik Tomasian, Los Angeles, CA

Fabio Triulzi, Milan, Italy

Arastoo Vossough, Philadelphia, PA

Richard Watts, New Haven, CT

Elysa Widjaja, Toronto, Ontario, Canada

Ronald Wolf, Philadelphia, Pennsylvania

Shuang Xia, Tianjin, China

Leonard Yeo, Singapore

Woong Yoon, Gwangju, South Korea

David M. Yousem, Evergreen, CO

Carlos Zamora, Chapel Hill, NC

Chengcheng Zhu, Seattle, WA

### EDITORIAL FELLOW

Alexandre Boutet, Toronto, Ontario, Canada

### SPECIAL CONSULTANTS TO THE EDITOR

#### AJNR Blog Editor

Neil Lall, Denver, CO

#### Case of the Month Editor

Nicholas Stence, Aurora, CO

#### Case of the Week Editors

Matylda Machnowska, Toronto, Ontario, Canada

Anvita Pauranik, Calgary, Alberta, Canada

#### Classic Case Editor

Sandy Cheng-Yu Chen, Taipei, Taiwan

#### Health Care and Socioeconomics Editor

Pina C. Sanelli, New York, NY

#### Physics Editor

Greg Zaharchuk, Stanford, CA

#### Podcast Editor

Kevin Hiatt, Winston-Salem, NC

#### Twitter Editor

Jacob Ormsby, Albuquerque, NM

### Official Journal:

American Society of Neuroradiology

American Society of Functional Neuroradiology

American Society of Head and Neck Radiology

American Society of Pediatric Neuroradiology

American Society of Spine Radiology

Founding Editor

Juan M. Taveras

Editors Emeriti

Mauricio Castillo, Robert I. Grossman,

Michael S. Huckman, Robert M. Quencer

Managing Editor

Karen Halm

Assistant Managing Editor

Laura Wilhelm

Executive Director, ASNR

Mary Beth Hepp





The Whirlpool Galaxy (NGC 5194) (aka Messier 51) is a spiral galaxy that is interacting with its smaller companion (NGC 5195). While the central globular structure is observable with small telescopes and binoculars, there is also an extensive nebula associated with these galaxies that is only observable with CCD images, as in this case. Discovered in 1773, M51 is located 31 million light-years from Earth in the constellation Canes Venatici. This image was acquired as a series of 34 5-minute exposures (2.8 hours) using red, green, and blue filters. The telescope was a Planewave 20" corrected Dall-Kirkham Astrograph, f/4.5 on a Planewave Ascension 200HR mount situated in New Mexico. The camera was a FLI ProLine PL11002M CCD, with Astrodon filters. The images were processed using PixInsight, Photoshop, and Topaz Labs Adjust AI and DeNoise AI.

*Jeffrey S. Ross, Mayo Clinic, Phoenix, Arizona*

# Symptomatic Developmental Venous Anomaly: State-of-the-Art Review on Genetics, Pathophysiology, and Imaging Approach to Diagnosis

C.C.-T. Hsu and T. Krings



## ABSTRACT

**SUMMARY:** Developmental venous anomalies (DVAs) are the most common slow-flow venous malformation in the brain. Most DVAs are benign. Uncommonly, DVAs can become symptomatic, leading to a variety of different pathologies. DVAs can vary significantly in size, location, and angioarchitecture, and imaging evaluation of symptomatic developmental venous anomalies requires a systematic approach. In this review, we aimed to provide neuroradiologists with a succinct overview of the genetics and categorization of symptomatic DVAs based on the pathogenesis, which forms the foundation for a tailored neuroimaging approach to assist in diagnosis and management.

**ABBREVIATIONS:** BRBNS = blue rubber bleb nevus syndrome; CCM = cerebral cavernous malformation; CMMRD = constitutional mismatch repair deficiency syndrome; CVMS = cerebrofacial venous metamerism syndrome; DVA = developmental venous anomaly; WMH = white matter hyperintensities

Developmental venous anomaly (DVA) is an extreme variation of a transmedullary vein composed of a radial complex of medullary veins resembling a “Medusa head,” which converges into a “collector” vein that ultimately drains into either the deep or superficial cerebral venous system. DVAs are the most common form of slow-flow venous malformation in the brain, with an estimated incidence of 2.6%–6.4%, and the overwhelming majority are asymptomatic.<sup>1</sup> Histologically, DVAs are composed of dilated venous channels that are interspersed in the white matter, with simple or complex variations in venous architecture and drainage patterns.<sup>2</sup> DVAs represent a less efficient form of the venous drainage route, which is dependent on one or few collector veins, and with time, the exposure to higher venous pressure may cause vascular remodeling with vessel wall thickening and microvascular hyalinization.<sup>2</sup> Evidence from cohort studies and case series suggests a diverse array of clinical manifestations related to symptomatic DVAs.<sup>3,4</sup> We performed a comprehensive review of the pathogenesis of DVAs and discuss imaging and management approaches to symptomatic DVAs.

## Neurovascular and Genetic Pathogenesis

The neurovascular hypothesis surrounding the etiology of DVA is based on the neurovascular adaptation of the brain venous vasculature secondary to a nonspecific insult during vasculogenesis, leading to the developmental arrest of medullary veins in the late first trimester of gestation.<sup>2,5</sup> The cerebral venous system will create compensatory pathways to counter the abnormality in the superficial or deep venous circulation during the period of venous plasticity in utero and early infancy.<sup>2,5</sup> This feature is supported by the observation of DVAs both in utero and in the perinatal period.<sup>6</sup> In recent years, genetic studies have advanced our understanding of the pathogenesis of DVAs. Genetic analysis of DVAs associated with a sporadic cerebral cavernous malformation (CCM) suggests that DVAs could be an intermediate lesion. DVAs may have a somatic activating mutation in the *PIK3CA* gene, leading to a gain of function, which acts as a genetic precursor to a sporadic CCM.<sup>7</sup> An acquired second-hit mutation in the CCM complex (*KRIT1*, *CCM2*, *PDCD10*) or *MAP3K3* then results in the formation of a sporadic CCM,<sup>7</sup> supported by the observation that sporadic CCMs often develop within the venous drainage territory of the DVA.<sup>8</sup> On the other hand, hereditary CCMs preferentially develop via a mutation in the CCM complex (*CCM1*, *CCM2*, *CCM3* gene loci) or the *MAP3K3* locus, causing multiple quiescent CCMs, which may acquire an additional mutation in *PIK3CA*, driving lesional growth.<sup>7</sup>

## Symptomatic DVA

Symptomatic DVA is an umbrella term that encompasses a diverse range of DVA-related complications. Systematic review predominately from low-level evidence (ie, case series or case-control studies) showed that an astounding 61% of DVAs are

Received October 15, 2022; accepted after revision February 23, 2023.

From the Division of Neuroradiology (C.C.-T.H.), Department of Medical Imaging, Gold Coast University Hospital, Southport, Queensland, Australia; Division of Neuroradiology (C.C.-T.H.), Lumus Imaging, Varsity Lakes, Queensland, Australia; and Division of Neuroradiology (T.K.), Department of Medical Imaging, Toronto Western Hospital; University Medical Imaging Toronto and University of Toronto, Ontario, Canada.

This review was presented as an education exhibit (NR118-ED-X) at the Radiological Society of North America (RSNA) Annual Meeting in 2016 and received a Certificate of Merit.

Please address correspondence to Dr. Charlie Chia-Tsong Hsu, MBBS, FRANZCR, Gold Coast University Hospital, Division of Neuroradiology, Department of Medical Imaging, 1 Hospital Boulevard, Southport, Queensland, Australia; e-mail: charlie.ct.hsu@gmail.com

Indicates open access to non-subscribers at [www.ajnr.org](http://www.ajnr.org)  
<http://dx.doi.org/10.3174/ajnr.A7829>

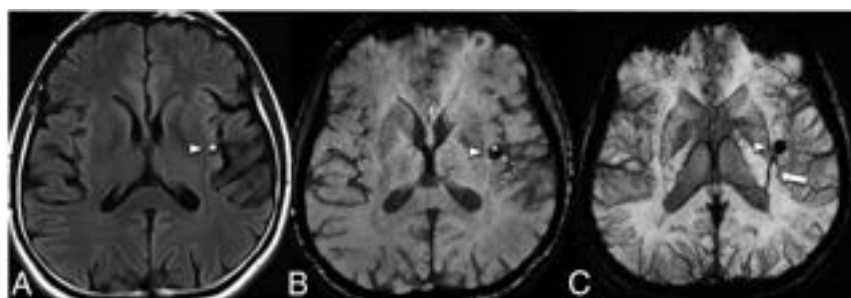


**FIG 1.** FLAIR (A) shows a mixed-signal-intensity CCM (arrowhead) in the left insular cortex with an internal blood-fluid level and no perilesional edema. A collector vein of a DVA (arrow) is seen from the ventricular ependyma to the CCM, which is barely visible on the SWI (B) and becomes more conspicuous on the susceptibility-weighted MIP image (C).

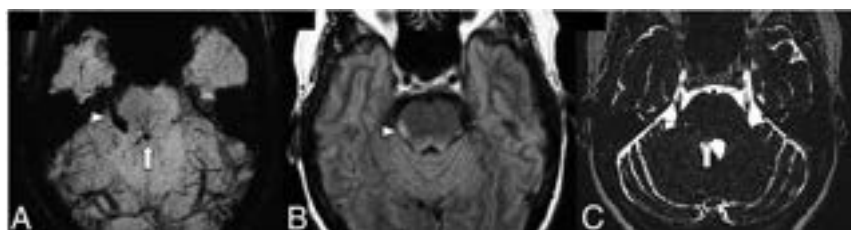


**FIG 2.** A patient with right facial pain and dysesthesia. SWI (A) shows a posterior pontine DVA (arrow) and an associated CCM (arrowhead) involving the intra-axial and cisternal segments of the right trigeminal nerve. FLAIR (B) demonstrates hyperintense edema along the right lateral aspect of the pons (arrowhead). Coregistered T2 sampling perfection with application-optimized contrasts by using different flip angle evolutions (SPACE sequence; Siemens) (C) confirms CCM involvement of the right trigeminal nerve.

asymptomatic: 23% with nonspecific clinical presentation, 6% with a focal neurologic deficit, 6% with hemorrhage, 4% with seizures, and <1% with infarct.<sup>1</sup> However, given our clinical experience, this reported incidence of symptomatic DVAs is very likely overestimated due to reporting bias. In fact, in a population-based study, most DVAs, ie, 98%, were detected incidentally, with only 2% of DVAs being symptomatic and attributed to hemorrhage or infarct.<sup>1</sup> The natural course of patients with DVA suggests a very low risk of hemorrhage after the first presentation, ranging from 0% to 1.28% per year.<sup>1</sup> During the past decade, advanced imaging techniques have aided our understanding of DVAs. Optimized imaging protocols should be applied to investigate symptomatic DVAs, tailored to clinicopathologic entities.

### **Coexisting CCM or Capillary Telangiectasia**

CCMs are vascular sinusoidal lesions lined by a single endothelial layer in a background of a collagenous matrix. CCMs are devoid of arterial or venous communication. They have a strong association with sporadic DVAs, with a frequency of coexistence of between 2% and 33% (Fig 1). The prevalence of CCMs with DVAs also have a positive correlation with increasing age.<sup>4</sup> SWI is the ideal sequence to detect DVAs with CCMs due to the increased contrast conspicuity of the deoxyhemoglobin in the venous blood and the presence of blood products in CCMs. The SWI sequence on high-field-strength 7T MR imaging is more sensitive for depicting smaller-sized DVAs associated with sporadic CCMs, which may otherwise not be visible on 3T MR imaging.<sup>9</sup>

As to the formation of CCMs in DVAs, there is a recently proposed genetic model for the formation of CCMs from a “2-hit hypothesis.”<sup>7</sup> However, a more mechanical model for the de novo formation of a CCM around a DVA is proposed on the basis of a combination of venous congestion and venous ischemia due to poor venous outflow leading to a release of local angiogenic factors and endothelial proliferation. Newly formed fragile vessels are prone to bleeding, creating an initial petechial hemorrhage, and repeat cycles of re-endothelialization and hemorrhage eventually lead to the classic multilobulated MR imaging appearance of a CCM.<sup>10</sup>

The triggered angiogenesis, which forms fragile vessels prone to hemorrhage as well as recurrent cycles of angiogenesis and microbleeds ultimately lead to the formation of CCMs.<sup>10</sup> The following anatomic factors predispose to the development of CCMs within the drainage territory of a DVA: infratentorial DVA location, drainage of the collector into a deep vein, torsion of the draining vein,  $\geq 5$  medullary veins

draining into a collector, stenosis of  $>55\%$  of the medullary veins, and an acute angle between the medullary and the collector vein of  $\leq 106.5^\circ$ .<sup>8,11-13</sup> Note that most of the above-mentioned anatomic factors contribute to a decreased outflow of the DVA, thus supporting a venous congestion model of the formation of CCMs in the vicinity of a DVA. Systematic factors such as major infectious illness, chronic inflammatory disorders, and radiation exposure/treatment are also implicated in the formation of CCMs.<sup>12</sup> The proinflammatory state is believed to promote thrombosis within the DVA, raising the venous pressure to promote an environment for CCM formation.<sup>12</sup> Topographical location of CCMs are important as cortical or juxtacortical location or limbic involvement are more prone to seizure.<sup>14</sup> Brainstem CCM may cause cranial neuropathy through the involvement of the cranial nerve nuclei, intra-axial cranial nerve pathway or even direct extension into the cisternal cranial nerves (Fig 2).<sup>15</sup> Hemorrhagic propensity of CCM hemorrhage is based on the history of prior hemorrhage and this can be quantitatively analyzed through the CCM hemosiderin burden and its evolution over time on quantitative susceptibility mapping (QSM).<sup>16,17</sup> Higher mean susceptibility value on QSM positively correlates with patient age and prior hemorrhagic episodes, whilst patients with clinically stable CCM demonstrate lower mean susceptibility value (Fig 3).<sup>16,17</sup>

Less commonly, capillary telangiectasias can be seen in the venous drainage territory of a DVA. Capillary telangiectasia consists of clusters of dilated capillaries with intervening normal brain parenchyma and is more commonly located in the brainstem but can also be found in the supratentorial brain. Capillary



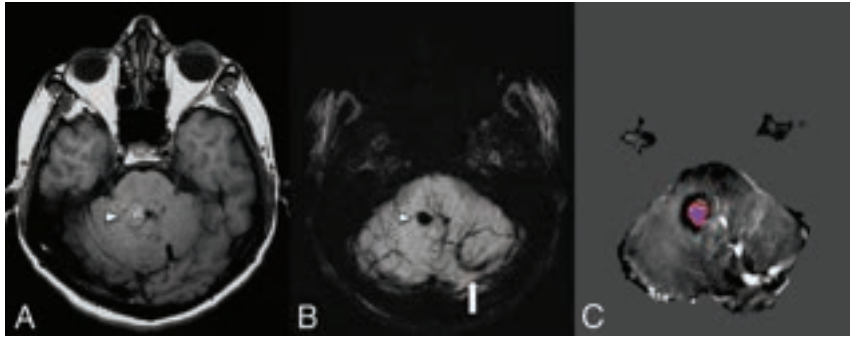


**FIG 3.** A middle-aged patient with new-onset ataxia. TIWI (A) and SWI MIP (B) show a CCM in the right superior cerebellar peduncle (*arrowheads*) and a large left cerebellar DVA with the collector vein (*arrow*) draining into the transverse sinus. Quantitative susceptibility mapping (C) analysis of the CCM shows a high mean susceptibility value of 858 parts per billion (with threshold). An ROI with a red boundary represents the exclusive object boundary, and the purple area represents thresholded pixels (150 parts per billion). SWIM (Siemens) parameters: TE = 20.00 ms; TR = 27.00 ms; flip angle = 15°; resolution = 0.937 × 0.937 × 2.5 mm. Images courtesy of Dr E. Mark Haacke.

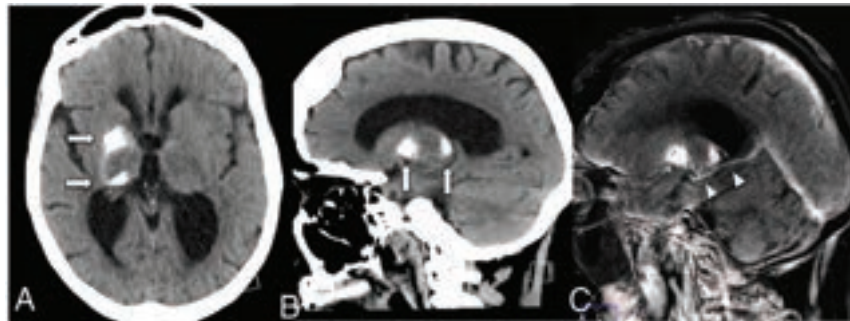


**FIG 4.** Noncontrast CT of the head (A and B) shows dystrophic calcification of the anterior right putamen and pulvinar of the thalamus (*arrows*). CTV MIP sagittal image (C) shows a right basal ganglia DVA (*arrowheads*) with the collector vein draining into the ipsilateral internal cerebral vein (*arrows*).

telangiectasia has a more benign natural history than CCMs, and its detection requires SWI and a gadolinium-enhanced T1-weighted sequence for diagnosis. Thus, coexisting capillary telangiectasia with a DVA may be underreported.

### Parenchymal Abnormalities

The brain parenchyma in the venous drainage territory of a DVA can be associated with white matter hyperintensities (WMH), microbleeds, mineralization, metabolic derangements and may even be more prone to the formation of demyelination plaque in patients with pre-existing demyelinating diseases such as MS. DVA drainage has a relatively larger venous territory compared with physiologically normal cortical or medullary veins and is reliant on usually  $\leq 1$  collector vein. The venous drainage territory of a DVA usually has only a deep or a superficial drainage route rather than multiple superficial and a deep drainage possibility. With time, the thus-impaired venous hemodynamics may contribute to the progressive thickening and hyalinization of the venous walls of DVAs, leading to increased resistance, decreased compliance, and venous hypertension causing focal edema and gliosis in the circumjacent white matter or mineralization of the adjacent gray matter. WMH around a DVA have an incidence of 12.5% (an adjusted prevalence of 7.8% after exclusion of patients with moderate-to-chronic white

matter disease) and are more common in a periventricular location of the DVA.<sup>18</sup> WMH associated with DVAs were statistically seen more frequently with coexisting microbleeds, supporting the notion of a common pathogenic (ie, venous congestive) process.<sup>19</sup>

Basal ganglia and deep cerebellar nuclei are regions of the brain with higher metabolic demands. The presence of a DVA in these locations across time may lead to increased mineralization within the affected deep gray matter structure (Fig 4).<sup>20</sup> Metabolic abnormalities can also be encountered in the venous drainage territory of a DVA. A small case series of 22 patients found that 76% of DVAs studied had metabolic changes on FDG-PET/CT scans in the form of hypometabolism, which was significantly more common in older patients (Fig 5).<sup>21</sup> A subsequent larger study with 54 patients with 57 DVAs showed evidence of metabolic abnormalities in 38% of patients; in this study, hypometabolism was more common in DVAs draining gray matter rather than white matter.<sup>22</sup> Hypometabolism has been reported in regions corresponding to neurologic symptoms; for example, hypometabolism was seen in the visual tracts in patients with visual symptoms and a corresponding DVA.<sup>23</sup> Most interesting, structural abnormalities (ie,

WMH) were not seen in these patients with abnormalities on functional images.<sup>21,22</sup> Again, this finding is supportive of the notion that DVAs have a less robust venous drainage pathway.

The relationship between DVA and demyelination is not well-understood. Demyelination is an autoimmune disease with a perivascular pattern of inflammatory response secondary to lymphocytic and monocytic infiltration. Brain parenchyma around a DVA may be more vulnerable to the formation of demyelinating plaques in patients with pre-existing demyelinating diseases such as MS (Fig 6).<sup>24</sup> A proposed theory is that venous congestion may lead to a higher and longer duration of lymphocytic infiltration and, thus, a greater degree of a neuroinflammatory reaction than a brain with a normal venous drainage pattern.

Uncommonly, DVAs can be seen in regions of malformation of cortical development (polymicrogyria, pachygyria, and focal cortical dysplasia). It is uncertain whether the coexistence of the 2 entities is incidental or due to a shared common insult in the pathway of cerebral venous development, with interruption of normal cortical development and of normal cortical and dural venous sinus development. The true incidence of the association of polymicrogyria and DVA is not known because the studies were based on case series with small sample sizes. However, it is unlikely that a DVA contributes to epileptogenesis. A case series

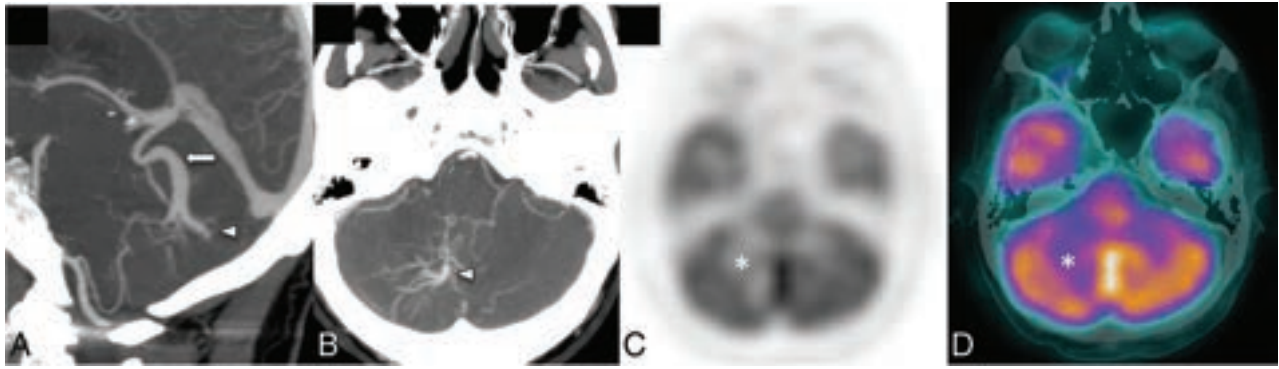


**FIG 5.** A patient with headache and ataxia. CTA sagittal and axial MIP images (A and B) show a right cerebellar hemisphere DVA (*arrowheads*) with the collector vein (*arrow*) draining into the vein of Galen. Corresponding [ $^{18}\text{F}$ ] FDG-PET/CT attenuation-corrected image (C) and a fused PET/CT image (D) show moderate reduction of [ $^{18}\text{F}$ ] FDG uptake in the right cerebellar hemisphere in the venous territory of the large DVA (*asterisk*).

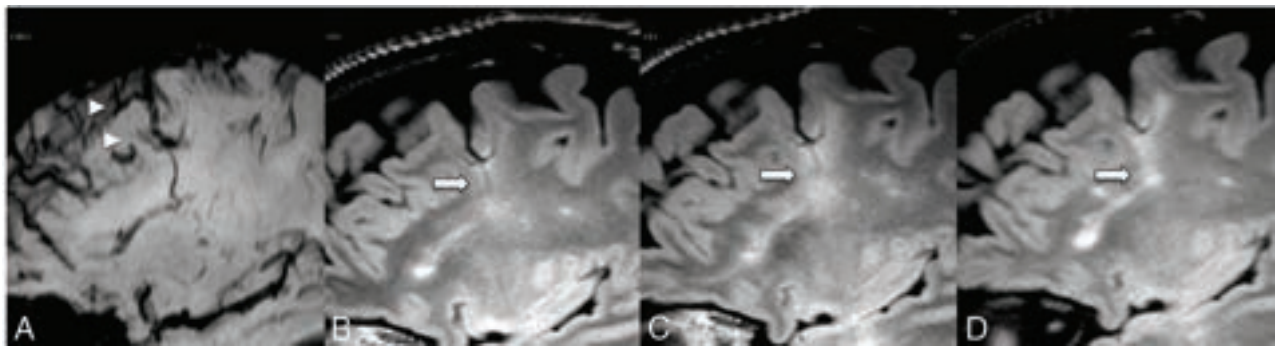


**FIG 6.** A patient with MS with an SWI (A) demonstrating a DVA. FLAIR at 6-month (B), 1-year (C), and 2-year (D) follow-up shows an enlarging demyelinating plaque (*arrows*) centered around the DVA.

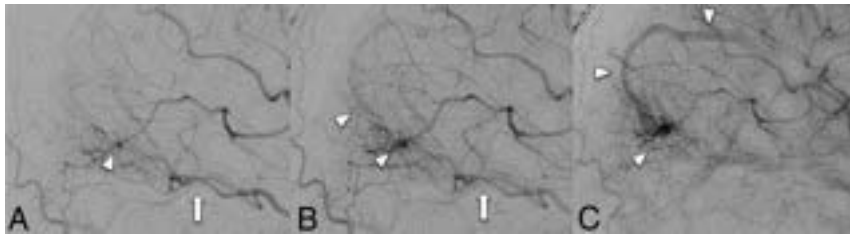


**FIG 7.** DSA cerebral catheter angiogram in the arterial phase image (A) demonstrates a left occipital AVM nidus (*arrowhead*) supplied by the left posterior cerebral artery (*arrow*). Subsequent late arterial (B) and early venous (C) images show the AVM nidus (*arrowhead*) draining into a right occipital DVA (*arrowhead*), with an early venous filling of the collector vein (*arrowhead*). The patient underwent stereotactic radiation treatment with successful obliteration of the AVM nidus with preservation of the DVA venous architecture.

by Striano et al<sup>25</sup> showed only 4 of 1020 patients with epilepsy had associated DVAs. It is uncertain whether DVAs and cortical dysplasia share a common cerebrovascular pathogenesis; however, DVAs are unlikely to constitute an epileptogenic focus. Nevertheless, it is important to identify the presence of a DVA in the area of cortical dysplasia. In the context of neurosurgical resection of a focal cortical dysplasia (FCD), unknowing or inadvertent resection of the DVA may result in catastrophic venous infarction due to its vulnerability to hemodynamic changes, further highlighting DVAs being “no-touch” lesions.

### Flow-Related Complications

As mentioned above, DVAs are related to a less compliant venous drainage of the brain because either the deep or the superficial venous routes are not established. Thus, a limited number of collector veins drain a relatively large territory of brain parenchyma. Collector veins can, therefore, be overloaded due to the multiple, dilated medullary veins feeding them. A disturbance in the balance between inflow and outflow of blood can lead to flow-related neurologic complications. Flow-related complications were found in up to 71% of symptomatic DVAs, though this study was likely biased, given its referral base from a neurovascular center.<sup>3</sup> Flow-related complications include increased flow from an arteriovenous shunt such as a DVA draining an AVM (Fig 7) or a “microshunting” phenomenon from increased arterial blood flow into a DVA, leading to early venous filling. DVA outflow complications can be attributed to either stenosis or thrombosis of the DVA collector vein. A DVA with a MicroShunt shows early venous filling of the DVA on angiography secondary to an increased arteriolar inflow of blood. This is a phenomenon most commonly seen in large-sized DVAs or DVAs



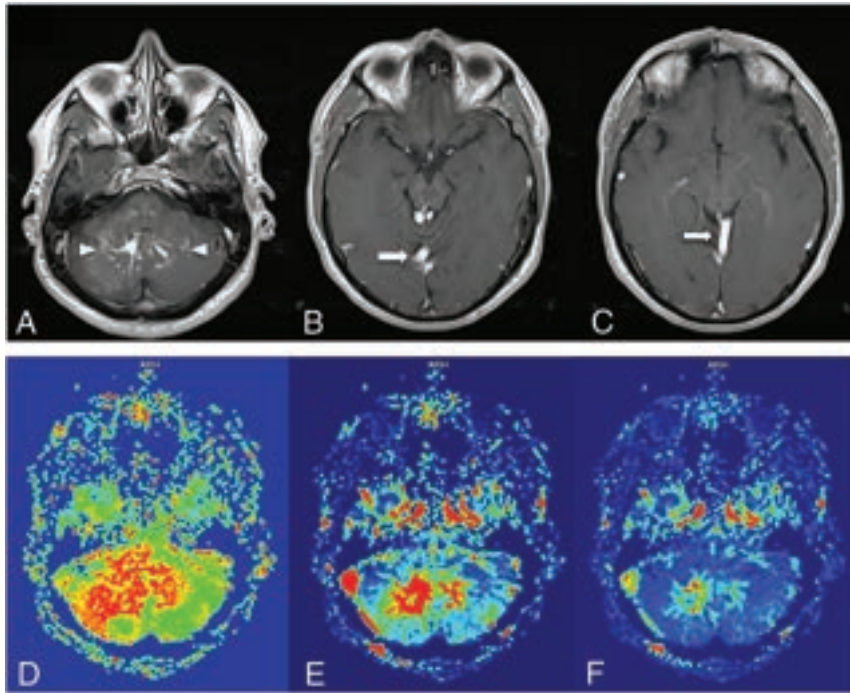


**FIG 8.** A patient with headache and ataxia. Contrast-enhanced T1WI (A–C) shows the DVA medusa veins in the cerebellar hemispheres (arrowheads) with a pair of draining veins and ultimately a common collector vein (arrows) draining into the right tentorial venous sinus. DSC MRI perfusion demonstrates a pronounced and asymmetrically increased MTT (D) in the right cerebellar hemisphere, consistent with venous hypertension. CBV (E) and CBF (F) images shows expected increased cerebral blood volume and flow in the DVA medusa veins.

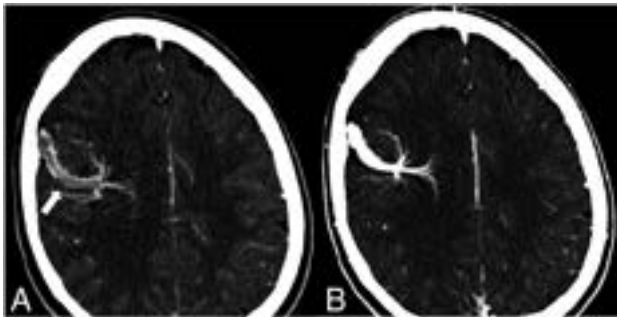


**FIG 9.** A young patient presented with a sudden onset of severe headaches after a marathon race. Presentation CTV (A) shows thrombosis of a DVA collector vein (arrow) overlying the right frontal cerebral convexity. The patient was placed on antiplatelet medication, and a follow-up CTV (B) showed a resolution of the thrombus.

with complex angioarchitecture. MR imaging perfusion techniques such as DSC and arterial spin-labeling can better characterize the microcirculation of a DVA.<sup>26–29</sup> On DSC perfusion, normal DVAs follow the cerebral vein and dural venous sinus hemodynamics, with elevated relative CBV and CBF. DVAs with venous outflow impairment may reveal an elevated MTT (Fig 8).<sup>26–29</sup> In a cohort study, Jung et al<sup>27</sup> demonstrated that the area around a DVA with increased signal intensity on T2 and FLAIR showed increased relative CBV and MTT compared with normal white matter. This finding is supportive of the hypothesis of symptomatic DVAs with a microshunt leading to venous congestion and, with time, perivascular gliosis around the DVA.

Venous thrombosis can occur in DVAs, leading to venous ischemia or hemorrhage. The paucity of reports of thrombosed DVAs in the earlier literature may be due to under-recognition and reporting. Marked hyperdensity of the collector vein on noncontrast CT may be a sign of a thrombosed DVA and warrants further investigation with CT or MRV. A literature review of a small number of cases of thrombosed DVAs suggests similar procoagulant risk factors, such as oral contraception, postpartum, or no identifiable risk.<sup>2</sup> There is currently no evidence to suggest that DVAs are more prone to thrombosis than normal cerebral veins. However, it is important for the radiologist to identify a thrombosed DVA because treatment is similar to that of venous or dural sinus thrombosis: Anticoagulation is used in the treatment of thrombosed DVAs, aiming to prevent the progression of the thrombus, limit new thrombus formation, and facilitate recanalization of the collector vein (Fig 9). The standard precaution for initiating anticoagulation is unchanged except for the potential

risk of bleeding when there is a coexisting CCM. DVAs with venous outflow obstruction due to narrowing or kinking of the collector veins can also lead to increased venous congestion. Neurovascular intervention could be considered in selective cases when conservative treatment fails. Recently, a case of rescue venous stent placement has been reported in a patient with a pontomedullary DVA with venous outflow obstruction despite conservative treatment with anticoagulation.<sup>30</sup>

Spontaneous hemorrhage related to a DVA is uncommon and should be attributed to an underlying CCM, venous outflow obstruction, or flow-related shunt with a microaneurysm unless proved otherwise, further highlighting DVAs being no-touch lesions, which should not be removed, irradiated, or embolized. Vascular imaging and recognition of the DVA are paramount because often the DVA could be masked or distorted by the hematoma. When the surgical evacuation of a cerebral hematoma is considered, effort should be made to preserve the DVA.

### Mechanical Effect

The collector vein of a DVA can rarely lead to a mechanical effect on adjacent structures. In the posterior fossa, collector veins near the root entry zone of cranial nerves can lead to neurovascular conflicts such as trigeminal neuralgia. The neurovascular decompression procedure requires more attention because the venous wall of the DVA collector vein is more delicate than an arterial vessel and has to be preserved. Rarely, the DVA collector vein can obstruct CSF flow at the cerebral aqueduct

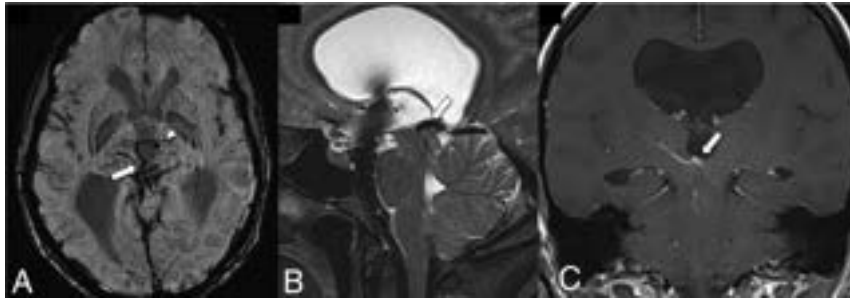


**FIG 10.** A midline midbrain DVA with the collection vein (arrow) obstructs the cerebral aqueduct leading to ventriculomegaly. SWI (A) shows the radially oriented medullary veins in the midbrain and an associated microbleed in the left anterior thalamus (arrowhead). T2-SPACE (B) and gadolinium-enhanced T1-weighted (C) images depict the location of a large collector vein obstructing the entrance into the cerebral aqueduct. Images courtesy of Dr Arjuna Somasundaram and Dr Christian Schwindack.

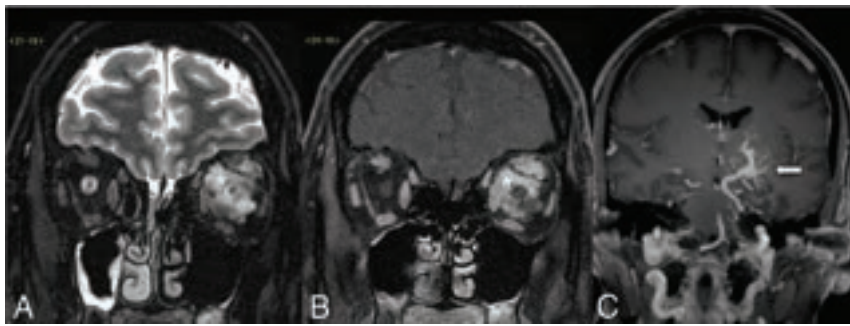


**FIG 11.** CVMS in a patient with a left orbital venous malformation depicted on the coronal T2-weighted fat saturated (A) and coronal post-gadolinium-enhanced T1-weighted fat saturated (B) images, which show an infiltrative T2-weighted hyperintense intraconal lesion with avid contrast enhancement (asterisk). Coronal gadolinium-enhanced T1-weighted image (C) reveals a large left basal ganglia DVA (arrow) with the collector vein draining in the left superior petrosal sinus.

(Fig 10).<sup>31</sup> Depending on the degree of obstruction and resultant hydrocephalus, there may be a need for CSF shunting or an endoscopic ventriculostomy CSF diversion procedure as a treatment.<sup>32</sup>

### Syndromic Association

Most DVAs have sporadic and isolated findings; however, DVAs can be part of a syndromic feature in patients with mutations in either shared RAS-MAPK and PI3K/AKT/mTOR intracellular signaling pathways, which are drivers of the phenotypic development of vascular malformations and tumors.<sup>33</sup> Most notably, syndromes associated with DVAs include blue rubber bleb nevus syndrome (BRBNS), constitutional mismatch repair deficiency syndrome (CMMRD), and the more recently described cerebrofacial venous metamerism syndrome (CVMS). BRBNS is mostly sporadic, but a few reported cases show autosomal dominant inheritance caused by TIE2/TEK somatic mutations, which encode the endothelial cell-specific tyrosine kinase receptor that functions via the PI3K/AKT/mTOR signaling pathway. The syndrome is characterized by multiple rubbery venous malformations found in the skin, brain, and visceral organs. The correlation between DVAs and BRBNS was underestimated in the older literature due to imaging techniques and the nonunified use of DVA as descriptive terminology.<sup>34</sup> CMMRD is also known to be associated with

DVAs. It is an autosomal recessive biallelic (homozygous) germline mutation in the mismatch repair genes (*MLH1*, *MSH2*, *MSH6*, and *PMS2*).<sup>35</sup> CMMRD manifests as neoplastic and non-neoplastic processes such as a DVA. Oncologic manifestations of the CMMRD are variable in the CNS, along with intestinal tumors and hematologic malignancy.<sup>35</sup> There is a robust association of CMMRD with DVAs, which has been suggested to be a potential quantifiable factor for CMMRD, and this is further support for a genetic basis for DVAs.<sup>35</sup> In CVMS, facial venous malformations have a 20%–28% association with DVAs, and most of the DVAs are ipsilateral and in the same metamere as the superficial venous malformation (Fig 11).<sup>36,37</sup> The association between DVAs and head and neck venous malformations may share a common developmental pathogenesis.

### CONCLUSIONS

Symptomatic DVAs can lead to a diverse array of clinical diseases, which can be categorized on the basis of their pathophysiologic mechanism. Neuroimaging plays a fundamental role in characterizing the angioarchitecture of the DVA and assessment of the parenchyma surrounding the DVA, using conventional, advanced, or functional imaging techni-

ques. An accurate depiction of the pathophysiologic mechanism responsible for symptomatic DVAs are crucial for management and prognosis.

### ACKNOWLEDGMENTS

Dr Krings acknowledges the generous support from the Patricia Holt-Hornsby and Dan Andreae Vascular Research Unit and UMIT (University Medical Imaging Toronto).

Disclosure forms provided by the authors are available with the full text and PDF of this article at [www.ajnr.org](http://www.ajnr.org).

### REFERENCES

- Hon JM, Bhattacharya JJ, Counsell CE, et al. **The presentation and clinical course of intracranial developmental venous anomalies in adults: a systematic review and prospective, population-based study.** *Stroke* 2009;40:1980–85 CrossRef Medline
- Ruiz DS, Yilmaz H, Gailloud P. **Cerebral developmental venous anomalies: current concepts.** *Ann Neuro* 2009;66:271–83 CrossRef Medline
- Pereira VM, Geibprasert S, Krings T, et al. **Pathomechanisms of symptomatic developmental venous anomalies.** *Stroke* 2008;39:3201–15 CrossRef Medline
- Nabavizadeh SA, Mamourian AC, Vossough A, et al. **The many faces of cerebral developmental venous anomaly and its mimicks:**



- spectrum of imaging findings. *J Neuroimaging* 2016;26:463–72 CrossRef Medline
5. Rammos SK, Maina R, Lanzino G. **Developmental venous anomalies: current concepts and implications for management.** *Neurosurgery* 2009;65:20–29; discussion 29–30 CrossRef Medline
  6. Geraldo AF, Melo M, Monteiro D, et al. **Developmental venous anomaly depicted incidentally in fetal MRI and confirmed in post-natal MRI.** *Neuroradiology* 2018;60:993–94 CrossRef Medline
  7. Snellings DA, Girard R, Lightle R, et al. **Developmental venous anomalies are a genetic primer for cerebral cavernous malformations.** *Nat Cardiovasc Res* 2022;1:246–52 CrossRef Medline
  8. Meng G, Bai C, Yu T, et al. **The association between cerebral developmental venous anomaly and concomitant cavernous malformation: an observational study using magnetic resonance imaging.** *BMC Neurol* 2014;14:50 CrossRef Medline
  9. Frischer JM, Göd S, Gruber A, et al. **Susceptibility-weighted imaging at 7 T: Improved diagnosis of cerebral cavernous malformations and associated developmental venous anomalies.** *Neuroimage Clin* 2012;1:116–20 CrossRef Medline
  10. Su IC, Krishnan P, Rawal S, et al. **Magnetic resonance evolution of de novo formation of a cavernoma in a thrombosed developmental venous anomaly: a case report.** *Neurosurgery* 2013;73:E739–44; discussion E745 CrossRef Medline
  11. Yu T, Liu X, Lin X, et al. **The relation between angioarchitectural factors of developmental venous anomaly and concomitant sporadic cavernous malformation.** *BMC Neurol* 2016;16:183 CrossRef Medline
  12. Kumar S, Lanzino G, Brinjikji W, et al. **Infratentorial developmental venous abnormalities and inflammation increase odds of sporadic cavernous malformation.** *J Stroke Cerebrovasc Dis* 2019;28:1662–67 CrossRef Medline
  13. Maish WN. **Developmental venous anomalies and brainstem cavernous malformations: a proposed physiological mechanism for haemorrhage.** *Neurosurg Rev* 2019;42:663–70 CrossRef Medline
  14. Khallaf M, Abdelrahman M. **Supratentorial cavernoma and epilepsy: experience with 23 cases and literature review.** *Surg Neurol Int* 2019;10:117 CrossRef Medline
  15. Adachi K, Hasegawa M, Hayashi T, et al. **A review of cavernous malformations with trigeminal neuralgia.** *Clin Neurol Neurosurg* 2014;125:151–54 CrossRef Medline
  16. Tan H, Liu T, Wu Y, et al. **Evaluation of iron content in human cerebral cavernous malformation using quantitative susceptibility mapping.** *Invest Radiol* 2014;49:498–504 CrossRef Medline
  17. Tan H, Zhang L, Mikati AG, et al. **Quantitative susceptibility mapping in cerebral cavernous malformations: clinical correlations.** *AJNR Am J Neuroradiol* 2016;37:1209–15 CrossRef Medline
  18. Santucci GM, Leach JL, Ying J, et al. **Brain parenchymal signal abnormalities associated with developmental venous anomalies: detailed MR imaging assessment.** *AJNR Am J Neuroradiol* 2008;29:1317–23 CrossRef Medline
  19. Takasugi M, Fujii S, Shinohara Y, et al. **Parenchymal hypointense foci associated with developmental venous anomalies: evaluation by phase-sensitive MR imaging at 3T.** *AJNR Am J Neuroradiol* 2013;34:1940–44 CrossRef Medline
  20. Dehkharghani S, Dillon WP, Bryant SO, et al. **Unilateral calcification of the caudate and putamen: association with underlying developmental venous anomaly.** *AJNR Am J Neuroradiol* 2010;31:1848–52 CrossRef Medline
  21. Larvie M, Timerman D, Thum JA. **Brain metabolic abnormalities associated with developmental venous anomalies.** *AJNR Am J Neuroradiol* 2015;36:475–80 CrossRef Medline
  22. Lazor JW, Schmitt JE, Loevner LA, et al. **Metabolic changes of brain developmental venous anomalies on <sup>18</sup>F-FDG-PET.** *Acad Radiol* 2019;26:443–49 CrossRef Medline
  23. Imai M, Tanaka M, Ishibashi K, et al. **Glucose hypometabolism in developmental venous anomaly without apparent parenchymal damage.** *Clin Nucl Med* 2017;42:361–63 CrossRef Medline
  24. Rogers DM, Peckham ME, Shah LM, et al. **Association of developmental venous anomalies with demyelinating lesions in patients with multiple sclerosis.** *AJNR Am J Neuroradiol* 2018;39:97–101 CrossRef Medline
  25. Striano S, Nocerino C, Striano P, et al. **Venous angiomas and epilepsy.** *Neurol Sci* 2000;21:151–55 CrossRef Medline
  26. Iv M, Fischbein NJ, Zaharchuk G. **Association of developmental venous anomalies with perfusion abnormalities on arterial spin labeling and bolus perfusion-weighted imaging.** *J Neuroimaging* 2015;25:243–50 CrossRef Medline
  27. Jung HN, Kim ST, Cha J, et al. **Diffusion and perfusion MRI findings of the signal-intensity abnormalities of brain associated with developmental venous anomaly.** *AJNR Am J Neuroradiol* 2014;35:1539–42 CrossRef Medline
  28. Sharma A, Zipfel GJ, Hildebolt C, et al. **Hemodynamic effects of developmental venous anomalies with and without cavernous malformations.** *AJNR Am J Neuroradiol* 2013;34:1746–51 CrossRef Medline
  29. Zhang M, Telischak NA, Fischbein NJ, et al. **Clinical and arterial spin labeling brain MRI features of transitional venous anomalies.** *J Neuroimaging* 2018;28:289–300 CrossRef Medline
  30. Kishore K, Bodani V, Olatunji R, et al. **Venous outflow stenting for symptomatic developmental venous anomaly.** *Interv Neuroradiol* 2022 Aug 17. [Epub ahead of print] CrossRef Medline
  31. Blackmore CC, Mamourian AC. **Aqueduct compression from venous angioma: MR findings.** *AJNR Am J Neuroradiol* 1996;17:458–60 Medline
  32. Xian Z, Fung SH, Nakawah MO. **Obstructive hydrocephalus due to aqueductal stenosis from developmental venous anomaly draining bilateral medial thalami: a case report.** *Radiol Case Rep* 2020;15:730–32 CrossRef Medline
  33. Borst AJ, Nakano TA, Blei F, et al. **A primer on a comprehensive genetic approach to vascular anomalies.** *Front Pediatr* 2020;8:579591 CrossRef Medline
  34. Chung JI, Alvarez H, Lasjaunias P. **Multifocal cerebral venous malformations and associated developmental venous anomalies in a case of blue rubber bleb nevus syndrome.** *Interv Neuroradiol* 2003;9:169–76 CrossRef Medline
  35. Shiran SI, Ben-Sira L, Elhasid R, et al. **Multiple brain developmental venous anomalies as a marker for constitutional mismatch repair deficiency syndrome.** *AJNR Am J Neuroradiol* 2018;39:1943–46 CrossRef Medline
  36. Brinjikji W, Mark IT, Silvera VM, et al. **Cervicofacial venous malformations are associated with intracranial developmental venous anomalies and dural venous sinus abnormalities.** *AJNR Am J Neuroradiol* 2020;41:1209–14 CrossRef Medline
  37. Brinjikji W, Nicholson P, Hilditch CA, et al. **Cerebrofacial venous met-amerism—spectrum of imaging findings.** *Neuroradiology* 2020;62:417–25 CrossRef Medline

# Erdheim-Chester Disease

J.C. Benson, R. Vaubel, B.A. Ebne, I.T. Mark, M. Peris Celda, C.C. Hook, W.O. Tobin, and C. Giannini

## ABSTRACT

**SUMMARY:** Erdheim-Chester disease is a rare non-Langerhans cell histiocytosis. The disease is widely variable in its severity, ranging from incidental findings in asymptomatic patients to a fatal multisystem illness. CNS involvement occurs in up to one-half of patients, most often leading to diabetes insipidus and cerebellar dysfunction. Imaging findings in neurologic Erdheim-Chester disease are often nonspecific, and the disease is commonly mistaken for close mimickers. Nevertheless, there are many imaging manifestations of Erdheim-Chester disease that are highly suggestive of the disease, which an astute radiologist could use to accurately indicate this diagnosis. This article discusses the imaging appearance, histologic features, clinical manifestations, and management of Erdheim-Chester disease.

**ABBREVIATIONS:** CLIPPERS = chronic lymphocytic inflammation with pontine perivascular enhancement responsive to steroids; ECD = Erdheim-Chester disease; LCH = Langerhans cell histiocytosis; MAPK = mitogen-activated protein kinase; MEK = mitogen-activated ERK kinase; RDD = Rosai-Dorfman disease

A 24-year-old previously healthy man presented to an outside institution with a subacute history of neurologic symptoms that began 2 weeks after a coronavirus disease 2019 (COVID-19) immunization booster, including headaches, slurred speech, and imbalance. MR imaging showed multifocal enhancing abnormalities of his brainstem and spinal cord. CSF analysis detected no oligoclonal bands and 2 white blood cells/high power field (protein = 99 mg/dL, glucose = 67 mg/dL). The patient was given IV methylprednisolone and an oral prednisone taper after testing had ruled out an infection. His symptoms subsequently improved but did not resolve. On examination at our institution, he had an ataxic dysarthria, gait ataxia, and bilateral leg spasticity. After a water-deprivation test, blood and urine analysis revealed elevated prolactin and central diabetes insipidus, with plasma hyperosmolality (302 mOsm/kg) and low urine osmolality (144 mOsm/kg) in the setting of polyuria. Repeat CSF analysis findings were unremarkable except for 8 white cells/high power field (protein = 136 mg/dL and glucose = 49 mg/dL). The patient was then sent for additional MR imaging of his neuraxis.

## Imaging

Initial CT images obtained at the outside institution demonstrated patchy areas of hypoattenuation centered around the

dentate nuclei of both cerebellar hemispheres. MR imaging demonstrated extensive multifocal T2-hyperintense signal abnormalities and regions of poorly marginated patchy enhancement. These were predominantly located in an almost symmetric distribution in the midbrain, dentate nuclei, and cerebellar peduncles (Fig 1). None of the abnormalities demonstrated restricted diffusion. There was a mild local mass effect associated with these findings, without obstructive hydrocephalus. Lesser involvement was observed in the periaxial white matter and optic chiasm. The pituitary infundibulum was thickened and demonstrated prominent enhancement. In the spine, similar T2-hyperintense enhancing abnormalities were seen throughout the cervical and thoracic cord (Fig 2). A whole-body PET was performed to evaluate a systemic disorder, which revealed FDG uptake in the distal femoral diaphysis with increased intramedullary density on the corresponding CT images.

During the patient's numerous imaging examinations, a long list of potential diagnoses was brought forth. The imaging appearance and temporal relation with the patient's immunization booster raised the question of a viral encephalomyelitis. Neurosarcoidosis, tuberculous, and primary CNS lymphoma were also considered as possibilities, given the multifocal signal abnormalities. Demyelinating disease was thought unlikely, given the distribution of findings and lumbar puncture results. Chronic lymphocytic inflammation with pontine perivascular enhancement responsive to steroids (CLIPPERS) was similarly considered unlikely, given the lack of a complete radiologic response to steroids and the size of the enhancing lesions.

Received January 12, 2023; accepted after revision February 23.

From the Departments of Radiology (J.C.B., I.T.M.), Laboratory Medicine and Pathology (R.V., B.A.E., C.G.), Neurosurgery (M.P.C.), Hematology and Oncology (C.C.H.), and Neurology (W.O.T.), Mayo Clinic, Rochester, Minnesota.

Please address correspondence to John C. Benson, MD, Department of Radiology, Mayo Clinic, 200 1st St SW, Rochester, MN 55902; e-mail: benson.john3@mayo.edu  
<http://dx.doi.org/10.3174/ajnr.A7832>

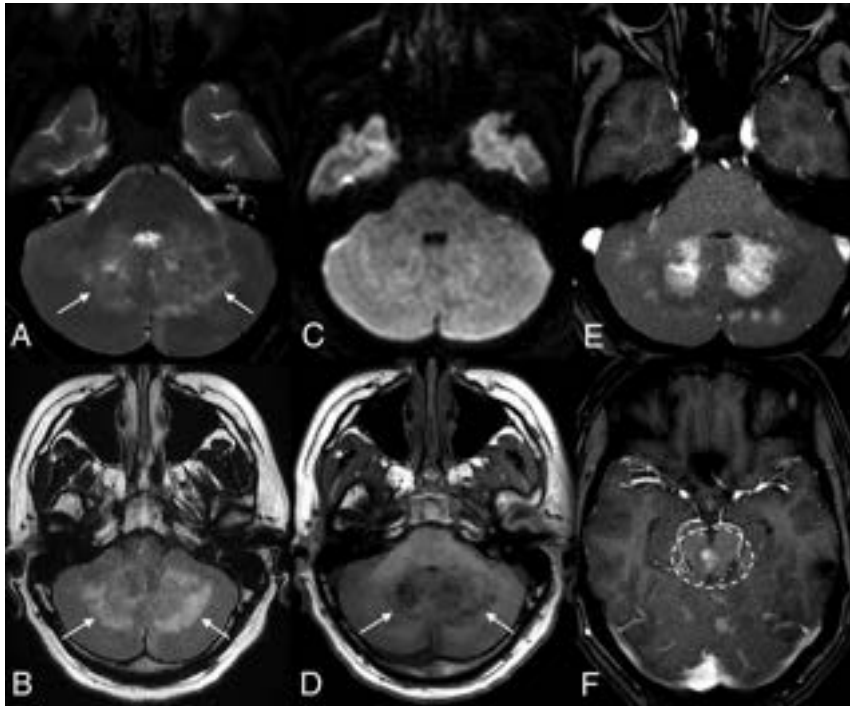


**FIG 1.** MR images of the posterior fossa demonstrate multifocal abnormalities involving both cerebellar hemispheres, particularly located around the dentate nuclei. These regions are bright on T2 and FLAIR (arrows in A and B), lack restricted diffusion (C), are hypointense on T1 (arrows in D), and demonstrate patchy enhancement on postcontrast T1 fat-saturated images (E). Similar patchy enhancement is also noted in the midbrain (dashed oval on F).

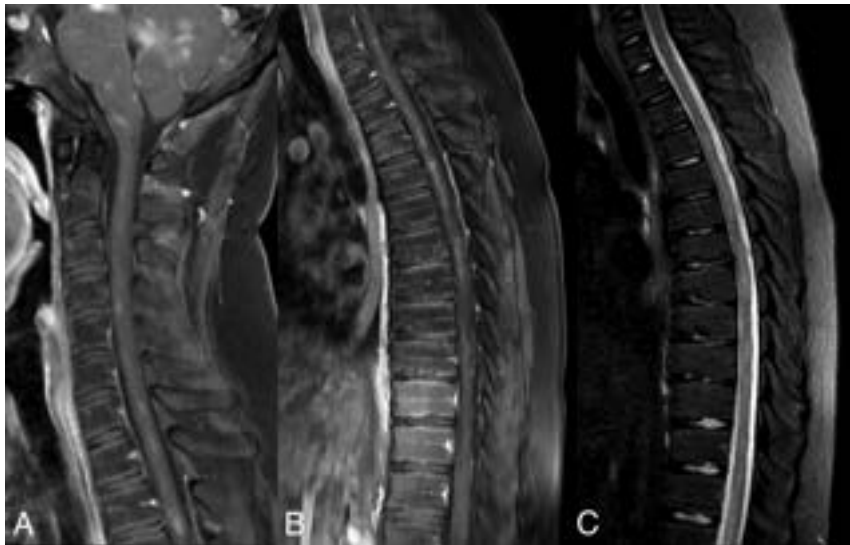


**FIG 2.** MR imaging of the cervical (A) and thoracic (B and C) spine demonstrates numerous patchy areas of enhancement along the cervicothoracic cord (A and B). Corresponding fat-saturated STIR images of the thoracic spine demonstrate multifocal T2 hyperintensities in these regions (C).

### Operative Report

The decision was made to perform a left cerebellar stereotactic needle biopsy, because it was deemed the safest area with the highest yield for diagnosis. An initial biopsy attempt was

aborted because brisk bleeding was encountered after early tissue sampling, pathology was nondiagnostic, and the patient's postoperative course was uneventful. The second procedure was planned a few weeks later using a slightly different trajectory while targeting the same region. The patient was anesthetized and positioned lateral with the head fixed in a Mayfield head holder. By means of neuronavigation, a linear incision was performed over the planned entry point, and a new burr-hole was obtained. After a small durotomy and corticotomy were performed, a stereotactic biopsy needle was carefully advanced to the target under neuronavigation guidance. Several cylinders of tissue were obtained for biopsy without incident. Frozen pathology was consistent with lesional tissue. The patient awoke at his neurologic baseline and had an uneventful postoperative course.

### Pathology

Histopathologic diagnosis in this case was very challenging. The initial cerebellar biopsy was nondiagnostic, showing only the cerebellar cortex with nonspecific Purkinje cell loss and Bergmann gliosis. The subsequent biopsy demonstrated white matter with mild, diffuse hypercellularity (Fig 3). The increased cellularity was due predominantly to foamy macrophages with small nuclei, present in a perivascular distribution and infiltrating the white matter (highlighted by CD68 immunostain). Although cytologically bland, by immunohistochemistry, the foamy macrophages showed apparent expression of *BRAF* p.V600E, a finding that was confirmed by digital droplet polymerase chain reaction. There was no acute inflammation, multinucleated giant cells, or eosinophils. Stains to evaluate a viral etiology or glial neoplasm were negative. Overall, in the context of the clinical history and imaging, the findings were most consistent with Erdheim-Chester disease (ECD). Subsequently, the patient underwent biopsy of a skin lesion on his back. Histopathologic findings of that biopsy were much more impressive, with numerous, large *BRAF*-mutant foamy histocytes and Touton giant cells, findings characteristic of ECD.

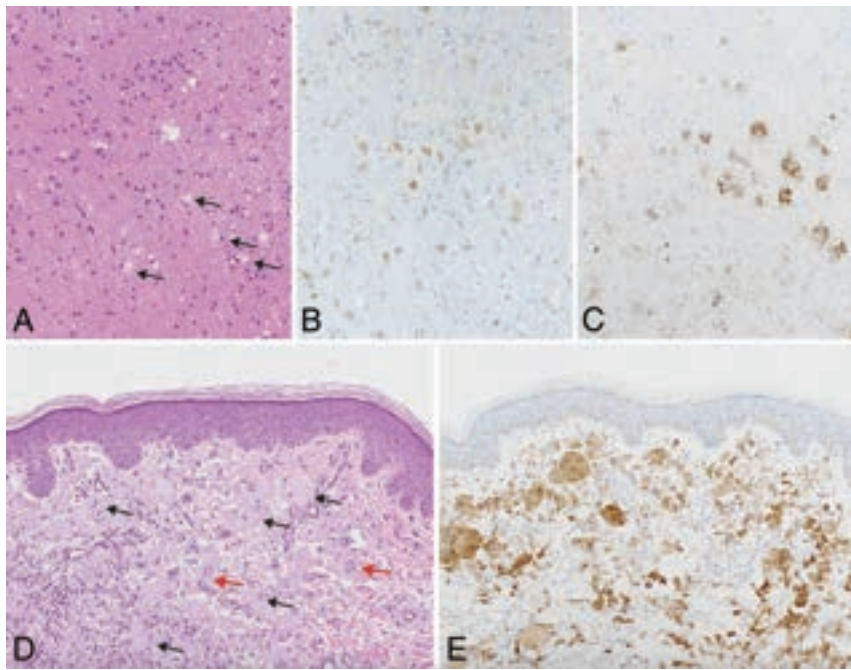


**FIG 3.** H&E-stained sections of the cerebellar biopsy (A) demonstrate mildly hypercellular white matter with increased foamy macrophages (black arrows), highlighted by CD68 immunostain (B). The macrophages were cytologically bland but show expression of *BRAF* p.V600E (C), supporting the presence of a histiocytic neoplasm. A subsequent skin biopsy (D) shows more characteristic features of ECD, including large, foamy macrophages (black arrows) and Touton giant cells (red arrows), which were positive for *BRAF* p.V600E (E). Original magnification  $\times 200$  for all images.

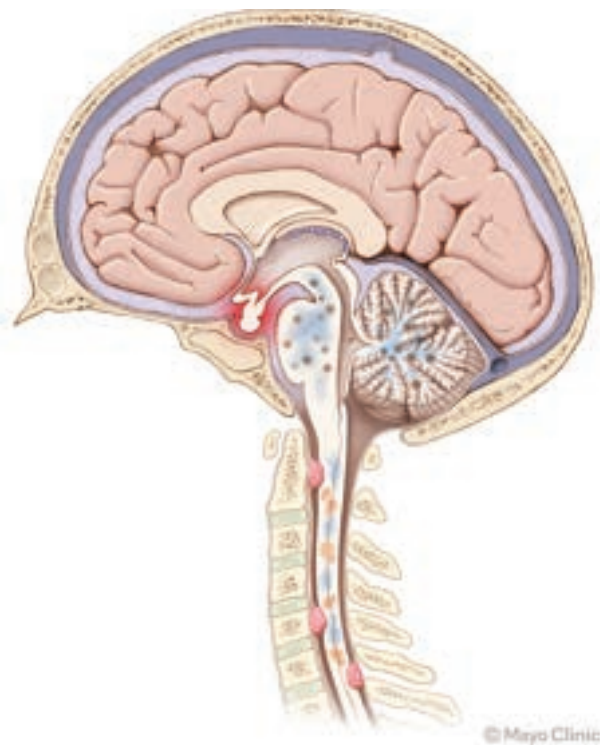


**FIG 4.** Schematic showing the various types of involvement of ECD in the CNS. Intracranially, the most common findings are focal areas of enhancement in the brainstem and/or cerebellum, with surrounding edema. The pituitary infundibulum is commonly enlarged. In the spine, both intramedullary lesions and extramedullary lesions are observed, which are often associated with adjacent edema.

## DISCUSSION

ECD is a rare non-Langerhans cell histiocytosis, in which tissues are infiltrated by lipid-laden histiocytes.<sup>1</sup> Affected patients are typically between their fifth and seventh decades of life, and the disease has a predilection for men.<sup>2</sup> ECD can affect any tissue, and the clinical manifestations are extremely heterogeneous.<sup>3</sup> Because bone, particularly the appendicular skeleton, is almost universally involved, patients may present with nonspecific bone pain; however, bony disease is frequently asymptomatic.<sup>4</sup> The severity of ECD ranges from incidental discovery in asymptomatic patients to smoldering focal involvement and multisystem fatal forms.<sup>5</sup>

CNS involvement occurs in up to 50% of patients with ECD.<sup>6,7</sup> The most commonly involved sites are the brain parenchyma, hypothalamic pituitary axis, and meninges.<sup>8</sup> Clinical symptoms of neurologic ECD are dependent on the sites of involvement. Diabetes insipidus is the most frequent manifestation; seizures, pontocerebellar dysfunction, and other neuroendocrine abnormalities including panhypopituitarism are also common.<sup>9</sup> In rare cases, ECD can present as a neuropsychiatric disorder or cognitive decline.<sup>10</sup>

The imaging appearance of neurologic ECD is dependent on distribution and extent. Intracranially, ECD often involves the posterior fossa. The most common findings are multifocal FLAIR hyperintensities of the dentate nuclei and brainstem, demonstrating variable enhancement, with or without atrophy of the affected structures.<sup>11</sup> Supratentorial structures, too, can be involved, though less often. In other patients, dural-based enhancing masses are seen, sometimes with a stellate appearance.<sup>1,12</sup> Sella imaging may demonstrate enlargement of the pituitary gland and/or stalk, sometimes with signal alterations of the affected structures, including absence of the expected hyperintense T1 signal in the posterior pituitary gland. Orbital involvement is frequent and includes infiltrating soft-tissue masses with concurrent exophthalmos. Associated osteosclerosis of the maxillofacial bones may be present.<sup>11</sup> Spinal involvement is less common and has variable appearances. Some patients have multifocal T2-hyperintense, enhancing intramedullary lesions.<sup>13</sup> Others have extramedullary masses that may compress or even infiltrate the cord (Fig 4).

The imaging findings of CNS ECD are protean and location-dependent; as a result, the differential considerations are highly variable. The patchy brainstem enhancement seen in many patients can mimic CLIPPERS or CNS lymphoma but tends to be more confluent than CLIPPERS and does not respond to steroids like these 2 entities.<sup>14</sup> Supratentorial involvement of white matter lesions, though rare, may raise concern for MS. Dural-based



## Demographics and most frequently observed CNS imaging features of ECD, RDD, and LCH

	ECD	LCH	RDD
Demographics	M >> F, 50–70 yrs	M > F, 1–3 yrs	M > F, young adults
Presentation	Commonly asymptomatic; CNS involvement leads to diabetes insipidus, pontocerebellar symptoms, and seizures	Nonspecific, including lethargy, fever, bone pain, diabetes insipidus	Lymphadenopathy, night sweats, weight loss
CNS imaging	Patchy enhancement and T2 hyperintensity in the posterior fossa; enlargement and enhancement of the pituitary stalk; loss of posterior pituitary T1 signal; intra- and extra medullary spinal lesions	Enlargement and enhancement of the pituitary stalk; loss of posterior pituitary T1 signal; neurodegenerative changes in the basal ganglia, pons, and dentate nuclei; parenchymal atrophy	Enlarged cervical lymph nodes; enhancing dural-based masses that mimic meningiomas

**Note:**—M indicates male; F, female.

masses can share the appearance of meningiomas, though this is more common in Rosai-Dorfman disease (RDD).<sup>15,16</sup> In the spine, extramedullary masses along nerve roots have been mistaken for schwannomas.<sup>17</sup>

Other histiocytic disorders can also involve the CNS. RDD is characterized by histiocyte proliferation that leads to lymphatic sinus dilation. Although patients often present with painless cervical lymphadenopathy, extranodal disease is not uncommon.<sup>18</sup> As stated above, intracranial manifestations of RDD mimic meningiomas: The disease typically presents as dural-based masses, often around the cavernous sinuses and sella region.<sup>19</sup>

Langerhans cell histiocytosis (LCH) is characterized by accumulations of epidermal dendritic cells. CNS involvement is relatively rare, usually presenting as a pituitary dysfunction such as diabetes insipidus. On imaging, the most common findings are thickening of the pituitary stalk, an enhancing suprasellar mass, and loss of normal T1 signal in the posterior pituitary gland.<sup>15</sup> Neurodegenerative changes can also be seen, presenting as symmetric signal abnormalities in the dentate nuclei, pons, and basal ganglia, as well as focal or diffuse parenchymal atrophy.<sup>20</sup> Patients also commonly have skeletal involvement, with lytic lesions in the skull and vertebra plana in the spine (Table).

Fortunately, involvement of extra-CNS organs can provide further diagnostic clues. The most common finding is sclerotic osseous lesions symmetrically involving the diaphysis of the long bones. On technetium Tc99m hydroxymethylene diphosphonate bone scans, these will demonstrate strong uptake, particularly in the distal metaphyseal regions of the femur and proximal epiphyseal regions of the tibia (the so-called “hot knees” sign, which is pathognomonic of ECD).<sup>21,22</sup> Perinephric fibrosis related to fat infiltration leads to the appearance of “hairy kidneys,” while retroperitoneal fibrosis can encase the descending aorta (“coated aorta”).<sup>23,24</sup>

Histologically, ECD is characterized by infiltrates of foamy, lipid-laden histiocytes with small nuclei. Multinucleated Touton giant cells are frequently present. By immunohistochemistry, the neoplastic cells are highlighted by the histiocytic markers CD68 and CD163 but are negative for CD1a and langerin, differentiating ECD from LCH, and are negative or weakly positive for S-100, differentiating ECD from RDD.<sup>25</sup> The histologic findings in CNS ECD may be subtle relative to other organ systems, and confirmation of a mitogen-activated protein kinase (MAPK) alteration is often necessary to establish a definitive diagnosis. The mutation-specific *BRAF* p.V600E antibody can identify cases having this alteration. Identification of other MAPK alterations requires sequencing studies. MAPK alterations are not specific to

ECD and may be observed in LCH as well as gliomas and other tumor types. Therefore, diagnosis of ECD requires integration of clinical, histologic, and molecular features.

Current treatment of these disorders relies on identification of pathogenic mutations in the affected tissue and treatment with pathway inhibitors. Patients with CNS involvement invariably require treatment, whereas isolated single-system disease such as pulmonary disease can often be monitored. Vemurafenib, a *BRAF* inhibitor, was the first FDA-approved therapy for histiocytic disorders for patients with the *BRAF* p.V600E mutation.<sup>26</sup> Cobimetinib is a mitogen-activated ERK kinase (MEK) inhibitor, which was approved in 2022 for treatment of ECD, regardless of mutation status. For patients not responding to these agents who do not have another targetable mutation, cytotoxic therapies such as cladribine or methotrexate are typically used.

The treatment of ECD has evolved with time.<sup>27</sup> Surgery, radiation therapy, steroids, cytotoxic drugs, and interferon- $\alpha$  have all been used with variable efficacy.<sup>28,29</sup> Then, multiple studies found that more than one-half of ECD tissue samples demonstrated *BRAF* p.V600E mutations.<sup>30,31</sup> This discovery led to the use of vemurafenib, a *BRAF* p.V600E inhibitor, which has shown remarkable efficacy in early reports.<sup>32,33</sup> It was subsequently found that patients lacking *BRAF* p.V600E mutations often have activating mutations elsewhere in the MAPK pathway.<sup>34</sup> This finding led to other treatment options, including MEK and rapidly accelerated fibrosarcoma inhibitors.<sup>35</sup> Still, no standardized treatment regimen exists; management is usually based on disease severity, the results of genomic analyses, and clinicians’ preferences.

The prognosis of patients with ECD is highly variable and is predominantly influenced by specific organ involvement. CNS disease tends to respond rapidly to *BRAF/MEK* inhibition if enhancing lesions are present, though in patients with nonenhancing, presumably chronic lesions, residual deficits are typical. A 2011 study of 53 patients found that the 5-year survival was 68%, though these results were published before recent treatment advances.<sup>36</sup> Both increased age and CNS involvement are independent predictors of poor prognoses.<sup>36,37</sup> In patients with *BRAF* p.V600E–mutated disease, almost all stabilize or respond to therapy if they tolerate the medication.<sup>5,38</sup> Follow-up imaging is typically performed every 3–6 months early on in the treatment course.

After initiation of vemurafenib, this patient had a substantial improvement in gait ataxia within 1 week, going from walking with a walker to no gait aid. At 3-month follow up, he was walking without aid, had returned to work, and had a persistent

moderate ataxic dysarthria. MR imaging of the brain at that time demonstrated a reduction in the degree of enhancement within his dentate nuclei.

### Case Summary

- CNS involvement of ECD is variable. Characteristic findings include patchy T2 hyperintensities and/or enhancement in the brainstem and cerebellum, thickening of the pituitary infundibulum, and dural-based extra-axial masses.
- Diabetes insipidus is the most common clinical manifestation of neurologic ECD and can precede the diagnosis by up to a decade. Other neurologic symptoms are dependent on the sites of involvement.
- Diagnosis is best made by biopsy, with molecular genetic testing to evaluate causative mutations.
- Identification of the biopsy target using vertex-to-toes PET/CT is an essential component of evaluation of these disorders.
- Histopathologic findings of CNS ECD can be very subtle relative to other organ systems. In the proper clinical context, molecular testing for *BRAF* or other MAPK pathway alterations can aid in establishing a definitive diagnosis.
- Treatment strategies have evolved during recent years. Targeted therapeutic regimens are now often based on genomic analyses of tissue samples.

Disclosure forms provided by the authors are available with the full text and PDF of this article at [www.ajnr.org](http://www.ajnr.org).

### REFERENCES

1. Sedrak P, Ketonen L, Hou P, et al. **Erdheim-Chester disease of the central nervous system: new manifestations of a rare disease.** *AJNR Am J Neuroradiol* 2011;32:2126–31 CrossRef Medline
2. Oliveira M, Monteiro S, Dos Santos J, et al. **Erdheim-Chester disease: a rare clinical entity.** *Eur J Case Rep Intern Med* 2020;7:001630 CrossRef Medline
3. Todisco A, Cavaliere C, Vaglio A, et al. **Erdheim-Chester disease: a challenging diagnosis for an effective therapy.** *Clin Neurol Neurosurg* 2020;194:105841 CrossRef Medline
4. Sánchez-Villalobos JM, Jimeno-Almazán A, López-Peña C, et al. **Erdheim-Chester disease mimicking multiple sclerosis or a new association?** *Mult Scler Relat Disord* 2019;30:94–97 CrossRef Medline
5. Pegoraro F, Papo M, Maniscalco V, et al. **Erdheim-Chester disease: a rapidly evolving disease model.** *Leukemia* 2020;34:2840–57 CrossRef Medline
6. Cohen Aubart F, Idbaih A, Galanaud D, et al. **Central nervous system involvement in Erdheim-Chester disease: an observational cohort study.** *Neurology* 2020;95:e2746–54 CrossRef Medline
7. Garg N, Lavi ES. **Clinical and neuroimaging manifestations of Erdheim-Chester disease: a review.** *J Neuroimaging* 2021;31:35–44 CrossRef Medline
8. Abdelfattah AM, Arnaout K, Tabbara IA. **Erdheim-Chester disease: a comprehensive review.** *Anticancer Res* 2014;34:3257–61 Medline
9. Manaka K, Sato J, Makita N. **Neuroendocrine manifestations of Erdheim-Chester disease.** *Handb Clin Neurol* 2021;181:137–47 CrossRef Medline
10. Cives M, Simone V, Rizzo FM, et al. **Erdheim-Chester disease: a systematic review.** *Crit Rev Oncol Hematol* 2015;95:1–11 CrossRef Medline
11. Kumar P, Singh A, Gamanagatti S, et al. **Imaging findings in Erdheim-Chester disease: what every radiologist needs to know.** *Pol J Radiol* 2018;83:e54–62 CrossRef Medline
12. Caparros-Lefebvre D, Pruvo JP, Rémy M, et al. **Neuroradiologic aspects of Chester-Erdheim disease.** *AJNR Am J Neuroradiol* 1995;16:735–40 Medline
13. Jeon I, Choi JH. **Isolated thoracic intramedullary Erdheim-Chester disease presenting with paraplegia: a case report and literature review.** *BMC Musculoskelet Disord* 2021;22:270 CrossRef Medline
14. Berkman J, Ford C, Johnson E, et al. **Misdiagnosis: CNS Erdheim-Chester disease mimicking CLIPPERS.** *Neuroradiol J* 2018;31:399–402 CrossRef Medline
15. Wang Y, Camelo-Piragua S, Abdullah A, et al. **Neuroimaging features of CNS histiocytosis syndromes.** *Clin Imaging* 2020;60:131–40 CrossRef Medline
16. Johnson MD, Aulino JP, Jagasia M, et al. **Erdheim-Chester disease mimicking multiple meningiomas syndrome.** *AJNR Am J Neuroradiol* 2004;25:134–37 Medline
17. Huang Z, Li S, Hong J, et al. **Erdheim-Chester disease mimicking lumbar nerve schwannoma: case report and literature review.** *Spinal Cord Ser Cases* 2019;5:90 CrossRef Medline
18. Unadkat BS, Kashikar SV, Bhansali PJ, et al. **Intracranial Rosai-Dorfman disease: a case to remember.** *Cureus* 2022;14:e32605 CrossRef Medline
19. Cheng X, Cheng JL, Gao AK. **A study on clinical characteristics and magnetic resonance imaging manifestations on systemic Rosai-Dorfman disease.** *Chin Med J (Engl)* 2018;131:440–47 CrossRef Medline
20. Prosch H, Grois N, Wnorowski M, et al. **Long-term MR imaging course of neurodegenerative Langerhans cell histiocytosis.** *AJNR Am J Neuroradiol* 2007;28:1022–28 CrossRef Medline
21. Cerudelli E, Gazzilli M, Bertoli M, et al. **Erdheim-Chester disease: the power of nuclear medicine imaging.** *Rev Esp Med Nucl Imagen Mol (Engl Ed)* 2020;39:323–24 CrossRef Medline
22. Fasulo S, Alkimos MF, Pjetergioka R, et al. **Erdheim-Chester disease presenting at the central nervous system.** *Autops Case Rep* 2021;11:e2021321 CrossRef Medline
23. Liu SZ, Zhou X, Song A, et al. **Exophthalmos and coated aorta in Erdheim-Chester disease.** *Rheumatology (Oxford)* 2020;59:2651–52 CrossRef Medline
24. Hazim AZ, Acosta-Medina AA, Young JR, et al; Mayo Clinic-University of Alabama at Birmingham Histiocytosis Working Group. **Classical and non-classical phenotypes of Erdheim-Chester disease: correlating clinical, radiographic and genotypic findings.** *Br J Haematol* 2022;199:454–57 CrossRef Medline
25. Emile JF, Tirabosco R, Demicco, Elizabeth. **WHO Classification of Tumors Editorial Board. Central Nervous System Tumours.** Vol 6. 5th ed. 2021
26. Go RS, Jacobsen E, Baiocchi R, et al. **Histiocytic Neoplasms, Version 2.2021, NCCN Clinical Practice Guidelines in Oncology.** *J Natl Compr Canc Netw* 2021;19:1277–303 CrossRef Medline
27. Munoz J, Janku F, Cohen PR, et al. **Erdheim-Chester disease: characteristics and management.** *Mayo Clin Proc* 2014;89:985–96 CrossRef Medline
28. Pan Z, Kleinschmidt-DeMasters BK. **CNS Erdheim-Chester disease: a challenge to diagnose.** *J Neuropathol Exp Neurol* 2017;76:986–96 CrossRef Medline
29. Haque A, Pérez CA, Reddy TA, et al. **Erdheim-Chester disease with isolated CNS involvement: a systematic review of the literature.** *Neurol Int* 2022;14:716–26 CrossRef Medline
30. Badalian-Very G. **A common progenitor cell in LCH and ECD.** *Blood* 2014;124:991–92 CrossRef Medline
31. Haroche J, Charlotte F, Arnaud L, et al. **High prevalence of BRAF V600E mutations in Erdheim-Chester disease but not in other non-Langerhans cell histiocytosis.** *Blood* 2012;120:2700–03 CrossRef Medline
32. Tzoulis C, Schwarzlmüller T, Gjerde IO, et al. **Excellent response of intramedullary Erdheim-Chester disease to vemurafenib: a case report.** *BMC Res Notes* 2015;8:171 CrossRef Medline

33. Costa S, Julião MJ, Silva S, et al. **Erdheim-Chester disease: a rare non-Langerhans histiocytosis.** *BMJ Case Rep* 2021;14:e24114 CrossRef Medline
34. Starkebaum G, Hendrie P. **Erdheim-Chester disease.** *Best Pract Res Clin Rheumatol* 2020;34:101510 CrossRef Medline
35. Diamond EL, Durham BH, Haroche J, et al. **Diverse and targetable kinase alterations drive histiocytic neoplasms.** *Cancer Discov* 2016;6:154–65 CrossRef Medline
36. Arnaud L, Hervier B, Néel A, et al. **CNS involvement and treatment with interferon- $\alpha$  are independent prognostic factors in Erdheim-Chester disease: a multicenter survival analysis of 53 patients.** *Blood* 2011;117:2778–82 CrossRef Medline
37. Veyssier-Belot C, Cacoub P, Caparros-Lefebvre D, et al. **Erdheim-Chester disease: clinical and radiologic characteristics of 59 cases.** *Medicine (Baltimore)* 1996;75:157–69 CrossRef Medline
38. Diamond EL, Subbiah V, Lockhart AC, et al. **Vemurafenib for BRAF V600-mutant Erdheim-Chester disease and Langerhans cell histiocytosis: analysis of data from the histology-independent, Phase 2, open-label VE-BASKET study.** *JAMA Oncol* 2018;4:384–88 CrossRef Medline

# Prospective Safety Study of Intrathecal Gadobutrol in Different Doses

A. Sperre, I. Karsrud, A.H.S. Rodum, A. Lashkarivand, L.M. Valnes, G. Ringstad, and P.K. Eide



## ABSTRACT

**BACKGROUND AND PURPOSE:** In our clinical practice, we increasingly use intrathecal contrast-enhanced glymphatic MR imaging to assess CSF disturbances. However, because intrathecal MR imaging contrast agents such as gadobutrol (Gadovist; 1.0 mmol/mL) are used off-label, a thorough understanding of the safety profile is required.

**MATERIALS AND METHODS:** We performed a prospective safety study from August 2020 to June 2022 of intrathecal gadobutrol, including consecutive patients who received either 0.50, 0.25, or 0.10 mmol. Serious and nonserious adverse events were recorded systematically at 1–3 days, 4 weeks, and >6 months after the intrathecal administration.

**RESULTS:** The study included 196 patients who received intrathecal gadobutrol, including patients assessed for idiopathic normal pressure hydrocephalus (iNPH,  $n = 144$ ) or patients examined for other CSF disorders (non-iNPH cohort;  $n = 52$ ). The intrathecal gadobutrol doses were either 0.50 mmol ( $n = 56$ ), 0.25 mmol ( $n = 111$ ), or 0.10 mmol ( $n = 29$ ). No serious adverse events were observed. Nonserious adverse events on days 1–3 after intrathecal gadobutrol were, to some degree, dose-dependent but mild-to-moderate, including severe headache, nausea, and/or dizziness in 6/196 (6.3%) patients, and they were more common in the non-iNPH than in the iNPH cohort. At 4 weeks, none reported severe nonserious adverse events, and 9/179 (5.0%) patients had mild-to-moderate symptoms. After >6 months, 2 patients reported mild headache.

**CONCLUSIONS:** The present study adds to the accumulating evidence that intrathecal gadobutrol in doses up to 0.50 is safe.

**ABBREVIATIONS:** GBCA = gadolinium-based contrast agents; gMRI = glymphatic MR imaging; iNPH = idiopathic normal pressure hydrocephalus

Since the description of the glymphatic system in rodents in 2012,<sup>1</sup> intrathecal contrast-enhanced MR imaging has become of interest for in vivo glymphatic imaging in humans.<sup>2–5</sup> A limitation with this imaging technique is that intrathecal gadolinium-based contrast agents (GBCA) are administered off-label. There are concerns regarding the risk of serious adverse events due to acute neurotoxic effects and the risk of deposition of gadolinium in the brain.<sup>6</sup> A recent systematic review and meta-analysis<sup>7</sup> reported that serious adverse events due to acute neurotoxicity have been observed when MR imaging contrast agents (linear or macrocyclic)

are given intrathecally at doses of >1.0 mmol. On the other hand, there are no reports in the literature of serious adverse effects when GBCA are given intrathecally at doses of <1.0 mmol.<sup>7</sup>

We have previously reported that intrathecal gadobutrol (Gadovist; Bayer Schering Pharma) in doses of  $\leq 0.50$  mmol is safe,<sup>8,9</sup> though it was difficult to determine the profile of nonserious adverse events because gadobutrol was co-administered with iodixanol (Visipaque; GE Healthcare), a CT contrast agent that may also cause adverse events. In addition, the MR imaging protocol itself with multiple MR imaging acquisitions might add to the patients' symptoms, and there may be further adverse effects from the spinal puncture. In our previous studies, intrathecal gadobutrol has mostly been given at a dose of 0.50 mmol; only 5 patients received an intrathecal dose of gadobutrol of 0.25 mmol.<sup>8</sup> In our clinical practice, we increasingly use intrathecal contrast-enhanced MR imaging (glymphatic MR imaging [gMRI]) in the assessment of CSF disturbances, particularly for assessment of idiopathic normal pressure hydrocephalus (iNPH).<sup>10,11</sup> More recently, we have administered intrathecal gadobutrol at lower doses of 0.25 and 0.1 mmol.<sup>11</sup>

When new indications for drugs are introduced in medicine, there must be an acceptable balance between usefulness and risk.

Received January 26, 2023; accepted after revision March 7.

From the Department of Neurosurgery (A.S., I.K., A.H.S.R., A.L., L.M.V., P.K.E.), and Institute of Clinical Medicine (A.L., P.K.E.), Faculty of Medicine, University of Oslo, Oslo, Norway; Department of Radiology and Nuclear Medicine (G.R.), and Neurosurgery (P.K.E.), Oslo University Hospital-Rikshospitalet, Oslo, Norway; and Department of Geriatrics and Internal Medicine (G.R.), Sorlandet Hospital, Arendal, Norway.

This work was supported by grants from Health South-East, Norway (grant No. 2020068) and from the Department of Neurosurgery, Oslo University Hospital-Rikshospitalet, Oslo, Norway.

Please address correspondence to Per Kristian Eide, MD, PhD, Department of Neurosurgery, Oslo University Hospital-Rikshospitalet, Postboks 4950 Nydalen, 0424 Oslo, Norway; e-mail: p.k.eide@medisin.uio.no

<http://dx.doi.org/10.3174/ajnr.A7841>



**Table 1: The 2 patient cohorts included (n = 196)**

	iNPH Cohort	Non-iNPH Cohort	Significance
No.	144	52	
Sex (F/M)	60:84	31:21	<i>P</i> = .872
Age (mean) (yr)	72.2 (SD, 8.1)	57.3 (SD, 10.8)	<i>P</i> < .001
BMI (mean) (kg/m <sup>2</sup> )	27.4 (SD, 4.7)	27.5 (SD, 5.6)	<i>P</i> = .436
Dose of i.th. gadobutrol (No.) (%)			
0.50 mmol	21 (14.6%)	35 (67.3%)	
0.25 mmol	94 (65.3%)	17 (31.8%)	
0.10 mmol	29 (20.1%)	0	

**Note:**—i.th. indicates intrathecal; BMI, body mass index.

As recently stated by Kanal,<sup>12</sup> controlled studies of off-label applications of drugs and devices have always been the mainstay of clinical advances in the medical sciences. Controlled studies of intrathecal GBCA in neuroimaging are, therefore, warranted.

With this background, we performed a prospective study to systematically determine the safety profile of various doses of intrathecal gadobutrol as a follow-up on our previous safety studies.<sup>8,9</sup>

## MATERIALS AND METHODS

### Approvals

The study was approved by the institutional review board (2015/1868), the Regional Ethics Committee (2015/96), and the National Medicines Agency (15/04932–7). Patients were included after written and oral informed consent was obtained.

### Patients

In this prospective, observational study, consecutive patients undergoing gMRI were included. Imaging was performed on clinical indication in patients admitted to the Department of Neurosurgery, Oslo University Hospital-Rikshospitalet, for the diagnosis of CSF circulation disorders. Patients excluded were those with a history of hypersensitivity reactions to contrast agents, severe allergic reactions in general, evidence of renal dysfunction, pregnant or breastfeeding women, and those younger than 18 years of age or older than 80 years of age. These exclusion criteria have been used since the ethics committee first approved the study in 2015.

### Intrathecal Gadobutrol

Under sterile conditions, a spinal puncture was performed at levels L2/L3, L3/L4, or L4/5. Verification of correct needle (22 ga × 3.5 inches) placement in the subarachnoid space was CSF backflow from the puncture needle. Following needle removal, the patients were in the supine position for at least 3–4 hours.

### MR Imaging Acquisitions

In this safety study, MR imaging was used to confirm the arrival of intrathecally injected gadobutrol within the intracranial compartment. The MR imaging acquisitions were primarily performed on a 1.5T Aera scanner (Siemens) or a 3T Ingenia MR imaging scanner (Philips Healthcare), and standardized sagittal 3D T1-weighted gradient-echo volume scans were obtained. The MR imaging acquisition parameters and image postprocessing routine have been previously described.<sup>3,11</sup>

### Serious and Nonserious Adverse Events

Study nurses (A.S., I.K., A.H.S.R), not otherwise involved in management of the patients, recorded prospectively and systematically the occurrence of serious and nonserious adverse events during days 1–3 after intrathecal gadobutrol, after 4 weeks, and finally after >6 months.

Serious adverse events refer to the following: any untoward medical occurrence that, at any dose, results in either

death, immediate life-threatening situations, requirement of hospitalization or prolongation of existing hospitalization, persistent or evident disability or incapacity, or an important medical event that may jeopardize the subject or may require medical intervention to prevent said outcomes.

Nonserious adverse events did not have the consequences characterizing serious adverse events. The patients were specifically asked for the presence of a defined set of symptoms presenting or being aggravated after intrathecal injection of gadobutrol: headache (mild/moderate/severe), nausea (mild/moderate/severe), dizziness (mild/moderate/severe), itch, warm feeling, paresthesia, visual problems, cognitive difficulties, muscle spasms, discomfort at the injection site, tremor, or other symptoms not specifically requested, independent of the possible cause.

### Statistics

Continuous data were assessed by an independent samples *t* test, and categorical data, using the Pearson  $\chi^2$  test. The statistical analysis was performed using SPSS, Version 29 (IBM). Statistical significance was .05 (2-tailed).

## RESULTS

### Patients

From August 2020 to June 2022, one hundred ninety-six patients underwent intrathecal contrast-enhanced MR imaging (gMRI), using gadobutrol in different doses (Table 1). Patients underwent a diagnostic work-up for various CSF diseases: One hundred forty-four patients were examined for iNPH, and 52, for possible CSF diseases other than iNPH: follow-up after subarachnoid hemorrhage (*n* = 36), follow-up after intracerebral hemorrhage (*n* = 2), brain tumor (*n* = 1), noncommunicating or communicating hydrocephalus (*n* = 3), arachnoid cysts (*n* = 3), and spontaneous intracranial hypotension leakage (*n* = 7).

Contrast enrichment in the cranial CSF spaces was verified in all patients by observation of any T1 signal enhancement in the cranial CSF spaces on MR imaging. Figure 1 shows contrast enrichment in the brain after 24 hours in patients with iNPH, depending on the dose of intrathecal gadobutrol, visualized by 1.5T MR imaging. The contrast enhancement in the ventricles is shown in Fig 2.

### Serious and Nonserious Adverse Events

None of the patients experienced serious adverse events (Table 2).

The occurrence of nonserious adverse events was higher in the non-iNPH cohort than in the iNPH cohort at days 1–3 (57.7% versus 32.6%, Pearson  $\chi^2$ ; *P* = .002), but not at 4 weeks (Pearson

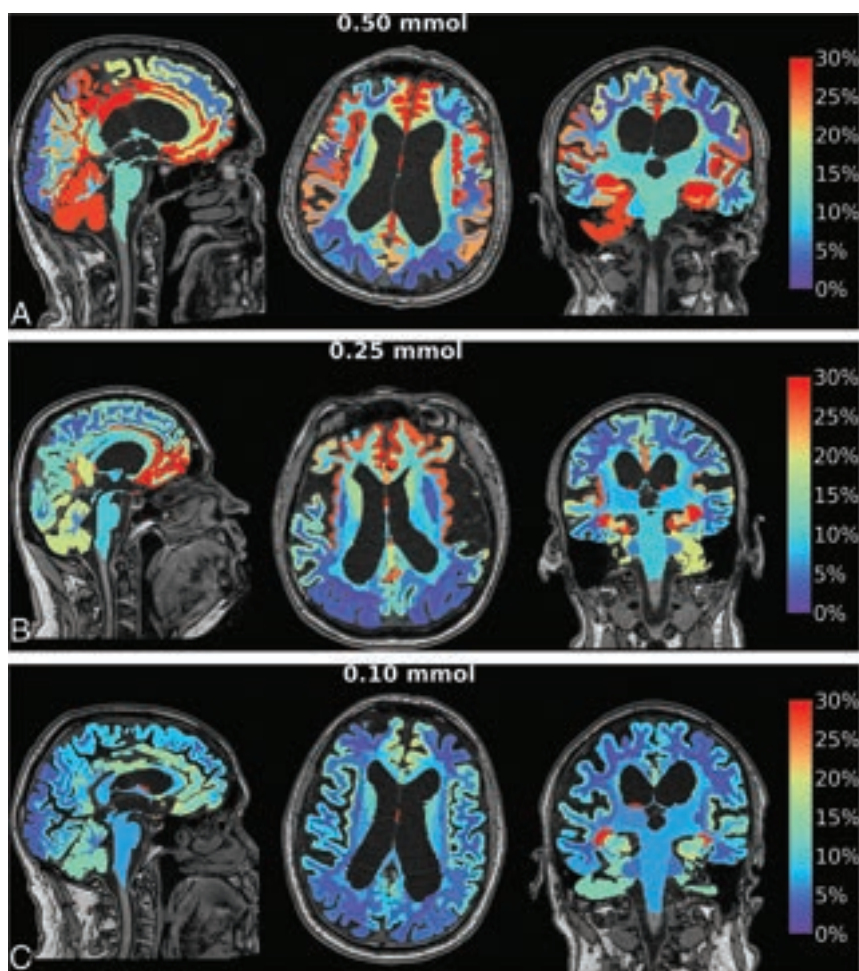


**FIG 1.** Enrichment in the brain by gadobutrol, used as a CSF tracer, in patients with iNPH. Axial, sagittal, and coronal MR imaging visualizes dose-dependent brain-wide tracer enrichment 24 hours after intrathecal gadobutrol in the iNPH cohort examined with 1.5T MR imaging at a group level in which intrathecal gadobutrol was given in the doses of 0.50 mmol ( $n = 19$ ) (A), 0.25 mmol ( $n = 68$ ) (B), and 0.10 mmol ( $n = 26$ ) (C). The percentage change in normalized T1 signal at 24 hours is shown on the color bar. In these images, tracer enrichment in the CSF is removed, demonstrating dose-dependent brain-wide tracer enrichment. The tracer enriches the brain centripetally from outside and inward. With 1.5T MR imaging, intrathecal gadobutrol in a dose of 0.10 mmol is not useful for diagnostic imaging, while the doses 0.25 and 0.50 mmol are adequate.

$\chi^2$ ,  $P = .649$ ) (Table 2). If one specifically addressed the dose of intrathecal gadobutrol, there was no significant difference in the occurrence of nonserious adverse events on days 1–3 between patients with and without iNPH for the dose of 0.50 mmol ( $P = .678$ ), while for the dose of 0.25 mmol, adverse events were more common in patients without iNPH ( $P = .005$ , Pearson  $\chi^2$  test; Table 3).

In the iNPH cohort, the occurrence of nonserious adverse events at days 1–3 was dose-dependent (0.50 versus 0.25 mmol,  $P = .049$ ; 0.25 versus 0.10 mmol,  $P = .013$ ), though the distribution of predominant symptoms was not dose-dependent (Table 3). The adverse events were, however, minor. In the iNPH cohort, severe headache, nausea, and/or dizziness occurred in 1/21 (4.8%) patients receiving gadobutrol at a dose of 0.50 mmol, and in 1/94 (1.1%) patients after a dose of 0.25 mmol. The occurrence of predominant adverse events was not dose-dependent (Table 3).

In comparison, in the non-iNPH cohort, nausea and/or dizziness and headache were observed in 4/35 (11.1%) patients after a dose of 0.50 mmol, but in 0/17 patients after 0.25 mmol, with no differences between the doses of 0.50 versus 0.25 mmol ( $P = .190$ , Table 3). The occurrence of predominant adverse events was not different for the doses of 0.50 and 0.25 mmol (Table 3).

The difference in the occurrence of nonserious adverse events between patients with and without iNPH at days 1–3 was not statistically different for the doses of 0.50 ( $P = .427$ ) or 0.25 mmol ( $P = .056$ , Table 3).

After 4 weeks, only minor-to-moderate nonserious adverse events were observed, and with no significant dose-dependency (Table 4). In the iNPH cohort, 6/134 (4.5%) patients reported mild-to-moderate headache, nausea, and/or dizziness, while in the non-iNPH cohort, 1/49 (2%) reported mild headache, nausea, and/or dizziness, 1/49 (2%) reported back pain from the spinal puncture, and 1/49 (2%) reported altered taste (Table 4).

At long-term follow-up after >6 months, 2/188 (1.1%) patients reported mild headache. No other symptoms were recorded.

Some missing data in Table 2 were due to not being able to contact patients at these particular follow-up time points.

## DISCUSSION

This study adds to previous results that intrathecal gadobutrol in a dose of  $\leq 0.50$  mmol is safe. Nonserious adverse events from intrathecal gadobutrol at 0.50, 0.25, or 0.10 mmol were observed, but the profile is favorable.

We have previously reported safety data from 149 patients who received intrathecal gadobutrol from October 2015 to December 2019, and we have concluded that intrathecal gadobutrol at a dose of  $\leq 0.5$  mmol is safe.<sup>8,9</sup> However, with regard to the occurrence of nonserious adverse events, our previous reports were limited because gadobutrol was commonly co-administered with iodixanol and multiple MR imaging acquisitions, making it difficult to specifically identify which adverse events were caused by gadobutrol alone. In addition, most patients had received gadobutrol at a dose of 0.50 mmol;<sup>8,9</sup> the safety profile of intrathecal gadobutrol at a dose of 0.25 mmol was examined in only 5 patients.<sup>8</sup> In the present study, we included new patients who had received intrathecal gadobutrol alone, not co-administered with other drugs, from August 2020 to June 2022, demonstrating a

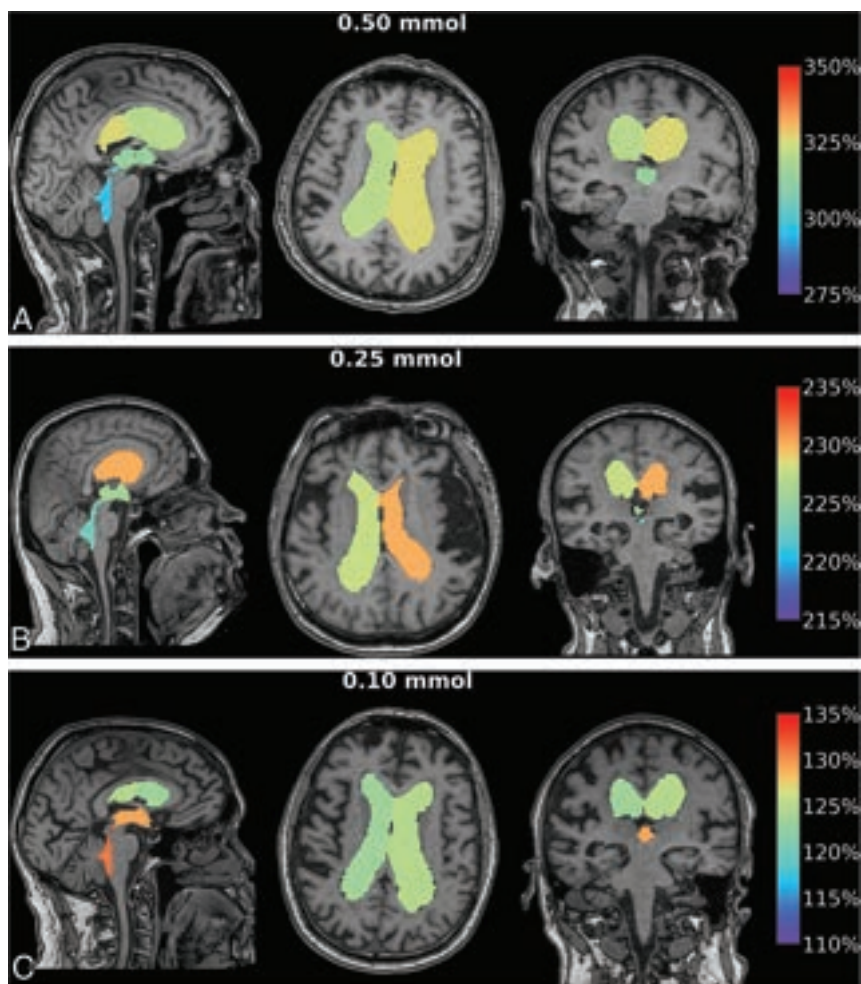


**FIG 2.** Enrichment in the ventricles by gadobutrol, used as a CSF tracer, in patients with iNPH. Axial, sagittal, and coronal MR imaging visualizes dose-dependent ventricular tracer enrichment 24 hours after intrathecal gadobutrol in the iNPH cohort examined with 1.5T MR imaging at the group level in which intrathecal gadobutrol was given in the doses of 0.50 mmol ( $n = 19$ ) (A), 0.25 mmol ( $n = 68$ ) (B), and 0.10 mmol ( $n = 26$ ) (C). The percentage change in normalized T1 signal at 24 hours is shown on the color bar. Here, CSF tracer in the brain is removed, showing CSF tracer enrichment of the cerebral ventricles. The high degree of ventricular CSF tracer enrichment is due to the high proportion of patients with iNPH in the study, in whom ventricular reflux of CSF tracer is typical.<sup>10</sup>

more favorable profile of nonserious adverse events than we have previously reported. The present results may, therefore, more correctly describe the safety of intrathecal gadobutrol, while some of the symptoms reported by patients may be related to their underlying disease as well.

The present results add evidence to the growing body of data that intrathecal GBCA in a low dose are safe. A recent systematic review and meta-analysis including 1036 patients from 53 studies concluded that serious adverse events have not been reported after intrathecal GBCA at doses of  $<1.0$  mmol.<sup>7</sup> Our previous studies including a total of 149 patients<sup>8,9</sup> that supported this conclusion were not included in the above-mentioned meta-analysis.<sup>13</sup> The present study of an additional 196 patients further adds support to the previous conclusions. However, GBCA in doses of  $>1.0$  mmol have been reported to cause serious adverse events; even a fatal outcome was reported in a 67-year-old man who accidentally

received ProHance (Bracco Diagnostics) in a dose of 2.5 mmol.<sup>7</sup> Accordingly, the therapeutic window for intrathecal gadobutrol is narrow. Thus, to prevent accidental overdosage, we always use 1.0-mL syringes to assure that even an accidental overdose cannot exceed 1.0 mmol.

Furthermore, intrathecal GBCA are accompanied by nonserious adverse events, in particular headache. The systematic review and meta-analysis identifying 19 studies including 806 participants reported headache in 120/806 (14.9%) patients after intrathecal GBCA in doses of  $<1$  mmol.<sup>7</sup> In comparison, among our 144 patients with iNPH, headache on days 1–3 after intrathecal gadobutrol (0.50 to 0.10 mmol) was observed in 22/144 (15.3%) patients, though it was severe in merely 1/144 (0.7%). Furthermore, among the non-iNPH cohort, 3/52 (5.8%) patients experienced severe headache while 10/52 (19.2%) patients reported mild-to-moderate headache. Thus, the spinal puncture itself may be an important contributor to the headache. Hence, a systematic review and meta-analysis including 31,412 patients showed that the incidence of post-dural puncture headache was 11.0% (95% CI, 9.1%–13.3%), though it was reduced to 4.2% (95% CI, 3.3%–5.2%) when using an atraumatic needle.<sup>14</sup> For this reason, we now exclusively use an atraumatic 22-ga syringe for spinal puncture, which expectedly will further reduce the occurrence of headache.

The present data support our previous findings<sup>8,9</sup> that the occurrence of nonserious adverse events depends on

the underlying disease. For the dose of 0.25 mmol, non-adverse events were more common at days 1–3 in patients without than in those with iNPH. The reason may be that symptoms like headache and dizziness were part of the symptom distribution in patients without iNPH, which included patients with idiopathic intracranial hypertension and intracranial cysts. A similar trend was seen in a previous study in which patients received intrathecal gadobutrol and iodixanol in combination.<sup>9</sup>

Four weeks after intrathecal gadobutrol, no patients reported severe headache, nausea, and/or dizziness. In both the iNPH and non-iNPH cohorts, symptoms were mild-to-moderate.

Accumulating evidence indicates the benefits of administering GBCA intrathecally. For years, clinicians have used intrathecal GBCA for visualization of CSF leakage in individuals with spontaneous intracranial hypotension.<sup>15,16</sup> In our clinical practice, we have also used gMRI for the diagnostic assessment of ventricular



**Table 2: Distribution of serious and nonserious adverse events days 1–3 or 4 weeks after intrathecal gadobutrol, independent of dose (n = 196)<sup>a</sup>**

	iNPH Cohort		Non-iNPH Cohort	
	Days 1–3	4 Weeks	Days 1–3	4 Weeks
Serious adverse events				
Present (No.)	0	0	0	0
Absent (No.) (%)	144 (100%)	134 (100%)	52 (100%)	49 (100%)
Nonserious adverse events				
Present (No.) (%)	47 (32.6%)	6 (4.5%)	30 (57.7%)	3 (6.1%)
Absent (No.) (%)	97 (67.4%)	128 (95.5%)	22 (42.3%)	46 (93.9%)
Missing data (No.)	0	10	0	3

<sup>a</sup>Data are presented as number of individuals (percentage are in parentheses). Comparison of the distribution of nonserious adverse events between the iNPH and non-iNPH cohorts after days 1–3 (Pearson  $\chi^2$ ,  $P = .002$ ) and 4 weeks (Pearson  $\chi^2$ ,  $P = .649$ ).

**Table 3: Specifications of predominant nonserious adverse events days 1–3 after intrathecal gadobutrol in various doses<sup>a</sup>**

	iNPH Cohort			Non-iNPH Cohort	
	0.50 mmol (n = 21)	0.25 mmol (n = 94)	0.10 mmol (n = 29)	0.50 mmol (n = 35)	0.25 mmol (n = 17)
No adverse events (No.) (%)	9 (42.9%)	62 (66.0%)	26 (89.7%)	17 (47.2%)	5 (29.4%)
Adverse events present (No.) (%)	12 (57.1%)	32 (34.0%)	3 (10.3%)	18 (51.4%)	12 (70.6%)
Predominant adverse events					
Mild headache, nausea, and/or dizziness (No.) (%)	2 (9.5%)	17 (18.1%)	1 (3.4%)	3 (8.3%)	2 (11.8%)
Moderate headache, nausea, and/or dizziness (No.) (%)	5 (23.8%)	4 (4.3%)	1 (3.4%)	8 (22.9%)	6 (35.3%)
Severe headache, nausea, and/or dizziness (No.) (%)	1 (4.8%)	1 (1.1%)	0	4 (11.1%)	0
Back pain from spinal puncture (No.) (%)	2 (9.5%)	5 (5.3%)	1 (3.4%)	3 (8.6%)	3 (17.6%)
Other (No.) (%)	2 (9.5%)	5 (5.3%)	0	0	1 (5.9%)

<sup>a</sup>Data are presented as the number of individuals (percentages are in parentheses).

**Table 4: Specifications of predominant nonserious adverse effects 4 weeks after intrathecal gadobutrol in various doses<sup>a</sup>**

	iNPH Cohort		Non-iNPH Cohort		
	0.50 mmol (n = 20)	0.25 mmol (n = 86)	0.10 mmol (n = 28)	0.50 mmol (n = 34)	0.25 mmol (n = 15)
No adverse events (No.) (%)	19 (95.0%)	82 (95.3%)	27 (96.4%)	33 (97.1%)	13 (86.7%)
Adverse events present (No.) (%)	1 (5.0%)	4 (4.7%)	1 (3.6%)	1 (2.9%)	2 (13.3%)
Predominant adverse events					
Mild headache, nausea, and/or dizziness (No.) (%)	1 (5.0%)	2 (2.3%)	1 (3.6%)	0	1 (6.7%)
Moderate headache, nausea, and/or dizziness (No.) (%)	0	2 (2.3%)	0	0	0
Severe headache, nausea, and/or dizziness (No.) (%)	0	0	0	0	0
Back pain from spinal puncture (No.) (%)	0	0	0	0	1 (6.7%)
Other (No.) (%)	0	0	0	1 (2.9%)	0

<sup>a</sup>Data are given as numbers (percentages are in parentheses). The Pearson  $\chi^2$  test showed no statistical differences between groups.

reflux (Fig 2) and for estimation of impaired molecular clearance from intracranial CSF spaces and the brain (Fig 1). Hence, we have reported its utility in iNPH,<sup>10</sup> idiopathic intracranial hypertension,<sup>17</sup> and chronic sleep disturbance.<sup>18</sup> Currently, we consider intrathecal contrast-enhanced MR imaging the criterion standard for imaging of glymphatic function, providing information not obtained by other imaging modalities. In a previous study, we showed that intrathecal gadobutrol in a dose of 0.25 mmol (but not 0.10 mmol) is sufficient for gMRI in iNPH using a 1.5T MR imaging scanner.<sup>11</sup> When intrathecal gadobutrol is given for the assessment of CSF-to-blood clearance capacity, a dose of 0.10 mmol is sufficient.<sup>19</sup>

Taken together, the diagnostic benefits of gMRI using gadobutrol in doses 0.5, 0.25, or 0.10 mmol have been demonstrated in several studies. The present data further show a favorable profile concerning the risk of nonserious adverse events after intrathecal gadobutrol at doses of  $\leq 0.50$  mmol. In general, the

therapeutic index of a drug refers to the balance between risk and benefit or, more specifically, the ratio of the dose in which 50% of subjects experience toxic effects and 50% report effective therapeutic effects. A good safety profile would generally be in the range of a therapeutic index of  $>10$ .<sup>20</sup> Intrathecal gadobutrol is in this range, given that a potential lethal dose is  $>2.0$  mmol and intrathecal gadobutrol at a dose of 0.25 mmol provides diagnostic information using 1.5T MR imaging.<sup>11</sup> Furthermore, 0.10 mmol is enough for estimation of CSF-to-blood clearance<sup>19</sup> and possibly for 3T MR imaging.

In addition to the safety profile of intrathecal GBCA, there is a concern about the possible deposition of gadolinium in the brain after intrathecal administration. In this context, IV GBCA are used on-label in much larger body doses. The presently used intrathecal doses of gadobutrol of 0.50, 0.25, or 0.10 mmol are 16, 32, or 80 times lower, respectively, than an intravenous dose of 8 mmol (0.1 mmol/kg in an 80-kg subject). For intravenous use,



gadobutrol can be given in doses up to a maximum of 0.3 mmol/kg. IV-administered GBCA also represent a dose to the CSF, even in subjects with normal renal function and an intact BBB.<sup>21–23</sup> Several possible leakage sites from blood to CSF have been proposed, such as the choroid plexus,<sup>24</sup> ciliary body,<sup>25</sup> and cortical veins, at least with increasing age.<sup>26</sup> Accordingly, even an intravenous dose of gadobutrol of 0.1 mmol/kg to an individual weighing 80 kg (8 mmol) may provide a substantial dose to the CSF, given that the half-life of gadobutrol in blood is about 2 hours. In older individuals with disrupted BBBs, 1 study estimated that an IV administration resulted in the CSF concentration of GBCA being one-fifth of the IV concentration.<sup>23</sup> Therefore, accumulating evidence indicates that the risk of macrocyclic GBCA deposition in the brain via CSF is less than previously assumed.<sup>27,28</sup>

The major limitation in the present study is that many of the patients, particularly in the non-iNPH cohort, reported symptoms similar to those recorded after intrathecal gadobutrol. Therefore, we cannot definitely conclude which of the nonserious adverse events resulted from intrathecal gadobutrol per se. To this end, we have not given intrathecal gadobutrol to healthy individuals.

## CONCLUSIONS

Taken together, intrathecal gadobutrol for gMRI was shown to be safe with no serious adverse events and with a favorable profile of nonserious adverse events. The body of evidence supporting the clinical use of intrathecal GBCA in low doses of  $\leq 0.50$  mmol is growing, though such use remains off-label. Further studies should address the clinical risk profile of intrathecal-versus-intravenous GBCA, particularly regarding GBCA deposition in the brain.

Disclosure forms provided by the authors are available with the full text and PDF of this article at [www.ajnr.org](http://www.ajnr.org).

## REFERENCES

- Iliff JJ, Wang M, Liao Y, et al. A paravascular pathway facilitates CSF flow through the brain parenchyma and the clearance of interstitial solutes, including amyloid  $\beta$ . *Sci Transl Med* 2012;4:147ra111 CrossRef Medline
- Ringstad G, Vatnehol SA, Eide PK. Glymphatic MRI in idiopathic normal pressure hydrocephalus. *Brain* 2017;140:2691–705 CrossRef Medline
- Ringstad G, Valnes LM, Dale AM, et al. Brain-wide glymphatic enhancement and clearance in humans assessed with MRI. *JCI Insight* 2018;3:121537 CrossRef Medline
- Benveniste H, Lee H, Ozturk B, et al. Glymphatic cerebrospinal fluid and solute transport quantified by MRI and PET imaging. *Neuroscience* 2021;474:63–79 CrossRef Medline
- Klostranec JM, Vucevic D, Bhatia KD, et al. Current concepts in intracranial interstitial fluid transport and the glymphatic system, Part II: imaging techniques and clinical applications. *Radiology* 2021;301:516–32 CrossRef Medline
- Mallio CA, Rovira À, Parizel PM, et al. Exposure to gadolinium and neurotoxicity: current status of preclinical and clinical studies. *Neuroradiology* 2020;62:925–34 CrossRef Medline
- Patel M, Atyani A, Salameh JP, et al. Safety of intrathecal administration of gadolinium-based contrast agents: a systematic review and meta-analysis. *Radiology* 2020;297:75–83 CrossRef Medline
- Halvorsen M, Edelev CS, Fraser-Green J, et al. Off-label intrathecal use of gadobutrol: safety study and comparison of administration protocols. *Neuroradiology* 2021;63:51–61 CrossRef Medline
- Edelev CS, Halvorsen M, Lovland G, et al. Intrathecal use of gadobutrol for glymphatic MR imaging: prospective safety study of 100 patients. *AJNR Am J Neuroradiol* 2019;40:1257–64 CrossRef Medline
- Eide PK, Pripp AH, Ringstad G. Magnetic resonance imaging biomarkers of cerebrospinal fluid tracer dynamics in idiopathic normal pressure hydrocephalus. *Brain Commun* 2020;2:faa187 CrossRef Medline
- Eide PK, Lashkarivand A, Hagen-Kersten ÅA, et al. Intrathecal contrast-enhanced magnetic resonance imaging of cerebrospinal fluid dynamics and glymphatic enhancement in idiopathic normal pressure hydrocephalus. *Front Neurol* 2022;13:857328 CrossRef Medline
- Kanal E. A reality check on intrathecal gadolinium-based contrast agents. *Radiology* 2020;297:84–86 CrossRef Medline
- Ringstad G, Eide PK. Safety of intrathecal gadolinium-based contrast agents and benefit versus risk. *Radiology* 2021;299:E223–24 CrossRef Medline
- Nath S, Koziarz A, Badhiwala JH, et al. Atraumatic versus conventional lumbar puncture needles: a systematic review and meta-analysis. *Lancet* 2018;391:1197–20 CrossRef Medline
- Akbar JJ, Luetmer PH, Schwartz KM, et al. The role of MR myelography with intrathecal gadolinium in localization of spinal CSF leaks in patients with spontaneous intracranial hypotension. *AJNR Am J Neuroradiol* 2012;33:535–40 CrossRef Medline
- Selcuk H, Albayram S, Ozer H, et al. Intrathecal gadolinium-enhanced MR cisternography in the evaluation of CSF leakage. *AJNR Am J Neuroradiol* 2010;31:71–75 CrossRef Medline
- Eide PK, Pripp AH, Ringstad G, et al. Impaired glymphatic function in idiopathic intracranial hypertension. *Brain Commun* 2021;3:fcab04 CrossRef Medline
- Eide PK, Pripp AH, Berge B, et al. Altered glymphatic enhancement of cerebrospinal fluid tracer in individuals with chronic poor sleep quality. *J Cereb Blood Flow Metab* 2022;42:1676–96 CrossRef Medline
- Hovd MH, Mariussen E, Uggerud H, et al. Population pharmacokinetic modeling of CSF to blood clearance: prospective tracer study of 161 patients under work-up for CSF disorders. *Fluids Barriers CNS* 2022;19:55 CrossRef Medline
- Tamargo J, Heuzey L, Mabo JY. Narrow therapeutic index drugs: a clinical pharmacological consideration to flecainide. *Eur J Clin Pharmacol* 2015;71:549–67 CrossRef Medline
- Nehra AK, McDonald RJ, Bluhm AM, et al. Accumulation of gadolinium in human cerebrospinal fluid after gadobutrol-enhanced MR imaging: a prospective observational cohort study. *Radiology* 2018;288:416–23 CrossRef Medline
- Berger F, Kubik-Huch RA, Niemann T, et al. Gadolinium distribution in cerebrospinal fluid after administration of a gadolinium-based MR contrast agent in humans. *Radiology* 2018;288:703–09 CrossRef Medline
- Cao D, Kang N, Pillai JJ, et al. Fast whole brain MR imaging of dynamic susceptibility contrast changes in the cerebrospinal fluid (cDSC MRI). *Magn Reson Med* 2020;84:3256–70 CrossRef Medline
- Jost G, Frenzel T, Lohrke J, et al. Penetration and distribution of gadolinium-based contrast agents into the cerebrospinal fluid in healthy rats: a potential pathway of entry into the brain tissue. *Eur Radiol* 2017;27:2877–85 CrossRef Medline
- Deike-Hofmann K, Reuter J, Haase R, et al. Glymphatic pathway of gadolinium-based contrast agents through the brain: overlooked and misinterpreted. *Invest Radiol* 2019;54:229–37 CrossRef Medline
- Naganawa S, Ito R, Kawai H, et al. Confirmation of age-dependence in the leakage of contrast medium around the cortical veins into cerebrospinal fluid after intravenous administration of gadolinium-based contrast agent. *Magnetic Reson Med* 2020;19:375–81 CrossRef Medline
- Green C, Jost G, Frenzel T, et al. The effect of gadolinium-based contrast agents on longitudinal changes of magnetic resonance imaging signal intensities and relaxation times in the aging rat brain. *Invest Radiol* 2022;57:453–62 CrossRef Medline
- Kobayashi M, Levendovszky SR, Hippe DS, et al. Comparison of human tissue gadolinium retention and elimination between gadoteridol and gadobenate. *Radiology* 2021;300:559–69 CrossRef Medline

# Post-COVID-19 Brain [<sup>18</sup>F] FDG-PET Findings: A Retrospective Single-Center Study in the United States

P. Debs, N. Khalili, L. Solnes, A. Al-Zaghal, H.I. Sair, V. Yedavalli, and L.P. Luna



## ABSTRACT

**BACKGROUND AND PURPOSE:** The pathophysiology of neurologic manifestations of postacute sequelae of Severe Acute Respiratory Syndrome coronavirus 2 (SARS-CoV-2) infection is not clearly understood. Our aim was to investigate brain metabolic activity on [<sup>18</sup>F] FDG-PET/CT scans in patients with a history of coronavirus disease 2019 (COVID-19) infection before imaging.

**MATERIALS AND METHODS:** This retrospective study included 45 patients who underwent [<sup>18</sup>F] FDG-PET/CT imaging for any reason and had, at least once, tested positive for COVID-19 at any time before imaging. Fifteen patients had available [<sup>18</sup>F] FDG-PET scans obtained under identical conditions before the infection. A group of 52 patients with melanoma or multiple myeloma who underwent [<sup>18</sup>F] FDG-PET/CT were used as controls. Whole-brain 2-sample *t* test analysis was performed using SPM software to identify clusters of hypo- and hypermetabolism and compare brain metabolic activity between patients with COVID-19 and controls. Paired sample *t* test comparison was also performed for 15 patients, and correlations between metabolic values of clusters and clinical data were measured.

**RESULTS:** Compared with the control group, patients with a history of COVID-19 infection exhibited focal areas of hypometabolism in the bilateral frontal, parietal, occipital, and posterior temporal lobes and cerebellum ( $P = .05$  uncorrected at the voxel level, family-wise error-corrected at the cluster level) that peaked during the first 2 months, improved to near-complete recovery around 6 months, and disappeared at 12 months. Hypermetabolism involving the brainstem, cerebellum, limbic structures, frontal cortex, and periventricular white matter was observed only at 2–6 months after infection. Older age, neurologic symptoms, and worse disease severity scores positively correlated with the metabolic changes.

**CONCLUSIONS:** This study demonstrates a profile of time-dependent brain PET hypo- and hypermetabolism in patients with confirmed SARS-CoV-2 infection.

**ABBREVIATIONS:** BMI = body mass index; COVID-19 = coronavirus disease 2019; FWE = family-wise error; GLM = general linear model; neuro-PASC = neurologic manifestations of postacute sequelae of SARS-CoV-2 infection; PASC = postacute sequelae of SARS-CoV-2; PCR = polymerase chain reaction; RT-PCR = reverse transcriptase PCR; SARS-CoV-2 = Severe Acute Respiratory Syndrome coronavirus 2; Tmax = time-to-maximum

As of December 2022, Severe Acute Respiratory Syndrome coronavirus 2 (SARS-CoV-2) has resulted in >97 million confirmed cases in the United States, with approximately 1 million all-time deaths, the highest among all countries and the sixteenth-highest per 100,000 population worldwide.<sup>1,2</sup> Knowledge of coronavirus disease 2019 (COVID-19) mainly focuses on the acute illness and related symptoms such as cough, fever, myalgia,

ageusia, and anosmia; nevertheless, the reality of the long-term consequences of COVID-19 is becoming more evident,<sup>3–5</sup> and many survivors of COVID-19 experience chronic postviral complications.<sup>3,6</sup>

Evidence of persistent neurologic symptoms following acute COVID-19 is increasing, and this process was recently termed neurologic manifestations of postacute sequelae of SARS-CoV-2 infection (neuro-PASC).<sup>3,7</sup> The most common neurologic manifestations are “brain fog”, fatigue, headache, numbness/tingling, dysgeusia, and anosmia.<sup>3,8,9</sup> Although neuro-PASC is more frequent in patients needing hospitalization,<sup>3,10,11</sup> studies have shown that postacute sequelae of SARS-CoV-2 (PASC) can also impact children, young adults, and those who experience only mild COVID-19 symptoms and do not require respiratory support or hospitalization.<sup>3,7,12</sup>

The mechanism behind SARS-CoV-2-induced pathologic changes in the CNS is still unclear.<sup>13,14</sup> Two main hypotheses

Received January 27, 2023; accepted after revision March 5.

From the Russell H. Morgan Department of Radiology and Radiological Science, Johns Hopkins University School of Medicine, Baltimore, Maryland.

Please address correspondence to Licia P. Luna, MD, PhD, Russell H. Morgan Department of Radiology and Radiological Science, Johns Hopkins Hospital, Division of Neuroradiology, 600 N Wolfe St, Phipps B100F, Baltimore, MD, 21287; e-mail: lluna6@jhmi.edu; @liciapluna

Indicates open access to non-subscribers at www.ajnr.org

Indicates article with online supplemental data.

<http://dx.doi.org/10.3174/ajnr.A7863>

attempt to explain this mechanism: indirect effects via peripheral inflammation and direct effects via SARS-CoV-2 CNS invasion. On the one hand, a cytokine storm (ie, an inflated immune response instigated by the infection) might play an indirect role in the neurologic manifestations of PASC;<sup>10</sup> on the other hand, some reports suggest that SARS-CoV-2 may directly invade the CNS and possibly infect brain cells via the functional receptor human angiotensin-converting enzyme 2.<sup>3</sup>

Despite these 2 hypotheses, questions regarding the mechanisms underlying the pathophysiology of neuro-PASC symptoms remain unanswered, and imaging could help elucidate the underlying processes. PET might meaningfully contribute to our understanding of the pathophysiologic changes in patients post-COVID-19 by identifying affected brain regions.<sup>15</sup> The underlying mechanisms can be explored by investigating changes in metabolic parameters, and [<sup>18</sup>F] FDG-PET/CT can be a valuable tool for detecting or ruling out severe coexistent processes and highlighting alterations in brain metabolism.<sup>16</sup>

Prior studies assessing imaging patterns associated with post-COVID-19 functional symptoms in PET/CT scans have compared whole-brain voxel-based analysis with a local database of healthy individuals to characterize cerebral metabolism patterns.<sup>17-20</sup> However, to our knowledge, no prior studies have assessed the potential alterations in brain metabolism in patients without functional symptoms at the time of imaging. We present a retrospective analysis of brain [<sup>18</sup>F] FDG-PET scans of patients with a biologically confirmed SARS-CoV-2 infection with and without persistent functional symptoms. On the basis of our clinical observations, we hypothesized that a history of COVID-19 infection may be associated with functional brain involvement that can be identified using [<sup>18</sup>F] FDG-PET. We aimed to compare PET scans using whole-brain voxel-based analysis with a local database of patients imaged under similar circumstances to characterize cerebral metabolism patterns, assess temporal evolution, and correlate PET abnormalities with patient characteristics and functional symptoms.

## MATERIALS AND METHODS

### Patient Selection

**Post-COVID Patients.** The institutional review board approved this retrospective single-center study and waived the requirement for written informed consent. The study complied with the Declaration of Helsinki and Health Insurance Portability and Accountability Act (HIPPA) regulations.

Forty-five patients underwent whole-body [<sup>18</sup>F] FDG-PET imaging between April 2020 and October 2021 at our institution. Inclusion criteria were adult patients older than 18 years of age with at least 1 documented case of SARS-CoV-2 infection confirmed by polymerase chain reaction (PCR) at any time before imaging. None of the patients had an active SARS-CoV-2 infection at time of imaging. We excluded patients with incomplete PET/CT imaging of the entire brain, patients with brain imaging showing major structural abnormalities (eg, tumors, prior surgery, ischemic infarcts, cerebral venous thrombosis) unrelated to the COVID-19 infection, and patients with documented neurologic/psychiatric antecedents or symptoms preceding the SARS-CoV-2 infection (ie, confounding clinical variables). The study flow diagram is shown in the Online Supplemental Data.

Clinical and laboratory data were extracted from the patients' electronic medical records. Variables at the initial infection were age, sex, medical comorbidities, and presenting symptoms. When patients required hospital admission, information regarding supplemental oxygenation, admission to the intensive care unit, and the development of new symptoms was also collected. COVID-19 cases were rated as mild, moderate, or severe according to international guidelines and using the National Early Warning Score 2.<sup>21</sup> Variables at the time of imaging included the time lag between the first COVID-19 test and the PET/CT scan, any persistent neurologic symptoms, body mass index (BMI), glucose levels, medications, administered [<sup>18</sup>F] FDG dose, and administration of any COVID-19 vaccine before imaging. Neurologic symptoms included persistent headaches, memory impairment, difficulty concentrating, fatigue, and insomnia. The presence of neurologic symptoms at the time of imaging was defined as persistent symptoms following COVID-19 infection that were reported in clinical notes dating no more than 7 days before PET imaging.

**Patients with Pre-COVID Imaging.** Among included patients, 15 had available [<sup>18</sup>F] FDG-PET scans obtained under identical conditions before the COVID-19 infection. Information on BMI, glucose levels, medications, and administered [<sup>18</sup>F] FDG pertaining to the pre-COVID scan dates was also collected for these patients.

**Controls.** A group of 52 age- and sex-matched controls who underwent PET/CT imaging for initial staging and were scanned under identical conditions before January 2021 was selected from our institutional database as follows: those with recently diagnosed melanoma or multiple myeloma, oncologically negative brain images, no history of neurologic disorders, and no recent use of psychotropic medications. All scans were obtained before administering any systemic chemotherapy or anticancer drugs. The limit date (December 31, 2020) used to select controls was settled on the basis of the latest epidemiologic data on the pandemic in the United States to avoid any potential bias. Information on controls regarding age, sex, medical comorbidities, medications, BMI, glucose levels, and administered [<sup>18</sup>F] FDG dose was subsequently collected from the electronic medical records.

### [<sup>18</sup>F] FDG-PET Imaging and Processing

[<sup>18</sup>F] FDG-PET scans were acquired in the same center using an acquisition protocol conforming to guidelines put forth by the American College of Radiology, the American College of Nuclear Medicine, and the Society of Nuclear Medicine and Molecular Imaging.<sup>22</sup> Whole-body scans were acquired on a Biograph mCT (Siemens; 36 patients and 47 controls) or a Discovery DRX or DLS (GE Healthcare; 9 patients and 5 controls) with in-line CT for attenuation correction at 60 minutes after the [<sup>18</sup>F] FDG intravenous administration in individuals fasting for at least 4 hours with a controlled, normal glycemic level. Brain images were extracted from the whole-body [<sup>18</sup>F] FDG-PET/CT as previously described<sup>20,23,24</sup> and converted to Analyze format for pre-processing in SPM software (<http://www.fil.ion.ucl.ac.uk/spm/software/spm12>).<sup>25</sup> The Montreal Neurological Institute 152 brain template was used as the standard template for registering PET/CT images to T1-weighted MR images using the FMRIB

## Subjects' baseline characteristics

	Post-COVID (n = 45)	Controls (n = 52) <sup>a</sup>
Age (mean) (range) (yr)	58 (18–87)	57 (24–73)
Male sex (No.) (%)	24 (53.33)	28 (53.85)
[ <sup>18</sup> F] FDG administered dose (mean) (SD) (mCi)	12.28 (3.18)	11.88 (2.59)
BMI (mean) (SD) (kg/m <sup>2</sup> )	28.62 (7.59)	28.45 (6.36)
Glucose levels (mean) (SD) (mg/dL)	95.13 (22.90)	98.04 (23.82)
Diabetes (No.) (%)	3 (6.67)	6 (11.54)
High blood pressure (No.) (%)	14 (31.11)	21 (40.38)
Delay between positive RT-PCR and imaging (mean) (SD) (mo)	6.57 (4.85)	–
COVID-19 severity mild/moderate or severe (No.) (%)	37/8 (82.22/17.78)	–
Hospitalization (No.) (%)	15 (33.33%)	–
Oxygen supplementation (No.) (%)	9 (20.00%)	–
Mechanical ventilation (No.) (%)	2 (4.44%)	–
COVID-19 vaccine at any time before [ <sup>18</sup> F] FDG-PET scan (No.) (%)	28 (62.2)	–
Symptoms (No.) (%)		
Dysosmia/dysgeusia <sup>b</sup>	17 (37.80)	–
Fever	16 (35.6)	–
Chills	6 (13.3)	–
Cough	16 (35.6)	–
Dyspnea	8 (17.8)	–
Chest pain	2 (4.4)	–
Pharyngitis	4 (8.9)	–
Rhinitis	3 (6.7)	–
Headache	4 (8.9)	–
Fatigue	7 (15.6)	–
Muscular pain	1 (2.2)	–
Dysgeusia	1 (2.2)	–
Anosmia/hyposmia	1 (2.2)	–
Diarrhea	4 (8.9)	–
Loss of appetite	2 (4.4)	–
Neurologic symptoms at time of imaging (No.) (%) <sup>c</sup>		
Persistent headaches	3 (6.7)	–
Memory impairment	1 (2.2)	–
Difficulty concentrating	1 (2.2)	–
Fatigue	1 (2.2)	–
Insomnia	1 (2.2)	–

**Note:**—The en dash indicates not applicable.

<sup>a</sup> No statistically significant difference was observed between patients post-COVID and sex- and age-matched controls ( $P < .05$ , 2-sample  $t$  test for continuous variables,  $\chi^2$  test for dichotomous variables).

<sup>b</sup> Between the time of the initial diagnosis and PET imaging. All other symptoms pertain to the time of the initial diagnosis.

<sup>c</sup> Persistent symptoms following COVID-19 infection that were reported in the patients' records dating no more than 7 days before PET imaging.

Linear Image Registration Tool (FLIRT; <http://www.fmrib.ox.ac.uk/fsl/fslwiki/FLIRT>).<sup>26,27</sup> Nonlinear spatial normalization of images to a specific [<sup>18</sup>F] FDG-PET template in the Montreal Neurological Institute space was performed using the SPM8 software. The images were then smoothed with a Gaussian kernel with a full width at half maximum of  $8 \times 8 \times 8$  mm to increase the SNR.<sup>28,29</sup> Global activity normalization was performed by proportional scaling (Online Supplemental Data). All images were checked for the presence of nonperfect fits before analysis.

### Single-Subject and Group-Level [<sup>18</sup>F] FDG-PET SPM Analyses

Whole-brain 2-sample  $t$  test analysis was initially performed at the voxel level using SPM8 software to compare patients with controls and identify clusters of hypometabolism in the patient group. Paired sample  $t$  test (single-subject) comparison between patients before and after COVID-19 infection was also performed.

Distinct  $t$ -contrasts identified brain areas where glucose metabolism was significantly lower or higher in the patient group than in the control group. Patients post-COVID were further subgrouped according to the time delay between the positive reverse transcriptase PCR (RT-PCR) and PET imaging: 0–2, 2–6, 6–12, and >12 months.

Correlations between metabolic values of clusters and demographic and clinical data were measured for group-level comparisons. A general linear model (GLM) of the preprocessed FDG-PET data of patients taken as 1 group was constructed. Age, sex, COVID-19 severity, presence of neurologic symptoms (eg, syncope, loss of taste and smell, generalized weakness, difficulty concentrating) at the time of infection and at the time of imaging and the time lag between imaging and infection were introduced as covariates of interest centered around condition means in separate GLMs. Separate  $t$ -contrasts identified brain regions showing significant positive or negative correlations between the covariates of interest and regional cerebral glucose metabolism. The SPM  $t$ -statistic (SPM[T]) maps were acquired at an uncorrected height threshold (voxel-level significance) of  $P < .05$ , with a correction for multiple comparisons at the level of the cluster using the family-wise error (FWE) rate for a corrected  $P$  value  $< .05$ .

## RESULTS

### Clinical Characteristics of Patients Post-COVID

The clinical characteristics of the 45 included post-COVID patients are detailed in the Table. No significant difference was found between the post-COVID and control groups in pre-PET glucose levels (mean, 95.13 [SD, 22.90] versus 98.04 [SD, 23.82]); mean BMI (mean, 28.62 [SD, 7.59] versus 28.45 [SD, 6.36]); and administered [<sup>18</sup>F] FDG activity (mean, 12.28 [SD, 3.18] versus 11.88 [SD, 2.59] mCi). The mean time delay between positive RT-PCR results and imaging was 6.57 (SD, 4.85) months (range, 1–24 months). At the time of diagnosis, the median National Early Warning 2 clinical score was 2, corresponding to a low-risk grading; 33.3% of patients required hospitalization (15/45), and 4.4% required mechanical ventilation (2/45).

Among the post-COVID patients, fever and cough were the most common manifestations at presentation (16/45, 35.6% each). Dyspnea, fatigue, and chills were reported in 8, 7, and 6 patients, respectively (17.8%, 15.6%, and 13.3%). On admission, 1 patient had loss of taste (1/45, 2.2%), while another had loss of



smell (1/45, 2.2%). A total of 17 patients reported experiencing loss of smell and taste between the initial diagnosis of COVID-19 and their PET imaging (17/45, 37.8%). At the time of imaging, a total of 6 patients (13%) reported  $\geq 1$  persistent neurologic symptom following COVID-19 infection, including persistent headaches (3/45, 6.7%), memory issues, focus impairment, fatigue, and insomnia (1/45 each, 2.2%) (Table).

### **Patterns of [ $^{18}$ F] FDG-PET Hypo- and Hypermetabolism**

All groups showed comparable global metabolism uptake values (Online Supplemental Data). Specifically, the comparison between the whole post-COVID ( $n = 45$ ), pre-COVID ( $n = 15$ ), and control patient ( $n = 52$ ) groups showed no significant differences ( $P = .18$ ).

### **PET Metabolic Profile of Post-COVID Scans Compared with Controls**

Clusters of significant hypo- and hypermetabolism in the whole group of post-COVID patients and subgroup analyses are reported in the Online Supplemental Data. In comparison with the 52 controls, post-COVID patients presented with significant hypometabolism ( $P$ -voxel  $< .05$  uncorrected,  $P$ -cluster  $< .05$ , FWE-corrected) involving the bilateral parietal lobes, including the precuneus regions (time-to maximum [Tmax] = 3.90); frontal lobes, including the anterior cingulate (Tmax = 2.40) and prefrontal cortices (Tmax = 3.04); occipital lobes (Tmax = 3.90); right temporal lobe (Tmax = 2.64); and right cerebellum (Tmax = 2.74). The whole group of post-COVID patients did not exhibit brain regions of statistically significant relative hypermetabolism compared with controls. In addition, cross-sectional imaging subgroup analyses showed more severe and extensive brain hypometabolism during the first 2 months after the infection onset, followed by a progressive return to normal metabolic activity. At 6–12 months, patients showed a near-complete recovery of brain abnormalities, with residual limited hypometabolic clusters in the anterior cingulate cortex, posterior inferior frontal gyri, right frontal operculum, and right temporal-insular region. The significantly reduced metabolism disappeared at 12 months. Hypermetabolism involving the brainstem, cerebellum, limbic structures (ie, amygdala and hippocampus bilaterally), a smaller region of the frontal cortex, and periventricular white matter was observed only at 2–6 months after infection (Online Supplemental Data).

### **PET Metabolic Profile of Patients Post- versus Pre-COVID**

At the group level, SPM paired samples  $t$  test comparison between PET scans of patients pre- and post-COVID ( $n = 15$ ,  $P$ -voxel  $< .05$  uncorrected,  $P$ -cluster  $< .05$  FWE-corrected) did not show statistically significant clusters. However, at 2–6 months after the infection onset, post-COVID patients presented with a significant decrease in regional glucose consumption in the bilateral parietal lobes, posterior frontal lobes including the frontal eye fields and the left cingulate cortex, and occipital lobes compared with their pre-COVID scans ( $n = 6$ ). Moreover, significant hypermetabolic areas were found in the bilateral limbic structures (anterior hippocampi and amygdala), brainstem, ventral thalami, left inferior frontal lobe, and left cerebellum during the 2- to 6-month interval (Online Supplemental Data).

### **Correlations between Brain Hypometabolism and Clinical Variables**

Age, neurologic symptoms at the time of imaging, and SARS-CoV-2 infection-severity scores were all significantly associated with the widespread extension and severity of brain metabolic patterns seen on post-COVID versus control scans. Precisely, older age, the presence of neurologic symptoms, and worse disease severity scores were positively correlated with the degree of hypometabolism in the bilateral parietal, posterior frontal, and temporal lobes, as well as the degree of hypermetabolism in the central cerebral and subcortical regions (Online Supplemental Data). In addition, SARS-CoV-2 infection severity scores were also significantly associated with the widespread extension and severity of brain metabolic patterns seen on post- versus pre-COVID scans (Online Supplemental Data).

## **DISCUSSION**

This whole-brain voxel-based PET study demonstrates brain metabolic abnormalities in patients with a history of biologically confirmed SARS-CoV-2 infection. Voxel-based brain analysis supported the recent hypothesis on SARS-CoV-2 infection-related brain metabolic impairment and provided new insights into the pathophysiology of COVID-related brain abnormalities. Cross-sectional subgroup analyses suggest that the brain metabolism remains mildly altered 6 months after disease onset and gradually improves after 6–12 months. Moreover, the significant brain hypermetabolism observed between 2 and 6 months after infection in subcortical brain regions, including the limbic structures (eg, hippocampi and amygdala), in patients post-COVID compared with both the control group and the pre-COVID imaging data set suggests that brain inflammation peaks and subsequently recovers after this time window.

A gradual change in the severity and extent of hypometabolism from a widespread pattern in  $< 2$  months to a limited involvement of the anterior cingulate cortex, right orbitofrontal cortex, bilateral posterior gyrus rectus, right insula, and medial temporal lobes was observed between 6 and 12 months postinfection. However, no significant hypometabolism was noted in these particular regions in the 0- to 2- and 2- to 6-month subgroups, raising the possibility that these regions might be preferentially impaired in the later stages of the disease. Conversely, significant areas of hypermetabolism involving the brainstem, cerebellum, and limbic structures were observed in the 2- to 6-month period subgroup. One explanation for this finding is that the regions of hypometabolism involving the frontoinsular areas and limbic system after 6 months may result from a peak in the active inflammation involving the central regions of the brain between 2 and 6 months after disease onset. Correspondingly, prior studies have reported a predominant involvement of the brainstem, cerebellum, and limbic structures (amygdala and hippocampus bilaterally) as hypermetabolic hallmarks.<sup>17,20,30</sup> Most interesting, this metabolic pattern was observed in our nonselected whole-patient group regardless of the individual's neurologic symptoms or lack thereof, highlighting some degree of abnormal cerebral metabolic activity possibly occurring even in the absence of clinical symptoms or during the subclinical phase of the infection. Yet, because previous prospective studies

had focused on comparing clinically symptomatic patients with healthy controls without including asymptomatic post-COVID patients, it remains unclear to which degree clinical symptoms correlate with specific abnormal brain metabolic patterns.<sup>17-20</sup>

To the best of our knowledge, no regional brain metabolic studies assessing intrasubject variability in patients before and after COVID-19 infections have been previously published. Therefore, we believe this approach reduces the potential bias of pre-existing regional metabolic changes in these individuals. Even though no significant regional metabolic changes were observed in the whole-group level analysis at the statistical threshold used, significant regional [<sup>18</sup>F] FDG-PET hypometabolism and hypermetabolism in the post-COVID subgroup of patients ( $n = 6$ ) imaged between 2 and 6 months after COVID-19 infection onset were noted. The lack of significant findings on [<sup>18</sup>F] FDG-PET in the whole patient group and other subgroups might be partly due to the FWE at the cluster level used and the small sample size, because the FWE rate may be considered conservative for group-level analyses with small sample sizes.

Correlation analyses revealed a relationship between regional cerebral glucose metabolism and age, neurologic symptoms at the time of imaging, and SARS-CoV-2 infection severity. This is consistent with previous studies documenting a correlation between the severity of SARS-CoV-2-related loss of smell and metabolic changes and an inverse correlation between an increased number of functional symptoms with alterations in the brainstem and cerebellum metabolism.<sup>19,31</sup> In addition, increased age has been reported as a predictor of more severe outcomes, explaining the correlation between age and the observed metabolic derangements.<sup>32,33</sup> Moreover, neurologic symptoms at the time of imaging also correlated with brain metabolic changes, in line with a study by Goehringer et al<sup>34</sup> showing correlations between metabolism in the orbitofrontal, internal temporal area, and the pons ROIs and multiple cognitive assessment scales. Also, the presence of persistent neurologic symptoms such as headaches, memory and concentration impairment, fatigue, and insomnia was positively correlated with decreased metabolism in the parietal lobes. As previously assessed, the strong correlation between changes in cerebral metabolism, specifically in the frontoparietal regions, and the cognitive functions served by those regions in COVID-19 encephalopathy suggests that these changes are interdependent.<sup>30,35</sup>

Limitations must be considered for the interpretation of this study. First, this retrospective, observational study evaluated a small group of patients who underwent FDG-PET imaging for other clinical indications, most of which were oncologic. Patients with brain lesions who underwent chemotherapy or radiation therapy to the head and neck area were excluded to reduce the confounding effect of such comorbidities. Second, patients selected for the control group were diagnosed with either multiple myeloma or melanoma, which could have affected the study results. Enrolling disease-free patients was not possible due to the retrospective nature of the study, because patients usually undergo PET imaging for a clinical indication. To minimize bias, we selected patients who had recently been diagnosed, were not experiencing symptoms, had not commenced any treatment, and did not show evidence of brain abnormalities on imaging. Nonetheless, both melanoma and multiple myeloma can have

direct and indirect effects on brain metabolism and could, therefore, affect the validity of our results. Third, the inclusion of patients who have had at least 1 dose of the COVID-19 vaccine before PET/CT may have impacted the clinical disease course and clinical-imaging correlations. Fourth, the 15 patients with pre-COVID imaging could have potentially had another earlier undocumented COVID-19 infection before the pre-COVID imaging, thus affecting the validity of that comparison.

## CONCLUSIONS

The present study demonstrates a pattern of reversible brain PET hypo- and hypermetabolic changes in patients with confirmed SARS-CoV-2 infection. The degree of observed alterations appears to be transient and positively correlates with older age, neurologic symptoms at the time of imaging, and worse disease severity scores. Even so, metabolic changes were detected in asymptomatic patients and patients without symptoms strongly suggestive of COVID-19. Brain imaging could potentially serve as a tool to identify asymptomatic cases whenever incidental [<sup>18</sup>F] FDG-PET/CT findings suspicious for SARS-CoV-2 are detected and to further understand the pathophysiology behind the neurologic symptoms observed with long COVID. Future studies must clarify how PET imaging can be used as a potential biomarker to follow-up patients clinically, monitor disease progression, and assess recovery.

Disclosure forms provided by the authors are available with the full text and PDF of this article at [www.ajnr.org](http://www.ajnr.org).

## REFERENCES

1. Johns Hopkins Coronavirus Resource Center. **Mortality Analyses.** March 10, 2023. <https://coronavirus.jhu.edu/data/mortality>. Accessed December 5, 2022
2. WHO Coronavirus (COVID-19). 2022. <https://covid19.who.int/table>. Accessed December 5, 2022
3. Rudroff T, Workman CD, Ponto LLB. **18F-FDG-PET imaging for post-COVID-19 brain and skeletal muscle alterations.** *Viruses* 2021;13:2283 CrossRef Medline
4. Havervall S, Rosell A, Phillipson M, et al. **Symptoms and functional impairment assessed 8 months after mild COVID-19 among health care workers.** *JAMA* 2021;325:2015–16 CrossRef Medline
5. Maltezou HC, Raftopoulos V, Vorou R, et al. **Association between upper respiratory tract viral load, comorbidities, disease severity, and outcome of patients with SARS-CoV-2 infection.** *J Infect Dis* 2021;223:1132–38 CrossRef Medline
6. Leung TY, Chan AY, Chan EW, et al. **Short-and potential long-term adverse health outcomes of COVID-19: a rapid review.** *Emerg Microbes Infect* 2020;9:2190–99 CrossRef Medline
7. Carfi A, Bernabei R, Landi F; Gemelli Against COVID-19 Post-Acute Care Study Group. **Persistent symptoms in patients after acute COVID-19.** *JAMA* 2020;324:603–05 CrossRef Medline
8. Goërtz YM, Herck MV, Delbressine JM, et al. **Persistent symptoms 3 months after a SARS-CoV-2 infection: the post-COVID-19 syndrome?** *ERJ Open Res* 2020;6:00542–2020 CrossRef Medline
9. Graham EL, Clark JR, Orban ZS, et al. **Persistent neurologic symptoms and cognitive dysfunction in non-hospitalized Covid-19 “long haulers.”** *Ann Clin Transl Neurol* 2021;8:1073–85 CrossRef Medline
10. Mehta P, McAuley DF, Brown M, et al; HLH Across Speciality Collaboration, UK. **COVID-19: consider cytokine storm syndromes and immunosuppression.** *Lancet* 2020;395:1033–34 CrossRef Medline

11. Song E, Zhang C, Israelow B, et al. **Neuroinvasion of SARS-CoV-2 in human and mouse brain.** *J Exp Med* 2021;218:e20202135 CrossRef Medline
12. Mandal S, Barnett J, Brill SE, et al; ARC Study Group. **'Long-COVID': a cross-sectional study of persisting symptoms, biomarker and imaging abnormalities following hospitalisation for COVID-19.** *Thorax* 2021;76:396–98 CrossRef Medline
13. Paterson RW, Brown RL, Benjamin L, et al. **The emerging spectrum of COVID-19 neurology: clinical, radiological and laboratory findings.** *Brain* 2020;143:3104–20 CrossRef Medline
14. Rubin R. **As their numbers grow, COVID-19 "long haulers" stump experts.** *JAMA* 2020;324:1381–83 CrossRef Medline
15. Fontana IC, Bongarzone S, Gee A, et al. **PET imaging as a tool for assessing COVID-19 brain changes.** *Trends Neurosci* 2020;43:935–38 CrossRef Medline
16. Rodríguez-Alfonso B, Solís SR, Silva-Hernández L, et al. **<sup>18</sup>F-FDG-PET/CT in SARS-CoV-2 infection and its sequelae.** *Rev Esp Med Nucl Imagen Mol (Engl Ed)* 2021;40:299–309 CrossRef Medline
17. Martini AL, Carli G, Kiferle L, et al. **Time-dependent recovery of brain hypometabolism in neuro-COVID-19 patients.** *Eur J Nucl Med Mol Imaging* 2022;50:90–102 CrossRef Medline
18. Kas A, Soret M, Pyatigorskaya N, et al; on the behalf of CoCo-Neurosciences study group and COVID SMIT PSL study group. **The cerebral network of COVID-19-related encephalopathy: a longitudinal voxel-based <sup>18</sup>F-FDG-PET study.** *Eur J Nucl Med Mol Imaging* 2021;48:2543–57 CrossRef Medline
19. Guedj E, Campion JY, Dudouet P, et al. **(<sup>18</sup>F)-FDG brain PET hypometabolism in patients with long COVID.** *Eur J Nucl Med Mol Imaging* 2021;48:2823–33 CrossRef Medline
20. Sollini M, Morbelli S, Ciccarelli M, et al. **Long COVID hallmarks on [<sup>18</sup>F]FDG-PET/CT: a case-control study.** *Eur J Nucl Med Mol Imaging* 2021;48:3187–97 CrossRef Medline
21. Gandhi RT, Lynch JB, Rio CD. **Mild or moderate Covid-19.** *N Engl J Med* 2020;383:1757–66 CrossRef Medline
22. Dietz M, Chironi G, Claessens YE, et al; MONACOVIC Group. **COVID-19 pneumonia: relationship between inflammation assessed by whole-body FDG PET/CT and short-term clinical outcome.** *Eur J Nucl Med Mol Imaging* 2021;48:260–68 CrossRef Medline
23. Hua C, Merchant TE, Li X, et al. **Establishing age-associated normative ranges of the cerebral <sup>18</sup>F-FDG uptake ratio in children.** *J Nucl Med* 2015;56:575–79 CrossRef Medline
24. Huang YC, Hsu CC, Huang P, et al. **The changes in brain metabolism in people with activated brown adipose tissue: a PET study.** *Neuroimage* 2011;54:142–47 CrossRef Medline
25. Friston KJ, Holmes AP, Worsley KJ, et al. **Statistical parametric maps in functional imaging: a general linear approach.** *Hum Brain Mapp* 1994;2:189–210 CrossRef
26. Jenkinson M, Bannister P, Brady M, et al. **Improved optimization for the robust and accurate linear registration and motion correction of brain images.** *Neuroimage* 2002;17:825–41 CrossRef Medline
27. Jenkinson M, Smith S. **A global optimisation method for robust affine registration of brain images.** *Med Image Anal* 2001;5:143–56 CrossRef Medline
28. Penny WD, Friston KJ, Ashburner JT, et al. *Statistical Parametric Mapping: The Analysis of Functional Brain Images.* Elsevier; 2011
29. Rosa PA, Cerami C, Gallivanone F, et al; EADC-PET Consortium. **A standardized [<sup>18</sup>F]-FDG-PET template for spatial normalization in statistical parametric mapping of dementia.** *Neuroinformatics* 2014;12:575–93 CrossRef Medline
30. Meyer PT, Hellwig S, Blazhenets G, et al. **Molecular imaging findings on acute and long-term effects of COVID-19 on the brain: a systematic review.** *J Nucl Med* 2022;63:971–80 CrossRef Medline
31. Niesen M, Trotta N, Noel A, et al. **Structural and metabolic brain abnormalities in COVID-19 patients with sudden loss of smell.** *Eur J Nucl Med Mol Imaging* 2021;48:1890–901 CrossRef Medline
32. Starke KR, Reissig D, Peterreit-Haack G, et al. **The isolated effect of age on the risk of COVID-19 severe outcomes: a systematic review with meta-analysis.** *BMJ Glob Health* 2021;6:e006434 CrossRef Medline
33. Statsenko Y, Zahmi FA, Habuza T, et al. **Impact of age and sex on COVID-19 severity assessed from radiologic and clinical findings.** *Front Cell Infect Microbiol* 2022;11:777070 CrossRef Medline
34. Goehringer F, Bruyere A, Doyen M, et al. **Brain <sup>18</sup>F-FDG PET imaging in outpatients with post-COVID-19 conditions: findings and associations with clinical characteristics.** *Eur J Nucl Med Mol Imaging* 2023;50:1084–89 CrossRef Medline
35. Hosp JA, Dressing A, Blazhenets G, et al. **Cognitive impairment and altered cerebral glucose metabolism in the subacute stage of COVID-19.** *Brain* 2021;144:1263–76 CrossRef Medline

# Dual-Layer Detector Cone-Beam CT Angiography for Stroke Assessment: First-in-Human Results (the Next Generation X-ray Imaging System Trial)

F. Ståhl, H. Almqvist, J. Kolloch, Å. Aspelin, V. Gontu, E. Hummel, M. van Vlimmeren, M. Simon, A. Thran, Å. Holmberg, M.V. Mazya, M. Söderman, and A.F. Delgado



## ABSTRACT

**BACKGROUND AND PURPOSE:** In patients with stroke, IV cone-beam CTA in the angiography suite could be an alternative to CTA to shorten the door-to-thrombectomy time. However, image quality in cone-beam CTA is typically limited by artifacts. This study evaluated a prototype dual-layer detector cone-beam CT angiography versus CTA in patients with stroke.

**MATERIALS AND METHODS:** A prospective, single-center trial enrolled consecutive patients with ischemic or hemorrhagic stroke on initial CT. Intracranial arterial segment vessel conspicuity and artifact presence were evaluated on dual-layer cone-beam CTA 70-keV virtual monoenergetic images and CTA. Eleven predetermined vessel segments were matched for every patient. Twelve patients were necessary to show noninferiority to CTA. Noninferiority was determined by the exact binomial test; the 1-sided lower performance boundary was prospectively set to 80% (98.75% CI).

**RESULTS:** Twenty-one patients had matched image sets (mean age, 72 years). After excluding examinations with movement or contrast media injection issues, all readers individually considered dual-layer cone-beam CT angiography noninferior to CTA (CI boundary, 93%, 84%, 80%, respectively) when evaluating arteries relevant in candidates for intracranial thrombectomy. Artifacts were more prevalent compared with CTA. The majority assessment rated each individual segment except M1 as having noninferior conspicuity compared with CTA.

**CONCLUSIONS:** In a single-center stroke setting, dual-layer detector cone-beam CTA virtual monoenergetic images are noninferior to CTA under certain conditions. Notably, the prototype is hampered by a long scan time and is not capable of contrast media bolus tracking. After excluding examinations with such scan issues, readers considered dual-layer detector cone-beam CTA noninferior to CTA, despite more artifacts.

**ABBREVIATIONS:** CBCT = cone-beam CT; CBCTA = cone-beam CTA; CNR = contrast-to-noise ratio; DL = dual-layer; VMI = virtual monoenergetic images

Cone-beam CT (CBCT) with flat image detectors was first demonstrated in 2000.<sup>1</sup> The technique is widely used in interventional radiology procedures for anatomic and pathology assessment.<sup>2-5</sup> In patients with stroke, IV CBCT angiography

(CBCTA) in the angiography suite could be an alternative to CTA to shorten the door-to-thrombectomy time.<sup>6</sup> CBCTA has been shown to be equal or better than CTA for the diagnosis of intracranial stenosis or proximal MCA occlusions.<sup>7,8</sup> A study in 10 patients indicated superior image-quality results in several CBCTA arterial segments compared with CTA; however, the patient cohort was heterogeneous and biased, and the results were only presented for individual vessel segments.<sup>9</sup> A retrospective study on 16 patients with stroke with large-vessel occlusion of the anterior circulation indicated that CBCTA generated from a volume perfusion scan can reliably identify the site of occlusion in the ICA and M1 segment of the MCA.<sup>10</sup> However, this study did not find CBCTA superior to CTA.<sup>10</sup>

In CTA, virtual monoenergetic images (VMIs) reconstructed from dual-energy scans have superior image quality and improve the diagnostic assessment of intracranial vessels compared with conventional polyenergetic images.<sup>11-13</sup> CBCTA image quality would likely benefit from dual-energy VMI reconstructions by means of

Received October 13, 2022; accepted after revision February 27, 2023.

From the Departments of Neuroradiology (F.S., H.A., J.K., Å.A., V.G., Å.H., M. Söderman, A.F.D.) and Neurology (M.V.M.), Karolinska University Hospital, Stockholm, Sweden; Department of Clinical Neuroscience (F.S., H.A., V.G., M.V.M., M. Söderman, A.F.D.) Karolinska Institutet, Stockholm, Sweden; Image Guided Therapy (E.H., M.v.V.), Phillips Healthcare, Best, the Netherlands; and Philips Research Hamburg (M. Simon, A.T.), Hamburg, Germany.

The trial was supported by a grant from the European Commission (Horizon 2020, NEXIS-project, grant number 780026).

Please address correspondence to Fredrik Ståhl, MD, Department of Neuroradiology, Karolinska University Hospital, Eugeniavaegen 3, 171 76 Stockholm, Sweden; e-mail: Fredrik.stahl@regionstockholm.se

Indicates open access to non-subscribers at [www.ajnr.org](http://www.ajnr.org)

Indicates article with online supplemental data.

<http://dx.doi.org/10.3174/ajnr.A7825>



reduced beam-hardening artifacts and an improved contrast-to-noise ratio (CNR).<sup>11-14</sup> Recently, performance characteristics of a prototype dual-layer detector CBCT (DL-CBCT) system were published, with the possibility of optimizing CNR by VMI energy selection.<sup>15</sup>

Because previous studies on CBCTA are small, heterogeneous, and selective, a trial enrolling consecutive patients is necessary to determine the role of CBCTA in the primary diagnostic setting of suspected stroke.<sup>7-10</sup> In this prospective trial, we assessed arterial visibility and artifact presence in patients with stroke when examined with DL-CBCT angiography (DL-CBCTA) and CTA. To our knowledge, this is the first trial on CBCTA with prospectively defined end points, enrolling awake patients with the aim of investigating noninferiority to CTA. Furthermore, this work presents the first-in-human results from a DL-CBCT prototype system.

## MATERIALS AND METHODS

### Trial Design and Participants

The Next Generation X-ray Imaging System (NEXIS) trial was a prospective, nonrandomized open-label single-sequence, 2-period crossover clinical trial with blinded image readers conducted at a comprehensive stroke center. The study sought to include patients evaluated for endovascular thrombectomy on arrival at the hospital. Patients with a suspected large-vessel occlusion of the anterior circulation underwent prehospital triage to bypass primary stroke centers as per clinical routine.<sup>16</sup> Patients 50 years of age or older with ischemic stroke of the anterior circulation or hemorrhagic stroke were consecutively enrolled from November 2020 to April 2021. Initial imaging was with CTA as per clinical routine and subsequently with the prototype DL-CBCT in an adjacent room. Depending on applicable eligibility criteria, patients were imaged once or twice with DL-CBCT (the same day as CTA or/and 1 day after CTA). Eligibility criteria, inclusion groups, and flow diagrams of study participation are presented in the Online Supplemental Data.

The study protocol and informed consent forms were approved by the Swedish Ethical Review Authority (approval No. 2020-00157). The prototype DL-CBCT system was approved by the Swedish Medical Products Agency (document No. 5.1-2020-6325), in accordance with the Medical Device Directive. Philips Healthcare was the formal sponsor of the study because of direct liability for the prototype DL-CBCT system. An independent qualified research organization contracted by the sponsor monitored the study. All patients signed an informed consent. The trial was supported by a grant from the European Commission (Horizon 2020, NEXIS-project, grant No. 780026). The study was registered prospectively at clinicaltrials.gov (identifier: NCT04571099).

### CTA and Prototype DL-CBCTA

The systems used for CTA were Aquilion ONE (Canon Medical Systems) and IQon Spectral CT (Philips Healthcare). The examination was according to clinical routine, typically including noncontrast CT of the head, multiphase CTA, and CTP. The prototype DL-CBCT system (Allura NEXIS Investigational Device; Philips Healthcare) was a commercial interventional C-arm x-ray system (Allura Xper FD20/15; Philips Healthcare) fitted with a dual-layer 20-inch (379.4 × 293.2 mm) non-CE marked detector prototype. The prototype detector has been previously described.<sup>15</sup> In essence,

the dual-layer detector captures more photons than a conventional CBCT detector. DL-CBCTA VMIs were derived from Compton and photoelectric base projections (basis material decomposition was performed in the projection domain). Vessel conspicuity may be improved due to intrinsic compensation of iodine beam-hardening artifacts in DL-CBCTA VMIs. Anticorrelated noise reduction was exploited as an inherent benefit of DL-CBCT.<sup>17</sup> All DL-CBCTA and CTA scans used the same automated injection protocol: 85 mL of iodine, 320 mg I/mL (iodixanol, Visipaque; GE Healthcare), 5 mL/s into a peripheral vein followed by an 80-mL saline chaser.

The second-phase CTA standard reconstruction was included in the study as a reference standard because it was reconstructed with a smaller FOV and the timing was typically more similar to the DL-CBCTA contrast phase (late arterial/arteriovenous). Phantom measurements indicated that the DL-CBCTA and CTA systems had comparable high-contrast spatial resolution. Scan details are shown in Table 1. In conjunction with the CTA and DL-CBCTA, the quality of the image acquisition was evaluated with regard to patient motion and timing of the contrast media injection. Scans were rated as good, acceptable, or poor.

### Diagnostic Image-Quality Assessment

A series of pilot studies were performed to determine the optimal VMI energy and noise-reduction levels for the DL-CBCTA images. We randomized 50- to 80-keV VMIs at 3 different noise-reduction levels, and expert readers evaluated them side-by-side blinded to noise and energy levels (F.S., H.A., V.G., M. Söderman, A.F.D.). Window settings were normalized to a previous publication on dual-energy CTA.<sup>18</sup> Images were ranked in order of preference with regard to image quality and artifact presence. The 70-keV images with a moderate noise reduction were best suited for the purpose of the study.

In the reader study, vessel conspicuity and artifact presence were evaluated separately on 5-point Likert scales, adopted with slight modifications from previous studies (5, excellent vessel conspicuity or no artifacts; 1, vessel not visible or extensive artifacts) (see the Online Supplemental Data for a detailed description).<sup>10,19</sup> All patients had unilateral ischemic or hemorrhagic stroke; thus, the affected hemispheres were not included in the analysis. Images were randomized and evaluated independently by 3 neuroradiologists (H.A., J.K., and Å.A.) each with >9 years of experience in a single-sequence, 2-period crossover design with a mean washout period of 4 weeks (range, 1-8 weeks). The readers were blinded to technique, and there was no clinical information. The study software allowed changes in section thickness, viewing plane, window level, and window width.

Sixteen intracranial arterial segments were prospectively defined for the readers' study. For the powered analysis, some arterial segments were merged to render 11 arterial segments per patient (Table 2). For merged segments, the scores of individually evaluated segments were averaged. The score difference between DL-CBCTA and CTA for each segment in each patient determined whether a segment was considered inferior, equal, or superior. In case of an absent segment due to variant anatomy, a vessel conspicuity score of 1 was given for the specific segment (see the previous paragraph). In addition to individual reader's results, the majority assessment is also presented, ie,

**Table 1: Scan details**

	Canon Aquilion ONE	Philips IQon	Prototype DL-CBCT
Tube (kV)	100	120	120
Tube current (mAs/mA) (average)	196 (Auto-modulation)	114 (Auto-modulation)	310
Scan time/rotation time (sec)	3.3/0.5 (Full rotation)	2.5/0.3 (Full rotation)	20.0/20.0 (200° rotation)
Nominal beam width (mm)	80 × 0.500	64 × 0.625	194.700
Pitch factor	0.813	0.671	NA
Display FOV coronal × sagittal × axial (mm <sup>3</sup> )	210.9 × 210.9 × 160.0	210.0 × 210.0 × 160.0	251.8 × 251.8 × 194.7
Section thickness (mm)	0.50	0.67	0.66
Matrix size	512 × 512	512 × 512	384 × 384
Reconstruction kernel	FC43	Filter UA	Ståhl et al <sup>15a</sup>
Reconstruction algorithm	AIDR 3D eStandard	iDose <sup>4</sup> level 4	Ståhl et al <sup>15a</sup>
Avg CTDIvol (16-cm phantom)	20.0 mGy	21.3 mGy	NA
Air kerma (in an 18-cm water phantom) <sup>b</sup>	NA	NA	57.6 mGy
MTF <sup>c</sup>	50%: 3.78 10%: 6.57	50%: 3.46 10%: 6.65	50%: 3.57 10%: 6.04

**Note:**—CTDIvol indicates volume CT dose index; MTF, modulation transfer function; NA, not applicable.

<sup>a</sup>Details of the prototype algorithm are described in Ståhl et al.<sup>15</sup>

<sup>b</sup>Air kerma in an 18-cm diameter plastic water phantom at the center of the scan length, measured in accordance with American Association of Physicists in Medicine Task Group Report 111.<sup>26</sup>

<sup>c</sup>Generated from consecutive scans of the upper bead of a Catphan CTP528 module (The Phantom Laboratory).

**Table 2: Arterial segments**

16 Segments	11 Segments (Powered)	11 Segments (Thrombectomy)
ICA	ICA	ICA
M1	M1	M1
M2	M2	M2
M3	M3-M4	M3
M4		M4
A1	A1-A2	A1
A2		A2
Lenticulostriate	Lenticulostriate	
Vertebral	Vertebral	Vertebral
Basilar	Basilar	Basilar
AICA	AICA-PICA-SCA	
PICA		
SCA		
Basilar perforators	Basilar perforators	
P1	P1-P2	P1
P2		P2

**Note:**—Lenticulostriate indicates lenticulostriate artery perforators; Vertebral, intracranial vertebral artery; Basilar perforators, basilar artery perforating branches; SCA, superior cerebellar artery.

segments judged as superior/equal or inferior compared to CTA by at least 2 out of 3 readers.

### Statistical Analysis

The powered outcome of this study was the proportion of arterial segments with equal or superior visibility compared with CTA (Table 2). The target proportion was 90% equal or superior ratings, with a lower boundary performance goal set to 80%. The 1-sided  $\alpha$  was modified from .025 to .0125, to account for multiple end points. A sample size of 126 was required to render 80% power. Because the powered end point was trait-based, 12 patients with a total of 132 arterial segments (11 segments each) constituted the minimum sample size. For these analyses, the exact binomial test with a 1-sided 98.75% CI was used. Within-subject correlation of arterial segments was assessed by the Cochran-Mantel-Haenszel test.<sup>20</sup> Interrater agreement was assessed by the Fleiss  $\kappa$ .<sup>21</sup> Statistical analyses and graphic presentations were made in R Studio (Version 1.4.1103; <http://rstudio.org/download/desktop>). A biostatistician was consulted at all stages of the study.

## RESULTS

### Population Characteristics

Of 28 consecutively enrolled patients, 5 had no in-house CTA and 2 underwent subcutaneous IV contrast media injection during the DL-CBCTA scan. Two patients were imaged twice with DL-CBCTA, and for those patients, the results from both scans were averaged. Consequently, 21 complete and matched DL-CBCTA and CTA image sets from 21 patients were included (Fig 1, flow diagram). The mean age was 72 (SD, 9) years, and 14 were women (67%). The right hemisphere was affected in 11 (57%) patients. Three patients had a hemorrhagic stroke. Of the remaining 18 patients with ischemic stroke, 17 (94%) presented with occlusion of the ICA or proximal MCA (M1 or M2 segment) on CTA. Seventeen patients (81%) were imaged with DL-CBCTA the day after CTA imaging (mean, 23.8 [SD, 3.0] hours), of whom 15 had been treated with thrombectomy the day before (modified TIC1 grade 2C reperfusion or better in 11 [73%]). Because only the unaffected hemisphere was included in the statistical analysis, the degree of reperfusion was not considered to influence the results. Four patients (19%) were only imaged with DL-CBCTA on the same day as CTA (mean, 1.2 [SD, 0.6] hours after CTA).

### Vessel Visibility Assessment

For the powered end point of overall arterial visibility, 21 patients with a total of 231 matched arterial segments (11 per patient) were evaluated by each reader. One reader scored equal or superior vessel visibility for DL-CBCTA and CTA in 90% of arterial segments (CI lower boundary of 84%) and met the predefined noninferiority criteria (lower performance boundary of >80%), whereas the other 2 readers did not (CI lower performance boundary of 58% and 53%, respectively). The result of the majority analysis was 77% of arterial segments being rated noninferior in DL-CBCTA (CI lower boundary of 71%). The Fleiss  $\kappa$  between readers was 0.25 (fair agreement). Examples of patient scans with no disagreement among readers and with considerable interrater variability are presented in the Online Supplemental Data.

### Post Hoc Subset Analyses

Nine of the 21 (43%) DL-CBCTA scans were of poor quality due to patient motion or suboptimal timing of the contrast media injection (Fig 2). No CTA scan was rated as poor. In a subset analysis including only the 12 matched scans of acceptable or good quality, the 3 readers rated vessel visibility as noninferior in 98%, 88%, and 78% of the cases, respectively, which meant that 2 readers met the predefined performance goal (CI lower boundary of >80%). The majority result for this subset was 98% (CI lower boundary of 93%). See Table 3 for a detailed display of the results.

Eleven arterial segments especially relevant for thrombectomy candidates were selected for evaluation in the same patient subset (Table 2). According to each reader, noninferior vessel visibility was

98%, 91%, and 88%, and all readers individually exceeded the CI lower performance boundary of 80% (Table 3). Majority results were identical to those of the powered subset (98%, CI lower boundary 93%). The Fleiss  $\kappa$  for this data set was 0.38 (fair agreement). There was no significant within-patient correlation of individual arterial segments for any of the individual readers in the thrombectomy data set or subset. However, a significant correlation was found for all majority analyses and most individual reader results for the powered data set and subset (Online Supplemental Data).

### Image Artifact Assessment

Image artifacts were assessed in the same arterial segments as used for vessel visibility. For the prospectively determined arterial segments, readers perceived artifact presence as noninferior to CTA in 58%, 42%, and 36% of the segments rated (Table 4). The Fleiss  $\kappa$  was 0.26 (fair agreement). After excluding the 9 scans of inferior quality, noninferiority to CTA for artifact assessment was perceived in 68%, 66%, and 55% of the cases. The lowest number of artifacts compared with CTA was observed in the subset of 11 arterial segments especially relevant for thrombectomy candidates (Table 4). The Fleiss  $\kappa$  for this data set was 0.34 (fair agreement). In summary, noninferiority in terms of artifacts was not seen in the full data set or any subset analysis, given a lower performance boundary of 80%.

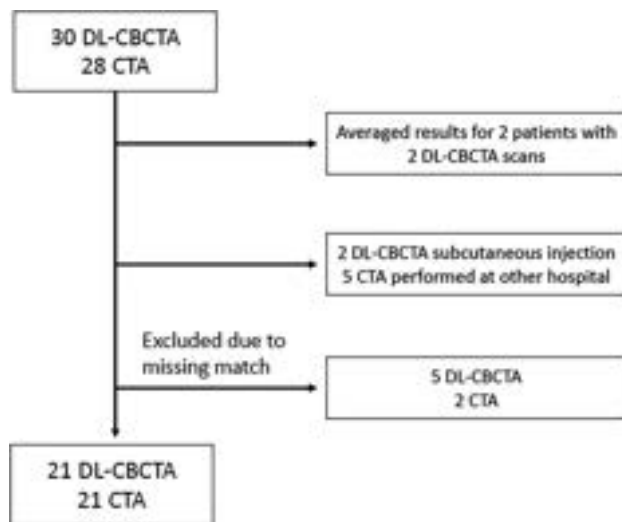


**FIG 1.** Of 28 consecutively enrolled patients, 5 had no in-house CTA and 2 had subcutaneous IV contrast media injection during the DL-CBCTA scan. Two patients were imaged twice with DL-CBCTA, and for those, the results from both scans were averaged. Consequently, 21 complete and matched DL-CBCTA and CTA image sets from 21 patients were included.

### Evaluation of Individual Arterial Segments

The Online Supplemental Data show the whole data set of individual arterial

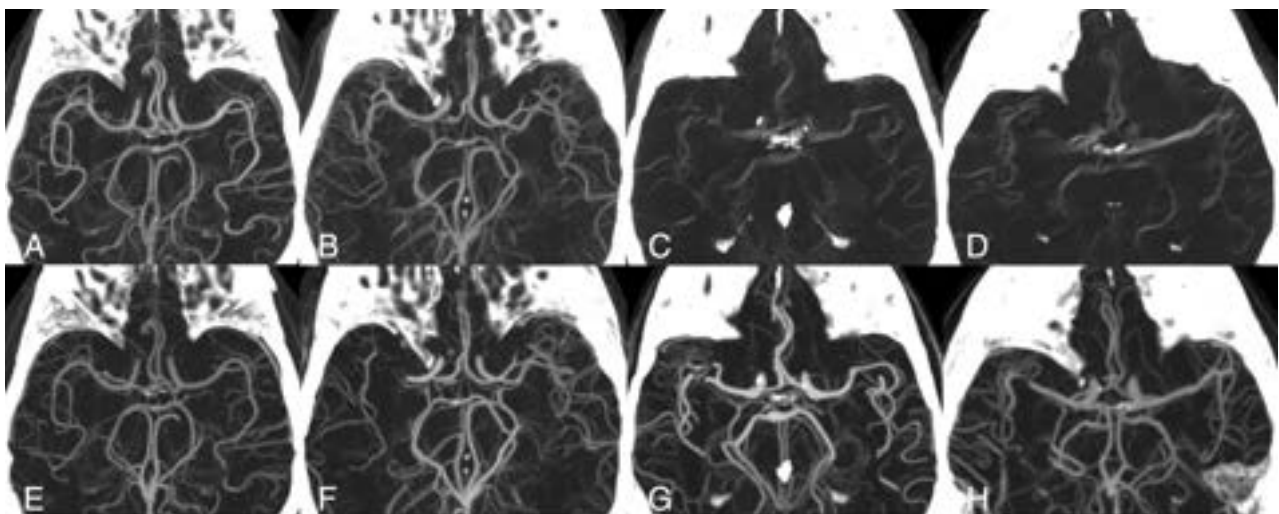


**FIG 2.** DL-CBCTA 70-keV images (upper row) and CTA (lower row) with MIP 35-mm section thickness. A and B, Acceptable-quality DL-CBCTA scans. C and D, Typical scans in the data set affected by motion artifacts. Lower row (E–H) shows the corresponding CTA. Note that images F, G, and H show a right-sided MCA occlusion, which have been resolved at the time for DL-CBCTA imaging. Only the arterial anatomy in the unaffected hemisphere was evaluated in this study.

**Table 3: Vessel visibility<sup>a</sup>**

	Powered Data Set	Powered Subset	Thrombectomy Data Set	Thrombectomy Subset
Patients	21	12	21	12
Segments rated	231	132	231	132
Majority	0.77 (0.70)	0.98 (0.93) <sup>b</sup>	0.77 (0.71)	0.98 (0.93) <sup>b</sup>
Reader 1	0.65 (0.58)	0.88 (0.80) <sup>b</sup>	0.67 (0.60)	0.91 (0.84) <sup>b</sup>
Reader 2	0.90 (0.84) <sup>b</sup>	0.98 (0.93) <sup>b</sup>	0.89 (0.83) <sup>b</sup>	0.98 (0.93) <sup>b</sup>
Reader 3	0.60 (0.53)	0.78 (0.69)	0.68 (0.61)	0.88 (0.80) <sup>b</sup>

<sup>a</sup> Proportion of DL-CBCTA arterial segment visibility rated equal or superior to CTA. The data set (21 patients) includes all scans; the subset (12 patients) excluded inferior scans. The 98.75% CI of the 1-sided lower performance boundary is in parentheses (lower boundary is defined as 80% rated equal or superior).

<sup>b</sup> Statistically significant result.

**Table 4: Artifacts<sup>a</sup>**

	Powered Data Set	Powered Subset	Thrombectomy Data Set	Thrombectomy Subset
Patients	21	12	21	12
Segments rated	231	132	231	132
Majority	0.41 (0.34)	0.63 (0.53)	0.55 (0.48)	0.81 (0.72)
Reader 1	0.42 (0.35)	0.68 (0.58)	0.54 (0.46)	0.85 (0.77)
Reader 2	0.58 (0.50)	0.66 (0.56)	0.65 (0.58)	0.74 (0.64)
Reader 3	0.36 (0.29)	0.55 (0.44)	0.52 (0.44)	0.73 (0.63)

<sup>a</sup> Proportion of DL-CBCTA arterial segment artifacts rated equal or superior to CTA. Data set (21 patients) includes all scans; subset (12 patients) excluded inferior scans. The 98.75% CI of the 1-sided lower performance boundary is in parentheses (lower boundary is defined as 80% rated equal or superior).

segment ratings per reader and according to the majority assessment. In summary, A2-, M4- and AICA-segment vessel conspicuity was most commonly rated as noninferior to CTA (at least 76% for each reader and segment), with high majority scores (range, 81%–90% rated noninferior). The lenticulostriate and basilar perforating arteries had high majority scores for vessel conspicuity; however, 1 reader's results largely differed from the other 2. It was noted that a safe distinction from small draining veins was difficult. Consequently, the majority score was interpreted with caution for these segments. The A2 segment was rated with the fewest artifacts (majority score, 76% rated noninferior), followed by A1, M2, M3, M4, P1, and P2 segments (majority score, 62%–67%, were rated noninferior).

In the subset of 12 acceptable scans (Online Supplemental Data), A2, M4, AICA, and P2 segments were the most commonly rated as noninferior vessel conspicuity to CTA (at least 92% for each reader and segment). According to the majority assessment, 100% noninferior vessel conspicuity to CTA was seen for all segments except M1 (75% rated noninferior). For artifacts, 100% of A1, A2, M3, M4, and P2 segments were noninferior in the subset according to the majority assessment.

M1-segment vessel conspicuity was noninferior to CTA in 57% of the whole data set and 75% of the subset, the lowest scores registered. The M1 segment also had a higher degree of artifacts (43% rated noninferior in the data set and 67% in the subset). The intracranial ICA segment similarly had a high prevalence of artifacts, and its scores were among the lowest registered.

## DISCUSSION

The study compared the intracranial artery visibility of IV DL- CBCTA images with the reference standard CTA in consecutively enrolled patients with stroke. Of dual-detector CBCTA scans, 43% were of poor quality due to movement artifacts or contrast media injection issues. In the subset of patients with acceptable scan quality, DL-CBCTA was noninferior to CTA with regard to intracranial artery conspicuity, despite more prominent image artifacts.

The strengths of the trial were the prospectively defined end points, the clinically relevant study population, and the assessment by blinded readers. The noninferiority lower boundary was set to 80% to minimize the risk of type I error. For the complete data set, 1 reader determined DL-CBCTA arterial visibility as noninferior to CTA, but the other 2 readers did not. However, after excluding DL-CBCTA scans with movement artifacts or suboptimal contrast media injections, 2 readers individually agreed on noninferiority of

DL-CBCTA versus CTA. In this subset, the majority score determined vessel conspicuity to be noninferior to CTA. Image artifacts were generally more abundant in the DL-CBCTA images, and the results did not reach noninferiority.

After we excluded scans of poor quality, all arterial segments except M1 showed noninferior conspicuity to CTA according to the majority assessment. With regard to individual reader results, the M4, A2, P2, and AICA segments had the best vessel visibility in the subset, and all except AICA expectedly indicated a low degree of artifacts in the corresponding segments. The M1 and ICA segments had the lowest scores for vessel visibility compared with CTA and indicated a higher prevalence of artifacts. Our results indicate that arteries that are not influenced by skull base artifacts may have superior conspicuity on DL-CBCTA compared with CTA. As the systems had comparable spatial resolution, this may be attributed to fundamental differences of the VMI (DL-CBCTA) and polyenergetic (CTA) reconstructions. DL-CBCTA VMIs had a lower absolute noise (achieved through anticorrelated noise reduction) and may be superior in mitigating beam-hardening artifacts from iodinated vessels (due to material decomposition in the projection space) compared with CTA. In contrast, arteries adjacent to the skull base showed an inferior visibility compared with CTA. Even though beam-hardening artifacts are mitigated by VMIs, the findings were expected because circular CBCT scans are highly susceptible to skull base artifacts such as beam-hardening.<sup>22</sup> Since the M1 and ICA segments are often involved in acute ischemic stroke, future effort should focus on improving visualization of these segments. Recently, a novel x-ray tube trajectory for CBCT was shown to improve intracranial image quality by reducing bone beam-hardening artifacts from the skull.<sup>22</sup>



The DL-CBCTA scan time was 20 seconds to enable dual-layer image acquisition. Nine scans (43%) were considered of poor quality, predominantly due to motion artifacts. No repeat scans were performed in this study, in accordance with the ethics approval and study protocol. Most interesting, all except 1 DL-CBCTA scan obtained on the day of admission showed some degree of motion artifacts despite efforts to fixate the head in the head rest. The long scan time is a characteristic disadvantage of CBCT, which must be considered when selecting an appropriate imaging technique for patients with stroke. In awake patients with limited compliance, efforts to minimize the risk of patient movement is warranted. An enhanced head fixation may decrease motion artifacts.<sup>23</sup> Moreover, novel reconstruction methods may mitigate the effects of patient motion in CBCT.<sup>24,25</sup> If there are still considerable motion artifacts present, one may consider a repeat scan.

Earlier studies evaluating the diagnostic accuracy of CBCTA either had patients under general anesthesia<sup>10</sup> or a highly selective patient cohort able to comply with instructions.<sup>9</sup> As expected, these studies did not report any significant impact on image quality from motion artifacts. In 1 study, it is unclear whether analyses were matched pair-wise, and the results were presented only for individual vessel segments and not for the CBCTA as a whole.<sup>9</sup> In addition, outcome measures from previous studies were not prospectively defined and typically were not adjusted for multiple comparisons.<sup>7-10</sup>

This trial has several limitations and technical considerations. The ethics approval did not allow inclusion of patients before treatment. Thus, nonsymptomatic vessel segment conspicuity and artifacts were evaluated as characteristics of diagnostic quality. The original intention was to perform a subset analysis on the diagnostic accuracy to identify intracranial occlusions in a subgroup of patients (inclusion group 3.I, Online Supplemental Data), but the analysis was not performed due to few patients ( $n = 3$ , of which 2 scans were of poor quality). The study design and power calculation aimed to assess the diagnostic quality of the entire intracranial artery vasculature. In the setting of large-vessel occlusion stroke, it may be favorable to power a diagnostic study with regard to number of patients or only large-diameter arteries, albeit with the risk of missing information about small vessels contributing to collateral flow and small concurrent occlusions.

The results in this study are derived by comparing the same vessel segment in the same patient. Consequently, absent vessel segments due to variant anatomy (for example absent A1 or PICA) received the same vessel conspicuity score in both DL-CBCTA and CTA (ie, 1). However, readers were not specifically instructed on how to assess segments with multiple vessels (lenticulostriate arteries, basilar perforating arteries) or certain variant anatomy (such as an azygos A2 or an AICA-PICA complex). This issue may have increased the interrater variability ( $\kappa$  values were only fair). In the majority results, as well as individual reader results of the powered data set and subset, we show a significant within-patient correlation of arterial segments. In the majority results, this is likely influenced by the M1 segment being most frequently rated inferior. For individual readers, the lenticulostriate arteries and basilar perforators are likely contributors in addition to M1 because they were interpreted inconsistently.

A minority of patients (19%) were imaged with DL-CBCTA shortly after CTA, which may have affected the distribution of iodine contrast media in the DL-CBCTA images. The impact of potential differences in flow dynamics and vessel status for patients imaged with DL-CBCTA 1 day after CTA is unknown. CNR comparison of DL-CBCTA and CTA was not possible because image acquisition timing after IV contrast injections were not identical. A previous study on CBCTA used a  $512 \times 512$  image pixel matrix, similar to CT.<sup>9</sup> Using a  $384 \times 384$  image pixel matrix for DL-CBCTA impacts the level of detail and noise characteristics, possibly affecting the perception of image quality. The DL-CBCTA scan time of 20 seconds made it prone to movement artifacts. Also, in some cases, image quality was poor due to suboptimal timing of the contrast media injection. Because the trial studied a prototype system, manual bolus tracking was not possible. Instead, a manual delay of 15–20 seconds was used for all patients. Furthermore, we used only 1 acquisition protocol. Future studies should involve image acquisition and reconstruction protocol optimization.

DL-CBCTA after IV contrast media injection in angiography suite enables the primary diagnostic work-up and subsequent treatment in the same room. In the clinical setting, this approach would require concurrent image evaluation of the brain to rule out intracranial hemorrhage and to enable assessment of irreversible brain ischemia and possibly brain perfusion. Noncontrast DL-CBCT of the brain has been studied within the scope of the NEXIS trial, and data are currently being prepared for final analysis. Visualization of the cervical vasculature is warranted in patients eligible for thrombectomy; however, this was not addressed in the scope of this study.

## CONCLUSIONS

In a single-center stroke setting, DL-CBCTA 70-keV virtual monoenergetic images are noninferior to CTA under certain conditions. Notably, the prototype system is hampered by a long scan time and is not capable of contrast media bolus tracking. After excluding examinations with such scan issues, readers considered DL-CBCTA noninferior to CTA, despite more artifacts.

## ACKNOWLEDGMENTS

We thank all members of the NEXIS consortium for a collaborative effort. We thank Kevin Najarian for biostatistics support. We thank Gavin Poludniowski, Artur Omar and Dirk Schäfer for their support in questions regarding medical physics and image reconstruction.

Disclosure forms provided by the authors are available with the full text and PDF of this article at [www.ajnr.org](http://www.ajnr.org).

## REFERENCES

1. Jaffray DA, Siewerdsen JH. **Cone-beam computed tomography with a flat-panel imager: initial performance characterization.** *Med Phys* 2000;27:1311–23 CrossRef Medline
2. Soderman M, Babic D, Holmin S, et al. **Brain imaging with a flat detector C-arm: Technique and clinical interest of XperCT.** *Neuroradiology* 2008;50:863–68 CrossRef Medline
3. Dijkstra ML, Eagleton MJ, Greenberg RK, et al. **Intraoperative C-arm cone-beam computed tomography in fenestrated/branched aortic endografting.** *J Vasc Surg* 2011;53:583–90 CrossRef Medline
4. Tacher V, Radaelli A, Lin M, et al. **How I do it: cone-beam CT during transarterial chemoembolization for liver cancer.** *Radiology* 2015;274:320–34 CrossRef Medline

5. Doerfler A, Golitz P, Engelhorn T, et al. **Flat-panel computed tomography (DYNA-CT) in neuroradiology: from high-resolution imaging of implants to one-stop-shopping for acute stroke.** *Clin Neuroradiol* 2015;25 Suppl 2:291–97 CrossRef Medline
6. Brehm A, Tsogkas I, Maier IL, et al. **One-stop management with perfusion for transfer patients with stroke due to a large-vessel occlusion: feasibility and effects on in-hospital times.** *AJNR J Neuroradiol* 2019;40:1330–34 CrossRef Medline
7. Struffert T, Deuerling-Zheng Y, Kloska S, et al. **Flat detector CT in the evaluation of brain parenchyma, intracranial vasculature, and cerebral blood volume: a pilot study in patients with acute symptoms of cerebral ischemia.** *AJNR Am J Neuroradiol* 2010;31:1462–69 CrossRef Medline
8. Struffert T, Deuerling-Zheng Y, Kloska S, et al. **Dynamic angiography and perfusion imaging using flat detector CT in the angiography suite: a pilot study in patients with acute middle cerebral artery occlusions.** *AJNR Am J Neuroradiol* 2015;36:1964–70 CrossRef Medline
9. Saake M, Breuer L, Goelitz P, et al. **Flat detector computed tomography angiography with intravenous contrast application: feasibility for visualization of cerebral arterial vasculature.** *J Neuroimaging* 2013;23:414–20 CrossRef Medline
10. Hoelter P, Goelitz P, Lang S, et al. **Visualization of large vessel occlusion, clot extent, and collateral supply using volume perfusion flat detector computed tomography in acute patients with stroke.** *Acta Radiol* 2019;60:1504–11 CrossRef Medline
11. Schneider D, Apfaltrer P, Sudarski S, et al. **Optimization of kiloelectron volt settings in cerebral and cervical dual-energy CT angiography determined with virtual monoenergetic imaging.** *Acad Radiol* 2014;21:431–36 CrossRef Medline
12. Leithner D, Mahmoudi S, Wichmann JL, et al. **Evaluation of virtual monoenergetic imaging algorithms for dual-energy carotid and intracerebral CT angiography: effects on image quality, artefacts and diagnostic performance for the detection of stenosis.** *Eur J Radiol* 2018;99:111–17 CrossRef Medline
13. Neuhaus V, Große Hokamp N, Abdullayev N, et al. **Comparison of virtual monoenergetic and polyenergetic images reconstructed from dual-layer detector CT angiography of the head and neck.** *Eur Radiol* 2018;28:1102–10 CrossRef Medline
14. Fredenberg E. **Spectral and dual-energy X-ray imaging for medical applications.** *Nuclear Instruments and Methods in Physics Research Section A: Accelerators, Spectrometers, Detectors and Associated Equipment* 2018;878:74–87 CrossRef
15. Stähl F, Schäfer D, Omar A, et al. **Performance characterization of a prototype dual-layer cone-beam computed tomography system.** *Med Phys* 2021;48:6740–54 CrossRef Medline
16. Keselman B, Berglund A, Ahmed N, et al. **The Stockholm Stroke Triage Project: outcomes of endovascular thrombectomy before and after triage implementation.** *Stroke* 2022;53:473–81 CrossRef Medline
17. Brown KM, Zabic S, Shechter G. **Impact of spectral separation in dual-energy CT with anti-correlated statistical reconstruction.** *Proceedings of the Fully Three-Dimensional Image Reconstruction in Radiology and Nuclear Medicine*, Worcester, Massachusetts. July 2, 2015:491–94
18. Zopfs D, Lennartz S, Abdullayev N, et al. **Generally applicable window settings of low-keV virtual monoenergetic reconstructions in dual-layer CT-angiography of the head and neck.** *Quant Imaging Med Surg* 2021;11:3408–17 CrossRef Medline
19. Hinkmann FM, Voit HL, Anders K, et al. **Ultra-fast carotid CT-angiography: low versus standard volume contrast material protocol for a 128-slice CT-system.** *Invest Radiol* 2009;44:257–64 CrossRef Medline
20. Mantel N, Haenszel W. **Statistical aspects of the analysis of data from retrospective studies of disease.** *J Natl Cancer Inst* 1959;22:719–48 Medline
21. Fleiss JL. **Measuring nominal scale agreement among many raters.** *Psychol Bull* 1971;76:378–82 CrossRef
22. Cancelliere NM, Hummel E, van Nijnatten F, et al. **The butterfly effect: improving brain cone-beam CT image artifacts for stroke assessment using a novel dual-axis trajectory.** *J Neurointerv Surg* 2023;15:283–87 CrossRef Medline
23. Leyhe JR, Tsogkas I, Hesse AC, et al. **Latest generation of flat detector CT as a peri-interventional diagnostic tool: a comparative study with multidetector CT.** *J Neurointerv Surg* 2017;9:1253–57 CrossRef Medline
24. Ouadah S, Jacobson M, Stayman JW, et al. **Correction of patient motion in cone-beam CT using 3D–2D registration.** *Phys Med Biol* 2017;62:8813–31 CrossRef Medline
25. Li Y, Garrett JW, Li K, et al. **Time-resolved C-arm cone beam CT angiography (TR-CBCTA) imaging from a single short-scan C-arm cone beam CT acquisition with intra-arterial contrast injection.** *Phys Med Biol* 2018;63:075001 CrossRef Medline
26. American Association of Physicists in Medicine. **Report of American Association of Physicists in Medicine Task Group 111: The Future of CT Dosimetry: Comprehensive Methodology for the Evaluation of Radiation Dose in X-Ray Computed Tomography** (2010). <https://www.aapm.org/pubs/reports/detail.asp?docid=109>. Accessed September 6, 2022

# Clinical Relevance of Plaque Distribution for Basilar Artery Stenosis

J. Luo, X. Bai, K. Huang, T. Wang, R. Yang, L. Li, Q. Tian, R. Xu, T. Li, Y. Wang, Y. Chen, P. Gao, J. Chen, B. Yang, Y. Ma, and L. Jiao



## ABSTRACT

**BACKGROUND AND PURPOSE:** There is no clear association between plaque distribution and postoperative complications in patients with basilar artery atherosclerotic stenosis. The aim of this study was to determine whether plaque distribution and postoperative complications after endovascular treatment for basilar artery stenosis are related.

**MATERIALS AND METHODS:** Our study enrolled patients with severe basilar artery stenosis who were scanned with high-resolution MR imaging and followed by DSA before the intervention. According to high-resolution MR imaging, plaques can be classified as ventral, lateral, dorsal, or involved in 2 quadrants. Plaques affecting the proximal, distal, or junctional segments of the basilar artery were classified according to DSA. An experienced independent team assessed ischemic events after the intervention using MR imaging. Further analysis was conducted to determine the relationship between plaque distribution and postoperative complications.

**RESULTS:** A total of 140 eligible patients were included in the study, with a postoperative complication rate of 11.4%. These patients were an average age of 61.9 (SD, 7.7) years. Dorsal wall plaques accounted for 34.3% of all plaques, and plaques distal to the anterior-inferior cerebellar artery accounted for 60.7%. Postoperative complications of endovascular treatment were associated with plaques located at the lateral wall (OR = 4.00; 95% CI, 1.21–13.23;  $P = .023$ ), junctional segment (OR = 8.75; 95% CI, 1.16–66.22;  $P = .036$ ), and plaque burden (OR = 1.03; 95% CI, 1.01–1.06;  $P = .042$ ).

**CONCLUSIONS:** Plaques with a large burden located at the junctional segment and lateral wall of the basilar artery may increase the likelihood of postoperative complications following endovascular therapy. A larger sample size is needed for future studies.

**ABBREVIATIONS:** HR-MR imaging = high-resolution MR imaging; LA = lumen area; MLN = maximal lumen narrowing; VA = vessel area; WA = wall area

The basilar artery is the main artery for the posterior intracranial circulation, where atherosclerotic stenosis is frequently discovered in patients with ischemic events, such as stroke and TIA, which are responsible for 10.7% of strokes annually.<sup>1</sup>

Patients with symptomatic and severe basilar artery stenosis ( $\geq 70\%$ ) may benefit from endovascular treatment, including primary angiography, balloon-mounted stent placement, and self-expanding stent placement.<sup>2</sup> Compared with the those in the anterior circulation, postoperative complications are higher in the posterior circulation with a reported risk of 21.6% in the basilar artery.<sup>3,4</sup> Therefore, it is crucial to understand and prevent a high risk of complications occurring during endovascular treatment in patients with basilar artery stenosis.

The distribution of atherosclerotic plaques is associated with the risk of ischemic events.<sup>5–7</sup> For example, it is more likely that atherosclerotic plaques located near perforating orifices are symptomatic during stent placement and may have a “snow plowing” effect.<sup>8</sup> Several postmortem studies have demonstrated that basilar artery perforators typically originate from the lateral and dorsal walls of the segment, distal from the anterior-inferior cerebellar artery, possibly explaining the high rate of postoperative complications.<sup>9,10</sup> However, the relationship between the distribution of basilar artery plaque and postoperative complications has not yet been reported.

Received November 20, 2022; accepted after revision March 1, 2023.

From the China International Neuroscience Institute (J.L., X.B., T.W., R.Y., L.L., R.X., T.L., Y.W., Y.C., P.G., J.C., B.Y., Y.M., L.J.), Beijing, China; Department of Neurosurgery (J.L., X.B., T.W., R.Y., L.L., R.X., T.L., Y.W., Y.C., P.G., J.C., B.Y., Y.M., L.J.), Xuanwu Hospital, Beijing Key Laboratory of Clinical Epidemiology (Q.T.), School of Public Health, and Department of Interventional Radiology (P.G., L.J.), Xuanwu Hospital, Capital Medical University, Beijing, China; and The Eighth Affiliated Hospital (K.H.), SUN YAT-SEN University, Shenzhen, Guangdong Province, China.

This study was funded by the National Key Research and Development Program of China (2016YFC1301703), Beijing Science and Technology Planning Project (Z20100005520019), and Beijing Hospitals Authority's Ascent Plan (DFL20220702).

Please address correspondence to Liqun Jiao, MD, PhD, Departments of Neurosurgery and Interventional Radiology, Xuanwu Hospital, Capital Medical University, No. 45 Changchun St, Xicheng District, 100053, Beijing, China; e-mail: liqunjiao@sina.cn

Indicates open access to non-subscribers at [www.ajnr.org](http://www.ajnr.org)

Indicates article with online supplemental data.

<http://dx.doi.org/10.3174/ajnr.A7839>

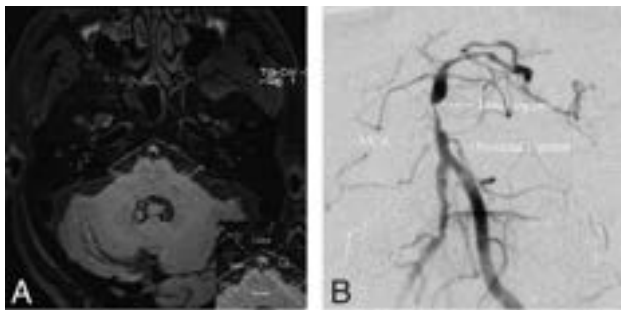


**FIG 1.** A, The basilar artery is divided into 4 quadrants at the axial position based on high-resolution MR imaging. B, The basilar artery is divided into 2 segments referring to the AICA on the basis of DSA, the proximal and distal segments. The junctional segment is defined when the plaque involves both segments across the anterior-inferior cerebellar artery.

Understanding the distribution of basilar artery plaques can help in reducing the incidence of postoperative complications. Evidence from studies since the Stenting versus Aggressive Medical Management for Preventing Recurrent Stroke in Intracranial Stenosis (SAMMPRIS) trial has shown that the postoperative risk of endovascular treatment for intracranial stenosis can be reduced from 14.7% to 9.4% by excluding symptomatic patients with perforating infarction.<sup>11</sup> The postoperative risk could be reduced excluding perforating infarction actually infers the plaque location, whether it is near perforating orifices, according to the phenotype of cerebral infarction. Presently, plaque distribution in axial and coronal positions can be precisely evaluated using high-resolution MR imaging (HR-MR imaging) and DSA.<sup>12,13</sup> However, very few studies have explored the direct relationship between plaque distribution and postoperative complications after endovascular treatment from the axial and coronal positions for basilar artery stenosis. The current study investigated the distribution of basilar artery atherosclerotic plaques and their clinical relevance using HR-MR imaging and DSA. Our findings can help neurointerventionalists with better patient selection and, thus, lower the procedural risk.

## MATERIALS AND METHODS

### Subjects

This study was based on the Clinical Registration Trial of Intracranial Stenting for Patients with Symptomatic Intracranial Artery Stenosis (CRITICAS) data base (ClinicalTrials.gov identifier: NCT01994161).<sup>14</sup> The protocol complies with ethics principles of the Declaration of Helsinki and good clinical practice and has been approved by the the review board and ethic committee of Xuanwu Hospital, Capital Medical University ([2013] 004). Written informed consent was obtained from all the patients. The results of this study have been reported in accordance with the Strengthening The Reporting Of Cohort Studies in Surgery (STROCSS) criteria.<sup>15</sup>

The study included patients with basilar artery stenosis who were enrolled between December 2013 and December 2015 in several high-volume tertiary centers in China. The inclusion criteria were as follows: 1) degree of stenosis of >70% as confirmed by DSA; 2) patients with basilar artery atherosclerotic stenosis who experienced ischemic symptoms, such as dizziness, vertigo, headache, double vision, slurred speech, and numbness or

weakness; 3) treatment using endovascular therapy; 4) HR-MR imaging performed before the intervention; and 5) MR imaging performed before and within 72 hours after the intervention. The exclusion criteria were as follows: 1) stroke caused by occlusion of the basilar artery, 2) concurrent endovascular treatment of another intracranial or extracranial vessel, 3) basilar artery stenosis accompanied by moderate-to-severe vertebral artery stenosis, and 4) nonatherosclerotic causes (eg, Moyamoya disease, vasculitis, or dissection).

### Imaging Protocols and Evaluation

Before the intervention, all eligible patients were examined using a 3T MR imaging scanner (Magnetom Spectra; Siemens) equipped with a standard 8-channel head coil. The scans were obtained using multiple sequences, including fast spin-echo T1-weighted imaging, TOF-MR angiography, and T1-weighted enhanced imaging. The parameters of the sequences are described in the Online Supplemental Data. HR-MR imaging was acquired in the sagittal plane covering the basilar artery vessel. Reconstruction of the axial, coronal, and sagittal views was required to analyze all the images. DSA examinations were also performed for all the eligible patients.

An image core lab (<http://imagecorelabcn.com/>) was used to review all the images. The clinical data of patients were undisclosed and not included in the statistical analyses. Before the formal assessment, 5% of data from the analyzed cohort was used to train raters. Whenever the agreement was excellent (reliability, >0.75) between 2 raters, the imaging data were formally evaluated. The maximal lumen narrowing (MLN) or reference site, lumen diameter, vessel area (VA), and lumen area (LA) at the MLN or reference site were manually evaluated. Reference sites were defined according to Warfarin versus Aspirin for Symptomatic Intracranial Disease (WASID) trial as normal segments proximal to the stenosis or distal vessels if the proximal segment was diseased.<sup>16</sup>

On the basis of HR-MR imaging and DSA, we observed the following vessel parameters:

- Wall area (WA): difference between VA and LA (VA - LA).
- Plaque burden:  $[(WA_{MLN} - WA_{reference}) / VA_{MLN}] \times 100\%$ .
- Remodeling index: VA MLN/VA reference.

Stenosis degree is (1-Luminal Diameter at MLN/Luminal Diameter at the Reference Site)  $\times$  100% from DSA.

Using 2 perpendicular lines, we divided the cross-sectional plaque into 4 quadrants at the MLN: ventral, dorsal, left, and right.<sup>17</sup> The left and right sites were classified as lateral sites. If the plaque was large and its thickest aspect spanned more than 2 quadrants, it was considered distributed between >2 quadrants (Fig 1A). In the coronal position, DSA was used to divide the basilar artery into 2 segments on the basis of the branches of the anterior-inferior cerebellar artery.<sup>18</sup> Lesions crossing the anterior-inferior cerebellar artery were categorized as junctional segment lesions (Fig 1B).

### Interventional Procedure and Assessment of Outcome

All patients were treated by a team of neurosurgeons and neuro-radiologists with extensive experience in endovascular treatment. Experienced operators determined the therapeutic strategy according to the lesion characteristics. Aspirin, 100 mg daily, was



**Table 1: Clinical and lesion characteristics**

Variables	All Patients (n = 140)	Ischemic Events (n = 16)	Nonischemic Events (n = 124)	P Value
Sex, male	106 (75.7%)	12 (75.0%)	87 (70.2%)	.914
Age (mean) (yr)	61.9 (SD, 7.7)	62.5 (SD, 6.6)	61.8 (SD, 7.9)	.728
BMI (mean) (kg/m <sup>2</sup> )	26.2 (SD, 3.0)	25.8 (SD, 2.2)	26.3 (SD, 3.1)	.522
Qualifying event				.419
TIA	23 (16.4%)	1 (6.3%)	22 (17.7%)	
Stroke	117 (83.6%)	15 (93.7%)	102 (82.3%)	
Hypertension	117 (83.6%)	14 (87.5%)	103 (83.1%)	.927
Diabetes mellitus	58 (41.4%)	7 (43.8%)	51 (41.1%)	.841
Hyperlipidemia	36 (25.7%)	4 (25.0%)	32 (25.8%)	1.000
CAD	14 (10.0%)	2 (12.5%)	12 (9.7%)	1.000
Smoking history	58 (41.4%)	6 (37.5%)	52 (41.9%)	.735
Drinking history	38 (27.1%)	3 (18.8%)	35 (28.2%)	.615
Preoperative mRS				.218
<2	125 (89.3%)	16 (100%)	109 (87.9%)	
≥2	15 (10.7%)	0	15 (12.1%)	
Stenosis degree (mean) (%)	77.7 (SD, 9.3)	76.2 (SD, 14.2)	77.9 (SD, 9.2)	.826
Plaque length (mean) (mm)	5.9 (SD, 3.8)	4.9 (SD, 3.2)	5.9 (SD, 3.9)	.212
Plaque burden (mean) (%)	5.5 (SD, 23.6)	19.3 (SD, 18.3)	3.7 (SD, 23.6)	.047
Remodeling index (mean)	0.8 (SD, 0.4)	0.9 (SD, 0.4)	0.8 (SD, 0.4)	.430
Treatment type				.323
PA	26 (18.6%)	5 (31.3%)	21 (16.9%)	
BMS	30 (21.4%)	2 (12.5%)	28 (22.6%)	
SES	84 (60.0%)	9 (56.2%)	75 (60.5%)	

**Note:**—BMI indicates body mass index; CAD, coronary artery disease; PA, primary angioplasty; BMS, balloon-mounted stent; SES, self-expansion stent.

combined with clopidogrel, 75 mg daily for 5 days before, or a loading dose of aspirin and clopidogrel, 300 mg each, was used 1 day before endovascular treatment. Standard protocols for the procedure were followed as described previously.<sup>14</sup> Three-month dual-antiplatelet therapy, comprising aspirin, 100 mg daily, and clopidogrel, 75 mg daily, was initiated following the intervention.

An experienced team of neurosurgeons and neuroradiologists investigated the postoperative ischemic events, including TIA and ischemic stroke. Ischemic stroke was defined as a neurologic deficit lasting >24 hours. TIA was defined as a neurologic deficit lasting <24 hours.<sup>19</sup> Depending on whether postoperative outcome events occurred after endovascular treatment, patients were classified into an either ischemic or nonischemic events group.

### Statistical Analysis

Data were analyzed using the SAS software (Version 9.4; SAS Institute). Quantitative variables are presented as means. Qualitative variables are presented as numbers and percentages. Descriptive analyses were performed for participants in the postoperative ischemic and nonischemic events group. The  $\chi^2$  test or Fisher exact test was used to compare the categorical variables, as appropriate. The Student *t* test or Wilcoxon test was used to compare the quantitative variables. Univariate and multivariate regression analyses were performed to investigate the factors influencing the postoperative ischemic events. Variables with  $P < .1$ , along with sex, age, and treatment type, were included in the multivariate regression analysis.  $P < .05$  was considered as statistically significant.

## RESULTS

In total, 281 consecutive patients with severe symptomatic basilar artery stenosis underwent endovascular treatment. Among them, 140 patients having complete HR-MR imaging and DSA data were finally included in the analysis (Online Supplemental Data).

The average age of these patients was 61.9 (SD, 7.7) years. Twenty-six (18.5%) patients underwent primary angioplasty, and 114 (81.5%) underwent stent placement, which included 30 balloon-mounted stents and 84 self-expansion stents. Furthermore, 16 patients with postoperative ischemic events, including 3 TIAs, 4 perforating infarctions, 7 artery-to-artery embolisms, and 2 mixed mechanisms were regarded as the ischemic events group, and 124 patients without postoperative ischemic events, as the nonischemic events group (Online Supplemental Data). Table 1 summarizes the clinical and lesion characteristics, with the exception of plaque burden (mean, 19.3% [SD, 18.3%] versus 3.7% [SD, 23.6%];  $P = .047$ ) between the ischemic events group and the nonischemic events group.

A total of 140 basilar artery plaques were reviewed from the axial and coronal positions. In the axial view at the MLN site, 12.9% of plaques were distributed ventral to the basilar artery wall, and 22.1% in the lateral, 34.3% in the dorsal, and 30.7% in  $\geq 2$  quadrants. The plaques distributed in the lateral wall were more common in the ischemic events group than in the nonischemic events group (43.8% versus 19.3%,  $P = .049$ ). In the coronal view, plaque distribution was most common at the segment distal to the anterior-inferior cerebellar artery (60.7%), followed by the segment proximal to the anterior-inferior cerebellar artery (35.0%), and least in the junctional segment (4.3%). Plaques distributed at the junctional segment in the ischemic events group were more frequent compared with the nonischemic events group (18.8% versus 2.4%,  $P = .020$ ). The additional details of plaque distribution are presented in Table 2. The risk of ischemic events was the highest in patients with plaques located at the lateral wall (22.5%) and junctional segment (50.0%) of the basilar artery (Online Supplemental Data). Additionally, the high risk of ischemic events in patients with plaques located at the junctional segment of the basilar artery was associated with a large remodeling index compared with that in the nonischemic events group

**Table 2: Plaque distribution of the basilar artery**

Plaque Distribution	All Patients (n = 140)	Ischemic Events (n = 16)	Nonischemic Events (n = 124)	P Value
Axial position				
Ventral	18 (12.9%)	2 (12.5%)	16 (12.9%)	1.000
Lateral	31 (22.1%)	7 (43.8%)	24 (19.3%)	.049
Dorsal	48 (34.3%)	3 (18.7%)	45 (36.3%)	.262
≥2 quadrants	43 (30.7%)	4 (25.0%)	39 (31.5%)	.776
Coronal position				
Proximal segment	49 (35.0%)	6 (37.5%)	43 (34.7%)	1.000
Distal segment	85 (60.7%)	7 (43.8%)	78 (62.9%)	.176
Junctional segment	6 (4.3%)	3 (18.8%)	3 (2.4%)	.020

**Table 3: Relationship between plaque distribution and ischemic events by multivariate analysis**

	OR (95% CI)	P Value
Age	1.00 (0.92–1.08)	.997
Treatment type	0.99 (0.50–1.99)	.994
Plaque burden	1.03 (1.01–1.06)	.042
Plaque distribution		
Lateral	4.00 (1.21–13.23)	.023
Junctional segment	8.75 (1.16–66.22)	.036

(mean, 1.38 [SD, 0.20] versus 0.82 [SD, 0.29]; 95% CI, 0.05–1.13;  $P = .049$ ) (Online Supplemental Data).

The multivariate logistic regression analysis showed that plaques distributed at the lateral wall (OR = 4.00; 95% CI, 1.21–13.23;  $P = .023$ ) and junctional segments (OR = 8.75; 95% CI, 1.16–66.22;  $P = .036$ ) as well as plaque burden (OR = 1.03; 95% CI, 1.01–1.06;  $P = .042$ ) were associated with a higher risk of postoperative ischemic events (Table 3, Fig 2).

## DISCUSSION

In this study, symptomatic patients with severe basilar artery stenosis were enrolled to investigate the correlation of atherosclerotic plaque distribution with postoperative complications. The risk of postoperative ischemic events in patients with severe symptomatic basilar artery stenosis was 11.4% (16/140). Although plaque distribution of the basilar artery was most commonly observed at the dorsal wall of the basilar artery in the axial (34.3%) and distal segments in the coronal view (60.7%), the risk of postoperative complications was highest when the plaques were situated in the lateral wall and junctional segment of the basilar artery. In addition to the large plaque burden, plaques located at the lateral wall and junctional segment of the basilar artery were independent risk factors for postoperative ischemic events.

The high risk of postoperative complications is a substantial limitation for endovascular treatment of intracranial atherosclerotic stenosis, especially in the posterior circulation.<sup>4,20</sup> The basilar artery is the main artery for the posterior circulation, which has the highest risk of postoperative complications for endovascular treatment among the intracranial arteries.<sup>3</sup> The posterior circulation appears to be more capable of plaque burden because it has a lower blood flow and less sympathetic innervation compared with the anterior circulation.<sup>21–24</sup> Additionally, the number of perforating arteries in the basilar artery is significantly higher than that of the other intracranial arteries.<sup>25</sup> These reasons

explain the high risk associated with endovascular treatment. Previous studies have suggested that SAMMPRIS, strict patient selection, technical development, and incremental experience of the operators reduces the risk of postoperative complications for endovascular treatment.<sup>26</sup> Our study showed a relatively lower risk compared with SAMMPRIS (21.6%) and is comparable with several studies (11.2%–14.2%).<sup>27,28</sup> However, the prevention of postoperative complications is necessary to maxi-

mize the benefits of endovascular treatment.

It is highly likely that postoperative complications can be reduced by assessing the plaque distribution and features.<sup>18</sup> Plaque distribution has been abundantly indicated to be a significant indicator of postoperative complications, thus revealing that postoperative complications of intracranial atherosclerotic plaques located in the posterior circulation were higher than those in the anterior circulation (12.1% versus 6.6,  $P < .01$ ).<sup>29–31</sup> However, the association of local distribution of basilar artery atherosclerotic plaques with postoperative complications is unclear. Several researchers have hypothesized that plaques near the perforating orifices might be a determinant of postoperative complications through narrative analysis in plaque microanatomy studies.<sup>6,18,32,33</sup>

In this study, plaques present in the lateral wall were associated with a higher risk of postoperative complications.<sup>34</sup> Penetrating arteries from the lateral and dorsal sides of the basilar artery have been observed in previous studies.<sup>10</sup> According to the anatomic studies, 65.3% of penetrating arteries originate from the lateral side of the basilar artery, whereas 34.7% originate from the dorsal side.<sup>35</sup> Additionally, the anastomosis rate of penetrating arteries emerging from the basilar artery is high (range, 41.6%–66.6%).<sup>9</sup> From an axial perspective, the anastomosis rate of penetrations emerging from the dorsal side was higher than that on the lateral side.<sup>36</sup> Moreover, 99% of the anastomoses of penetrating arteries from the dorsal side of basilar artery are located on the ventral surface of the pontocerebrum surface, 57.5% of the anastomoses occur between the penetrating arteries of the pontocerebrum, and 21.3%, between penetrations originating from the basilar artery and anterior-inferior cerebellar artery.<sup>36</sup> As a result, plaques involving the lateral side of the basilar artery may be a risk factor for endovascular treatment for patients with severe basilar artery stenosis.

In addition, a large plaque burden is associated with postoperative complications, which may be due to a large plaque burden being more vulnerable during the expansion process of the balloon or stent.<sup>37</sup> Furthermore, a large plaque burden has a high risk of initial and recurrent ischemic symptoms in patients with intracranial stenosis.<sup>38–40</sup> Thus, an evaluation of both plaque burden and distribution characteristics may be helpful in excluding high-risk patients from endovascular treatment of basilar artery stenosis.

This study has some limitations. First, although the study cohort had a larger sample size compared with other HR-MR imaging studies, the incidence of postoperative complications was low, comprising only 16 cases.<sup>17, 41</sup> Therefore, the impact of plaque location on different stroke mechanisms (eg, artery-to-artery and perforating

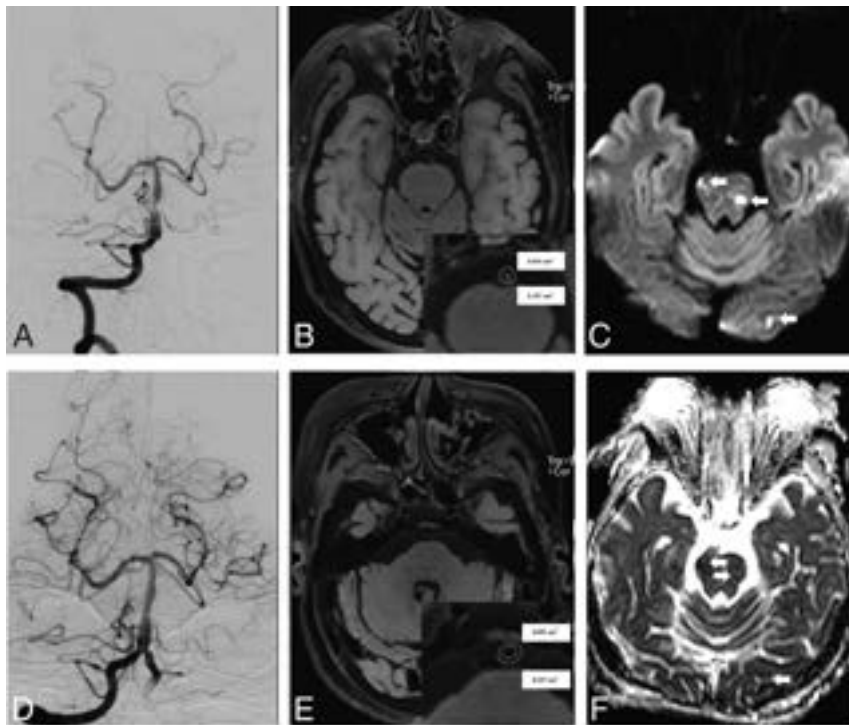


**FIG 2.** An adult patient presented with recurrent stroke for 1 month. A, Preoperative DSA revealed 79.3% stenosis at the distal segment of the basilar artery. The *middle column* shows cross-sectional T1-weighted basilar artery images at the MLN (B) and reference (REF) (E) sites. The VA and LA at the MLN (B, VA = 0.157 cm<sup>2</sup>, LA = 0.014 cm<sup>2</sup>) and REF (E, VA = 0.237 cm<sup>2</sup>, LA = 0.075 cm<sup>2</sup>) sites were manually traced for measuring after zooming in  $\times 400$ . The plaque burden was calculated as 16.6% using  $[(WA_{MLN} - WA_{REF}) / VA_{MLN}] \times 100\%$ . D, A 2.5  $\times$  8 mm Apollo balloon-mounted stent (MicroPort NeuroTech) was positioned at the stenotic segment. DWI (C) and ADC imaging (F) confirmed a new mixed type of infarction (white arrows) after the intervention.

stroke) in symptomatic basilar artery stenosis is currently unavailable and warrants further analysis. Second, plaque characteristics from the axial position based on HR-MR imaging were assessed at the site of the MLN and not in other planes of plaque. The site of MLN was considered as the evaluation level because stress is most pronounced during endovascular therapy and may be associated with postoperative complications. Third, plaque burden was not analyzed separately at various plaque distributions from the axial and coronal positions to determine the potential mechanism of plaque distribution, which was constrained by the small number of cases of postoperative complications. This issue warrants further analysis with a larger sample size.

## CONCLUSIONS

The current study showed that a large burden of plaques located at the lateral wall and junctional segment of the basilar artery may serve as predictive factors for postoperative complications during endovascular treatment. This finding may be helpful in selecting appropriate patients for endovascular treatment among symptomatic patients with basilar artery stenosis.

## ACKNOWLEDGMENTS

We would like to thank Editage ([www.editage.com](http://www.editage.com)) for English language editing.

Disclosure forms provided by the authors are available with the full text and PDF of this article at [www.ajnr.org](http://www.ajnr.org).

## REFERENCES

1. Prognosis of patients with symptomatic vertebral or basilar artery stenosis: the Warfarin-Aspirin Symptomatic Intracranial Disease (WASID) Study Group. *Stroke* 1998;29:1389–92 CrossRef Medline
2. Chow MM, Masaryk TJ, Woo HH, et al. Stent-assisted angioplasty of intracranial vertebrobasilar atherosclerosis: midterm analysis of clinical and radiologic predictors of neurological morbidity and mortality. *AJNR Am J Neuroradiol* 2005;26:869–74 Medline
3. Fiorella D, Derdeyn CP, Lynn MJ, et al. SAMMPRIS Trial Investigators. Detailed analysis of periprocedural strokes in patients undergoing intracranial stenting in Stenting and Aggressive Medical Management for Preventing Recurrent Stroke in Intracranial Stenosis (SAMMPRIS). *Stroke* 2012;43:2682–88 CrossRef Medline
4. Almallouhi E, Al Kasab S, Yamada L, et al. Relationship between vascular risk factors and location of intracranial atherosclerosis in the SAMMPRIS Trial. *J Stroke Cerebrovasc Dis* 2020;29:104713 CrossRef Medline
5. Ryu CW, Kwak HS, Jahng GH, et al. High-resolution MRI of intracranial atherosclerotic disease. *Neurointervention* 2014;9:9–20 CrossRef Medline
6. Deng S, Zheng J, Wu Y, et al. Geometrical characteristics associated with atherosclerotic disease in the basilar artery: a magnetic resonance vessel wall imaging study. *Quant Imaging Med Surg* 2021;11:2711–20 CrossRef Medline
7. Jia B, Liebeskind DS, Ma N, et al. Factors associated with perforator stroke after selective basilar artery angioplasty or stenting. *J Neurointerv Surg* 2017;9:738–42 CrossRef Medline
8. Xu WH, Li ML, Gao S, et al. Plaque distribution of stenotic middle cerebral artery and its clinical relevance. *Stroke* 2011;42:2957–59 CrossRef Medline
9. Marinković SV, Gibo H. The surgical anatomy of the perforating branches of the basilar artery. *Neurosurgery* 1993;33:80–87 CrossRef Medline
10. Saeki N, Rhoton AL Jr. Microsurgical anatomy of the upper basilar artery and the posterior circle of Willis. *J Neurosurg* 1977;46:563–78 CrossRef Medline
11. Abou-Chebl A, Steinmetz H. Critique of “Stenting versus aggressive medical therapy for intracranial arterial stenosis” by Chimowitz et al in the *New England Journal of Medicine*. *Stroke* 2012;43:616–20 CrossRef Medline
12. Wang M, Wu F, Yang Y, et al. Quantitative assessment of symptomatic intracranial atherosclerosis and lenticulostriate arteries in recent stroke patients using whole-brain high-resolution cardiovascular magnetic resonance imaging. *J Cardiovasc Magn Reson* 2018;20:35 CrossRef Medline
13. Mandell DM, Mossa-Basha M, Qiao Y, et al; Vessel Wall Imaging Study Group of the American Society of Neuroradiology. Intracranial vessel wall MRI: principles and expert consensus recommendations of the American Society of Neuroradiology. *AJNR Am J Neuroradiol* 2017;38:218–29 CrossRef Medline

14. Wang Y, Wang T, Dmytriw AA, et al. **Safety of endovascular therapy for symptomatic intracranial artery stenosis: a national prospective registry.** *Stroke Vasc Neurol* 2022;7:166–71 CrossRef Medline
15. Agha R, Abdall-Razak A, Crossley E, et al; Group S. STROCCS 2019 Guideline. **Strengthening the reporting of cohort studies in surgery.** *Int J Surg* 2019;72:156–65 CrossRef Medline
16. Samuels OB, Joseph GJ, Lynn MJ, et al. **A standardized method for measuring intracranial arterial stenosis.** *AJNR Am J Neuroradiol* 2000;21:643–46 Medline
17. Yu J, Li ML, Xu YY, et al. **Plaque distribution of low-grade basilar artery atherosclerosis and its clinical relevance.** *BMC Neurol* 2017;17:8 CrossRef Medline
18. Chen Z, Liu AF, Chen H, et al. **Evaluation of basilar artery atherosclerotic plaque distribution by 3D MR vessel wall imaging.** *J Magn Reson Imaging* 2016;44:1592–99 CrossRef Medline
19. Sacco RL, Kasner SE, Broderick JP, et al; Council on Nutrition, Physical Activity and Metabolism. **An updated definition of stroke for the 21st century: a statement for healthcare professionals from the American Heart Association/American Stroke Association.** *Stroke* 2013;44:2064–89 CrossRef Medline
20. Derdeyn CP, Chimowitz MI, Lynn MJ, et al; Stenting and Aggressive Medical Management for Preventing Recurrent Stroke in Intracranial Stenosis Trial Investigators. **Aggressive medical treatment with or without stenting in high-risk patients with intracranial artery stenosis (SAMMPRIS): the final results of a randomised trial.** *Lancet* 2014;383:333–41 CrossRef Medline
21. Buijs PC, Krabbe-Hartkamp MJ, Bakker C, et al. **Effect of age on cerebral blood flow: measurement with ungated two-dimensional phase-contrast MR angiography in 250 adults.** *Radiology* 1998;209:667–74 CrossRef Medline
22. Beausang-Linder M, Bill A. **Cerebral circulation in acute arterial hypertension: protective effects of sympathetic nervous activity.** *Acta Physiol Scand* 1981;111:193–99 Medline
23. Roth W, Morgello S, Goldman J, et al. **Histopathological differences between the anterior and posterior brain arteries as a function of aging.** *Stroke* 2017;48:638–44 CrossRef Medline
24. Ma N, Jiang WJ, Lou X, et al. **Arterial remodeling of advanced basilar atherosclerosis: a 3-Tesla MRI study.** *Neurology* 2010;75:253–58 CrossRef Medline
25. Kim BJ, Lee KM, Kim HY, et al. **Basilar artery plaque and pontine infarction location and vascular geometry.** *J Stroke* 2018;20:92–98 CrossRef Medline
26. Luo J, Wang T, Gao P, et al. **Endovascular treatment of intracranial atherosclerotic stenosis: current debates and future prospects.** *Front Neurol* 2018;9:666 CrossRef Medline
27. Bai WX, Gao BL, Li TX, et al. **Wingspan stenting can effectively prevent long-term strokes for patients with severe symptomatic atherosclerotic basilar stenosis.** *Interv Neuroradiol* 2016;22:318–24 CrossRef Medline
28. Luo J, Li L, Wang T, et al. **Risk factors of new cerebral infarctions after endovascular treatment for basilar artery stenosis based on high-resolution magnetic resonance imaging.** *Front Neurol* 2020;11:620031 CrossRef Medline
29. Nordmeyer H, Chapot R, Aycil A, et al. **Angioplasty and stenting of intracranial arterial stenosis in perforator-bearing segments: a comparison between the anterior and the posterior circulation.** *Front Neurol* 2018;9:533 CrossRef Medline
30. Gröschel K, Schnaudigel S, Pilgram SM, et al. **A systematic review on outcome after stenting for intracranial atherosclerosis.** *Stroke* 2009;40:e340–47 CrossRef Medline
31. Nordmeyer H, Chapot R, Aycil A, et al. **Angioplasty and stenting of intracranial arterial stenosis in perforator-bearing segments: a comparison between the anterior and the posterior circulation.** *Front Neurol* 2018;9:533 CrossRef Medline
32. Guo R, Zhang X, Zhu X, et al. **Morphologic characteristics of severe basilar artery atherosclerotic stenosis on 3D high-resolution MRI.** *BMC Neurol* 2018;18:206 CrossRef Medline
33. Lim SH, Choi H, Kim HT, et al. **Basilar plaque on high-resolution MRI predicts progressive motor deficits after pontine infarction.** *Atherosclerosis* 2015;240:278–83 CrossRef Medline
34. Huang B, Yang WQ, Liu XT, et al. **Basilar artery atherosclerotic plaques distribution in symptomatic patients: a 3.0T high-resolution MRI study.** *Eur J Radiol* 2013;82:e199–203 CrossRef Medline
35. Torche M, Mahmood A, Araujo R, et al. **Microsurgical anatomy of the lower basilar artery.** *Neurol Res* 1992;14:259–62 CrossRef Medline
36. Nishijima Y. **Anatomical analysis of the basilar artery and its branches with special reference to the arterial anastomosis, and its course and distribution on the pontine ventral surface** [in Japanese]. *Nihon Ika Daigaku Zasshi* 1994;61:529–47 CrossRef Medline
37. Sun B, Wang L, Li X, et al. **Intracranial atherosclerotic plaque characteristics and burden associated with recurrent acute stroke: a 3D quantitative vessel wall MRI study.** *Front Aging Neurosci* 2021;13:706544 CrossRef Medline
38. Li F, Chen QX, Chen ZB, et al. **Magnetic resonance imaging of plaque burden in vascular walls of the middle cerebral artery correlates with cerebral infarction.** *Curr Neurovasc Res* 2016;13:263–70 CrossRef Medline
39. Cao Y, Sun Y, Zhou B, et al. **Atherosclerotic plaque burden of middle cerebral artery and extracranial carotid artery characterized by MRI in patients with acute ischemic stroke in China: association and clinical relevance.** *Neurol Res* 2017;39:344–50 CrossRef Medline
40. Ran Y, Wang Y, Zhu M, et al. **Higher plaque burden of middle cerebral artery is associated with recurrent ischemic stroke: a quantitative magnetic resonance imaging study.** *Stroke* 2020;51:659–62 CrossRef Medline
41. Kim BJ, Kim HY, Jho W, et al. **Asymptomatic basilar artery plaque distribution and vascular geometry.** *J Atheroscler Thromb* 2019;26:1007–14 CrossRef Medline



# DWI-Based Radiomics Predicts the Functional Outcome of Endovascular Treatment in Acute Basilar Artery Occlusion

X. Zhang, J. Miao, J. Yang, C. Liu, J. Huang, J. Song, D. Xie, C. Yue, W. Kong, J. Hu, W. Luo, S. Liu, F. Li, and W. Zi



## ABSTRACT

**BACKGROUND AND PURPOSE:** Endovascular treatment is a reference treatment for acute basilar artery occlusion (ABAO). However, no established and specific methods are available for the preoperative screening of patients with ABAO suitable for endovascular treatment. This study explores the potential value of DWI-based radiomics in predicting the functional outcomes of endovascular treatment in ABAO.

**MATERIALS AND METHODS:** Patients with ABAO treated with endovascular treatment from the BASILAR registry (91 patients in the training cohort) and the hospitals in the Northwest of China (31 patients for the external testing cohort) were included in this study. The Mann-Whitney *U* test, random forests algorithm, and least absolute shrinkage and selection operator were used to reduce the feature dimension. A machine learning model was developed on the basis of the training cohort to predict the prognosis of endovascular treatment. The performance of the model was evaluated on the independent external testing cohort.

**RESULTS:** A subset of radiomics features ( $n = 6$ ) was used to predict the functional outcomes in patients with ABAO. The areas under the receiver operating characteristic curve of the radiomics model were 0.870 and 0.781 in the training cohort and testing cohort, respectively. The accuracy of the radiomics model was 77.4%, with a sensitivity of 78.9%, specificity of 75%, positive predictive value of 83.3%, and negative predictive value of 69.2% in the testing cohort.

**CONCLUSIONS:** DWI-based radiomics can predict the prognosis of endovascular treatment in patients with ABAO, hence allowing a potentially better selection of patients who are most likely to benefit from this treatment.

**ABBREVIATIONS:** ABAO = acute basilar artery occlusion; AUC = area under the receiver operating characteristic curve; CAPS = critical area perfusion score; EVT = endovascular treatment; LASSO = least absolute shrinkage and selection operator; ML = machine learning; pc = posterior circulation; pcASCO = posterior circulation ASPECTS-Collaterals score; RF = radiomics feature

Acute basilar artery occlusion (ABAO) is a rare but very aggressive subtype of ischemic stroke with high rates of mortality and disability, accounting for approximately 1% of all ischemic strokes and

5%–10% of large-vessel occlusion strokes.<sup>1–3</sup> Recently, 2 prospective multicenter randomized clinical trials (the Basilar Artery Occlusion Chinese Endovascular trial [BAOCHE]<sup>4</sup> and the Endovascular Treatment for Acute Basilar-Artery Occlusion trial [ATTENTION<sup>5</sup>]) and our previous the EVT for Acute Basilar Artery Occlusion Study (BASILAR) registry study<sup>6</sup> indicated that endovascular treatment (EVT) for patients with ABAO resulted in better functional outcomes than the best medical treatment. However, current evaluation methods for preoperative images of ABAO are limited compared with anterior circulation ischemic stroke.

Previous studies have identified several indicators and scoring systems that predict the prognosis of patients with ABAO, such as ASPECTS, the combined collateral status and ASPECTS scores (PCASCO), and infarct volume. However, their performance in predicting outcomes is not satisfactory. This issue may be explained by the posterior fossa radiologic particularities and the anatomic differences in the posterior circulation. Accurate and specific preoperative assessment and selection are key to determining EVT prognosis. Thus, there is an urgent need to develop an effective method for assessing the benefits of EVT in patients with ABAO.

Received December 27, 2022; accepted after revision March 15, 2023.

From the Department of Neurology (X.Z., J.M., J.Y., C.L., J.H., J.S., D.X., C.Y., W.K., J.H., W.L., S.L., F.L., W.Z.), Xinqiao Hospital and The Second Affiliated Hospital, Army Medical University (Third Military Medical University), Chongqing, China; Department of Neurology (X.Z.), The Affiliated Hospital of Northwest University Xi'an No.3 Hospital, Xian, China; and Department of Neurology (J.M.), Xianyang Hospital of Yan'an University, Xianyang, China.

Xiao Zhang, Jian Miao, and Jie Yang contributed equally as co-first authors.

Both Wenjie Zi and Fengli Li are co-senior authors.

This work was supported by the National Natural Science Foundation of China (No. 82071323), and the Chongqing Natural Science Foundation (cstc2020jcyj-msxmX0926).

Please address correspondence to Wenjie Zi, MD, Department of Neurology, Xinqiao Hospital and The Second Affiliated Hospital, Army Medical University (Third Military Medical University), No. 183 Xinqiao Main St, Shapingba District, Chongqing 400037, China; e-mail: ziwjenjie1981@163.com

Indicates open access to non-subscribers at [www.ajnr.org](http://www.ajnr.org)

Indicates article with online supplemental data.

<http://dx.doi.org/10.3174/ajnr.A7851>

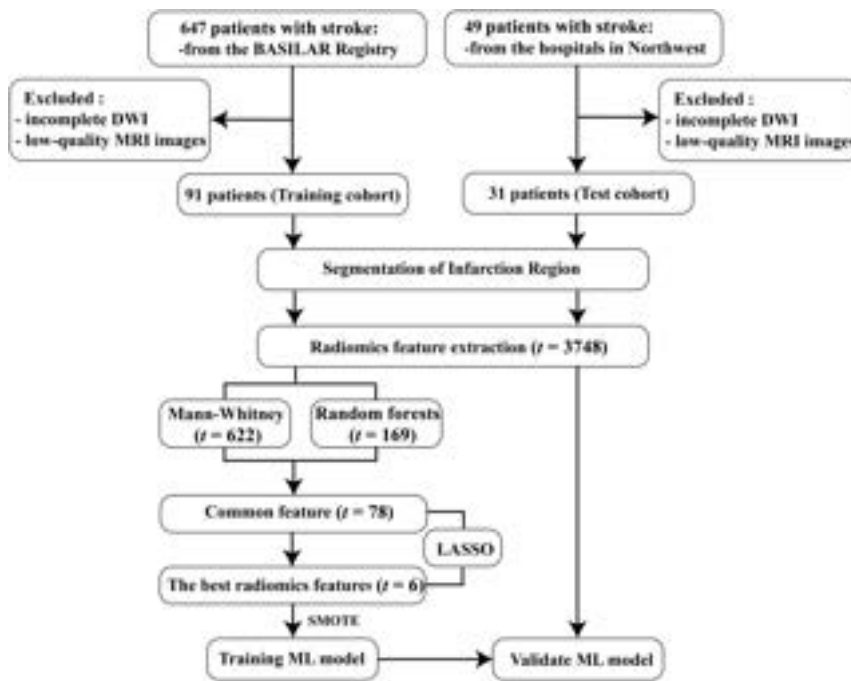


**FIG 1.** Flowchart of research patients and process. SMOTE indicates synthetic minority oversampling technique.

The concept of radiomics has recently been applied in many fields to quantitatively assess lesions by extracting large amounts of high-dimensional imaging information from conventional images, helping to reflect lesion characteristics beyond morphologic features and adding value to MR imaging guides for early stroke treatment.<sup>7</sup> In contrast to measuring features, such as the volume and signal intensity of infarct regions of brain tissue, radiomics is characterized by the ability to detect many-but-subtle changes in the area of interest that are not recognizable to the human eye.<sup>8</sup> The fusion of deeply mined imaging information with machine learning (ML) techniques can provide valuable diagnostic, prognostic, or predictive information for the treatment of clinical diseases.<sup>9</sup> Recently, a novel prognostic evaluation consisting of radiomics and ML has been proposed to predict the time to onset<sup>10</sup> and prognosis<sup>11,12</sup> of acute ischemic stroke in the anterior circulation. These high-dimensional features exhibited superior diagnostic advantages and ability, with good sensitivity and specificity in predicting prognosis and treatment strategies.<sup>13-15</sup> To our knowledge, no other study based on radiomics has predicted the functional outcome of patients with ABAO on presurgical DWI.

Therefore, our study aimed to investigate the value of DWI-based radiomics in predicting the functional outcomes of EVT for ABAO. Additionally, we tested the diagnostic performance of the model in an independent external testing cohort.

## MATERIALS AND METHODS

### Ethics Statements

Permission was obtained from the ethics committee of the Xinqiao Hospital (Second Affiliated Hospital), Army Medical

University Board (2013-yandi-08701), and written informed consent was obtained from all patients or their legal representatives.<sup>6</sup> The research of clinical features and imaging material was decided by the group. The BASILAR study was registered with the Chinese Clinical Trial Registry (<http://www.chictr.org.cn>; ChiCTR1800014759). The study has been conducted according to the principles expressed in the Declaration of Helsinki.

### Participants

The training cohort used the BASILAR registry, a multicenter, observational study including 647 consecutive patients with ABAO who underwent EVT from January 2014 to May 2019 in 47 senior stroke centers across 15 provinces in China. The test cohort enrolled patients with ABAO from Xianyang Hospital of Yan'an University and The Affiliated Hospital of Northwest University between April 2018 and June 2022 (Fig 1). We have verified that there are

no overlapping patients in the 2 cohorts. The study followed the Strengthening the Reporting of Observational Studies in Epidemiology (STROBE) reporting guideline. We included only patients who underwent both NCCT and DWI before EVT. Patients were excluded in case of low-quality images (eg, motion artifacts or metal artifacts). The training cohort was used to select relevant radiomics features (RFs) and build a predictive ML model; then, we used the testing cohort to evaluate the accuracy of the predictive model. Because patients with ABAO have a worse prognosis than those with anterior circulation stroke, patients with an mRS of  $\leq 3$  on the 90th day after EVT were defined as having a favorable functional outcome, whereas those with an mRS  $> 3$  showed an unfavorable functional outcome.

### Segmentation of the Infarct Region

Infarct regions were manually segmented with 3D Slicer (Version 4.11; <http://www.slicer.org>).<sup>16</sup> Additionally, we viewed the corresponding ADC image for guidance. The ROI (infarct region) of segmentation was based on the weight of the posterior circulation (pc)-ASPECTS. Two points each are subtracted for high signal in the right or left pons or midbrain, independently, and 1 point each is subtracted for high signal in any part of the cerebellum, thalamus, or occipital cortex.<sup>17</sup> The ROI (infarct region) in both cohorts has manually segmented the images by an experienced neuroradiologist (reader A, blinded to the eventual diagnosis) along the intraparenchymal regions of the high-signal contour on each transverse section (Fig 2A, -B). With reference to a guideline of reliability research,<sup>18</sup> we selected all patients for assessing the interoperator agreement of feature extraction. A senior neuroradiologist re-segmented the images of all patients (reader B, blinded to the eventual diagnosis). Both neuroradiologists were

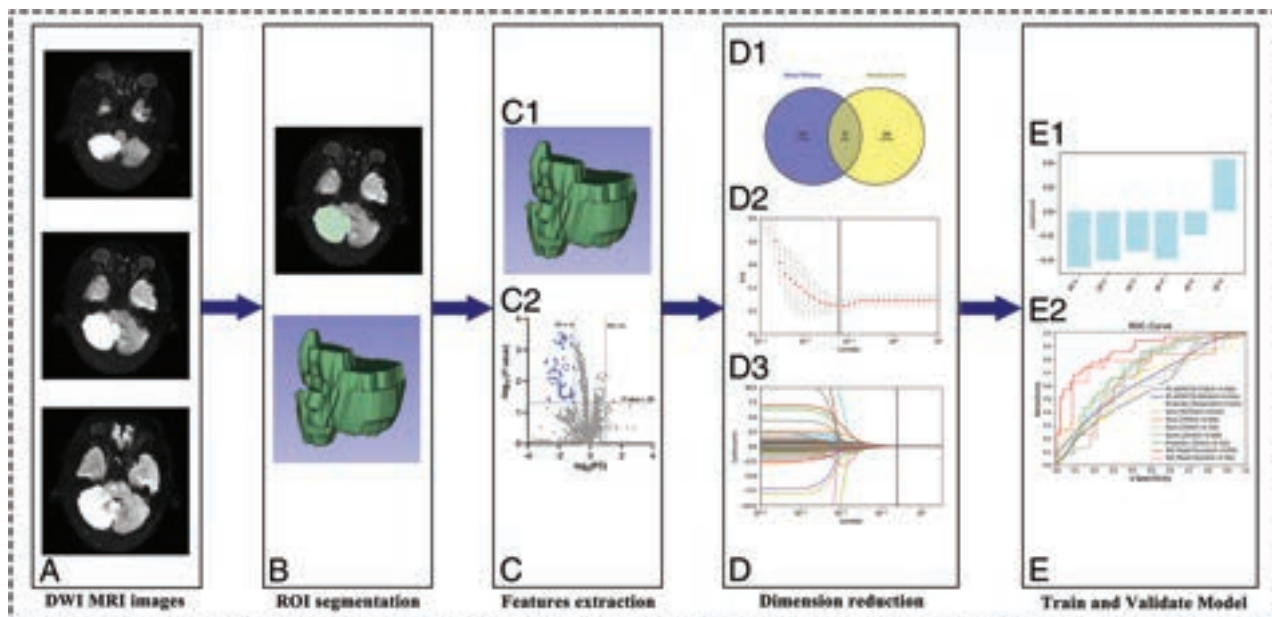


**FIG 2.** The radiomics analysis schematic. A, DWI. B, ROI. C1, ROI in 3D space. C2, Overall distribution of different RFs. The different features were analyzed between the 2 groups using a volcano plot. Red dots represent positive correlations with good outcomes, whereas blue dots represent negative correlations. FC indicates fold change. D1, Venn diagram (Mann-Whitney *U* test and random forests). D2, Radiomics feature determination using the LASSO regression with 5-fold cross-validation. The smallest mean squared error (MSE) corresponds to the number of horizontal coordinates for the best  $\lambda$  value. D3, LASSO coefficient profiles of the 78 RFs. The best RFs with nonzero coefficients at a  $\lambda$  value of 0.06 were selected. E1, The selected RFs and their coefficients. A coefficient of  $>0$  means that the characteristic is positively correlated with the outcome, whereas a coefficient of  $<0$  means that it is negatively correlated with the outcome. E2, Receiver operating characteristic curve results of the best RFs from different feature classifications compared with ASPECTS from conventional imaging.

**Table 1: Feature classification**

RF Class	No. of RFs
Set 1: First-order statistics	36
Set 2: Shape-based	28
Set 3: Textural features	
Gray-level co-occurrence matrix	48
Gray-level dependence matrix	28
Gray-level run length matrix	32
Gray-level size zone matrix	32
Neighboring gray tone difference matrix	10
Image filter	
LoG	930
Wavelet	1488
Square	186
Square root	186
Logarithm	186
Exponential	186
Gradient	186
Lbp2D	186

**Note:**—LoG indicates laplacian of gaussian; Lbp2D, local binary pattern 2D.

blinded to the final diagnosis. Interobserver repeatability of lesion segmentation was assessed by calculating the  $\kappa$  coefficients of the extracted RFs ( $\kappa = 0.97$ , 95% CI, 0.894–0.980). Good agreement was defined as RFs with  $\kappa$  coefficients of  $>0.75$ .

### RF Extraction

Substantial RFs were automatically extracted from the diffusion-weighted images with the use of pyradiomics (Version: latest; <https://pyradiomics.readthedocs.io/en/latest/>), including first-order statistics, shape-based features, and textural features (Table 1):

Set 1: First-order statistics can quantify the intensity characteristics by calculating all voxels within the infarct region.

Set 2: This set included shape features, eg, the infarct length, surface, and volume.

Set 3: Textural features quantify textural heterogeneity within the infarct region.

Further higher-order features were found by applying filters to native DWI (Table 1). A detailed definition of RFs can be obtained from the pyradiomics Web site (<https://pyradiomics.readthedocs.io/en/latest/>).

### RF Selection and Classification

Before building a prognostic prediction model for ABAO, we used the Mann-Whitney *U* test and the random forests algorithm to screen relevant features in the training cohort (Fig 1). On the basis of 5-fold cross-validation, the least absolute shrinkage and selection operator (LASSO) regression model selected the optimal features and extracted those with nonzero coefficients. RFs were tested for collinearity using the collinearity diagnosis in the linear regression analysis, and features with a variance inflation factor of  $>10$  were excluded. To eliminate the biases of class in the negative and positive distributions, radiomics data adopted the synthetic minority oversampling technique, which can potentially improve the efficacy of the model.<sup>19</sup> The predictive model was based on a support vector machine classifier, and its best parameters were evaluated by the grid search cross-validation method in the training cohort. A radiomics model was constructed on the training cohort and then validated on the testing cohort. The predictive performance of the radiomics model was assessed using accuracy, specificity, sensitivity, negative predictive value, positive predictive value, and the area under the receiver operating

characteristic curve (AUC). The dimension reduction of the radiomics features and the development of the radiomics models were implemented in scikit-learn (Version 1.0.2; <https://scikit-learn.org/stable/>).

### **Clinical Data Collection and Statistical Analysis**

All neuroimaging scores were evaluated using an imaging core laboratory. Continuous variables such as demographic data and clinical characteristics were compared using the independent samples *t* test or Mann-Whitney *U* test. Categorical variables were tested using the  $\chi^2$  test or Fisher exact test. Descriptive statistics are expressed as mean (SD) or median (interquartile range) for continuous variables and as frequency (percentage) for categorical variables. The *P* values for all tests were 2-tailed. All tests were considered statistically significant at *P* < .05. We excluded patients with missing essential data from this analysis; thus, there was no need for imputation. All of the aforementioned analyses were implemented using the Python platform with an in-house code (Version 3.9; Guido van Rossum) and SPSS statistical analysis software (Version 26.0; IBM).

## **RESULTS**

### **Patient Characteristics**

All patients completed the 90 days of follow-up and were included in the final analysis. The Online Supplemental Data present the differences in the baseline characteristics of the patients in the training cohort by favorable and unfavorable functional outcomes. Except for the baseline NIHSS score, pc-ASPECTS (DWI), infarct volume, expanded TICl, and recanalization time, no other characteristics were significantly different (*P* < .05).

Among the patients with different clinical outcomes at 90 days, those with favorable functional outcomes had a lower initial NIHSS score (15 [range, 6–23] versus 28 [range, 20–32], *P* < .001) than those with unfavorable functional outcomes before EVT. In both groups, the DWI ASPECTS was slightly lower than the NCCT ASPECTS (7 [range, 6–8] versus 6 [range, 5–7]; *P* = .019 and 8 [range, 7–9] versus 8 [range, 6–9]; *P* = .15, respectively). Compared with patients with unfavorable functional outcomes, patients with favorable functional outcomes had lower baseline mean infarct volumes in the pons and midbrain (1.2 [SD, 0.9] versus 2.3 [SD, 1.8]; *P* = .001; Online Supplemental Data). Patients with favorable functional outcomes had higher rates of substantial reperfusion (expanded TICl score) on the final angiogram than those in the unfavorable functional outcomes group (*P* = .001). The baseline characteristics of the patients in the testing cohort are shown in the Online Supplemental Data.

### **Selecting the Best RFs**

We found good agreement between the 2 readers after assessing the interobserver reliability of morphology measurements using  $\kappa$  coefficients ( $\kappa$  = 0.97; 95% CI, 0.894–0.980). According to the pc-ASPECTS regions, many RFs were automatically extracted from the infarct regions using pyradiomics. A total of 3748 RFs were extracted from the DWI, including 14 shape-based features, 18 first-order statistical parameters, 24 gray-level co-occurrence matrix indexes, 14 gray-level dependence matrix features, 16 gray-level run length matrix parameters, 16 gray-level size zone

matrixes, and 5 neighboring gray tone difference matrix features. Further higher-order features were extracted after applying the filters to the DWI (Table 1).

The volcano plot demonstrates the distribution of different RFs between the 2 groups (Fig 2C2), according to the criteria of  $|\log_2(\text{fold change})| \geq 1$  and *P* < .05. The results showed that features marked in red represent up-regulation, features marked in blue represent down-regulation, and features marked in gray represent no significant difference between the 2 groups. The 3748 features were preliminarily screened using 2 algorithms: the *t* test and random forests (Fig 2D1). Most of the 78 features preliminarily screened by these 2 algorithms were all related to the brainstem infarct region (Online Supplemental Data). The LASSO regression model (Fig 2D2, -D3) was further used to reduce the dimensionality of the RFs, resulting in 6 DWI features to build the radiomics models. The following characteristic was positively associated with a favorable functional outcome: wavelet-HLL\_glcM\_MCC. The remaining 5 characteristics were negatively associated with favorable functional outcomes: 1) brainstem-log-sigma-1-0-mm-3D\_glcM\_ClusterProminence; 2) brainstem-log-sigma-2-0-mm-3D\_glcM\_ClusterTendency; 3) brainstem-wavelet-LHH\_glszm\_ZoneVariance; 4) brainstem-wavelet-HHL\_firstorder\_Median; and 5) brainstem-lbp-2D\_firstorder\_TotalEnergy (Fig 2E1).

### **Predictive Role of Traditional Imaging Indicators and RFs in Prognosis**

The traditional imaging and radiomics indicators related to prognosis are shown in Fig 3. Among traditional imaging indicators, DWI ASPECTS (AUC = 0.644; 95% CI, 0.528–0.760) had a slightly higher predictive value than CT ASPECTS (AUC = 0.588; 95% CI, 0.469–0.708) for favorable functional outcome.<sup>20</sup> The AUC is 0.701 (95% CI, 0.609–0.80) for the infarct volume in the pons and midbrain.

The predictive accuracy of RFs was higher than that of conventional imaging metrics, such as wavelet-HLL\_glcM\_MCC (AUC = 0.633; 95% CI, 0.525–0.731); brainstem-lbp-2D\_firstorder\_TotalEnergy (AUC = 0.722; 95% CI, 0.619–0.811); brainstem-log-sigma-1-0-mm-3D\_glcM\_ClusterProminence (AUC = 0.694; 95% CI, 0.588–0.786); brainstem-log-sigma-2-0-mm-3D\_glcM\_ClusterTendency (AUC = 0.710; 95% CI, 0.605–0.800); brainstem-wavelet-HHL\_firstorder\_Median (AUC = 0.632; 95% CI, 0.524–0.731); and brainstem-wavelet-LHH\_glszm\_ZoneVariance (AUC = 0.688; 95% CI, 0.582–0.781). After the covariance test was performed for the radiomics indicators, all tolerances were >0.1, and all variance inflation factors were <10; thus, it was thought that there was no covariance among the variables (Online Supplemental Data). Figure 4 shows 2 examples of segmentations from patients with ABAO with favorable (case 2) and unfavorable (case 1) outcomes.

### **External Validation of the Prognostic Prediction Models**

The radiomics model based on the 7 selected RFs accurately predicted different prognoses after EVT in the independent testing cohort. It had an overall accuracy of 77.4%, a sensitivity of 78.9%, a specificity of 75%, a positive predictive value of 83.3%, and a negative predictive value of 69.2%. In the training cohort,



the AUC of the radiomics model was 0.870 (95% CI, 0.784–0.932). In the testing cohort, the AUC of the radiomics model was 0.781 (95% CI, 0.596–0.908). Detailed information is provided in Table 2.

## DISCUSSION

To our best knowledge, this is the first multicenter MR imaging study to investigate the value of DWI-based radiomics in predicting

the functional outcome of EVT in ABAO.<sup>21</sup> We aimed to predict a favorable prognosis for patients with ABAO based on the RFs obtained in the infarct region on preoperative DWI. One of the 6 selected RFs was positively associated with a favorable prognosis: the maximal correlation coefficient. Five of the 6 selected RFs were negatively associated with a favorable prognosis: cluster prominence, cluster tendency, zone variance, median, and total energy. Median and total energy are first-order features describing the distribution of voxel intensities within the infarct region (image gray-scale values). Cluster prominence, cluster tendency, and maximal correlation coefficient belong to the gray-level co-occurrence matrix feature, which is used to describe the spatial relationship between the gray-scale values of neighboring voxels in the infarct region. Zone variance is classified as a gray size area matrix feature that describes the spatial distribution of neighboring voxels with similar gray-scale values in the infarct region. A more detailed description of the radiomics features is shown on the Web site <https://pyradiomics.readthedocs.io/en/latest/>. The formula and method of calculating the RFs are shown in the Online Supplemental Data.

Whether EVT will likely lead to a favorable prognosis for patients with ABAO is, in our view, an important piece of information that can help doctors make applicable decisions about the transport, triage, and treatment of patients, particularly when the risks of performing EVT are considered. The aims of prognostic prediction for patients before EVT are to exclude those for whom intervention may be futile and to evaluate which patients may benefit. Patients in whom the possibility of a favorable prognosis with EVT is very high and who may have a lower risk of bleeding may benefit from direct transport to EVT. Patients in whom the possibility of a favorable prognosis with EVT is very low and who may have difficult or risky endovascular access could be given conservative drug treatment and observed for improvement. These considerations can also be

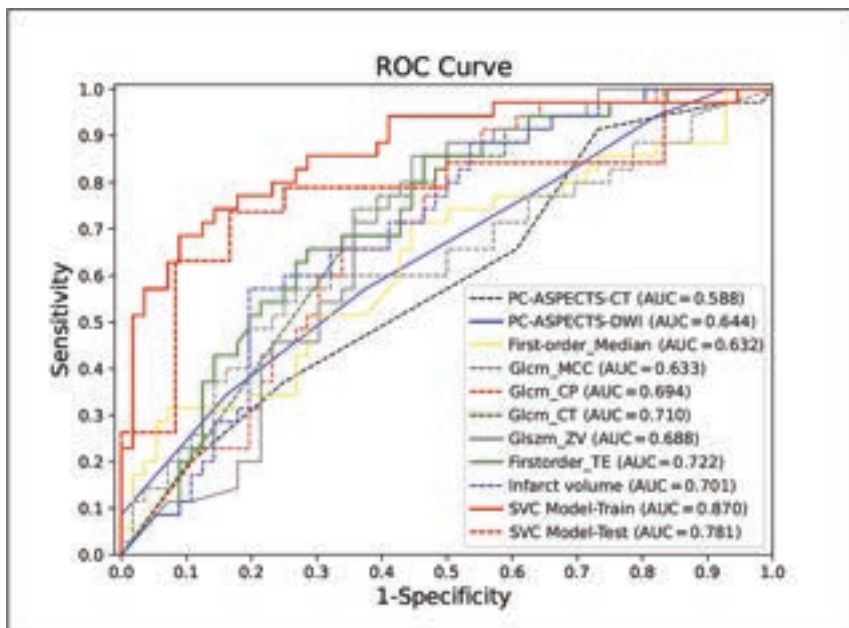


**FIG 3.** ROC curve results of the best radiomics features from different feature classifications compared with ASPECTS from conventional imaging. PC indicates posterior circulation; CP, cluster prominence; CT, cluster tendency; ZV, zone variance; TE, total energy; ROC, receiver operating characteristic; MCC, maximal correlation coefficient; GLCM, gray level co-occurrence matrix; GLSZM, gray level size zone matrix; SVC, support vector classifier.

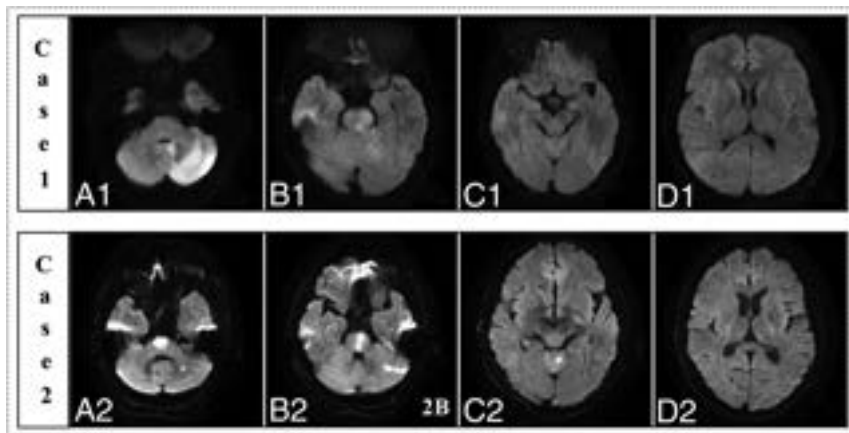


**FIG 4.** Examples of segmentations from patients with ABAO with favorable (case 2) and unfavorable outcomes (case 1).

**Table 2: Diagnostic performance of the radiomics model in the training and testing cohorts**

	AUC (95% CI)	Accuracy	Sensitivity	Specificity	PPV	NPV
Training cohort	0.870 (0.784–0.932)	80.4%	82.9%	71.4%	64.5%	86.9%
Testing cohort	0.781 (0.596–0.908)	77.4%	78.9%	75%	83.3%	69.2%

**Note:**—NPV indicates negative predictive value; PPV, positive predictive value.

weighed when deciding on transport for patients who have received IV thrombolysis or who are imaged at primary hospitals and awaiting transport to comprehensive hospitals.

Currently, there is no established and specific imaging method for preoperative screening of patients with ABAO suitable for EVT. Pc-ASPECTS is a 10-point score widely used in clinical practice to evaluate early ischemic changes. Recently, it has been reported that patients with ABAO with a CT pc-ASPECTS of  $\geq 5$  benefit from EVT.<sup>22</sup> However, it has also been discovered that patients with a higher CT pc-ASPECTS still show significant differences in functional outcomes, with only 11.2% of these patients showing functional independence at 90 days. The posterior fossa radiologic particularities and the anatomic differences in the posterior circulation tend to produce bony artifacts and partial volume effects that reduce its sensitivity and diagnostic accuracy.<sup>23-25</sup> Parenchymal changes in the ischemic region may be more easily detected on MR imaging than on CT.<sup>26</sup> However, the current research on this aspect is controversial.<sup>27,28</sup> The possible reasons are that the borderline mRS is different and the assessment method of pc-ASPECTS itself is flawed.

Further calculation of the ischemic degree in the infarct regions and not just the infarct site may be more valuable in evaluating prognosis. Recently, Broocks et al<sup>29</sup> created a new imaging score called PCASCO, which combines the collateral circulation status and pc-ASPECTS to predict the prognosis of ABAO stroke. Sun et al<sup>30</sup> and Cereda et al<sup>31</sup> used the critical area perfusion score (CAPS) to quantify serious hypoperfusion (time-to-maximum > 10) in the thalamus and/or midbrain (2 points), pons (2 points), and cerebellum (1 point/hemisphere). Regardless of recanalization, a CAPS of  $\leq 3$  is a strong independent predictor of a favorable prognosis. The CAPS reweights the infarct region and increases the prognostic value of these imaging markers by adding perfusion information. The CAPS and other scales that consider the topography of the brain are easily accessible and generalizable in the clinical setting and are the cornerstone of diagnostic imaging. RFs can quantitatively describe the spatial relationship of voxels with different gray-scale values within the infarcted region. Driven by the increasing availability of medical data and rapid advances in analytics, RF-based predictive models may provide a new pattern for medical diagnosis and treatment.

Cho et al<sup>32</sup> selected 3 typical DWI sections of the brainstem and scored ABAO according to these new slices. Li et al<sup>33</sup> found that the maximum length multiplied by thickness in the brainstem may be a predictor for assessing neurologic deterioration. Consistent with our findings, Liu et al<sup>34</sup> and Tajima et al<sup>35</sup> found significantly reduced infarct volumes from the midbrain and pons and that increased caudate volumes had favorable clinical outcomes in patients after EVT. Mourand et al<sup>36</sup> showed that pre-EVT cerebellar infarct volume was an independent predictor of 90-day functional independence. Because the spatial distribution of nuclear masses in the brain tissue is multilevel,<sup>37</sup> using a single level in each brain region may not be sufficient to indicate the severity of the infarct region. Meanwhile, we found that RFs provide quantitative information at each plane and zone and highlight essential brain regions in evaluating the extent of damage more comprehensively.

RFs<sup>38</sup> are calculated in a high-dimensional feature space that is transformed from imaging information using massive data-characterization algorithms. These subtle changes, which are difficult to detect by the human eye, are captured by radiologic features in the brain tissue environment. After we analyzed the RFs, the features of predictive value were extracted from the brainstem infarct region. The occipital cortex, thalamus, and cerebellum lesions are less involved in functional outcome than those in the brainstem.<sup>35</sup> The numerous key conduction systems that maintain consciousness and physiologic activities cross the brainstem.<sup>37</sup> This may explain the worse clinical outcome of infarcts in the brainstem region. Moreover, our algorithm provides quantitative information on RFs, which reduces the interference of human measurements and demonstrates the generalizability of the model on an independent testing set. These findings may help neurologists in the prognosis of patients with ABAO in the EVT era.

Our study has several limitations. First, the small sample size in this study demands a cautious interpretation of the findings and limits the generalization of our results. Future studies should be performed with a larger sample size to better draw clinical inferences. Second, the imaging information used in our study was collected from imaging facilities at multiple centers, resulting in various MR imaging acquisition parameters. The use of multi-vendor images for artificial intelligence algorithms is advocated.<sup>39</sup> In our view, radiomics-based models predicting the prognosis of ABAO can be further optimized with much better standardization of imaging data protocols. Third, after acquiring the patient's imaging information, this technique can be used by a neuroradiologist or neurologists. Manual processing of the images takes approximately 20 minutes. The manual segmentation of the ROI on DWI is inefficient in an emergency surgery setting, and future research will have to demonstrate whether this prediction can be performed using automated algorithms. Currently, the software and time required to make predictions are not suitable for clinical applications. Further research in artificial intelligence software may help obtain accurate predictions more quickly.

## CONCLUSIONS

The extraction of RFs from the infarct region visualized on preoperative DWI provides information on the prognosis of EVT in patients with ABAO. Characterizing the infarct region, the target of EVT, by radiomics might be a technique that is worth developing to personalize the EVT of patients with ABAO.

Disclosure forms provided by the authors are available with the full text and PDF of this article at [www.ajnr.org](http://www.ajnr.org).

## REFERENCES

1. Mattle HP, Arnold M, Lindsberg PJ, et al. **Basilar artery occlusion.** *Lancet Neurol* 2011;10:1002-14 CrossRef Medline
2. Schonewille WJ, Wijman CA, Michel P, et al. **Treatment and outcomes of acute basilar artery occlusion in the Basilar Artery International Cooperation Study (BASICS): a prospective registry study.** *Lancet Neurol* 2009;8:724-30 CrossRef Medline
3. Liu X, Xu G, Liu Y, et al. **Acute basilar artery occlusion: Endovascular Interventions versus Standard Medical Treatment (BEST) trial: design and protocol for a randomized, controlled, multicenter study.** *Int J Stroke* 2017;12:779-85 CrossRef Medline

4. Li C, Wu C, Wu L, et al; BAOCHE Investigators. **Basilar Artery Occlusion Chinese Endovascular Trial: protocol for a prospective randomized controlled study.** *Int J Stroke* 2022;17:694–97 CrossRef Medline
5. Tao C, Li R, Zhu Y, et al. **Endovascular treatment for acute basilar artery occlusion: a multicenter randomized controlled trial (ATTENTION).** *Int J Stroke* 2022;17:815–19 CrossRef Medline
6. Zi W, Qiu Z, Wu D, et al; Writing Group for the BASILAR Group. **Assessment of endovascular treatment for acute basilar artery occlusion via a nationwide prospective registry.** *JAMA Neurol* 2020;77:561–73 CrossRef Medline
7. Feng R, Badgeley M, Mocco J, et al. **Deep learning guided stroke management: a review of clinical applications.** *J Neurointerv Surg* 2018;10:358–62 CrossRef Medline
8. Gillies RJ, Kinahan PE, Hricak H. **Radiomics: images are more than pictures, they are data.** *Radiology* 2016;278:563–77 CrossRef Medline
9. Kim JY, Park JE, Jo Y, et al. **Incorporating diffusion- and perfusion-weighted MRI into a radiomics model improves diagnostic performance for pseudoprogression in glioblastoma patients.** *Neuro Oncol* 2019;21:404–14 CrossRef Medline
10. Zhang YQ, Liu AF, Man FY, et al. **MRI radiomic features-based machine learning approach to classify ischemic stroke onset time.** *J Neurol* 2022;269:350–60 CrossRef Medline
11. Quan G, Ban R, Ren JL, et al. **FLAIR and ADC image-based radiomics features as predictive biomarkers of unfavorable outcome in patients with acute ischemic stroke.** *Front Neurosci* 2021;15:730879 CrossRef Medline
12. Wang H, Sun Y, Ge Y, et al. **A clinical-radiomics nomogram for functional outcome predictions in ischemic stroke.** *Neurol Ther* 2021;10:819–32 CrossRef Medline
13. Hofmeister J, Bernava G, Rosi A, et al. **Clot-based radiomics predict a mechanical thrombectomy strategy for successful recanalization in acute ischemic stroke.** *Stroke* 2020;51:2488–94 CrossRef Medline
14. Chen X, Li Y, Zhou Y, et al. **CT-based radiomics for differentiating intracranial contrast extravasation from intraparenchymal haemorrhage after mechanical thrombectomy.** *Eur Radiol* 2022;32:4771–79 CrossRef Medline
15. Qiu W, Kuang H, Nair J, et al. **Radiomics-based intracranial thrombus features on CT and CTA predict recanalization with intravenous alteplase in patients with acute ischemic stroke.** *AJNR Am J Neuroradiol* 2019;40:39–44 CrossRef Medline
16. Fedorov A, Beichel R, Kalpathy-Cramer J, et al. **3D Slicer as an image computing platform for the Quantitative Imaging Network.** *Magn Reson Imaging* 2012;30:1323–41 CrossRef Medline
17. Puetz V, Sylaja PN, Coutts SB, et al. **Extent of hypoattenuation on CT angiography source images predicts functional outcome in patients with basilar artery occlusion.** *Stroke* 2008;39:2485–90 CrossRef Medline
18. Koo TK, Li MY. **A guideline of selecting and reporting intraclass correlation coefficients for reliability research.** *J Chiropr Med* 2016;15:155–63 CrossRef Medline
19. Liu J, Tao W, Wang Z, et al. **Radiomics-based prediction of hemorrhage expansion among patients with thrombolysis/thrombectomy related-hemorrhagic transformation using machine learning.** *Ther Adv Neurol Disord* 2021;14:17562864211060029 CrossRef Medline
20. Hui FK, Obuchowski NA, John S, et al. **ASPECTS discrepancies between CT and MR imaging: analysis and implications for triage protocols in acute ischemic stroke.** *J Neurointerv Surg* 2017;9:240–43 CrossRef Medline
21. Kniep HC, Elsayed S, Nawabi J, et al. **Imaging-based outcome prediction in posterior circulation stroke.** *J Neurol* 2022;269:3800–09 CrossRef Medline
22. Sang H, Li F, Yuan J, et al. **Values of baseline posterior circulation acute stroke prognosis early computed tomography score for treatment decision of acute basilar artery occlusion.** *Stroke* 2021;52:811–20 CrossRef Medline
23. Pallesen LP, Khomenko A, Dzialowski I, et al. **CT-angiography source images indicate less fatal outcome despite coma of patients in the Basilar Artery International Cooperation Study.** *Int J Stroke* 2017;12:145–51 CrossRef Medline
24. Ravindren J, Aguilar Perez M, Hellstern V, et al. **Predictors of outcome after endovascular thrombectomy in acute basilar artery occlusion and the 6hr time window to recanalization.** *Front Neurol* 2019;10:923 CrossRef Medline
25. Hwang DY, Silva GS, Furie KL, et al. **Comparative sensitivity of computed tomography vs. magnetic resonance imaging for detecting acute posterior fossa infarct.** *J Emerg Med* 2012;42:559–65 CrossRef Medline
26. Warach S, Chien D, Li W, et al. **Fast magnetic resonance diffusion-weighted imaging of acute human stroke.** *Neurology* 1992;42:1717–23 CrossRef Medline
27. Yang H, Ma N, Liu L, et al. **Early diffusion-weighted imaging brain stem score for acute basilar artery occlusion treated with mechanical thrombectomy.** *J Stroke Cerebrovasc Dis* 2018;27:2822–28 CrossRef Medline
28. Yoon W, Kim SK, Heo TW, et al. **Predictors of good outcome after stent-retriever thrombectomy in acute basilar artery occlusion.** *Stroke* 2015;46:2972–75 CrossRef Medline
29. Broocks G, Meyer L, Faizy TD, et al. **New imaging score for outcome prediction in basilar artery occlusion stroke.** *Eur Radiol* 2022;32:4491–99 CrossRef Medline
30. Sun D, Huo X, Raynald, et al. **Outcome prediction value of critical area perfusion score for acute basilar artery occlusion.** *Interv Neuroradiol* 2022 Sep 13. [Epub ahead of print] CrossRef Medline
31. Cereda CW, Bianco G, Mlynash M, et al. **Perfusion imaging predicts favorable outcomes after basilar artery thrombectomy.** *Ann Neurol* 2022;91:23–32 CrossRef Medline
32. Cho TH, Nighoghossian N, Tahon F, et al. **Brain stem diffusion-weighted imaging lesion score: a potential marker of outcome in acute basilar artery occlusion.** *AJNR Am J Neuroradiol* 2009;30:194–98 CrossRef Medline
33. Li H, Dai Y, Wu H, et al. **Predictors of early neurologic deterioration in acute pontine infarction.** *Stroke* 2020;51:637–40 CrossRef Medline
34. Liu C, Song JX, Guo ZB, et al. **Prognostic structural neural markers of MRI in response to mechanical thrombectomy for basilar artery occlusion.** *Front Neurol* 2021;12:593914 CrossRef Medline
35. Tajima Y, Hayasaka M, Ebihara K, et al. **Predictors of very poor outcome after mechanical thrombectomy for acute basilar artery occlusion.** *Neurol Med Chir (Tokyo)* 2020;60:507–13 CrossRef Medline
36. Mourand I, Mahmoudi M, Dargazanli C, et al. **DWI cerebellar infarct volume as predictor of outcomes after endovascular treatment of acute basilar artery occlusion.** *J Neurointerv Surg* 2021;13:995–1001 CrossRef Medline
37. Sciacca S, Lynch J, Davagnanam I, et al. **Midbrain, pons, and medulla: anatomy and syndromes.** *Radiographics* 2019;39:1110–25 CrossRef Medline
38. Sarioglu O, Sarioglu FC, Capar AE, et al. **Clot-based radiomics features predict first pass effect in acute ischemic stroke.** *Interv Neuroradiol* 2022;28:160–68 CrossRef Medline
39. Bluemke DA, Moy L, Bredella MA, et al. **Assessing radiology research on artificial intelligence: a brief guide for authors, reviewers, and readers—From the Radiology Editorial Board.** *Radiology* 2020;294:487–89 CrossRef Medline

# Deep Learning of Time–Signal Intensity Curves from Dynamic Susceptibility Contrast Imaging Enables Tissue Labeling and Prediction of Survival in Glioblastoma

J. Yun, S. Yun, J.E. Park, E.-N. Cheong, S.Y. Park, N. Kim, and H.S. Kim



## ABSTRACT

**BACKGROUND AND PURPOSE:** An autoencoder can learn representative time–signal intensity patterns to provide tissue heterogeneity measures using dynamic susceptibility contrast MR imaging. The aim of this study was to investigate whether such an autoencoder-based pattern analysis could provide interpretable tissue labeling and prognostic value in isocitrate dehydrogenase (*IDH*) wild-type glioblastoma.

**MATERIALS AND METHODS:** Preoperative dynamic susceptibility contrast MR images were obtained from 272 patients with *IDH* wild-type glioblastoma (training and validation, 183 and 89 patients, respectively). The autoencoder was applied to the dynamic susceptibility contrast MR imaging time–signal intensity curves of tumor and peritumoral areas. Representative perfusion patterns were defined by voxelwise K-means clustering using autoencoder latent features. Perfusion patterns were labeled by comparing parameters with anatomic reference tissues for baseline, signal drop, and percentage recovery. In the validation set ( $n = 89$ ), a survival model was created from representative patterns and clinical predictors using Cox proportional hazard regression analysis, and its performance was calculated using the Harrell C-index.

**RESULTS:** Eighty-nine patients were enrolled. Five representative perfusion patterns were used to characterize tissues as high angiogenic tumor, low angiogenic/cellular tumor, perinecrotic lesion, infiltrated edema, and vasogenic edema. Of these, the low angiogenic/cellular tumor (hazard ratio, 2.18;  $P = .047$ ) and infiltrated edema patterns (hazard ratio, 1.88;  $P = .009$ ) in peritumoral areas showed significant prognostic value. The combined perfusion patterns and clinical predictors (C-index, 0.72) improved prognostication when added to clinical predictors (C-index, 0.55).

**CONCLUSIONS:** The autoencoder perfusion pattern analysis enabled tissue characterization of peritumoral areas, providing heterogeneity and dynamic information that may provide useful prognostic information in *IDH* wild-type glioblastoma.

**ABBREVIATIONS:** CEL = contrast-enhancing lesion; *EGFR* = epidermal growth factor receptor; HR = hazard ratio; *IDH* = isocitrate dehydrogenase; KPS = Karnofsky Performance Score; NEL = peritumoral nonenhancing lesion; OS = overall survival; rCBV = relative CBV; RT = radiation therapy; TMZ = temozolomide

Intratumoral heterogeneity has been identified as a key factor indicating treatment resistance in glioblastoma,<sup>1,2</sup> with various

microenvironments and their genetic subtypes containing treatment-resistant cell populations that result in disease recurrence. The vascular microenvironment of glioblastoma distinguishes it from lower-grade gliomas,<sup>3</sup> and vascular co-option, angiogenesis, and vasculogenesis result in hypoxia, treatment resistance, and a poor prognosis.<sup>4</sup> Thus, defining the vascular characteristics of glioblastoma can facilitate elucidation of potential treatment resistance and provide prognostic value in patients with glioblastoma. Recurrence of glioblastoma typically develops around the primary tumor site and may be attributed to the remaining nonenhancing peritumoral area.<sup>5</sup> Intratumoral heterogeneity is also important in nonenhancing peritumoral areas that have malignant tumor cells and contain different levels of genetic mutations.<sup>6</sup> Therefore, noninvasive demonstration of intratumoral heterogeneity, including vasogenic edema and infiltrative tumor tissue, may provide value for survival prediction.<sup>7</sup>

Dynamic susceptibility contrast MR imaging (DSC MR imaging) is a noninvasive imaging technique that can provide vascular

Received June 29, 2022; accepted after revision March 21, 2023.

From the Departments of Convergence Medicine (J.Y., N.K.), Radiology and Research Institute of Radiology (J.Y., J.E.P., N.K., H.S.K.), Asan Medical Center, and Medical Science and Asan Medical Institute of Convergence Science and Technology (E.-N.C.), University of Ulsan College of Medicine, Seoul, Korea; Department of Radiology (S.Y.), Busan Paik Hospital, Inje University College of Medicine, Busan, Korea; and Department of Statistics and Data Science (S.Y.P.), Korea National Open University, Seoul, Korea.

J. Yun and S. Yun contributed equally.

This research was supported by the Ministry of Health and Welfare, South Korea (HI21C1161 and HI22C0471).

Please address correspondence to Ji Eun Park, MD, PhD, Department of Radiology and Research Institute of Radiology, University of Ulsan College of Medicine, Asan Medical Center, 88 Olympic-ro 43-gil, Songpa-Gu, Seoul 05505, Korea; e-mail: jieunp@gmail.com

Indicates open access to non-subscribers at [www.ajnr.org](http://www.ajnr.org)

Indicates article with online supplemental data.

<http://dx.doi.org/10.3174/ajnr.A7853>



information.<sup>7,8</sup> The most widely used perfusion parameter is the relative cerebral blood volume (rCBV), with high preoperative rCBV values in tumor and peritumoral areas being associated with a poor prognosis in patients with glioblastoma.<sup>9-11</sup> However, rCBV imaging provides a 1D (scalar) value that does not allow complete characterization of dynamic perfusion information.<sup>12</sup> The original complex dynamic information of DSC-MR imaging time-signal intensity curves may contain hidden information, and autoencoders may provide more robust representations of this information by reconstructing unlabeled input data from the latent representation space.<sup>13</sup> We hypothesized that essential information could be extracted using an autoencoder to analyze the entirety of the perfusion signal intensity derived from DSC MR imaging.

An autoencoder is a type of artificial neural network used to learn unlabeled data and efficiently compress data in feature space.<sup>14-16</sup> An autoencoder can be used to capture the variance of time-signal intensity curves from DSC imaging,<sup>12</sup> and various aspects of the DSC time-signal intensity curves can be captured in the feature space and clustered to provide unique perfusion patterns when translated to the data (imaging) space.

The preoperative characterization of vascular heterogeneity has been studied using vascular habitat analysis of rCBV,<sup>10</sup> but direct perfusion pattern analysis of DSC MR imaging time-signal intensity curves has not been previously performed. We hypothesized that an autoencoder-derived time-signal intensity analysis would allow high-dimensionality perfusion pattern analysis of DSC-MR imaging data and provide useful imaging signatures for prognostication. We limited our study to *isocitrate dehydrogenase (IDH)* wild-type glioma because the *IDH*-mutant type has a better prognosis, and the term “glioblastoma” was limited to *IDH* wild-type according to the World Health Organization 2021 classification of CNS tumors. The aim of this study was to investigate whether an autoencoder-based pattern analysis of tumor and peritumoral areas on perfusion MR imaging could provide interpretable tissue labeling and prognostic value in preoperative treatment-naïve *IDH* wild-type glioblastoma.

## MATERIALS AND METHODS

### Patients

The study protocol was approved by the institutional review board of Asan Medical Center, and the requirement for informed patient consent was waived because of the retrospective study design (No. 2019-0594). The inclusion process is shown in the Online Supplemental Data. The training data set was part of a cohort used in a previous autoencoder study of brain tumor differentiation.<sup>12</sup> The patient eligibility criteria were pathologically confirmed glioblastomas identified from the radiologic database of Asan Medical Center from September 2016 to March 2019; two hundred fifty-three patients were identified. Among them, 70 patients were excluded because 1) either immunohistochemistry for the *IDH1 R132H* mutation or *IDH2* sequencing was not performed when the patients were 55 years of age or younger ( $n = 23$ ), or 2) they were diagnosed with *IDH*-mutant gliomas according to the World Health Organization 2021 classification of CNS tumors ( $n = 47$ ). This process led to 183 patients being included in the training set.

For the network validation set (study population), the same eligibility criteria were used; a total of 113 patients with newly diagnosed (treatment-naïve) *IDH* wild-type glioblastoma treated at the same tertiary hospital between April 2019 and March 2021 were included. Preoperative structural imaging and DSC imaging were performed. Among them, patients were excluded if they had undergone surgical treatment before MR imaging ( $n = 15$ ) or if the quality of DSC imaging was inadequate for image analysis because of the presence of artifacts ( $n = 9$ ). Therefore, the autoencoder was pretrained on a set that included 183 patients (mean age, 58.52 years; 110 [60.1%] men), and the study population included 89 patients (mean age, 57.83 years; 43 [48.3%] men).

### Clinical Predictors and Endpoints

The recorded patient characteristics included age at diagnosis, sex, *epidermal growth factor receptor (EGFR)* mutation status, Karnofsky Performance Score (KPS,  $\geq 80$  or  $< 80$ ), maximum tumor diameter, extent of resection (biopsy, partial resection, or gross total resection), and methods of chemoradiation therapy. Standard concurrent chemoradiotherapy<sup>17</sup> consisted of fractionated focal radiation therapy (RT) at a dose of 2 Gy per fraction administered once daily 5 days per week for 6 weeks, for a total dose of 60 Gy. Concomitant chemotherapy consisted of temozolomide (TMZ) at a dose of 75 mg/m<sup>2</sup> per day, administered 7 days per week from the first to the last day of RT. After a 4-week break, the patients then received up to 6 cycles of adjuvant TMZ according to the standard 5-day schedule every 4 weeks. RT+TMZ therapy refers to hypofractionated RT for elderly patients with a hypofractionated radiation schedule (40 Gy in 15 fractions for 3 weeks), which has been suggested for elderly patients and found to be equivalent<sup>18</sup> to a standard 6-week schedule (60 Gy in 30 fractions for 6 weeks). For the study population, overall survival (OS) was calculated from the day of histopathologic diagnosis until the day of death, as obtained from the national health care data linked to our hospital. Patients who were alive at the time of analysis ( $n = 33$ , 35.1% of the validation set) were right-censored and included in the analysis. All patients were followed up every 3–6 months after surgical treatment. The minimum follow-up time to ascertain survival was 1 year.

### Imaging Acquisition and Preprocessing

All MR imaging of the enrolled patients was acquired on a 3T scanner (Achieva or Ingenia; Philips Healthcare) equipped with a 32-channel head coil. The imaging acquisition and preprocessing methods are described in the Online Supplemental Data.

### Autoencoder Analysis and Perfusion Patterns

The overall study process is shown in Fig 1. The proposed algorithm consists of 3 main stages: 1) autoencoder analysis and clustering of contrast-enhancing lesions (CELs) and nonenhancing lesions (NELs), 2) creation of perfusion patterns from autoencoder clusters, and 3) characterization of perfusion patterns using reference tissue.

**Preprocessing and Network Architecture.** For scale normalization, the DSC time-signal intensity curves were rescaled according to the mean value of the white matter of each brain. A total of 3,103,293 time-signal intensity curves were used for the network

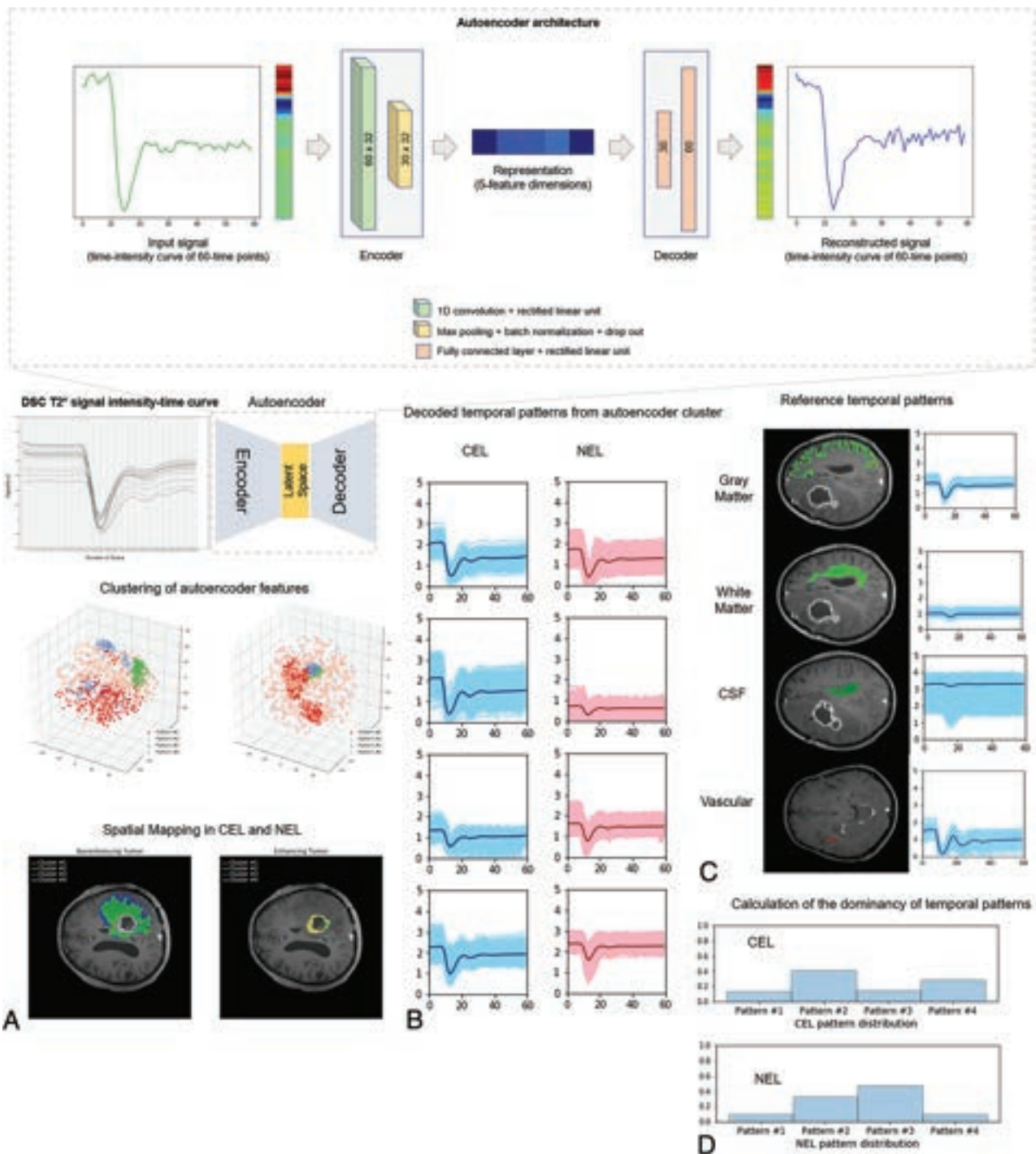


**FIG 1.** Summary of the extraction of autoencoder features from DSC imaging. The structure of the autoencoder network showed that the encoder is a 1D convolutional layer, and the decoder consists of 2 fully connected layers of the neural network. The number of latent spaces was set at 5. *A*, DSC time–signal intensity curves were learned by an autoencoder, and the latent spaces were obtained as autoencoder features. *B*, The autoencoder features were clustered into 8 patterns representing 4 perfusion patterns in CEL and 4 in NEL. *C*, Perfusion patterns of reference tissues (gray matter, white matter, CSF, and arteries) were separately obtained. *D*, The distributions of perfusion patterns within CEL and NEL were calculated. Note that the numbers indicate scale-normalized signal intensities of the time–signal intensity of DSC imaging.

training set, 587,184 (19%), 2,166,171 (70%), and 349,938 (11%) for CELs, NELs, and necrotic lesions, respectively.

Representations were extracted from high-dimensional DSC time–signal intensity data using an autoencoder that consisted of 2 parts: an encoder and a decoder. Each time–signal intensity

curve of 60 timepoints was compressed into 5 feature dimensions using the encoder and then decompressed to a representation of the original curve using the decoder. The encoder had a single 1D convolution block with 32 learnable filters using a kernel size of 2 and was followed by a rectified linear unit, max pooling, and

batch normalization. A connection dropout probability of 0.7 was introduced to prevent overfitting. Using 2 fully-connected layers, the decoder reconstructed the representations derived from the encoder into representations of the original 60-time point data. The autoencoder was trained by minimizing the mean squared error between the input and reconstructed signals. An Adam optimizer with a learning rate of  $1 \times 10^{-8}$  and a batch size of 100,000 was used.

**Optimization of Autoencoder Clusters.** K-means clustering was applied to the autoencoder-derived representations of the CELs and NELs. The optimal number of clusters is an important issue in K-means clustering, and silhouette analysis was, therefore, used to define the optimal number.<sup>19</sup> The silhouette method calculates how close each point in 1 cluster is to points in neighboring clusters and thus provides a way to assess parameters such as the number of clusters. Silhouette scores have a range of  $[-1, 1]$ ; a score of zero indicates that the sample is on or very close to the decision boundary between 2 neighboring clusters, while a score near to +1 indicates that the sample is far away from neighboring clusters; a high value indicates that the clustering configuration is appropriate. *EGFR* mutation status was set as the output value to optimize the number of clusters because it is a binary outcome.<sup>12,20</sup> We chose *EGFR* mutation status as the output value to optimize the number of clusters because it is a binary outcome and because previous literature demonstrated differences in perfusion parameters between *EGFR*-amplified and nonamplified groups, with a higher mean normalized CBV and higher 95th percentile of normalized CBF following *EGFR* amplification in *IDH* wild-type glioblastoma.<sup>21</sup>

The autoencoder representations in the latent space were clustered and mapped onto the anatomic images for visualization using the optimal number of clusters defined above. The distributions of perfusion patterns were calculated within CELs and NELs.

**Tissue Labeling of Perfusion Patterns.** To characterize the perfusion patterns, we calculated the baseline signal, depth of the signal drop, slope of the signal decrease (drop speed), and percentage recovery from each perfusion pattern (Fig 2). The perfusion patterns were first normalized using minimum-maximum scaling before we applied the following processing steps:

- 1) The baseline signal ( $S_0$ ) was calculated as the median signal intensity between timepoints 3 and 9.
- 2) The depth of the signal drop was calculated as the difference between the baseline signal and the minimum signal intensity ( $S_{\min}$ ):  $(S_0 - S_{\min})$ .
- 3) The drop speed was calculated as the depth of the signal drop divided by the time ( $t$ ) for baseline to reach minimum:  $(S_0 - S_{\min}/t)$ . Here, the time ( $t$ ) was defined as the initial time at which a signal decrease of  $>5\%$  of the maximum signal decrease was observed across serial timepoints.
- 4) The percentage recovery (adopted from previous studies<sup>22,23</sup>) representing the percentage of signal intensity recovered at the end of the first pass of contrast agent, relative to baseline, was calculated. The postcontrast signal intensity  $S_1$  was calculated as the average signal intensity between 30 and 50 timepoints.

With  $S_1$  as the postcontrast signal intensity, the percentage recovery was described as  $(S_1 - S_{\min}) / (S_0 - S_{\min})$ .

Reference tissue was defined for arteries, gray matter, white matter, and CSF using probability template matching in SPM12 (<http://www.fil.ion.ucl.ac.uk/spm/software/spm12>) to label brain regions.<sup>24</sup> For arteries, an expert neuroradiologist (J.E.P., with 8 years of neuroradiology experience) carefully selected 2-3 slices and drew an ROI within the MCA ipsilateral to the tumor. For gray matter, white matter, and CSF, the same reader refined the ROIs using brain templates obtained from SPM (SPM12). The mean ROI sizes were 30 voxels for arteries, 1845 voxels for gray matter, 7380 voxels for white matter, and 1528 voxels for CSF (Fig 1).

**ADC Calculation for Each Perfusion Pattern.** To support tissue assignment using perfusion parameters, the mean ADC value within each perfusion pattern was extracted. The details of this procedure are provided in the Online Supplemental Data.

According to signal drop, drop speed, baseline, and percentage recovery compared with reference tissues of artery, gray matter, white matter, and CSF, each perfusion pattern within the tumoral ROI was assigned one of the following: high angiogenic tumor, low angiogenic/cellular tumor, perinecrotic lesion, infiltrative edema, or vasogenic edema. The ADC value was also considered. High angiogenic tumor was assigned when a perfusion pattern showed a high signal drop and drop speed, and low angiogenic/cellular tumor, when the perfusion pattern showed a low baseline and signal drop, as well as a low ADC value. Perinecrotic lesion was assigned to a contrast-enhancing lesion when a perfusion pattern showed a high baseline with a low percentage recovery. Infiltrative edema was assigned when a perfusion pattern showed an intermediate-to-high baseline and drop speed. Vasogenic edema was assigned when a perfusion pattern showed a high baseline with a low percentage recovery.

### Statistical Analysis

Categorical variables are reported as frequencies and proportions, and continuous variables are reported as means. Differences among categorical variables and differences among continuous variables were assessed using the  $\chi^2$  test and independent  $t$  test, respectively.

The silhouette score was calculated to predict the *EGFR* mutation status. The proportions of autoencoder clusters (perfusion patterns) were tested for group differences between *EGFR*-amplified and -nonamplified groups using MANCOVA.

For the ADC values, differences between each perfusion parameter were compared using ANOVA. The ADC values showed normality on an D'Agostino-Pearson test. Correlation coefficients between characteristics of the time-signal intensity curves and ADC were calculated with a Pearson correlation.

For survival analysis, univariate analysis with Cox regression or the Kaplan-Meier method (log-rank test) was performed to analyze associations of perfusion patterns with OS. First, the number of voxels in each pattern was calculated. Second, the percentage of each pattern within the contrast-enhancing lesion (CEL) volume or peritumoral nonenhancing lesion (NEL) volume was calculated (number of voxels in pattern/number of voxels in the CEL volume). Hazard ratios (HRs) reported herein indicate the relative change in hazard that a 1-U (10,000 voxels

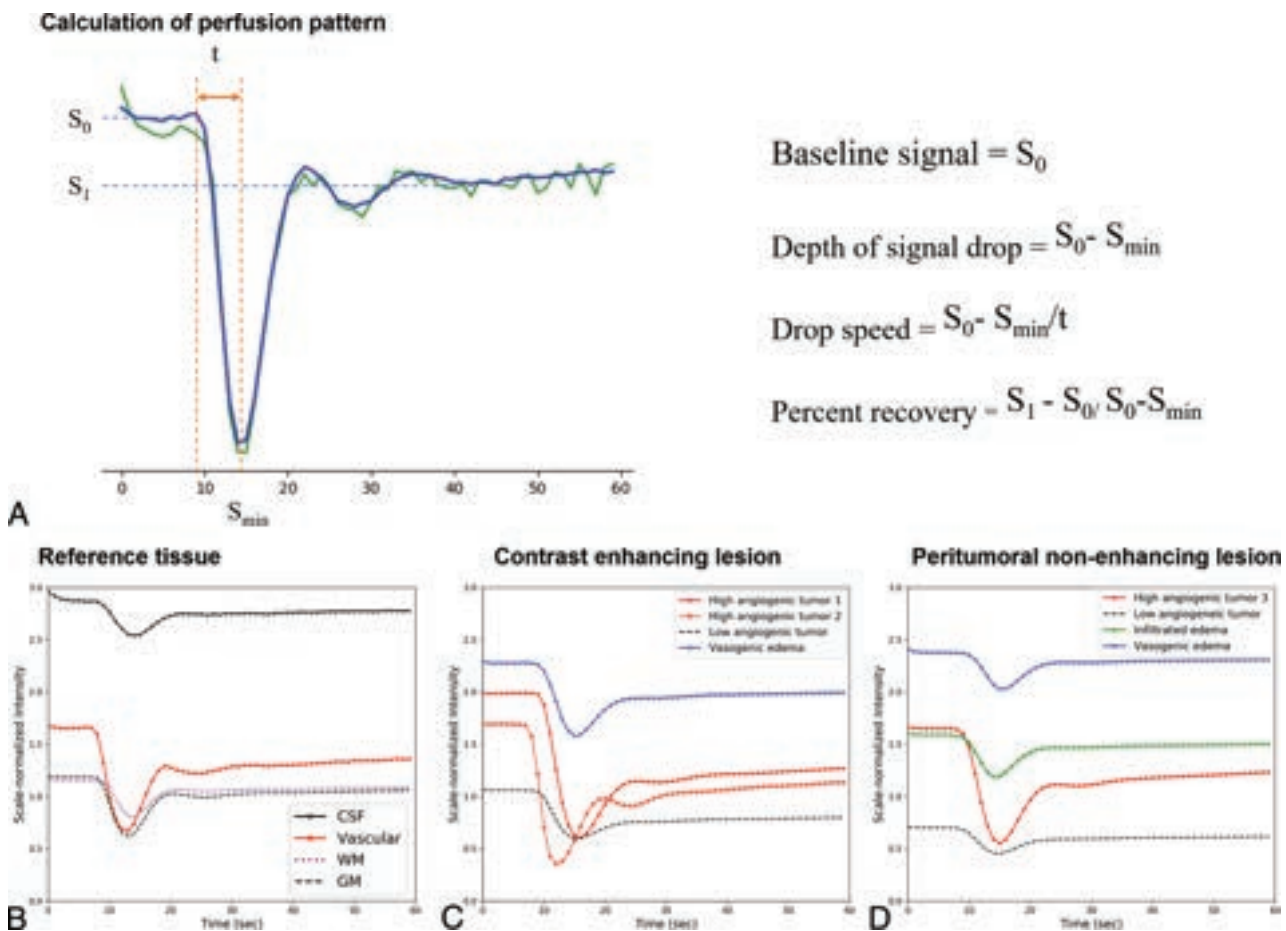


**FIG 2.** Calculation of perfusion patterns (A) and representative perfusion patterns (B–D). A, The graph shows signal intensity–time curve elements that can reflect the characteristics of each tissue, such as the baseline signal, minimum signal intensity, and postcontrast signal intensity. On the right side is a summary of the formulas used to calculate each element. Representative perfusion patterns of the reference tissues (B), CEL (C), and NEL (D). B, CSF shows the highest baseline (black line), vascular tissue shows the highest signal drop and drop speed (red line), and normal brain tissue shows the lowest baseline (dotted lines). C, In CELs, perfusion patterns with high signal drop and drop speed are labeled as high angiogenic tumor (red lines), perfusion patterns with the highest baseline and lowest percent recovery are labeled perinecrotic lesion (blue line), and perfusion patterns with the lowest baseline and lowest signal drop are labeled low angiogenic/cellular tumor (black dotted line). D, In NEL, a perfusion pattern with intermediate-to-high baseline and intermediate-to-low signal drop and drop speed is labeled infiltrated edema (green line). A perfusion pattern with the highest baseline and lowest percentage recovery is labeled vasogenic edema (blue line).

for the number of voxels and 1% for percentage) increase in each imaging parameter incurred in this study. A univariate Cox proportional hazard regression analysis was also used to test associations between OS and clinical predictors. A model combining statistically significant perfusion patterns and clinical predictors was created, and its prognostic performance was calculated using 10-fold cross-validation, which enables unbiased prediction within the sample.<sup>25</sup> Discrimination was measured with the Harrell concordance probability index (C-index).

Statistical analyses were performed using R statistical software (R version 4.0.2; <http://www.r-project.org/>). A  $P$  value < .05 was considered statistically significant.

## RESULTS

### Patient Demographics

The clinical characteristics of the included patients are summarized in Table 1. The validation set included 89 patients (mean age, 57.8 [SD, 12.8] years; 46 women), most of whom (57.3%) underwent gross total resection. The median OS was 14.4 months.

### Perfusion Patterns of Reference Tissues

The Online Supplemental Data show the values of the 4 parameters extracted from the DSC time–signal intensity curve and the ADC values of the perfusion patterns of the reference tissue. On the basis of the scale-normalized signal intensity of the DSC imaging (expressing the entire signal intensity between a minimum of 0 and maximum of 5), the perfusion patterns of arteries exhibited the highest signal drop (1.16) and drop speed (0.24). The perfusion patterns of gray matter had higher mean baseline signal (1.18 versus 1.11), signal drop (0.64 versus 0.37), and drop speed (0.14 versus 0.07) but a lower percentage recovery (0.79 versus 0.81) than those of white matter. The perfusion patterns of CSF showed higher baseline (3.04) and lower percentage recovery (0.65) than the other tissue types.

### Determination of Autoencoder Clusters and Tissue Labeling

Four clusters were chosen for the CELs and NELs of glioblastomas because this number had the highest silhouette score for the distinction of *EGFR* mutation status. The Online



**Table 1: Baseline clinical characteristics of the study population (n = 89)**

Characteristics	
Age (yr) <sup>a</sup>	57.8 (SD, 12.8)
Sex (male/female)	43:46
EGFR mutation—positive	41 (46.1)
MGMT promoter methylation—positive status	30 (33.7)
KPS at treatment initiation (%)	
>70	75 (84.3)
≤70	14 (15.7)
Surgical extent (%)	
Gross total resection	51 (57.3)
Partial resection	28 (31.5)
Biopsy	10 (11.2)
Maximal diameter (mm) <sup>a</sup>	44.9 (SD, 15.4)
Adjuvant treatment (%)	
Standard CCRT+TMZ	82 (92.1)
RT+TMZ	11 (12.4)
OS (months) <sup>a</sup>	17.7 (SD, 11.7)

**Note:**—CCRT indicates concurrent chemoradiation therapy; RT+TMZ, hypofractionated RT for elderly patients with a hypofractionated radiation schedule (40 Gy in 15 fractions for 3 weeks) with TMZ.

<sup>a</sup>Data are expressed as means.

Supplemental Data demonstrate the results of the K-means clustering and silhouette scores. A MANCOVA was used to compare the proportions of temporal patterns as a group analysis for *EGFR*; however, there was no significant difference in the distribution of clustering patterns in CELs ( $P = .446$ ) or NELs ( $P = .974$ ).

The perfusion patterns of the 4 clusters were then compared with the perfusion patterns of reference tissues (Fig 2 and Online Supplemental Data).

ANOVA showed statistically significant differences ( $P < .001$ ) among the perfusion patterns in both CELs and NELs. Among these, perinecrotic lesions in CELs had the highest ADC, while low angiogenic/cellular tumor had the lowest ADC.

There was a strong positive correlation between the ADC value and baseline signal intensity in both CELs ( $r = 0.448$ ,  $P < .001$ ) and NELs ( $r = 0.631$ ,  $P < .001$ ). There was a mild negative correlation between the ADC value and signal drop ( $r = -0.253$ ,  $P < .001$ ) and between the ADC value and drop speed ( $r = -0.256$ ,  $P < .001$ ) in NELs. These findings correspond well with the angiogenic assignment of the tumors in this study.

In CELs, 2 perfusion patterns had the highest signal drop (1.32 and 0.95) and drop speed (0.23 and 0.21) and were labeled “high angiogenic tumor.” A perfusion pattern with the highest baseline (2.08) and the lowest percent recovery (0.58) was labeled “perinecrotic lesion.” In NELs, a perfusion pattern with the highest signal drop (1.1) and drop speed (0.2) was labeled “high angiogenic tumor.” In NELs, perfusion patterns with the highest baseline (2.25) and the lowest percent recovery (0.78) were labeled “vasogenic edema,” whereas perfusion patterns with the lowest baseline (0.76 in CELs and 0.81 in NELs) and lowest signal drop (0.62 in CELs and 0.51 in NELs) as well as the lowest ADC were labeled “low angiogenic/cellular tumor.” In NELs, a perfusion pattern with intermediate-to-high baseline (1.58) and intermediate-to-low signal drop (0.51) and drop speed (0.10) was labeled “infiltrated edema.”

**Table 2: Exploratory analysis of perfusion patterns for predicting time-to-progression in patients with glioblastoma**

CEL (No. of voxels)	Time-to-Progression		
	HR <sup>a</sup>	95% CI	P Value
High angiogenic tumor (1)	0.13	0.01–4.59	.25
High angiogenic tumor (2)	4.74	0.01–231.7	.62
Low angiogenic/cellular tumor	0.99	0.10–9.91	.99
Perinecrotic lesion	22.3	0.44–111.30	.11
CEL (%)			
High angiogenic tumor (1)	0.71	0.20–2.51	.59
High angiogenic tumor (2)	0.65	0.21–2.04	.46
Low angiogenic/cellular tumor	2.14	0.33–14.03	.42
Perinecrotic lesion	2.67	0.52–13.63	.24
NEL (No. of voxels)			
High angiogenic tumor (3)	0.95	0.29–3.06	.93
Low angiogenic/cellular tumor	2.18	1.01–12.57	.047
Infiltrated edema	1.88	1.35–2.78	.009
Vasogenic edema	1.04	0.71–1.52	.84
NEL			
High angiogenic tumor (3)	0.25	0.21–5.31	.37
Low angiogenic/cellular tumor	0.41	0.08–1.99	.27
Infiltrated edema	2.14	0.40–11.35	.37
Vasogenic edema	4.20	0.52–33.98	.18

<sup>a</sup>HRs reported here indicate the relative change in hazard that a 1-U (10,000 voxels for the number of voxels and 1% for percentage) increase in each imaging parameter incurs.

### Exploratory Analysis of Survival Prediction Using Perfusion Patterns

The results of association of perfusion patterns with survival are shown in Table 2. The anonymized data for perfusion parameters including the number of voxels and percentages are in the Online Supplemental Data. In the univariable analysis, no association with OS was found for any of the perfusion patterns in CELs. However, in NELs, low angiogenic/cellular tumors (HR, 3.57;  $P = .047$ ) and infiltrated edema patterns (HR, 1.79;  $P = .009$ ) in the peritumoral area showed significant associations with OS. There was no significant association between the percentage of perfusion parameters and OS.

Among clinical predictors, a high KPS score equal to >90 (HR, 0.85; 95% CI, 0.79–0.93;  $P = .21$ ) and extent of resection (biopsy or partial resection compared with gross total resection, HR, 2.12–2.43; 95% CI, 1.01–5.04; largest  $P$  value = .04) were significantly associated with OS (Online Supplemental Data). There was no association between the ADC (either the ADC in CELs or NELs) and OS (Online Supplemental Data).

The C-index for NEL perfusion patterns alone was 0.57 (95% CI, 0.55–0.60), while that for NEL perfusion patterns combined with clinical predictors (extent of resection and age) was 0.72 (95% CI, 0.70–0.74). Representative cases are shown in Fig 3 and the Online Supplemental Data. Patients with tumors showing a high proportion of infiltrative edema and low angiogenesis died earlier than those with tumors with a low proportion of infiltrative edema and low angiogenesis but similar conditions of tumor resection.

The Kaplan-Meier survival curve for OS based on the presence of infiltrative edema is shown in Fig 4. The optimal cutoff value for distinguishing the low- and high-risk groups was >6017 voxels showing infiltrative edema. A log-rank test showed a significant difference between the low- and high-risk groups ( $P = .011$ ).

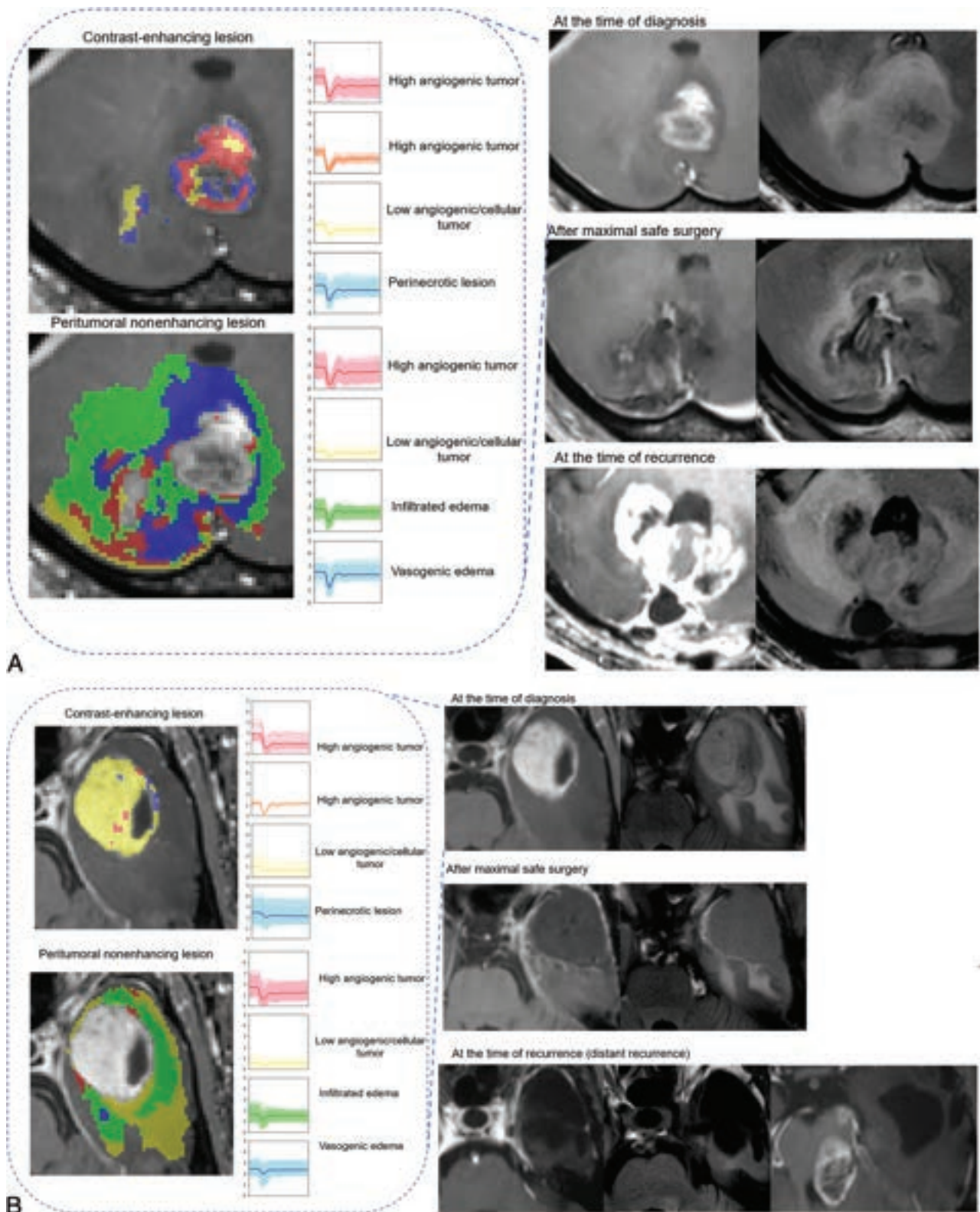


**FIG 3.** Prognostic implication of perfusion patterns of NEL in patients with glioblastoma. **A**, A 62-year-old man with *IDH* wild-type glioblastoma (*EGFR*-negative) exhibited high proportions of infiltrated edema in an NEL in the cerebellum. After maximal safe resection of the contrast-enhancing lesion and concurrent chemoradiotherapy, the patient showed progression at 120 days and died 182 days after diagnosis. Note that the recurrence occurred in both the NEL and the original CEL. **B**, A 59-year-old man with *IDH* wild-type glioblastoma (*EGFR*-negative) had high proportions of infiltrative edema within the NEL. After maximal safe resection, the infiltrative edema was mostly resected. After concurrent chemoradiotherapy, the patient showed progression at 1200 days and died 1237 days after diagnosis. Note that the recurrence occurred distant from the primary site.

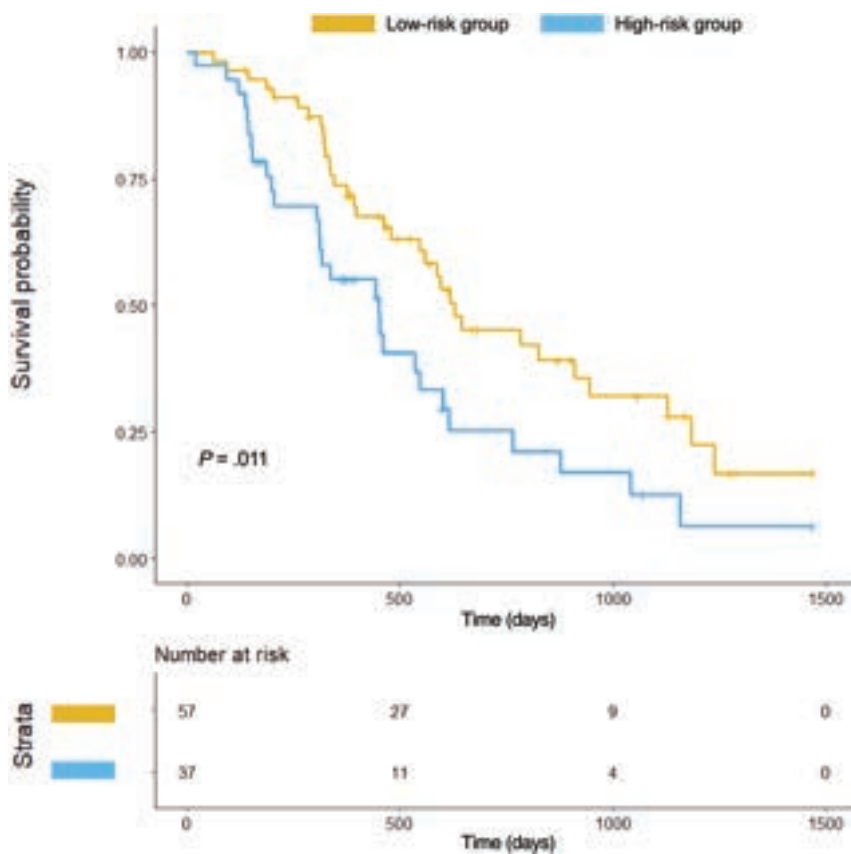


**FIG 4.** Kaplan-Meier survival curve for overall survival based on infiltrative edema. The optimal cutoff value for distinguishing the low- and high-risk groups was  $>6017$  voxels of infiltrative edema. This cutoff value separated the survival groups with a significant difference according to a log-rank test ( $P = .011$ ).

## DISCUSSION

In this study, we investigated whether an autoencoder trained to analyze perfusion patterns extracted from DSC imaging could depict perfusion heterogeneity and whether it had prognostic value in patients with *IDH* wild-type glioblastoma. Using perfusion patterns based on unsupervised learning by the autoencoder and K-means clustering, we performed tissue labeling by comparison with the perfusion patterns obtained from reference tissues of the MCA, gray matter, white matter, and CSF. Our results demonstrate that the preoperative perfusion patterns, especially those from the peritumoral nonenhancing region, contained prognostic information. A high proportion of infiltrative edema and low angiogenic/cellular tumor in the peritumoral nonenhancing region, old age, and a low extent of surgery indicated poor patient survival. Thus, along with a maximal safe resection strategy according to the current guidelines for patients with glioblastoma, the depiction of preoperative perfusion patterns and localization of infiltrative and low angiogenic/cellular tumor portions could be helpful for providing important early information on survival.

The nonenhancing regions of glioblastoma consist of areas of edema and infiltrative tumor tissue that usually remain after surgical resection, and most recurrences occur within the original treatment field.<sup>26-29</sup> Several studies have investigated perfusion MR imaging findings in the nonenhancing peritumoral area as

potential prognostic factors.<sup>5,11,30</sup> Jain et al<sup>11</sup> revealed that rCBV measurements of the nonenhancing region of glioblastoma provide unique prognostic information independent of morphologic, genomic, and clinical features. Lee et al<sup>30</sup> investigated tumor-derived texture feature ratios extracted from contrast-enhancing and nonenhancing lesions on perfusion MR imaging-based CBV maps. A recent voxelwise rCBV and CBF analysis showed that vascular habitats had prognostic value in patients with glioblastoma.<sup>10</sup> Nevertheless, rCBV analysis does not allow depiction of the complex nature of DSC time-signal intensity curves, such as drop speed and percentage recovery, and vascular habitat is derived from a unidirectional high or low pattern of vascular density. For example, rCBV does not reflect the permeability of tumor vessels, which can be determined using parameters such as the percentage recovery calculated from DSC MR imaging.<sup>31</sup>

However, recent machine learning and deep learning studies have revealed possibilities for analyzing the high-dimensional data of the time-signal intensity curves obtained from DSC images.<sup>12,20,31,32</sup> Akbari et al<sup>20</sup> character-

ized perfusion characteristics with a support vector machine classifier to create a map of heterogeneity within the peritumoral region. Bakas et al<sup>32</sup> constructed a quantitative within-patient peritumoral heterogeneity index for evaluating *EGFR* status using contrasting perfusion patterns of immediate and distant peritumoral edema. A recent study used a long short-term memory-based model to predict *IDH* genotypes on DSC MR imaging of gliomas.<sup>31</sup> These studies have revealed that DSC MR imaging contains more voxelwise information than is represented by a simple rCBV map. Our study is in accordance with the above-mentioned studies, in that we found that analysis of the entire DSC time-signal intensity curve with a deep learning technique using an autoencoder made it possible to compress voxelwise data while extracting essential information.<sup>12,13</sup>

The interpretation of high-dimensional information from unsupervised learning is challenging. The tissue interpretation performed in this study differs from that in previous work in 2 ways: First, the perfusion patterns were labeled according to similarities with reference tissues of the ipsilateral MCA, contralateral normal-appearing gray/white matter, and CSF. For the reference tissues, we applied robust tissue segmentation using established software and included a large number of voxels, differing from a previous study that included 2–3 voxels of reference tissue.<sup>20</sup> Second, the perfusion patterns used entire tumoral and peritumoral voxels, labeling them as high angiogenic tumor,



perinecrotic lesion, low angiogenic/cellular tumor, infiltrative edema, or vasogenic edema by considering their perfusion parameters, including baseline signal, signal drop, drop speed, and percentage recovery.

Previous unsupervised learning studies used a heterogeneity index,<sup>20,32</sup> but this is an oversimplified measure and limits biologic interpretation. In addition, infiltrated edema was limited to a 2-cm margin around the enhancing tumor,<sup>10</sup> whereas we were able to identify infiltrated edema from all peritumoral voxels. This finding highlights a strength of our study, in that we first applied tissue labeling using the perfusion patterns of the entire tumoral and peritumoral voxels, enhancing the interpretability of unsupervised learning including clustering and autoencoder analysis. In this study, edema was assigned using a higher baseline value than white matter in NELs. Furthermore, assignment of angiogenic tumors was possible using high signal drop and drop speed compared with gray and white matter. We believe that this method will help researchers to identify the perfusion pattern of tumor in comparison with reference tissues.

Moreover, the ADC value was adjunctly used to explain the tissue labeling, which enhances the biologic explanation of the perfusion patterns by combining both cellularity and characteristics of time–signal intensity curve analyses including baseline, signal drop, and percentage recovery. In particular, percentage recovery is known to be helpful for characterizing permeability, with high permeability leading to low percentage recovery<sup>22,23</sup> because of the high T1 effect of gadolinium-based contrast leakage into interstitial spaces.

In CELs, there were 2 each of high angiogenic tumors, low angiogenic/cellular tumors, and perinecrotic lesions. This finding was also supported by ADC analysis, which showed that perinecrotic lesions exhibited a high ADC, while low angiogenic/cellular tumor exhibited a low ADC. On histopathology, the tumorigenic “perinecrotic niche” is known to have quiescent stemlike tumor cells in glioblastoma<sup>33</sup> and is distinct from other tissue types. High angiogenic tumors exhibited the highest signal drop (1.32 and 0.95) and drop speed (0.23 and 0.21), demonstrating neoangiogenesis within the tumor because high signal drop and drop speed are correlated with a high rCBV.<sup>34</sup> It is unclear why 2 distinct high angiogenic perfusion patterns were obtained, and future studies with further molecular subgroups may reveal the meaning of this difference.

There are several limitations to this study. First, it used a retrospective design and had a small cohort size; these factors limit the generalizability and statistical power of our findings. Second, despite the use of an optimized number of clusters identified by silhouette analysis, MANCOVA showed no significant difference in the distribution of clustering patterns between CELs and NELs. In a previous study, a higher mean nCBV and higher 95th percentile of nCBF were significant predictors of *EGFR* amplification in *IDH* wild-type glioblastoma.<sup>21</sup> Therefore, we expected that the perfusion MR imaging values would change according to the *EGFR* amplification results, but our results showed no difference. MANCOVA is extremely sensitive to outliers, which may produce either type I or type II error.<sup>35</sup> It is, therefore, necessary to perform further research with more clusters or optimized clusters of perfusion patterns.

## CONCLUSIONS

Autoencoder-derived perfusion patterns could be labeled with different brain tissues on the basis of the interpretation of perfusion patterns of reference tissues. The perfusion patterns could be useful biomarkers for prognostication, especially low angiogenic/cellular tumor and infiltrative edema perfusion patterns in non-enhancing peritumoral areas. Autoencoder analysis enabled capture of infiltrative tumorlike perfusion patterns in the brain, and this study demonstrated the feasibility of voxelwise temporal information as a prognostic indicator in patients with *IDH* wild-type glioblastoma.

Disclosure forms provided by the authors are available with the full text and PDF of this article at [www.ajnr.org](http://www.ajnr.org).

## REFERENCES

1. Friedmann-Morvinski D. **Glioblastoma heterogeneity and cancer cell plasticity.** *Crit Rev Oncog* 2014;19:327–36 CrossRef Medline
2. Qazi MA, Vora P, Venugopal C, et al. **Intratumoral heterogeneity: pathways to treatment resistance and relapse in human glioblastoma.** *Ann Oncol* 2017;28:1448–56 CrossRef Medline
3. Das S, Marsden PA. **Angiogenesis in glioblastoma.** *N Engl J Med* 2013;369:1561–63 CrossRef Medline
4. Hardee ME, Zagzag D. **Mechanisms of glioma-associated neovascularization.** *Am J Pathol* 2012;181:1126–41 CrossRef Medline
5. Jo SW, Choi SH, Lee EJ, et al. **Prognostic prediction based on dynamic contrast-enhanced MRI and dynamic susceptibility contrast-enhanced MRI parameters from non-enhancing, T2-high-signal-intensity lesions in patients with glioblastoma.** *Korean J Radiol* 2021;22:1369 CrossRef Medline
6. Kelly PJ, Dumas-Duport C, Kispert DB, et al. **Imaging-based stereotaxic serial biopsies in untreated intracranial glial neoplasms.** *J Neurosurg* 1987;66:865–74 CrossRef Medline
7. Zhang J, Liu H, Tong H, et al. **Clinical applications of contrast-enhanced perfusion MRI techniques in gliomas: recent advances and current challenges.** *Contrast Media Mol Imaging* 2017;2017:7064120 CrossRef Medline
8. Kickingereder P, Wiestler B, Burth S, et al. **Relative cerebral blood volume is a potential predictive imaging biomarker of bevacizumab efficacy in recurrent glioblastoma.** *Neuro Oncol* 2015;17:1139–47 CrossRef Medline
9. Law M, Young RJ, Babb JS, et al. **Gliomas: predicting time to progression or survival with cerebral blood volume measurements at dynamic susceptibility-weighted contrast-enhanced perfusion MR imaging.** *Radiology* 2008;247:490–98 CrossRef Medline
10. Juan-Albarracín J, Fuster-García E, Pérez-Girbés A, et al. **Glioblastoma: vascular habitats detected at preoperative dynamic susceptibility-weighted contrast-enhanced perfusion MR imaging predict survival.** *Radiology* 2018;287:944–54 CrossRef Medline
11. Jain R, Poisson LM, Gutman D, et al. **Outcome prediction in patients with glioblastoma by using imaging, clinical, and genomic biomarkers: focus on the nonenhancing component of the tumor.** *Radiology* 2014;272:484–93 CrossRef Medline
12. Park JE, Kim HS, Lee J, et al. **Deep-learned time–signal intensity pattern analysis using an autoencoder captures magnetic resonance perfusion heterogeneity for brain tumor differentiation.** *Sci Rep* 2020;10:1–11 CrossRef Medline
13. Creswell A, Bharath AA. **Denoising adversarial autoencoders.** *IEEE Trans Neural Netw Learn Syst* 2019;30:968–84 CrossRef Medline
14. Bank D, Koenigstein N, Giryas R. **Autoencoders.** April 3, 2021. *arXiv* <https://arxiv.org/abs/2003.05991>. Accessed June 29, 2022
15. Hinton GE, Salakhutdinov RR. **Reducing the dimensionality of data with neural networks.** *Science* 2006;313:504–07 CrossRef Medline
16. Ranzato MA, Huang FJ, Boureau Y-L, et al. **Unsupervised learning of invariant feature hierarchies with applications to object**



- recognition.** 2007 *IEEE Conference on Computer Vision and Pattern Recognition*, Minneapolis, Minnesota. June 17, 2007:1–8
17. Stupp R, Mason WP, van den Bent MJ, et al; National Cancer Institute of Canada Clinical Trials Group. **Radiotherapy plus concomitant and adjuvant temozolomide for glioblastoma.** *N Engl J Med* 2005;352:987–96 CrossRef Medline
  18. Roa W, Brasher PM, Bauman G, et al. **Abbreviated course of radiation therapy in older patients with glioblastoma multiforme: a prospective randomized clinical trial.** *J Clin Oncol* 2004;22:1583–88 CrossRef Medline
  19. Rousseeuw PJ. **Silhouettes: a graphical aid to the interpretation and validation of cluster analysis.** *J Comput Appl Math* 1987;20:53–65 CrossRef
  20. Akbari H, Macyszyn L, Da X, et al. **Pattern analysis of dynamic susceptibility contrast-enhanced MR imaging demonstrates peritumoral tissue heterogeneity.** *Radiology* 2014;273:502–10 CrossRef Medline
  21. Park YW, Park JE, Ahn SS, et al. **Magnetic resonance imaging parameters for noninvasive prediction of epidermal growth factor receptor amplification in isocitrate dehydrogenase-wild-type lower-grade gliomas: a multicenter study.** *Neurosurgery* 2021;89:257–65 CrossRef Medline
  22. Cha S, Lupo JM, Chen MH, et al. **Differentiation of glioblastoma multiforme and single brain metastasis by peak height and percentage of signal intensity recovery derived from dynamic susceptibility-weighted contrast-enhanced perfusion MR imaging.** *AJNR Am J Neuroradiol* 2007;28:1078–84 CrossRef Medline
  23. Mangla R, Kolar B, Zhu T, et al. **Percentage signal recovery derived from MR dynamic susceptibility contrast imaging is useful to differentiate common enhancing malignant lesions of the brain.** *AJNR Am J Neuroradiol* 2011;32:1004–10 CrossRef Medline
  24. Ashburner J, Friston KJ. **Unified segmentation.** *Neuroimage* 2005;26:839–51 CrossRef Medline
  25. Ingrisch M, Schneider MJ, Norenberg D, et al. **Radiomic analysis reveals prognostic information in T1-weighted baseline magnetic resonance imaging in patients with glioblastoma.** *Invest Radiol* 2017;52:360–66 CrossRef Medline
  26. Parsa AT, Wachhorst S, Lamborn KR, et al. **Prognostic significance of intracranial dissemination of glioblastoma multiforme in adults.** *J Neurosurg* 2005;102:622–28 CrossRef Medline
  27. Stecco A, Pisani C, Quarta R, et al. **DTI and PWI analysis of perienhancing tumoral brain tissue in patients treated for glioblastoma.** *J Neurooncol* 2011;102:261–71 CrossRef Medline
  28. Aerts HJ, Velazquez ER, Leijenaar RT, et al. **Decoding tumour phenotype by noninvasive imaging using a quantitative radiomics approach.** *Nat Commun* 2014;5:4006 CrossRef Medline
  29. Kumar V, Gu Y, Basu S, et al. **Radiomics: the process and the challenges.** *Magn Reson Imaging* 2012;30:1234–48 CrossRef Medline
  30. Lee J, Jain R, Khalil K, et al. **Texture feature ratios from relative CBV maps of perfusion MRI are associated with patient survival in glioblastoma.** *AJNR Am J Neuroradiol* 2016;37:37–43 CrossRef Medline
  31. Choi KS, Choi SH, Jeong B. **Prediction of IDH genotype in gliomas with dynamic susceptibility contrast perfusion MR imaging using an explainable recurrent neural network.** *Neuro Oncol* 2019;21:1197–209 CrossRef Medline
  32. Bakas S, Akbari H, Pisapia J, et al. **In vivo detection of EGFRvIII in glioblastoma via perfusion magnetic resonance imaging signature consistent with deep peritumoral infiltration: the  $\varphi$ -index.** *Clin Cancer Res* 2017;23:4724–34 CrossRef Medline
  33. Ishii A, Kimura T, Sadahiro H, et al. **Histological characterization of the tumorigenic “peri-necrotic niche” harboring quiescent stem-like tumor cells in glioblastoma.** *PLoS One* 2016;11:e0147366 CrossRef Medline
  34. Lee MD, Baird GL, Bell LC, et al. **Utility of percentage signal recovery and baseline signal in DSC-MRI optimized for relative CBV measurement for differentiating glioblastoma, lymphoma, metastasis, and meningioma.** *AJNR Am J Neuroradiol* 2019;40:1445–50 CrossRef Medline
  35. French A, Macedo M, Poulsen J, et al. **Multivariate analysis of variance (MANOVA).** 2008

# Associating *IDH* and *TERT* Mutations in Glioma with Diffusion Anisotropy in Normal-Appearing White Matter

H. Halilibrahimoğlu, K. Polat, S. Keskin, O. Genç, O. Aslan, E. Öztürk-Işık, C. Yakıcıer, A.E. Danyeli, M.N. Pamir, K. Özduvan, A. Dinçer, and A. Özcan



## ABSTRACT

**BACKGROUND AND PURPOSE:** *IDH* and *TERT* mutations might infiltratively manifest within normal-appearing white matter with specific phenotypes such as microstructural changes undetectable by standard MR imaging contrasts but potentially associable with DTI variables. The aim of this retrospective glioma study was to statistically investigate *IDH* and *TERT* associations and classifications with DTI reported microstructure in normal-appearing white matter.

**MATERIALS AND METHODS:** Retrospective data from patients imaged between March 2012 and February 2016 were analyzed by grouping them as *IDH-TERT* subgroups and by *IDH* and *TERT* mutation status. DTI variables in the *IDH-TERT* subgroups were first identified by the Kruskal-Wallis test, followed by Dunn-Šidák multiple comparisons with Bonferroni correction. *IDH* and *TERT* mutations were compared with the Mann-Whitney *U* test. Classification by thresholding was tested using receiver operating characteristic analysis.

**RESULTS:** Of 170 patients, 70 patients (mean age, 43.73 [SD, 15.32] years; 40 men) were included. Whole-brain normal-appearing white matter fractional anisotropy (FA) and relative anisotropy (RA) ( $P = .002$ ) were significantly higher and the contralateral-ipsilateral hemispheric differences,  $\Delta$ FA and  $\Delta$ RA, ( $P < .001$ ) were significantly lower in *IDH*only patients compared with *TERT*only, with a higher whole-brain normal-appearing white matter FA and RA ( $P = .01$ ) and  $\Delta$ FA and  $\Delta$ RA ( $P = .002$ ) compared to double positive patients. Whole-brain normal-appearing white matter ADC ( $P = .02$ ), RD ( $P = .001$ ),  $\lambda_2$  ( $P = .001$ ), and  $\lambda_3$  ( $P = .001$ ) were higher in *IDH* wild-type. Whole-brain normal-appearing white matter  $\lambda_1$  (AD) ( $P = .003$ ), FA ( $P < .001$ ), and RA ( $P = .003$ ) were higher, but  $\Delta\lambda_1$  ( $P = .002$ ),  $\Delta$ FA, and  $\Delta$ RA ( $P < .001$ ) were lower in *IDH* mutant versus *IDH* wild-type.  $\Delta$ FA ( $P = .01$ ) and  $\Delta$ RA ( $P = .02$ ) were significantly higher in *TERT* mutant versus *TERT* wild-type.

**CONCLUSIONS:** Axial and nonaxial diffusivities, anisotropy indices in the normal-appearing white matter and their interhemispheric differences demonstrated microstructural differences between *IDH* and *TERT* mutations, with the potential for classification methods.

**ABBREVIATIONS:** AD = axial diffusivity; AUC = area under the curve; DAI = diffusion anisotropy indices; DN = double negative; DP = double positive; FA = fractional anisotropy; HMeD = hemispherical mean differences; LBTh = lower bound thresholding; mut = mutant; NAWM = normal-appearing white matter; NPV = negative predictive value; PPV = positive predictive value; RA = relative anisotropy; RD = radial diffusivity; ROC = receiver operating characteristic; UBTh = upper bound thresholding; WB = whole brain; wt = wild-type

**G**lioma is the most common CNS tumor with overall survival ranging from 12 to 15 months to several years, depending on tumor severity.<sup>1</sup> Recently, genotype information in clinical workflow proved to be valuable<sup>2</sup> and was integrated into the

WHO classification.<sup>3</sup> Therein, *isocitrate dehydrogenase (IDH)* mutation is associated with longer overall survival, around 57 months, and is commonly seen in low-grade (grade 2, grade 3) gliomas.<sup>2,4-6</sup> *Telomerase reverse transcriptase (TERT)* mutation presents with a more aggressive disease course, eg, with neutrophil infiltration,<sup>7</sup> leading to a lower overall survival of 11.5 months, mostly in high-grade (grade 4) tumors.<sup>2,8</sup> Remarkably, overall survival increases to 125 months when the tumor is both *IDH*- and *TERT*-mutated.<sup>6</sup>

Received October 29, 2022; accepted after revision March 21, 2023.

From the Department of Electrical and Electronics Engineering (K.P., A.Ö.), Boğaziçi University, Bebek, Istanbul, Turkey; Department of Biomedical Engineering (H.H.), McGill University, Montréal, Quebec, Canada; Biomedical Imaging Research and Development Center (H.H., K.P., S.K., O.A.), Department of Pathology (A.E.D.), Department of Neurosurgery (M.N.P., K.Ö.), Department of Radiology (A.D.), Brain Tumor Research Group (E.Ö.-I., A.E.D., M.N.P., K.Ö., A.D.), and Center for Neuroradiological Advanced Research (E.Ö.-I., M.N.P., K.Ö., A.D.), Acibadem Mehmet Ali Aydınlar University, Ataşehir, Istanbul, Turkey; Institute of Biomedical Engineering (H.H., O.G., E.Ö.-I.), Boğaziçi University Kandilli Campus, Çengelköy, Istanbul, Turkey; and YoctoSensum Biotechnology (C.Y.), Fenerbahçe, Istanbul, Turkey.

The Scientific and Technological Research Council of Türkiye (TUBITAK) funded this work [2165432].

Please address correspondence to Alpay Özcan, DSc, Electrical & Electronics Engineering Department, Boğaziçi University, Bebek, Beşiktaş, Istanbul, 34342, Turkey; e-mail: alpay.ozcan@boun.edu.tr

Indicates open access to non-subscribers at www.ajnr.org

Indicates article with online supplemental data.

<http://dx.doi.org/10.3174/ajnr.A7855>

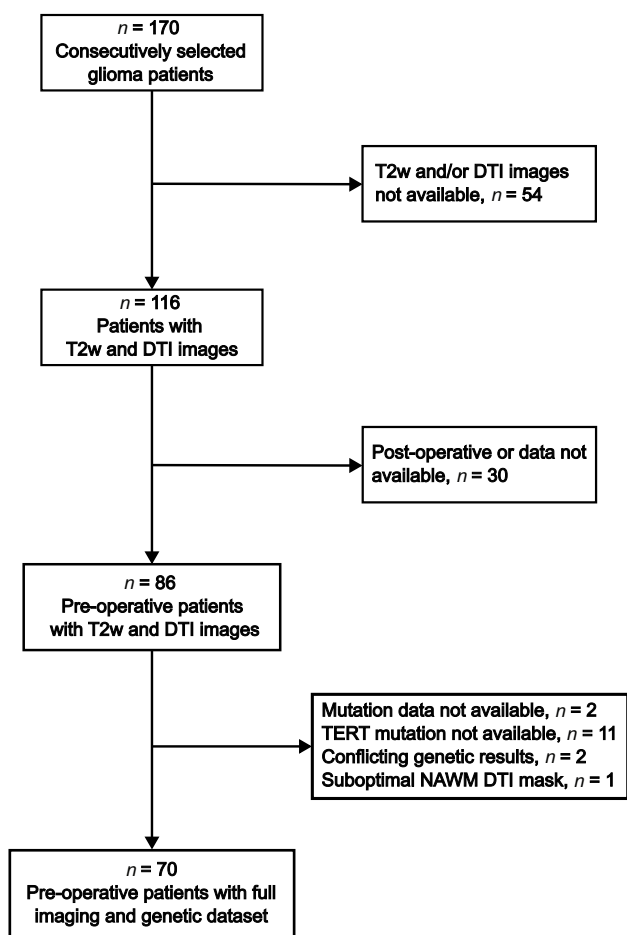


**FIG 1.** Patient-selection flowchart.

**Table 1: Cohort characteristics**

Patient Demographics (n = 70)	
Mean age (yr)	43.73 (SD, 15.32)
Sex (female/male)	30:40
Tumor characteristics	
Mutation status wt/mut (No.) (%)	
IDHmut	29/41 (41%/59%)
TERTmut	33/37 (47%/53%)
Tumor grade, mutation (No.) (%)	
1, IDHmut/TERTmut	1 (1%), 0/0
2, IDHmut/TERTmut	29 (41%), 24/16
3, IDHmut/TERTmut	22 (31%), 15/8
4, IDHmut/TERTmut	18 (26%), 2/13

When identifying genotypes, biopsy might miss relevant loci due to the notorious heterogeneity of gliomas.<sup>9</sup> Complete organ coverage by MR imaging might provide a more accurate assessment, especially by analyzing the normal-appearing white matter (NAWM) for the diffuse properties of the disease such as infiltrative tendencies to migrate through white matter fibers.<sup>10,11</sup>

The migration process involves complex interactions with extracellular matrix components and cytokines, which, in turn, lead to displacement or, for grade 4, destruction of the white matter fibers.<sup>12</sup> T1WI and T2WI might not be sufficiently sensitive to NAWM infiltration,<sup>13</sup> whereas microstructural changes such as neoplastic angiogenesis and elevated cellular density<sup>14,15</sup> are investigated with DTI and quantified by its eigenvalues and diffusion anisotropy indices (DAIs).<sup>16</sup>

In the past, decreased relative anisotropy (RA) found in the NAWM of patients with high-grade gliomas,<sup>17</sup> and increased ADC coupled with decreased *N*-acetylaspartate in the contralateral NAWM suggested microstructural damage possibly caused by infiltrating tumor cells.<sup>18</sup> Tumor grades histopathologically report microstructure;<sup>19</sup> so low-grade and, therefore, *IDH* mutated (*IDH*mut) tumors exhibit higher diffusion anisotropy and lower ADC in the NAWM compared with high-grade<sup>17,20</sup> and *IDH* wild-type (wt)<sup>21</sup> tumors. In addition, DAI changes in the distal NAWM have been reported for different glioma grades.<sup>22</sup>

Complementing tumor-site-focused past studies by investigating regions outside the tumor might potentially be relevant because it would inform on the diffuse nature of the disease. The aim of this study was to investigate microstructural changes in the NAWM by analyzing comprehensively the DTI variables within the whole brain (WB) and between “healthy” and “pathologic” hemispheres, for statistically associating them with *IDH* and *TERT* mutations.

## MATERIALS AND METHODS

### Clinical Data

In this institutional review board–approved retrospective study, the cohort was gathered without recruitment from existing data of clinical patients who had consented. Of 170 consecutive patients with gliomas treated at Acibadem Hospitals (Istanbul, Turkey) between March 2012 and February 2016, with written informed consent, 54 without T2WI and/or DTI, 30 postoperative, 2 with unavailable mutation data and 11 with unavailable *TERT* status, 2 with conflicting genetic results, and 1 with a suboptimal NAWM DTI mask were excluded (Fig 1), leaving 70 patients (mean age, 43.73 [SD, 15.32] years of age; female/male ratio: 30/40), with 1 grade 1, 29 grade 2, 22 grade 3, and 18 grade 4 gliomas and 41 patients with *IDH*mut (29 *IDH*wt); 37 patients were *TERT*mut (33 *TERT*wt).

Histopathologic analysis was performed on surgically removed tumor samples. *IDH* and *TERT* mutations were determined using either minisequencing or Sanger sequencing. Patients were stratified into 4 molecular subgroups, hereafter referred to as *IDH-TERT* subgroups (Table 1):

- 1) Double negative (DN): *IDH*wt, *TERT*wt (*n* = 9).
- 2) *IDH*only: *IDH*mut, *TERT*wt (*n* = 24).
- 3) *TERT*only: *IDH*wt, *TERT*mut (*n* = 20).
- 4) Double positive (DP): *IDH*mut, *TERT*mut (*n* = 17).

### MR Imaging Data

MR imaging was performed on a 3T Magnetom Tim Trio MR imaging scanner (Siemens) with a 32–channel head coil, 1–7 days before the operation. The scanning protocol included T2WI acquired using a 2D turbo spin-echo sequence with voxel dimensions of 0.26 × 0.26 × 0.26 mm with 20 axial slices, TE/TR = 107/3470 ms, slice thickness/spacing = 5/6.5 mm, flip angle = 120°. DTI data were acquired using a 2D diffusion EPI sequence with 1.8 × 1.8 × 1.8 mm voxels, 60 axial slices, TE/TR = 107/3470 ms, slice thickness/spacing = 1.8/2.34 mm, flip angle = 90°, and b-value = 1000 ms/mm<sup>2</sup> with 20 diffusion gradient vectors. Eigenvalue maps for the 3 eigenvalues ( $\lambda_1 \geq \lambda_2 \geq \lambda_3$ ) were computed by the console computer of the scanner.

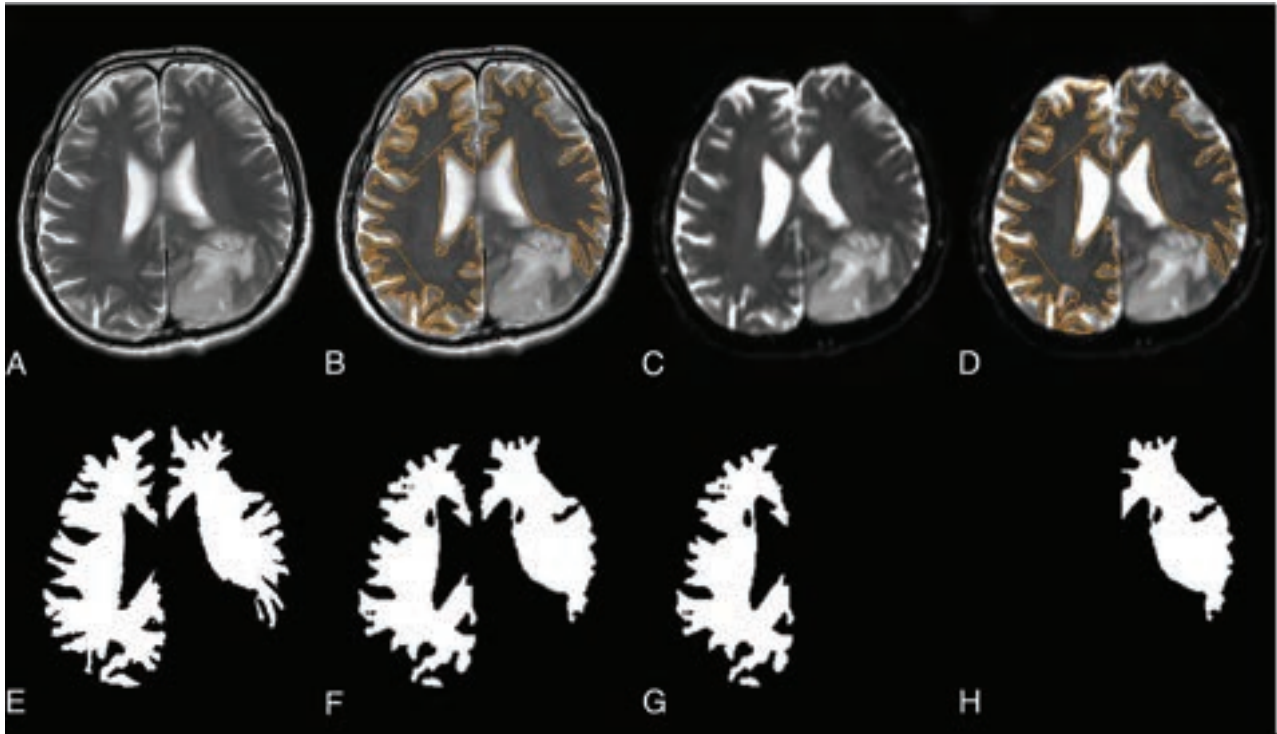


**FIG 2.** NAWM segmentations and masks. T2WI (A), semiautomatic NAWM boundary demarcations overlaid on T2WI (B), the coregistered  $B_0$  image (C), NAWM boundary demarcations on the coregistered  $B_0$  image (D), total NAWM mask on T2WI (E), on  $B_0$  image (F), and the corresponding right (G) and left (H) hemisphere masks.

All image volumes were transferred in DICOM format, then anonymized using in-house-developed scripts based on the Grassroots DICOM library<sup>23</sup> and were converted to Neuroimaging Informatics Technology Initiative (NIfTI) format using Medical Image Processing, Analysis, and Visualization software (MIPAV; <http://mipav.cit.nih.gov>).<sup>24</sup>

### NAWM Segmentation and Coregistration

NAWM regions were selected on T2WI using semiautomatic level set segmentation tools in MIPAV by 2 trainees with 2 years of experience OG and OA, inspected by an imaging scientist with 25+ years of experience AÖ, and approved by a neuroradiologist with 30+ years of experience, AD.

Images obtained without diffusion weighting ( $B_0$  images) were coregistered onto T2WI with the FSL software package (<http://www.fmrib.ox.ac.uk/fsl>)<sup>25</sup> using the mutual information cost function with the trilinear interpolation method. The transformation optimizing the  $B_0 \rightarrow$  T2WI coregistration problem was applied for coregistering eigenvalue maps onto T2WI by interpolating with the nearest neighbor method (Fig 2).

The distortion of NAWM masks caused by the difference of total slice numbers among the MR imaging modalities while coregistering was corrected with an in-house-developed Matlab (MathWorks) code (KP, 2+ years of experience), which identifies shared pixel coordinates in matching  $B_0$  images mapped to T2WI and the original  $B_0$  image. The code infers mask pixels in the “sandwich” slices from the “shell” slices.

Furthermore, an in-house-developed (KP, 2+ years of experience) Matlab code subdivided the mask images automatically into left and right hemispheres, which were used for computing

contralateral and ipsilateral DAI and eigenvalue distributions (Fig 2). Quality assurance for the image-processing routines was conducted by HH, SK and KP, each with 2+ years of experience, and inspected and approved as aforementioned.

### Variables

For each patient, DAIs (Online Supplemental Data) were computed from the eigenvalues ( $\lambda_1 \geq \lambda_2 \geq \lambda_3$ ) on WB, contralateral, and ipsilateral NAWM pixels. For each patient, each variable's mean over WB,  $Mean_{WB}$ , and the hemispheres,  $Mean_{contralat}$ ,  $Mean_{ipsilat}$  were calculated. Each patient's ipsilateral hemisphere mean was subtracted from the contralateral hemisphere mean for obtaining in-patient hemispherical mean differences (HMeD) of DAIs and eigenvalues:

$$HMeD(I) = \Delta I = Mean_{contralat}(I) - Mean_{ipsilat}(I),$$

where  $I$  denotes any of the DTI variables. All of the computations were implemented with in-house-developed Matlab code (HH, 2+ years of experience).

### Statistical Analysis

Statistical power calculations indicate that with the exception of ADC, whose results were nevertheless reported herein, all of the variables had acceptable statistical power for the number of included patients (Online Supplemental Data).

The Kruskal-Wallis test with a  $P < .05$  threshold was used for testing whether DAIs and eigenvalues could detect differences among *IDH-TERT* subgroups. Variables with statistical significance were then subjected to a Dunn-Šidák multiple comparison analysis with pair-wise subgroup comparisons for identifying differentiating variables. Subsequently,  $P$  values of multiple comparison analysis



**Table 2: Comparison of WB-NAWM means and HMeD of diffusion parameters for IDH-TERT molecular subgroups**

	ADC	$\lambda_1$ (AD)	RD	$\lambda_2$	$\lambda_3$	FA	RA
<i>IDH-TERT</i> subgroup Kruskal-Wallis test <i>P</i> values							
WB-NAWM	.10	.03 <sup>a</sup>	.01 <sup>a</sup>	.01 <sup>a</sup>	.01 <sup>a</sup>	.001 <sup>a</sup>	.001 <sup>a</sup>
HMeD	.10	.01 <sup>a</sup>	.04 <sup>a</sup>	.044 <sup>a</sup>	.02 <sup>a</sup>	<.001 <sup>a</sup>	<.001 <sup>a</sup>
<i>IDH-TERT</i> subgroup multiple comparisons <i>P</i> values							
WB-NAWM							
DN vs IDHonly	–	.59	.64	.61	.74	.52	.58
DN vs TERTonly	–	.99	.87	.88	.86	.82	.77
DN vs DP	–	.70	.82	.91	.79	.68	.69
IDHonly vs TERTonly	–	.04 <sup>a</sup>	.01 <sup>b</sup>	.007 <sup>b</sup>	.01 <sup>a</sup>	.002 <sup>b</sup>	.002 <sup>b</sup>
IDHonly vs DP	–	>.99	>.99	.99	>.99	>.99	>.99
TERTonly vs DP	–	.10	.04 <sup>a</sup>	.08	.03 <sup>a</sup>	.01 <sup>a</sup>	.01 <sup>a</sup>
HMeD							
DN vs IDHonly	–	.02 <sup>a</sup>	.61	.26	.99	.86	.79
DN vs TERTonly	–	.89	.04 <sup>a</sup>	.04 <sup>a</sup>	.06	.21	.30
DN vs DP	–	.25	.91	.75	>.99	.96	.89
IDHonly vs TERTonly	–	.07	.44	.87	.07	<.001 <sup>b</sup>	<.001 <sup>b</sup>
IDHonly vs DP	–	.87	>.99	.96	>.99	>.99	>.99
TERTonly vs DP	–	.75	.22	.41	.08	.002 <sup>b</sup>	.002 <sup>b</sup>

**Note:**—En dash indicates that multiple comparisons were not performed due to lack of statistical significance in the Kruskal-Wallis test.

<sup>a</sup>*P* < .05.

<sup>b</sup>*P* < .008.

were adjusted with the Bonferroni correction (*P* < .008). Anisotropy differences between *IDH* and *TERT* mutation status were compared using the Mann-Whitney *U* test with a threshold of *P* < .05.

Statistical analysis was performed with Matlab Statistics and Machine Learning Toolbox (<https://www.mathworks.com/products/statistics.html>) by HH under the supervision of AÖ with 6+ and 25+ years of experience, respectively.

### Classification by Thresholding

For investigating genotype classification as proof of principle, decision by thresholding was tested on each variable for separating each mutation group from the rest. Classifier performance was investigated with the receiver operating characteristic<sup>26</sup> (ROC) curve's area under the curve (AUC)<sup>26</sup> (with AUC = 1 as the best performance indicator) and positive and negative predictive values (PPV, NPV) at the optimal operating threshold identified by determining on each ROC curve the closest point to the top left corner (False Positive Rate = 0, True Positive Rate = 1), corresponding to sensitivity = 1 and specificity = 1 (Online Supplemental Data).

The steps were applied using each threshold as a lower bound (Value ≥ Threshold) and as an upper bound (Value ≤ Threshold). Therein, AUC values for these decision criteria add up to 1, leading to select the thresholding criterion (upper or lower bound) with a higher AUC for a given variable. By contrast, an AUC close to 0.5 indicates poor classification capability of the variable (Online Supplemental Data).

ROC analysis and reporting were implemented with in-house Matlab code developed by AÖ with 25+ years of experience.

## RESULTS

### IDH-TERT Subgroups

**Whole Brain.** Among *IDH-TERT* subgroups, in the WB-NAWM, there was a statistically significant difference in all DAIs and

eigenvalues (*P* < .05), with the exception of ADC (*P* = .10 for WB-NAWM ADC) (Table 2). In pair-wise *IDH-TERT* subgroup comparisons, WB-NAWM radial diffusivity (RD) was higher in TERTonly patients compared to IDHonly (*P* = .01), with higher values in TERTonly compared to DP patients (*P* = .04) (Fig 3). WB-NAWM fractional anisotropy (FA) and RA were significantly higher in IDHonly patients compared to TERTonly (*P* = .002 for both), with a higher WB-NAWM FA and RA compared to DP (*P* = .01 for both). WB-NAWM axial diffusivity (AD) had higher values in the IDHonly subgroup compared with TERTonly (*P* = .04), whereas WB-NAWM  $\lambda_2$  had significantly higher values (*P* = .007) and WB-NAWM  $\lambda_3$  showed higher values (*P* = .01) in the TERTonly gliomas compared to IDHonly. WB-NAWM  $\lambda_3$  also had higher values in TERTonly patients compared to DP (*P* = .03).

**Interhemispheric Differences.** When comparing hemispheres within *IDH-TERT* subgroups, there was a statistically significant difference in the interhemispheric mean differences of all DAIs and eigenvalues (*P* < .05), with the exception of ADC (*P* = .10 for  $\Delta$ ADC) (Table 2). With the exception of DN and DP groups,  $\Delta$ ADC distributions completely shifted to negative values, indicating that in the presence of only a single mutation, ADC values on the “healthy” (contralateral) side tend to be lower than those of the tumor (ipsilateral) side.

For all *IDH-TERT* subgroups,  $\lambda_2$ ,  $\lambda_3$ , and thus RD had larger values ipsilaterally. TERTonly had the largest shift, followed by IDHonly. HMeD medians in DN and DP were negative but closer to zero. With the exception of  $\lambda_1$  (AD) of the DN, all the diffusivities had higher values ipsilaterally for the *IDH-TERT* subgroups. This finding might potentially indicate an overall disruption of the microstructure in the tumor hemisphere.

For TERTonly and DP, the median of  $\Delta\lambda_1$  was negative but closer to zero, indicating a higher  $\lambda_1$  ipsilaterally.  $\Delta\lambda_1$  was lower in IDHonly gliomas compared to DN (*P* = .02). DN and TERTonly distributions point to higher contralateral anisotropy significantly in TERTonly and mildly in DN.  $\Delta$ RD and  $\Delta\lambda_2$  had higher values in DN patients in comparison to TERTonly (*P* = .04 for both).

Distributions of  $\Delta$ FA and  $\Delta$ RA from IDHonly and DP had median values close to zero, indicating anisotropy resemblance of the hemispheres for these mutations.  $\Delta$ FA and  $\Delta$ RA were significantly higher in TERTonly gliomas compared to IDHonly (*P* < .001 for both) and DP (*P* = .002 for both) (Fig 4 and Table 2). Lastly, distributions of DN and TERTonly point to higher contralateral anisotropy significantly in TERTonly and mildly in DN.

### IDH and TERT Mutation Status

**Whole Brain.** Among IDHwt and IDHmut gliomas, WB-NAWM ADC (*P* = .02), RD (*P* = .001),  $\lambda_2$  (*P* = .001), and  $\lambda_3$  (*P* = .001)

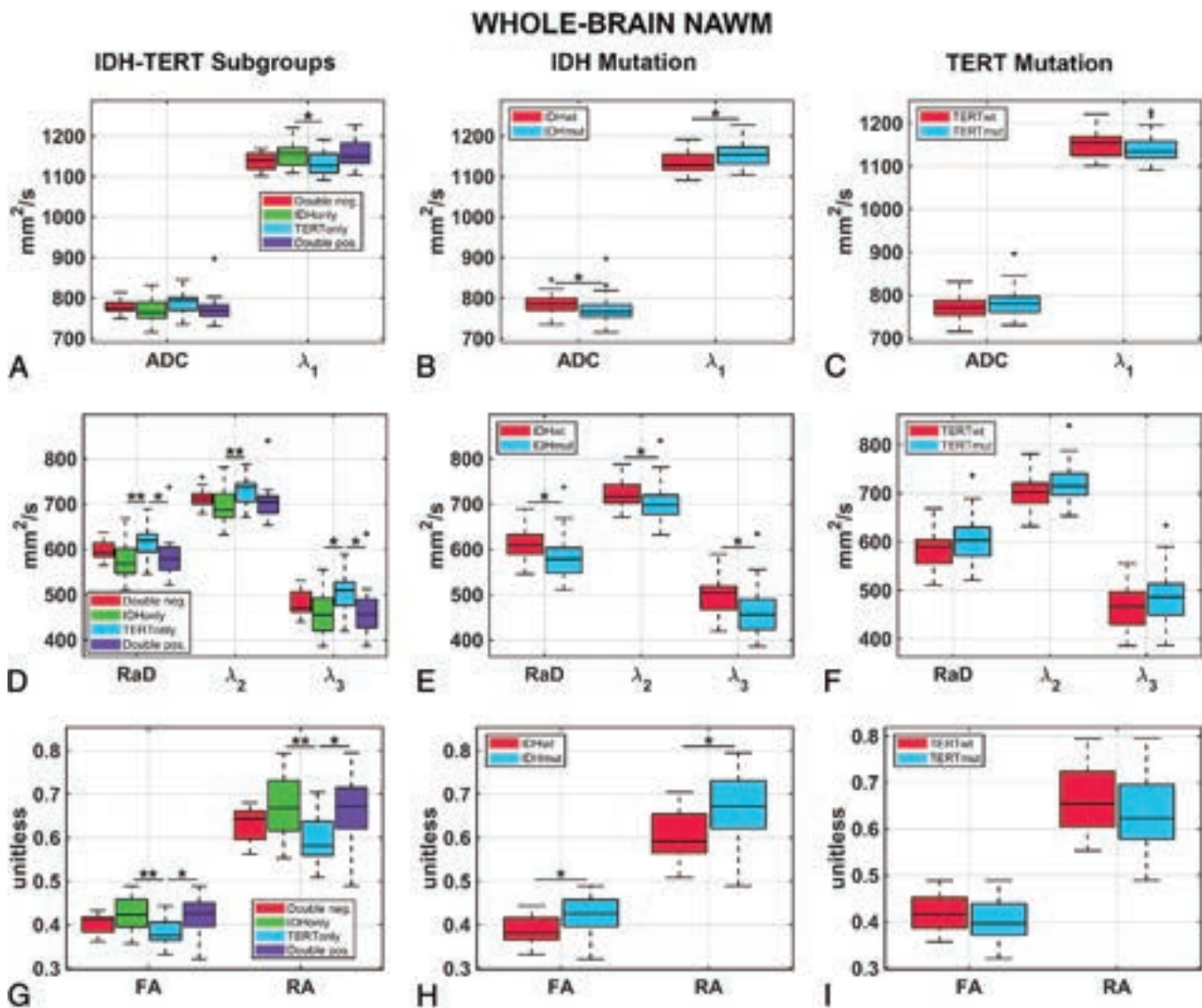


**FIG 3.** Boxplots of WB-NAWM means of ADC,  $\lambda_1$ , RD,  $\lambda_2$ ,  $\lambda_3$ , FA, and RA grouped by *IDH-TERT* subgroups (A), *IDH* mutation (B), and *TERT* (C) mutation statuses, respectively. The asterisk indicates  $P < .05$ , and double asterisks indicate  $P < .008$  according to the Bonferroni correction for multiple-comparison analysis. The plus sign indicates outlier values, whiskers indicate minimum and maximum values, the box limits are 25th and 75th percentiles, and the midline shows the median. Neg. indicates negative; pos., positive.

were higher in the IDHwt group (Table 3). In contrast, WB-NAWM  $\lambda_1$  ( $P = .003$ ), FA ( $P < .001$ ), and RA ( $P = .003$ ) were higher in IDHmut gliomas compared to IDHwt.

When TERTwt and TERTmut gliomas were compared, none of the WB-NAWM DAIs and eigenvalues demonstrated a statistically significant difference ( $P > .05$ ).

In consequence, similar relative median levels presented in all of the variables when comparing IDHwt and TERTmut versus their respective counterparts (eg, lower AD and higher RD for IDHwt and TERTmut versus IDHmut and TERTwt, respectively) demonstrated a common phenotype for these aggressive genotypes.

**Interhemispheric Differences.** For wild-type and mutant pairs, all of the diffusivity variables for all of the genotype pairs showed higher values ipsilaterally.  $\Delta$ ADC,  $\Delta$ RD, and  $\Delta\lambda_2$  were leveled;  $\Delta\lambda_1$  differed more for IDHmut and TERTwt, and, likewise,  $\Delta\lambda_3$  for IDHwt and TERTmut. IDHmut and TERTwt did not show interhemispheric difference for any anisotropy index, whereas

IDHwt and TERTmut had higher values contralaterally for RA and FA.

$\Delta$ FA,  $\Delta$ RA ( $P < .001$  for both), and  $\Delta\lambda_1$  ( $P = .002$ ) were higher in the IDHwt group compared to IDHmut.  $\Delta$ ADC ( $P = .48$ ),  $\Delta$ RD ( $P = .32$ ),  $\Delta\lambda_2$  ( $P = .73$ ), and  $\Delta\lambda_3$  ( $P = .055$ ) had no statistically significant difference among IDH mutation statuses.

With a remarkable resemblance,  $\Delta$ FA ( $P = .01$ ) and  $\Delta$ RA ( $P = .02$ ) were higher in TERTmut patients compared to TERTwt.  $\Delta$ ADC ( $P = .73$ ),  $\Delta\lambda_1$  ( $P = .31$ ),  $\Delta$ RD ( $P = .14$ ),  $\Delta\lambda_2$  ( $P = .27$ ), and  $\Delta\lambda_3$  ( $P = .054$ ) had no statistically significant difference among TERT mutation statuses.

### Classification by Thresholding

Numeric results in this section are fully presented in the Online Supplemental Data.

**IDH-TERT Subgroups.** For WB-NAWM, the best PPV was obtained for TERTonly by FA and RA (0.6842 for both) with

## HEMISPHERE DIFFERENCE NAWM

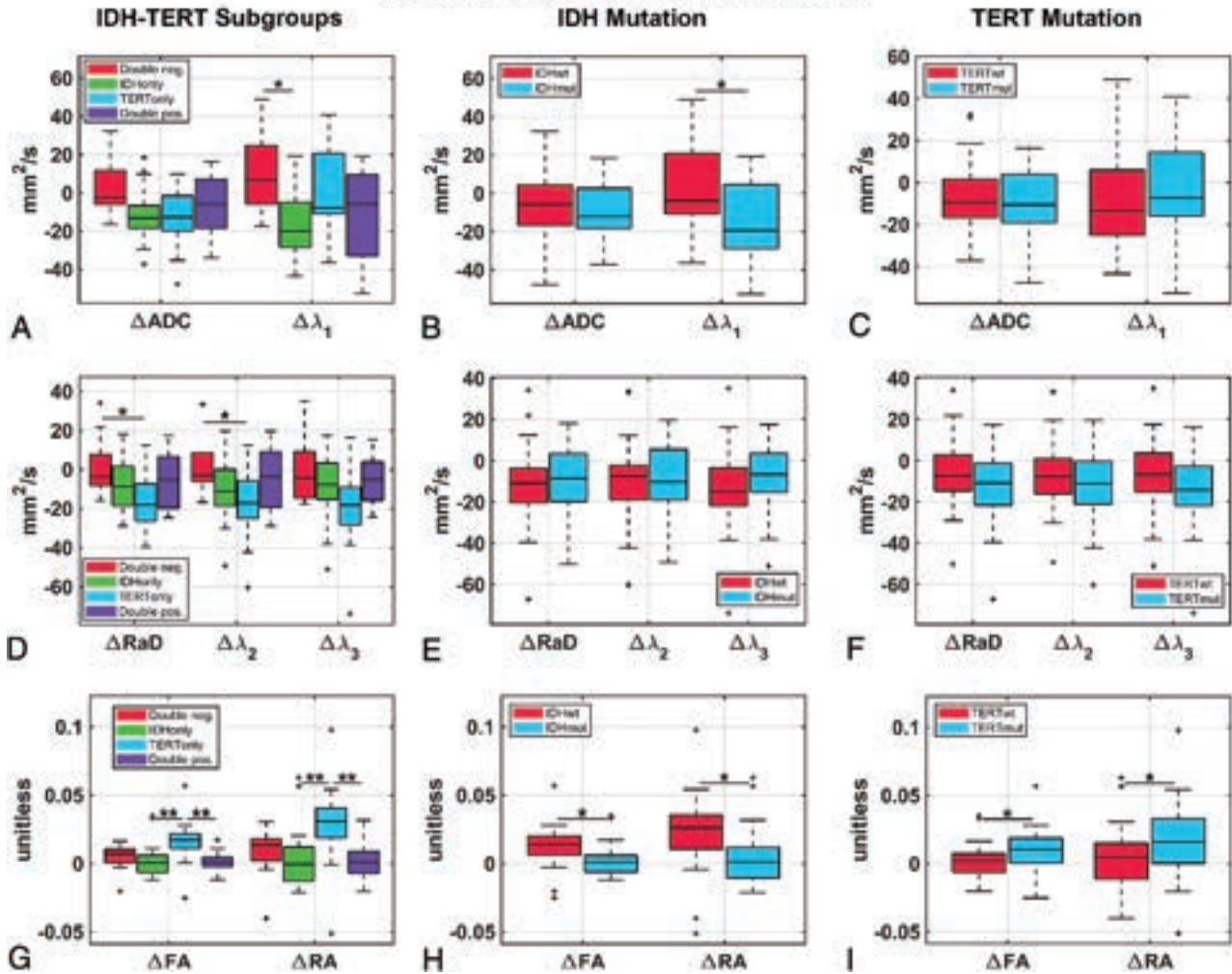


**FIG 4.** Boxplots of HMeD (contralateral-ipsilateral) of ADC,  $\lambda_1$ , RD,  $\lambda_2$ ,  $\lambda_3$ , FA, and RA grouped by *IDH-TERT* subgroups (A), *IDH* mutation (B), and *TERT* mutation (C) statuses, respectively. Fig 3 and Fig 4 legends are the same.

upper bound thresholding (UBTh); overall, PPVs were low (minimum 0.1429 DN with RA lower bound thresholding [LBTh], and 0.1464 DN ADC with UBTh). In contrast, NPVs had higher values with the highest from 0.9355 for DN with RD LBTh. DN had higher NPVs for all variables for LBTh and UBTh, followed by DP, TERTonly, and IDHonly (Online Supplemental Data).

AUC values from WB-NAWM reported TERTonly classification as the best for RA (0.7800), FA (0.7760), and  $\lambda_1$  (AD) (0.7030) with UBTh and RD (0.7470),  $\lambda_3$  (0.7460),  $\lambda_2$  (0.7400), and ADC (0.670) with LBTh. DN had the worst performance with AUC values close to 0.5, which was also supported by the poor PPV performance for LBTh.  $\lambda_1$  (AD), FA, and RA had above-average performance on IDHonly and DP using LBTh (Online Supplemental Data).

The WB-NAWM findings are aligned with the results of the “Whole Brain” section of the “*IDH-TERT* Subgroups” section. Overall poor classification performance on DN agreed with its lack of a statistically significant difference from the other groups. FA and RA, which showed the most statistically significant differences among subgroups, especially for TERTonly classification (Fig 3A,-D, -G), had the best classifier performances.

Interhemispheric differences had poor PPVs for LBTh with the highest 0.7895 for  $\Delta$ RA on TERTonly followed by 0.6296 for  $\Delta$ FA on TERTonly, then followed by a substantial drop to 0.4324. For UBTh,  $\Delta$ RA provided for TERTonly PPV = 1; however, the second highest value was 0.5667, which is a significant drop reflecting on overall performance. Interhemispheric NPVs had much higher values over different variables and genotypes, and higher values were concentrated on DN (maximum = 0.9750 from  $\Delta$ ADC and  $\Delta$  $\lambda_2$  for LBTh; maximum = 0.9167 from  $\Delta$ FA for UBTh), presenting with high values overall (minimum = 0.5750 for LBTh, 0.6304 for UBTh) (Online Supplemental Data).

Interhemispheric differences demonstrated the best AUC values on TERTonly from  $\Delta$ FA (0.8330) and  $\Delta$ RA (0.8280) with LBTh. DN has good performance for  $\Delta$  $\lambda_1$  ( $\Delta$ AD) (0.7377),  $\Delta$ ADC (0.7341),  $\Delta$  $\lambda_2$  (0.7341), and  $\Delta$ RD (0.7013) with LBTh. Performance on DP and IDHonly was poor with the exception of  $\Delta$ FA (DP: 0.6349, IDHonly: 0.6902) and  $\Delta$ RA (DP: 0.6448, IDHonly: 0.6866) performing better for both, and  $\Delta$  $\lambda_1$  ( $\Delta$ AD) (0.6975), for IDHonly (Online Supplemental Data), all using UBTh.

For interhemispheric differences, good performance of  $\Delta$ FA and  $\Delta$ RA for the TERTonly classification was in line with the



**Table 3: Comparison of WB-NAWM means and HMeD of diffusion parameters for IDH and TERT mutation status**

	ADC	$\lambda_1$ (AD)	RD	$\lambda_2$	$\lambda_3$	FA	RA
IDHmut Mann-Whitney test <i>P</i> values							
WB-NAWM	.02 <sup>a</sup>	.003 <sup>a</sup>	.001 <sup>a</sup>	.001 <sup>a</sup>	.001 <sup>a</sup>	<.001 <sup>a</sup>	.03 <sup>a</sup>
HMeD	.48	.002 <sup>a</sup>	.32	.73	.055	<.001 <sup>a</sup>	<.001 <sup>a</sup>
TERTmut Mann-Whitney test <i>P</i> values							
WB-NAWM	.21	.22	.09	.057	.12	.07	.07
HMeD	.73	.31	.14	.27	.054	.01 <sup>a</sup>	.02 <sup>a</sup>

<sup>a</sup> *P* < .05.

results of the “Interhemispheric Differences” section under the “RESULTS” section (Fig 4G), while AUC values of  $\Delta$ ADC,  $\Delta$ AD,  $\Delta$ RD, and  $\Delta\lambda_2$  for classifying DN aligned with the separation of DN from the other subgroups in Fig 4A, -D.

**IDH and TERT Mutation Status.** For WB-NAWM, PPVs were higher compared with NPVs. The highest PPV (0.7714) was obtained with LBTh of FA on IDHmut followed by  $\lambda_1$  (AD) (0.7500) and RA (0.7381), while  $\lambda_2$  (0.7647), RD (0.7632), ADC (0.7576), and  $\lambda_3$  (0.7568) also performed well using UBTh. PPVs for the TERTmut classification were modest with RD (0.6897) and FA (0.4828) providing maximum and minimum PPVs for LBTh, and  $\lambda_1$  (AD) (0.6563) and  $\lambda_2$  (0.4545), for UBTh. NPVs, on the other hand, had poor values with maximum values from RA (0.6429) using LBTh and RD (0.6250) using UBTh for IDHmut, and  $\lambda_3$  (0.5882) using LBTh and FA (0.5833) using UBTh for TERTmut, with minimum values from RD (0.3333) using LBTh and RA (0.2778) using UBTh for IDHmut, and RA (0.4359) using LBTh and  $\lambda_2$  (0.4054) using UBTh for TERTmut (Online Supplemental Data).

AUC values from WB-NAWM indicated good performance for IDHmut: FA and RA (0.7653 both) and  $\lambda_1$  (AD) (0.7115) for LBTh, and RD (0.7359),  $\lambda_3$  (0.7325), and  $\lambda_2$  (0.7283) for UBTh. In contrast, TERTmut had mediocre performance with  $\lambda_2$  (0.6331), RD (0.6200), and  $\lambda_3$  (0.6077) using LBTh and FA (0.6282) and RA (0.6274) using UBTh (Online Supplemental Data).

The better classifier performance of WB-NAWM on IDHmut was in line with its statistically significant difference from IDHwt present for all variables, shown in Fig 3B, -E, -H, whereas the lack of statistical significance for TERTmut depicted in Fig 3C, -F, -I reflected a mediocre classifier performance.

Interhemispheric difference PPVs had the highest values for IDHmut with  $\Delta$ AD (0.8519),  $\Delta$ FA (0.8250), and  $\Delta$ RA (0.8158) using UBTh which agrees with Fig 4A-H where the IDHmut distributions for the aforementioned variables lie below the IDHwt distributions. These variables also had statistically significant differences. The highest PPV for TERTmut occurred for  $\Delta$ RA (0.8182) followed by  $\Delta$ FA (0.7778), both using LBTh, in accordance with Fig 4I, where the  $\Delta$ FA and  $\Delta$ RA distributions of TERTmut were placed slightly higher than TERTwt distributions; also,  $\Delta$ FA and  $\Delta$ RA were the only variables presenting a statistically significant difference (Fig 4C, -F, -I).

IDHmut NPVs for  $\Delta$ FA and  $\Delta$ RA were both equal to 1 for LBTh, which was in accordance with Fig 4H where IDHmut  $\Delta$ FA and  $\Delta$ RA distributions were below IDHwt distributions and presented statistically significant differences. However, the remaining

NPVs were all below 0.5625 ( $\Delta\lambda_3$ ). The highest NPVs for TERTmut were all from LBTh for  $\Delta$ AD (0.6333),  $\Delta$ FA (0.6279), and  $\Delta$ RA (0.6042), with  $\Delta$ FA and  $\Delta$ RA being the only variables with statistically significant differences in Fig 4C, -F, -I.

The AUC classifier performance agreed with the predictive value and statistical findings:  $\Delta$ RA (0.7830),  $\Delta$ FA (0.7788), and  $\Delta$ AD (0.7149) had the best values for IDHmut all using UBTh; likewise, the best AUC values of TERTmut were  $\Delta$ FA (0.6732),  $\Delta$ RA (0.6618), and  $\Delta$ AD (0.5717) all using LBTh.

## DISCUSSION

In this study, DTI variables from the WB-NAWM of patients with gliomas and their interhemispheric differences were investigated for their association with IDH-TERT-based genotypes. DTI variables were analyzed as indicators of microstructural integrity in the NAWM for associating them as phenotypes of the mutations.

By probing the diffuse nature of the disease, which was scarcely studied in the past, this investigation complemented the studies focusing solely on the tumor region characteristics. In fact, there are very few glioma NAWM investigations with limited basis and scope: limited coverage of NAWM, relating interhemispheric FA differences to neurometabolites with contralateral FA increase,<sup>27</sup> positively correlating ADC to tumor grades,<sup>22</sup> and suggesting radiation-induced fiber damage for reducing interhemispheric FA difference.<sup>28</sup> In contrast, for this study, NAWM data were obtained comprehensively from the WB, the hemispheres, and interhemispheric computations for radiogenomics analysis.

First, while lacking statistical significance in this study, if AD and  $\lambda_2$  can also differentiate between TERTonly and DP for a larger cohort in the future, DTI variables might be considered as markers separating TERTonly from groups containing IDHmut.

In aggressive gliomas, ie, IDHwt and its subset TERTonly, WB-NAWM exhibited higher ADC. However, this observation does not necessarily grant a relevance to WB-NAWM ADC due to the canceling by AD and nonaxial diffusivities when computing ADC as their sum. Nevertheless, in the literature, NAWM ADC increase in patients with IDHwt has been related to vasogenic edema and tumor infiltration-related tissue damage.<sup>18,29,30</sup> Our results for IDHmut matched those in a recent study that showed lower NAWM FA and higher NAWM ADC and RD in IDHwt versus IDHmut,<sup>21</sup> but a decrease in AD reported therein contradicts our observations. This issue potentially stems from using the analysis variable FA in the skeletonization algorithm<sup>31</sup> for NAWM masking in Jütten et al<sup>21</sup> versus our comprehensive nonselective NAWM masking.

Taking the AD and RD are markers for axonal integrity,<sup>32</sup> in agreement with the findings of this study, a decrease in AD and FA and an increase in RD after radiation therapy were reported as resulting from radiation-related NAWM damage.<sup>33</sup> A recent study found lower FA, and AD as well as higher ADC and RD in regions with high tumor infiltration.<sup>34</sup> Furthermore, histopathologic studies also agree with higher ADC and lower FA of more



aggressive genotypes, suggesting tumor infiltration-related damage with increasing infiltration.<sup>35,36</sup> This also agrees with the observation where lower FA and RA for TERTonly indicate a tendency for molecular-motion isotropy in the WB-NAWM. However, pinpointing the microstructural changes behind the observations reported herein, especially in *TERT* subgroups, requires further histopathologic investigations.

In the IDHonly group, mostly negatively valued  $\Delta AD$  distribution showed that AD tends to be larger on the ipsilateral side, arguing that the deformation/pressure caused by the tumor might be pushing the molecular motion in the direction of the major axis of the microstructure. In contrast, in the DN subgroup, the contralateral side tended to have larger AD, accordingly,  $\Delta AD$  differentiates between only DN and IDHonly. Without notable physical deformation in the contralateral side, the causes behind major axis directional preference in groups with IDHwt are an open problem.

The interhemispheric observations, especially in aggressive genotypes such as IDHwt and TERTmut, including TERTonly, suggest that molecular motion was more isotropic in the ipsilateral hemisphere, potentially indicating loss of microstructural integrity therein. This suggestion agrees with findings in previous studies of decreasing microstructural organization in distal NAWM near the tumor.<sup>27</sup> The observation in more aggressive genotypes may link the increased NAWM damage to higher-grade tumors where IDHwt and TERTmut genotypes are more prevalent.<sup>22</sup>

This investigation was limited by a construct of its methodology. Summarizing the properties of large ROIs such as the WB or the hemispheres with a single number, ie, the mean, is suitable for statistical analysis but limits their rich information content. Differing distributions from different patients might have the same mean, which raises the concern of hampering classification and thereby genotype prediction when the ROI means are used as features. By contrast, the full properties of distributions might better characterize microstructural phenotypes associated with the mutations, resulting in more accurate prediction thereof.

## CONCLUSIONS

For NAWM, statistical analysis indicated that axial and nonaxial diffusivities, anisotropy indices, and interhemispheric differences proved to be the most associating variables for subgroups of *IDH* and *TERT* mutations. Additionally, the most basic classification methodology, ie, thresholding, provided optimistic classification performance despite its shortcoming as an one dimensional decision criterion. In the future, full distributions of the DTI variables from the WB, hemispheres, and their interhemispheric differences should be analyzed with machine learning methods for fully taking advantage of their richer information content residing in high-dimensional data spaces.

## ACKNOWLEDGMENTS

Hande Halilibrahimoğlu extends her special thanks to Seher Aydınlar and Mehmet Ali Aydınlar for their support in her research efforts while an undergraduate. The authors extend their deepest gratitude to the patients who consented to sharing their data for this effort against a complex and devastating disease.

Disclosure forms provided by the authors are available with the full text and PDF of this article at [www.ajnr.org](http://www.ajnr.org).

## REFERENCES

1. Ostrom QT, Patil N, Cioffi G, et al. **CBTRUS Statistical Report: primary brain and other central nervous system tumors diagnosed in the United States in 2013–2017.** *Neuro Oncol* 2020;22:iv1–96 CrossRef Medline
2. Eckel-Passow JE, Lachance DH, Molinaro AM, et al. **Glioma groups based on 1p/19q, IDH, and TERT promoter mutations in tumors.** *N Engl J Med* 2015;372:2499–508 CrossRef Medline
3. Louis DN, Perry A, Wesseling P, et al. **The 2021 WHO Classification of Tumors of the Central Nervous System: a summary.** *Neuro Oncol* 2021;23:1231–51 CrossRef Medline
4. Parsons DW, Jones S, Zhang X, et al. **An integrated genomic analysis of human glioblastoma multiforme.** *Science* 2008;321:1807–12 CrossRef Medline
5. Brat DJ, Verhaak RG, Aldape KD, et al; Cancer Genome Atlas Research Network. **Comprehensive, integrative genomic analysis of diffuse lower-grade gliomas.** *N Engl J Med* 2015;372:2481–98 CrossRef Medline
6. Killela PJ, Pirozzi CJ, Healy P, et al. **Mutations in IDH1, IDH2, and in the TERT promoter define clinically distinct subgroups of adult malignant gliomas.** *Oncotarget* 2014;5:1515–25 CrossRef Medline
7. Gao M, Lin Y, Liu X, et al. **TERT mutation is accompanied by neutrophil infiltration and contributes to poor survival in isocitrate dehydrogenase wild-type glioma.** *Front Cell Dev Biol* 2021;9:654407 CrossRef Medline
8. Colebatch AJ, Dobrovic A, Cooper WA. **TERT gene: its function and dysregulation in cancer.** *J Clin Pathol* 2019;72:281–84 CrossRef Medline
9. Barbaro M, Fine HA, Magge RS. **Scientific and clinical challenges within neuro-oncology.** *World Neurosurg* 2021;151:402–10 CrossRef Medline
10. Sahn F, Capper D, Jeibmann A, et al. **Addressing diffuse glioma as a systemic brain disease with single-cell analysis.** *Arch Neurol* 2012;69:523–26 CrossRef Medline
11. Esmaeili M, Stensjoen AL, Berntsen EM, et al. **The direction of tumour growth in glioblastoma patients.** *Sci Rep* 2018;8:1199 CrossRef Medline
12. Tysnes BB, Mahesparan R. **Biological mechanisms of glioma invasion and potential therapeutic targets.** *J Neurooncol* 2001;53:129–47 CrossRef Medline
13. Zetterling M, Roodakker KR, Berntsson SG, et al. **Extension of diffuse low-grade gliomas beyond radiological borders as shown by the coregistration of histopathological and magnetic resonance imaging data.** *J Neurosurg* 2016;125:1155–66 CrossRef Medline
14. Barajas RF Jr, Hodgson JG, Chang JS, et al. **Glioblastoma multiforme regional genetic and cellular expression patterns: influence on anatomic and physiologic MR imaging.** *Radiology* 2010;254:564–76 CrossRef Medline
15. Ellingson BM, Malkin MG, Rand SD, et al. **Validation of functional diffusion maps (fDMs) as a biomarker for human glioma cellularity.** *J Magn Reson Imaging* 2010;31:538–48 CrossRef Medline
16. Basser PJ, Pierpaoli C. **Microstructural and physiological features of tissues elucidated by quantitative-diffusion-tensor MRI.** *J Magn Reson B* 1996;111:209–19 CrossRef Medline
17. Price SJ, Burnet NG, Donovan T, et al. **Diffusion tensor imaging of brain tumours at 3T: a potential tool for assessing white matter tract invasion?** *Clin Radiol* 2003;58:455–62 CrossRef Medline
18. Inglese M, Brown S, Johnson G, et al. **Whole-brain N-acetylaspartate spectroscopy and diffusion tensor imaging in patients with newly diagnosed gliomas: a preliminary study.** *AJNR Am J Neuroradiol* 2006;27:2137–40 Medline
19. Kleihues P, Soylemezoglu F, Schäuble B, et al. **Histopathology, classification, and grading of gliomas.** *Glia* 1995;15:211–21 CrossRef Medline

20. Won YI, Chung CK, Kim CH, et al. **White matter change revealed by diffusion tensor imaging in gliomas.** *Brain Tumor Res Treat* 2016;4:100–06 CrossRef Medline
21. Jütten K, Mainz V, Gauggel S, et al. **Diffusion tensor imaging reveals microstructural heterogeneity of normal-appearing white matter and related cognitive dysfunction in glioma patients.** *Front Oncol* 2019;9:536 CrossRef Medline
22. Maudsley AA, Roy B, Gupta RK, et al. **Association of metabolite concentrations and water diffusivity in normal appearing brain tissue with glioma grade.** *J Neuroimaging* 2014;24:585–89 CrossRef Medline
23. Malaterre M. **GDCM: Grassroots DICOM Library.** [https://gdcmsourceforge.net/wiki/index.php/Main\\_Page](https://gdcmsourceforge.net/wiki/index.php/Main_Page). Accessed October 29, 2022
24. Bazin PL, Cuzzocreo JL, Yassa MA, et al. **Volumetric neuroimage analysis extensions for the MIPAV software package.** *J Neurosci Methods* 2007;165:111–21 CrossRef Medline
25. Jenkinson M, Bannister P, Brady M, et al. **Improved optimization for the robust and accurate linear registration and motion correction of brain images.** *Neuroimage* 2002;17:825–41 CrossRef Medline
26. Fawcett T. **An introduction to ROC analysis.** *Pattern Recognition Letters* 2006;27:861–74 CrossRef
27. Goebell E, Fiehler J, Ding XQ, et al. **Disarrangement of fiber tracts and decline of neuronal density correlate in glioma patients: a combined diffusion tensor imaging and <sup>1</sup>H-MR spectroscopy study.** *AJNR Am J Neuroradiol* 2006;27:1426–31 Medline
28. Kassubek R, Gorges M, Westhoff MA, et al. **Cerebral microstructural alterations after radiation therapy in high-grade glioma: a diffusion tensor imaging-based study.** *Front Neurol* 2017;8:286 CrossRef Medline
29. Horváth A, Perlaki G, Tóth A, et al. **Biexponential diffusion alterations in the normal-appearing white matter of glioma patients might indicate the presence of global vasogenic edema.** *J Magn Reson Imaging* 2016;44:633–41 CrossRef Medline
30. Kallenberg K, Goldmann T, Menke J, et al. **Abnormalities in the normal appearing white matter of the cerebral hemisphere contralateral to a malignant brain tumor detected by diffusion tensor imaging.** *Folia Neuropathol* 2014;52:226–33 CrossRef Medline
31. Baykara E, Gesierich B, Adam R, et al. **Alzheimer's Disease Neuroimaging Initiative. A novel imaging marker for small vessel disease based on skeletonization of white matter tracts and diffusion histograms.** *Ann Neurol* 2016;80:581–92 CrossRef Medline
32. Song SK, Sun SW, Ramsbottom MJ, et al. **Dysmyelination revealed through MRI as increased radial (but unchanged axial) diffusion of water.** *Neuroimage* 2002;17:1429–36 CrossRef Medline
33. Uh J, Merchant TE, Li Y, et al. **Differences in brainstem fiber tract response to radiation: a longitudinal diffusion tensor imaging study.** *Int J Radiat Oncol Biol Phys* 2013;86:292–97 CrossRef Medline
34. Latini F, Fahlström M, Behánčová A, et al. **The link between gliomas infiltration and white matter architecture investigated with electron microscopy and diffusion tensor imaging.** *Neuroimage Clin* 2021;31:102735 CrossRef Medline
35. Stadlbauer A, Ganslandt O, Buslei R, et al. **Gliomas: histopathologic evaluation of changes in directionality and magnitude of water diffusion at diffusion-tensor MR imaging.** *Radiology* 2006;240:803–10 CrossRef Medline
36. Deng Z, Yan Y, Zhong D, et al. **Quantitative analysis of glioma cell invasion by diffusion tensor imaging.** *J Clin Neurosci* 2010;17:1530–36 CrossRef Medline

# 3D Capsule Networks for Brain Image Segmentation

A. Avesta, Y. Hui, M. Aboian, J. Duncan, H.M. Krumholz, and S. Aneja



## ABSTRACT

**BACKGROUND AND PURPOSE:** Current autosegmentation models such as UNets and nnUNets have limitations, including the inability to segment images that are not represented during training and lack of computational efficiency. 3D capsule networks have the potential to address these limitations.

**MATERIALS AND METHODS:** We used 3430 brain MRIs, acquired in a multi-institutional study, to train and validate our models. We compared our capsule network with standard alternatives, UNets and nnUNets, on the basis of segmentation efficacy (Dice scores), segmentation performance when the image is not well-represented in the training data, performance when the training data are limited, and computational efficiency including required memory and computational speed.

**RESULTS:** The capsule network segmented the third ventricle, thalamus, and hippocampus with Dice scores of 95%, 94%, and 92%, respectively, which were within 1% of the Dice scores of UNets and nnUNets. The capsule network significantly outperformed UNets in segmenting images that were not well-represented in the training data, with Dice scores 30% higher. The computational memory required for the capsule network is less than one-tenth of the memory required for UNets or nnUNets. The capsule network is also >25% faster to train compared with UNet and nnUNet.

**CONCLUSIONS:** We developed and validated a capsule network that is effective in segmenting brain images, can segment images that are not well-represented in the training data, and is computationally efficient compared with alternatives.

**ABBREVIATIONS:** CapsNet = capsule network; Conv1 = first network layer made of convolutional operators; ConvCaps3 = third network layer made of convolutional capsules; ConvCaps4 = fourth network layer made of convolutional capsules; DeconvCaps8 = eighth network layer made of deconvolutional capsules; FinalCaps13 = final thirteenth network layer made of capsules; FinalCaps1 = final layer; GPU = graphics processing unit; PrimaryCaps2 = second network layer made of primary capsules

Neuroanatomic image segmentation is an important component in the management of various neurologic disorders.<sup>1-3</sup> Accurate segmentation of anatomic structures on brain MRIs is

an essential step in a variety of neurosurgical and radiation therapy procedures.<sup>1,3-6</sup> Manual segmentation is time-consuming and is prone to intra- and interobserver variability.<sup>7,8</sup> With the advent of deep learning to automate various image-analysis tasks,<sup>9,10</sup> there has been increasing enthusiasm for using deep learning for brain image autosegmentation.<sup>11-14</sup>

UNets are among the most popular and successful deep learning autosegmentation algorithms.<sup>11,15-17</sup> Despite the broad success of UNets in segmenting anatomic structures across various imaging modalities, they have well-described limitations. UNets perform best on images that closely resemble the images used for training but underperform on images that contain variant

Received September 13, 2022; accepted after revision March 11, 2023.

From the Department of Radiology and Biomedical Imaging (A.A., M.A., J.D.), Department of Therapeutic Radiology (A.A., Y.H., S.A.), Center for Outcomes Research and Evaluation (A.A., Y.H., H.M.K., S.A.), and Division of Cardiovascular Medicine (H.M.K.), Yale School of Medicine, New Haven, Connecticut; and Departments of Statistics and Data Science (J.D.) and Biomedical Engineering (J.D., S.A.), Yale University, New Haven, Connecticut.

Arman Avesta is a PhD student in the Investigative Medicine Program at Yale, which is supported by Clinical and Translational Science Awards grant No. ULI TR001863 from the National Center for Advancing Translational Science, a component of the National Institutes of Health (NIH). This work was also directly supported by the National Center for Advancing Translational Science grant number KL2 TR001862 as well as by the Radiological Society of North America's (RSNA) Fellow Research Grant Number RF2212. The contents of this article are solely the responsibility of the authors and do not necessarily represent the official views of NIH or RSNA.

The investigators within the Alzheimer's Disease Neuroimaging Initiative contributed to the design and implementation of Alzheimer's Disease Neuroimaging Initiative but did not participate in the analysis or writing of this article.

The contents of this article are solely the responsibility of the authors and do not necessarily represent the official views of NIH.

Please address correspondence to Sanjay Aneja, MD, Department of Therapeutic Radiology, Yale School of Medicine, Center for Outcomes Research and Evaluation, 195 Church St, 6th Floor, New Haven, CT 06510; e-mail: sanjay.aneja@yale.edu; @SanjayAnejaMD

Indicates open access to non-subscribers at [www.ajnr.org](http://www.ajnr.org)

Indicates article with online supplemental data.  
<http://dx.doi.org/10.3174/ajnr.A7845>

**Table 1: Study participants tabulated by the training, validation, and test sets**

Data Partitions	No. of MR Imaging Volumes	No. of Patients	Age (mean) (yr)	Sex	Diagnosis
Training set	3199	841	76 (SD, 7)	42% F, 58% M	29% CN, 54% MCI, 17% AD
Validation set	117	30	75 (SD, 6)	30% F, 70% M	21% CN, 59% MCI, 20% AD
Test set	114	30	77 (SD, 7)	33% F, 67% M	27% CN, 47% MCI, 26% AD

**Note:**—F indicates female; M, male; CN, cognitively normal; MCI, mild cognitive impairment; AD, Alzheimer disease.

anatomy or pathologies that change the appearance of normal anatomy.<sup>8</sup> Additionally, UNets have a large number of trainable parameters; hence, training and deploying UNets for image segmentation often requires substantial computational resources that may not be scalable in all clinical settings.<sup>15</sup> There is a need for fast, computationally efficient segmentation algorithms that can segment images not represented in the training data with high fidelity.

Capsule networks (CapsNets) represent an alternative autosegmentation method that can potentially overcome the limitations of UNets.<sup>18–20</sup> CapsNets can encode and manipulate spatial information such as location, rotation, and size about structures within an image and use this spatial information to produce accurate segmentations. Encoding spatial information allows CapsNets to well generalize on images that are not effectively represented in the data used to train the algorithm.<sup>19,20</sup> Moreover, CapsNets use a smarter paradigm for information encoding, which relies on fewer parameters leading to increased computational efficiency.<sup>18–20</sup>

Capsule networks have shown promise on some biomedical imaging tasks<sup>20</sup> but have yet to be fully explored for segmenting anatomic structures on brain MRIs. In this study, we explore the utility of CapsNets for segmenting anatomic structures on brain MRIs using a multi-institutional data set of >3000 brain MRIs. We compare the segmentation efficacy and computational efficiency of CapsNets with popular UNet-based models.

## MATERIALS AND METHODS

### Data Set

The data set for this study included 3430 T1-weighted brain MR images belonging to 841 patients from 19 institutions enrolled in the Alzheimer's Disease Neuroimaging Initiative study.<sup>21</sup> The inclusion criteria of the Alzheimer's Disease Neuroimaging Initiative have been previously described.<sup>22</sup> On average, each patient underwent 4 MRI acquisitions. Details of MRI acquisition parameters are provided in the Online Supplemental Data.<sup>21</sup> We randomly split the patients into training (3199 MRI, 93% of the data), validation (117 MR imaging volumes, 3.5% of the data), and test (114 MRI volumes, 3.5% of the data) sets. Data were divided at the patient level to assure that all images belonging to a patient were assigned to either the training, validation, or test set. Patient demographics are provided in Table 1. This study was approved by the institutional review board of Yale School of Medicine (No. 2000027592).

### Anatomic Segmentations

We trained our models to segment 3 anatomic structures of the brain: the third ventricle, thalamus, and hippocampus. These structures were chosen to represent structures with varying degrees of segmentation difficulty. Preliminary ground truth segmentations were initially generated using FreeSurfer (<http://surfer.nmr.mgh.harvard.edu>)<sup>23–25</sup> and then manually corrected

by 1 board-eligible radiologist with 9 years of experience in brain image analysis. The Online Supplemental Data detail the process by which ground truth segmentations were established.

### Image Preprocessing

MR imaging preprocessing included correction for intensity inhomogeneities, including B<sub>1</sub> field variations.<sup>26,27</sup> We used FSL's Brain Extraction Tool (<http://fsl.fmrib.ox.ac.uk/fsl/fslwiki/BET>) to remove the skull, face, and neck tissues, resulting in the extracted 3D image of the brain.<sup>28,29</sup> To overcome memory limitations, we performed segmentations on 64 × 64 × 64 voxel patches of the MR imaging volume that contained the segmentation target. The patch was automatically placed over the expected location of the segmentation target using predefined coordinates referenced from the center of the image. The coordinates of each patch were computed during training and were fixed during testing, without any manual input and without using the ground truth segmentations. Details of preprocessing are provided in the Online Supplemental Data.

### CapsNets

CapsNets have 3 main components: 1) capsules that each encode a structure together with the pose of that structure: the pose is an n-dimensional vector that learns to encode orientation, size, curvature, location, and other spatial information about the structure; 2) a supervised learning paradigm that learns how to transform the poses of the parts (eg, head and tail of the hippocampus) to the pose of the whole (eg, the entire hippocampus); and 3) a clustering paradigm that detects a whole if the poses of all parts transform into matching poses of the whole. Further details regarding differences between CapsNets and other deep learning models are provided in the Online Supplemental Data.

2D CapsNets were previously introduced by LaLonde et al<sup>20</sup> to segment 1 section of the image at a time. We developed 3D CapsNets for volumetric segmentation of a 3D volume, with the architecture shown in Fig 1A.<sup>20</sup> We developed 3D CapsNets for volumetric segmentation of a 3D volume, with the architecture shown in Fig 1A. The first layer, Conv1, performs 16 convolutions (5 × 5 × 5) on the input volume to generate 16 feature volumes, which are reshaped into 16D vectors at each voxel. The 16D vector at each voxel is reshaped into a pose that learns to encode spatial information at that voxel. The next layer, PrimaryCaps2, has 2 capsule channels that learn two 16D-to-16D convolutional transforms (5 × 5 × 5) from the poses of the previous-layer parts to the poses of the next-layer wholes. Likewise, all capsule layers (green layers in Fig 1A) learn m- to n-dimensional transforms from the poses of parts to the poses of wholes.

Our CapsNet has downsampling and upsampling limbs. The downsampling limb learns what structure is present at each voxel, and the skip connections from downsampling to upsampling limbs



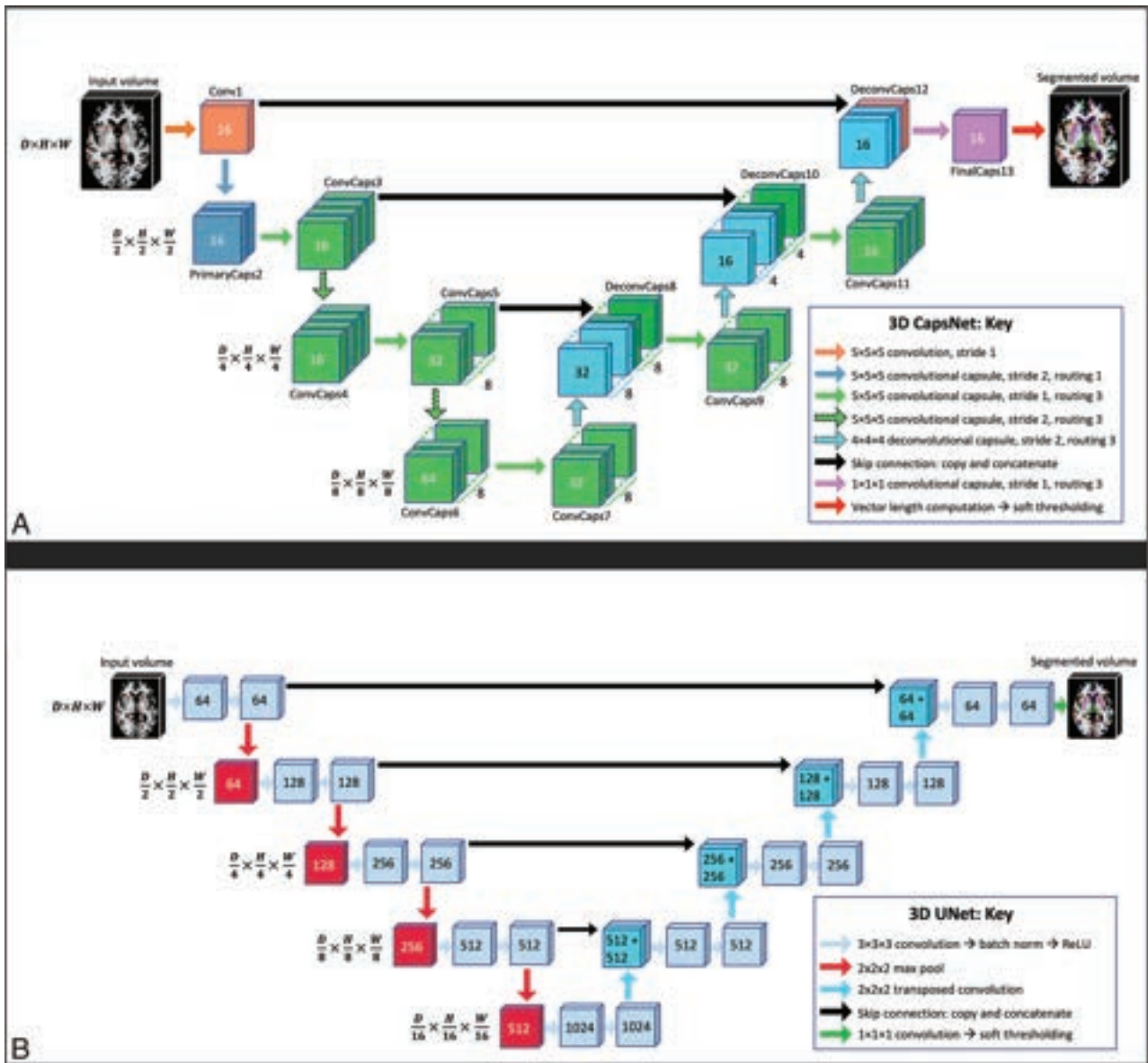


**FIG 1.** CapsNet (A) and UNet (B) architectures. The nnUNet architecture was self-configured by the model and is already published.<sup>16</sup> All models process 3D images in all layers, with dimensions shown on the left side. The depth, height, and width of the image in each layer is shown by  $D$ ,  $H$ , and  $W$ , respectively. A, The number over the Conv1 layer represents the number of channels. The numbers over the capsule layers (ConvCaps, DeconvCaps, and FinalCaps) represent the number of pose components. The stacked layers represent capsule channels. B, The numbers over each layer represent the number of channels. In UNet and nnUNet, the convolutions have stride = 1 and the transposed convolutions have stride = 2. Note that the numbers over the capsule layers show the number of pose components, while the numbers over the noncapsule layers show the number of channels.

preserve where each structure is on the image. Downsampling uses  $5 \times 5 \times 5$  convolutional transforms with stride = 2. Layers in the deeper parts of CapsNet contain more capsule channels (up to 8) and poses with more components (up to 64) to be able to encode more complex structures, because each capsule in the deeper parts of the model should be able to detect complex concepts in the entire image. Upsampling uses  $4 \times 4 \times 4$  transposed convolutional transforms with stride = 2 (turquoise layers in Fig 1A). The final layer, FinalCaps13, contains 1 capsule channel that learns to activate capsules within the segmentation target and deactivate them outside the target. The Online Supplemental Data explain the options that we explored for developing our 3D CapsNets and

how we chose the best design options. The Online Supplemental Data explain how the final layer activations were converted into segmentations. Details about how the model finds agreeing poses of parts that vote for the pose of the whole are provided in the Online Supplemental Data.

**Comparisons: UNets and nnUNets**

Optimized 3D UNets and nnUNets were also trained on the same training data,<sup>11-13,30</sup> and their segmentation efficacy and computational efficiency were compared with our CapsNet using the same test data. UNets and nnUNets have shown strong autosegmentation performance across a variety of different imaging modalities and

anatomic structures and are among the most commonly used segmentation algorithms in biomedical imaging.<sup>11-13,15,31,32</sup> Figure 1B shows the architecture of our UNet. The input image undergoes 64 convolutions ( $3 \times 3 \times 3$ ) to generate 64 feature maps. These maps then undergo batch normalization and rectified linear unit activation. Similar operations are performed again, followed by downsampling using max pooling ( $2 \times 2 \times 2$ ). The downsampling and upsampling limbs each include 4 units. Upsampling uses  $2 \times 2 \times 2$  transposed convolutions with stride = 2. The final layer performs a  $1 \times 1 \times 1$  convolution to aggregate all 64 channels, followed by soft thresholding using the sigmoid function. The model learns to output a number close to 1 for each voxel inside the segmentation target and a number close to zero for each voxel outside the target. We also trained self-configuring nnUNets that automatically learn the best architecture as well as the optimal training hyperparameters.<sup>16</sup>

### Model Training

The CapsNet and UNet models were trained for 50 epochs using the Dice loss and the Adam optimizer.<sup>33</sup> The initial learning rate was set at 0.002. We used dynamic paradigms for learning rate scheduling, with a minimal learning rate of 0.0001. The hyperparameters for our UNet were chosen on the basis of the best-performing model over the validation set. The hyperparameters for the nnUNet were self-configured by the model.<sup>16</sup> The training hyperparameters for CapsNet and UNet are detailed in the Online Supplemental Data.

### Model Performance

The segmentation efficacy of the 3 models was measured using Dice scores. To compare the performance of each segmentation model when training data are limited, we also trained the models using subsets of the training data with 600, 240, 120, and 60 MRIs. We then compared the segmentation efficacy of the models using the test set. The relative computational efficiency of the models was measured by the following: 1) the computational memory required to run the model (in megabytes), 2) the computational time required for training each model, and 3) the time that each model takes to segment 1 MR imaging volume.

### Out-of-Distribution Testing

To evaluate the performance of CapsNet and UNet models on the images that were not represented during training, we trained the models using images of the right hemisphere of the brain that only contained the right thalamus and right hippocampus. Then, we evaluated the segmentation efficacy of the trained models on the images of the left hemisphere of the brain that contained the contralateral left thalamus and left hippocampus. Because the left-hemisphere images in the test set are not represented in the right-hemisphere images in the training set, this experiment evaluates the out-of-distribution performance of the models. We intentionally did not use any data augmentation during training to assess out-of-distribution performance of the models. Given that nnUNet paradigm requires data augmentation, the nnUNet was not included in this experiment. We additionally tested whether the fully-trained models can generalize to segment raw images that did not undergo steps of preprocessing. The

Online Supplemental Data summarize the results of these experiments.

### Implementation

Images were preprocessed using Python (Version 3.9) and FreeSurfer (Version 7). PyTorch (Version 1.11; <https://pytorch.org/>) was used for model development and testing. Training and testing of the models were run on graphics processing unit (GPU)-equipped servers (4 virtual CPUs, 61 GB RAM, 12 GB NVIDIA GK210 GPU with Tesla K80 accelerators; <https://www.nvidia.com/>). The code used to train and test our models, our pretrained models, and a sample MR imaging is available on the GitHub page of our lab ([www.github.com/Aneja-Lab-Yale/Aneja-Lab-Public-CapsNet](http://www.github.com/Aneja-Lab-Yale/Aneja-Lab-Public-CapsNet)).

### RESULTS

All 3 segmentation models showed high performance across all 3 neuroanatomic structures with Dice scores of >90% (Fig 2). Performance was highest for the third ventricle (95%–96%) followed by the thalamus (94%–95%) and hippocampus (92%–93%). Dice scores between the CapsNet and UNet-based models were within 1% for all neuroanatomic structures (Table 2).

Although both CapsNet and UNet had difficulty segmenting contralateral structures, the CapsNet significantly outperformed the UNet (thalamus  $P$  value < .001, hippocampus  $P$  value < .001) (Table 3). CapsNet models frequently identified the contralateral structure of interest but underestimated the size of the segmentation, resulting in Dice scores between 40% and 60%. In contrast, the UNet models frequently failed to identify the contralateral structure of interest, resulting in Dice scores of <20% (Fig 3).

Segmentation performance for each model remained high across training data sets of varying sizes (Fig 4). When trained on 120 brain MRIs, all three models maintained their segmentation accuracy within 1% compared to models trained on 3199 brain MRIs. However, segmentation performance did decrease for all three models when trained on 60 brain MRIs (83% for CapsNet, 84% for UNet, and 88% for nnUNet).

The CapsNet was more computationally efficient compared with UNet-based models (Fig 5). The CapsNet required 228 MB, compared with 1364 MB for UNet and 1410 MB for nnUNet. The CapsNet trained 25% faster than the UNet (1.5 versus 2 seconds per sample) and 100% faster than the nnUNet (1.5 versus 3 seconds per sample). When we compared the deployment times of the fully-trained models, CapsNet and UNet could segment images equally fast (0.9 seconds per sample), slightly faster than the nnUNet (1.1 second per sample).

### DISCUSSION

Neuroanatomic segmentation of brain structures is an essential component in the treatment of various neurologic disorders. Deep learning-based autosegmentation methods have shown the ability to segment brain images with high fidelity, which was previously a time-intensive task.<sup>13,14,17,34</sup> In this study, we compared the segmentation efficacy and computational efficiency of CapsNets with UNet-based autosegmentation models. We

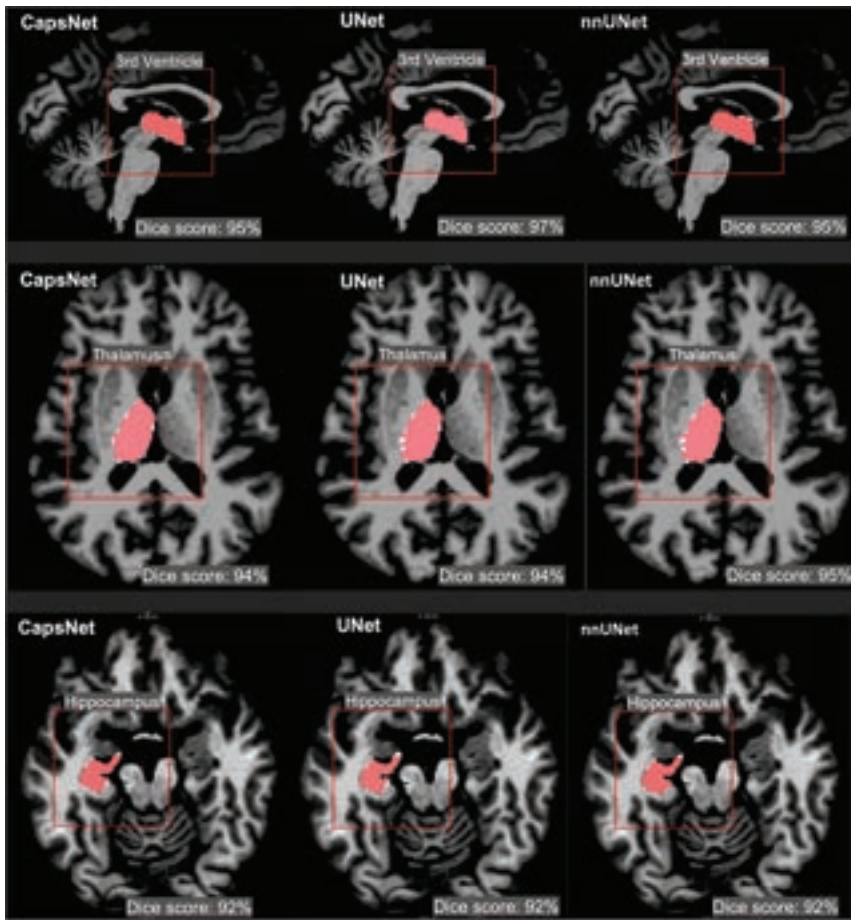


**FIG 2.** CapsNet, UNet, and nnUNet segmentation of brain structures that were represented in the training data. Segmentations for three structures are shown: third ventricle, thalamus, and hippocampus. Target segmentations and model predictions are, respectively, shown in red and white. Dice scores are provided for the entire volume of the segmented structure in this patient (who was randomly chosen from the test set).

**Table 2: Comparing the segmentation efficacy of CapsNets, UNets, and nnUNets in segmenting brain structures that were represented in the training data<sup>a</sup>**

Brain Structure	CapsNet Dice (95% CI)	UNet Dice (95% CI)	nnUNet Dice (95% CI)	Repeated Measures ANOVA P Value <sup>b</sup>
Third ventricle	95% (94–96)	96% (95–97)	96% (95–97)	.03
Thalamus	94% (93–95)	95% (94–96)	94% (92–96)	.1
Hippocampus	92% (91–93)	93% (92–94)	92% (91–93)	.1

<sup>a</sup> The segmentation accuracy was quantified using Dice scores on the test set (114 brain MRIs). The third ventricle, thalamus, and hippocampus, respectively, represent easy, medium, and difficult structures to segment.

<sup>b</sup>  $df = 3 - 1 = 2$ .

**Table 3: Comparing the efficacy of CapsNets and UNets in segmenting images that were not represented in the training data<sup>a</sup>**

Brain Structure	CapsNet Dice (95% CI)	UNet Dice (95% CI)	CapsNet vs UNet (P Value <sup>b</sup> )
Thalamus	52% (46–58)	16% (11–21)	< .01
Hippocampus	43% (38–48)	10% (6–14)	< .01

<sup>a</sup> Both models were trained to segment the right thalamus and hippocampus. Then, they were tested on segmenting the contralateral left thalamus and hippocampus.

<sup>b</sup>  $df = 114 - 1 = 113$ .

found CapsNets to be reliable and computationally efficient, achieving segmentation accuracy comparable with commonly used UNet-based models. Moreover, we found CapsNets to have higher segmentation performance on out-of-distribution

data, suggesting an ability to generalize beyond their training data.

Our results corroborate previous studies demonstrating the ability of deep learning models to reliably segment anatomic structures on diagnostic images.<sup>11,12,14</sup> UNet-based models have been shown to effectively segment normal anatomy across a variety of different imaging modalities including CT, MR imaging, and x-ray images.<sup>15,31,32,35–37</sup> Moreover, Isensee et al<sup>16</sup> showed the ability of nnUNets to generate reliable segmentations across 23 biomedical image-segmentation tasks with automated hyperparameter optimization. We have extended prior work by demonstrating similar segmentation efficacy between CapsNets and UNet-based models, with CapsNets being notably more computationally efficient. Our CapsNets require <10% of the amount of memory required by UNet-based methods and train 25% faster.

Our findings are consistent with prior studies demonstrating the efficacy of CapsNets for image segmentation.<sup>20,38</sup> LaLonde et al<sup>20</sup> previously demonstrated that 2D CapsNets can effectively segment lung tissues on CT images and muscle and fat tissues on thigh MRIs. Their group similarly found that CapsNets can segment images with performance rivaling UNet-based models while requiring <10% of the memory required by UNet-based models. Our study builds on prior studies by showing the efficacy of CapsNets for segmenting neuroanatomic substructures on brain MRIs. Additionally, when we compared this work with prior work, we have implemented 3D CapsNet architecture, which has not been previously described in the literature.

Previous studies have suggested that CapsNets are able to generalize beyond their training data.<sup>19,20</sup> Hinton et al<sup>19</sup> demonstrated that CapsNets can learn spatial information about the objects in the image and can then generalize this information beyond what is present in the training data, which gives CapsNet out-of-distribution generalization capability. The ability to segment out-of-distribution images was also shown by LaLonde et al<sup>20</sup> for their 2D CapsNet model, which segments images. We built on previous studies by demonstrating out-of-distribution generalizability of 3D CapsNets for segmenting medical images.

Although we found CapsNets to be effective in biomedical image segmentation, previous studies on biomedical imaging have shown mixed results.<sup>38</sup> Survarachakan et al<sup>38</sup> previously found 2D



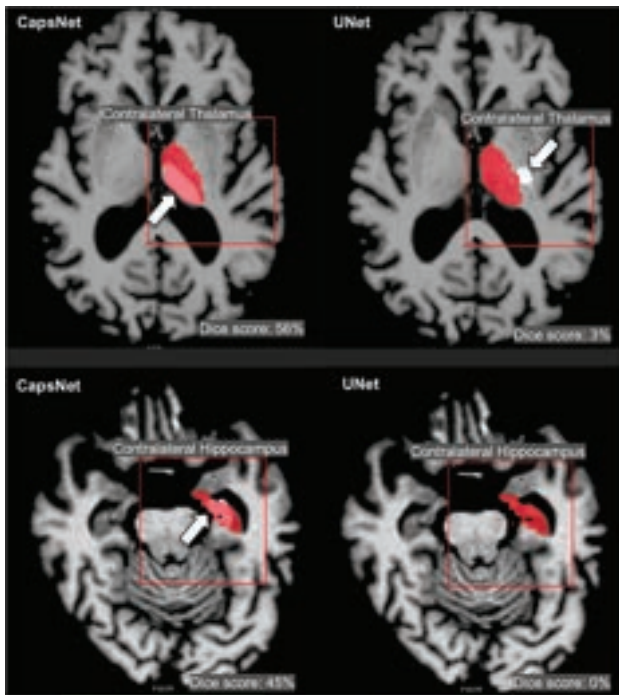


**FIG 3.** CapsNets outperforms UNets in segmenting images that were not represented in the training data. Both models were trained to segment right-brain structures and were tested to segment contralateral left-brain structures. Target segmentations and model predictions are, respectively, shown in red and white. Dice scores are provided for the entire volume of the segmented structure in this patient. The CapsNet partially segmented the contralateral thalamus and hippocampus (*white arrows*), but the UNet poorly segmented the thalamus (*white arrow*) and entirely missed the hippocampus.

CapsNets to be effective for segmenting heart structures but ineffective for segmenting the hippocampus on brain images. Our more favorable results in segmenting the hippocampus are likely because of the 3D structure of our CapsNet, which can use the contextual information in the volume of the image rather than just a section of the image to better segment the complex shape of the hippocampus.<sup>39</sup>

Our study has several limitations. Our models were tested on only 3 brain structures that are commonly segmented on brain MRIs, meaning that our findings may not generalize across other imaging modalities and anatomic structures. Nevertheless, our findings show the efficacy of CapsNets on brain structures with different levels of segmentation difficulty, suggesting the potential utility for a variety of scenarios. Computational efficiency across models was measured using the same computing resources and GPU memory, and our findings may not translate to different computational settings. Future studies can further explore the relative computational efficiency of CapsNets compared with other auto-segmentation models across different computing environments. We only compared the efficacy of CapsNets with UNet-based models. While there are multiple other auto-segmentation models, UNet-based models are currently viewed as the most successful deep learning models for segmenting biomedical images. Further studies comparing the CapsNet with other deep learning models are an area of future research. Last, we found CapsNets to outperform UNet models when segmenting contralateral structures

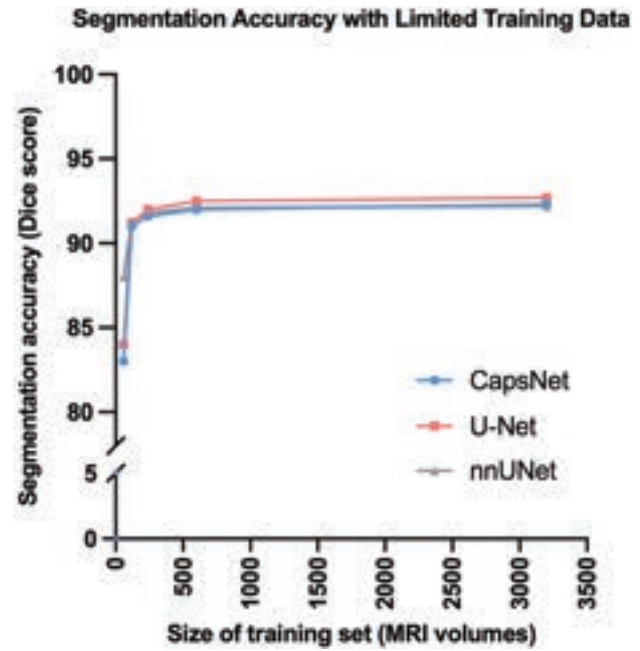


**FIG 4.** Comparing CapsNets, UNets, and nnUNets when training data are limited. When the size of the training set was decreased from 3199 to 120 brain MRIs, hippocampus segmentation accuracy (measured by Dice score) of all 3 models did not decrease >1%. Further decrease in the size of the training set down to 60 MRIs led to worsened segmentation accuracy.

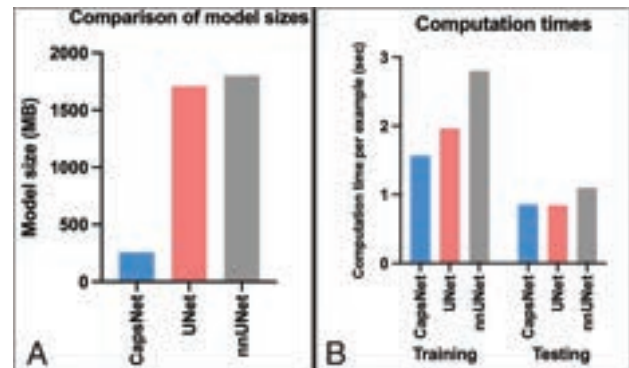


**FIG 5.** Comparing the computational efficiency among CapsNets, UNets, and nnUNets, in terms of memory requirements (A) and computational speed (B). A, The bars represent the computational memory required to accommodate the total size of each model, including the parameters plus the cumulative size of the forward- and backward-pass feature volumes. B, CapsNet trains faster, given that its trainable parameters are 1 order of magnitude fewer than UNets or nnUNets. The training times represent the time that each model took to converge for segmenting the hippocampus, divided by the number of training examples and the training epochs (to make training times comparable with test times). The test times represent how fast a fully-trained model can segment a brain image.

not represented in the training data. Techniques like data augmentation have shown the ability to improve the generalizability of UNet models in this scenario. Nevertheless, our findings demonstrate the ability of CapsNets to encode spatial information without the need for such techniques, which often require additional computational resources. This result further highlights the potential computational advantages of CapsNets for medical image segmentation.



## CONCLUSIONS

In this study, we showed that 3D CapsNets can accurately segment neuroanatomic structures on brain MR images with segmentation accuracy similar to that of UNet-based models. We also showed that CapsNets outperformed UNet-based models in segmenting out-of-distribution data. CapsNets are also more computationally efficient compared with UNet-based models because they train faster and require less computation memory.

Disclosure forms provided by the authors are available with the full text and PDF of this article at [www.ajnr.org](http://www.ajnr.org).

## REFERENCES

1. Feng CH, Cornell M, Moore KL, et al. **Automated contouring and planning pipeline for hippocampal-avoidant whole-brain radiotherapy.** *Radiat Oncol* 2020;15:251 CrossRef Medline
2. Dasenbrock HH, See AP, Smalley RJ, et al. **Frameless stereotactic navigation during insular glioma resection using fusion of three-dimensional rotational angiography and magnetic resonance imaging.** *World Neurosurg* 2019;126:322–30 CrossRef Medline
3. Dolati P, Gokoglu A, Eichberg D, et al. **Multimodal navigated skull base tumor resection using image-based vascular and cranial nerve segmentation: a prospective pilot study.** *Surg Neurol Int* 2015;6:172 CrossRef Medline
4. Thompson RF, Valdes G, Fuller CD, et al. **Artificial intelligence in radiation oncology: a specialty-wide disruptive transformation?** *Radiother Oncol* 2018;129:421–26 CrossRef Medline
5. Kotecha R, Aneja S. **Opportunities for integration of artificial intelligence into stereotactic radiosurgery practice.** *Neuro Oncol* 2021;23:1629–30 CrossRef Medline
6. Aneja S, Chang E, Omuro A. **Applications of artificial intelligence in neuro-oncology.** *Curr Opin Neurol* 2019;32:850–56 CrossRef Medline
7. Nalepa J, Marcinkiewicz M, Kawulok M. **Data augmentation for brain-tumor segmentation: a review.** *Front Comput Neurosci* 2019;13:83 CrossRef Medline
8. Despotović I, Goossens B, Philips W. **MRI segmentation of the human brain: challenges, methods, and applications.** *Comput Math Methods Med* 2015;2015:e450341 CrossRef Medline
9. Joel MZ, Umrao S, Chang E, et al. **Using adversarial images to assess the robustness of deep learning models trained on diagnostic images in oncology.** *JCO Clin Cancer Inform* 2022;e2100170 CrossRef Medline
10. Chang E, Joel MZ, Chang HY, et al. **Comparison of radiomic feature aggregation methods for patients with multiple tumors.** *Sci Rep* 2021;11:9758 CrossRef Medline
11. Rudie JD, Weiss DA, Colby JB, et al. **Three-dimensional U-Net convolutional neural network for detection and segmentation of intracranial metastases.** *Radiol Artif Intell* 2021;3:e200204 CrossRef Medline
12. Rauschecker AM, Gleason TJ, Nedelec P, et al. **Interinstitutional portability of a deep learning brain MRI lesion segmentation algorithm.** *Radiol Artif Intell* 2022;4:e200152 CrossRef Medline
13. Weiss DA, Saluja R, Xie L, et al. **Automated multiclass tissue segmentation of clinical brain MRIs with lesions.** *Neuroimage Clin* 2021;31:102769 CrossRef Medline
14. Rudie JD, Weiss DA, Saluja R, et al. **Multi-disease segmentation of gliomas and white matter hyperintensities in the BraTS data using a 3D Convolutional Neural Network.** *Front Comput Neurosci* 2019;13:84 CrossRef Medline
15. Punn NS, Agarwal S. **Modality specific U-Net variants for biomedical image segmentation: a survey.** *Artif Intell Rev* 2022; 55:5845 Medline
16. Isensee F, Jaeger PF, Kohl SA, et al. **nnU-Net: a self-configuring method for deep learning-based biomedical image segmentation.** *Nat Methods* 2021;18:203–11 CrossRef Medline
17. Duong MT, Rudie JD, Wang J, et al. **Convolutional neural network for automated FLAIR lesion segmentation on clinical brain MR imaging.** *AJNR Am J Neuroradiol* 2019;40:1282–90 CrossRef Medline
18. Sabour S, Frosst N, Hinton GE. **Dynamic routing between capsules.** In: *Proceedings of the 31st International Conference on Neural Information Processing Systems. NIPS'17*, Red Hook, New York. December 4–9, 2017:3859–69
19. Hinton GE, Sabour S, Frosst N. **Matrix capsules with EM routing.** In: *International Conference on Learning Representations*, Vancouver, British Columbia, Canada. April 30 to May 3, 2018
20. LaLonde R, Xu Z, Irmakci I, et al. **Capsules for biomedical image segmentation.** *Med Image Anal* 2021;68:101889 CrossRef Medline
21. Crawford KL, Neu SC, Toga AW. **The Image and Data Archive at the Laboratory of Neuro Imaging.** *Neuroimage* 2016;124:1080–83 CrossRef Medline
22. Weiner M, Petersen R, Aisen P. **Alzheimer's Disease Neuroimaging Initiative.** September 16, 2014. <https://clinicaltrials.gov/ct2/show/NCT00106899>. Accessed March 21, 2022
23. Clerx L, Gronenschild EH, Echavarrri C, et al. **Can FreeSurfer compete with manual volumetric measurements in Alzheimer's disease?** *Curr Alzheimer Res* 2015;12:358–67 CrossRef Medline
24. Ochs AL, Ross DE, Zannoni MD, et al. **Comparison of automated brain volume measures obtained with NeuroQuant and FreeSurfer.** *J Neuroimaging* 2015;25:721–27 CrossRef Medline
25. Fischl B. **FreeSurfer.** *Neuroimage* 2012;62:774–81 CrossRef Medline
26. Fischl B, Salat DH, Busa E, et al. **Whole brain segmentation: automated labeling of neuroanatomical structures in the human brain.** *Neuron* 2002;33:341–55 CrossRef Medline
27. Ganzetti M, Wenderoth N, Mantini D. **Quantitative evaluation of intensity inhomogeneity correction methods for structural MR brain images.** *Neuroinformatics* 2016;14:5–21 CrossRef Medline
28. Somasundaram K, Kalaiselvi T. **Automatic brain extraction methods for T1 magnetic resonance images using region labeling and morphological operations.** *Comput Biol Med* 2011;41:716–25 CrossRef Medline
29. Popescu V, Battaglini M, Hoogstrate WS, et al. **Optimizing parameter choice for FSL-Brain Extraction Tool (BET) on 3D T1 images in multiple sclerosis.** *Neuroimage* 2012;61:1484–94 CrossRef Medline
30. Cardenas CE, Yang J, Anderson BM, et al. **Advances in auto-segmentation.** *Semin Radiat Oncol* 2019;29:185–97 CrossRef Medline
31. Elguindi S, Zelefsky MJ, Jiang J, et al. **Deep learning-based auto-segmentation of targets and organs-at-risk for magnetic resonance imaging only planning of prostate radiotherapy.** *Phys Imaging Radiat Oncol* 2019;12:80–86 CrossRef Medline
32. Francis S, Jayaraj PB, Pournami PN, et al. **ThoraxNet: a 3D U-Net based two-stage framework for OAR segmentation on thoracic CT images.** *Phys Eng Sci Med* 2022;45:189–203 CrossRef Medline
33. Yaqub M, Jinchao F, Zia MS, et al. **State-of-the-art CNN optimizer for brain tumor segmentation in magnetic resonance images.** *Brain Sci* 2020;10:427 CrossRef Medline
34. Guha Roy A, Conjeti S, Navab N, et al. **QuickNAT: a fully convolutional network for quick and accurate segmentation of neuroanatomy.** *Neuroimage* 2019;186:713–27 CrossRef Medline
35. Yahyatabar M, Jouvet P, Chieriet F. **Dense-Unet: a light model for lung fields segmentation in chest x-ray images.** *Annu Int Conf IEEE Eng Med Biol Soc* 2020;2020:1242–45 CrossRef Medline
36. Chi J, Zhang S, Han X, et al. **MID-UNet: multi-input directional UNet for COVID-19 lung infection segmentation from CT images.** *Signal Process Image Commun* 2022;108:116835 CrossRef Medline
37. Agnes SA, Anitha J. **Efficient multiscale fully convolutional UNet model for segmentation of 3D lung nodule from CT image.** *J Med Imaging Bellingham Wash* 2022;9:052402 CrossRef Medline
38. Survarachakan S, Johansen JS, Aarseth M, et al. **Capsule Nets for Complex Medical Image Segmentation Tasks.** In: *Proceedings of the 10th Colour and Visual Computing Symposium 2020 (CVCS 2020)*, Gjøvik, Norway; Virtual. September 16–17, 2020
39. Avesta A, Hossain S, Lin M, et al. **Comparing 3D, 2.5D, and 2D approaches to brain image auto-segmentation.** *Bioengineering (Basel)* 2023;10:181 CrossRef Medline

# Assessing the Equivalence of Brain-Derived Measures from Two 3D T1-Weighted Acquisitions: One Covering the Brain and One Covering the Brain and Spinal Cord

D. Pareto, J.F. Corral, A. Garcia-Vidal, M. Alberich, C. Auger, J. Rio, N. Mongay, J. Sastre-Garriga, and À. Rovira



## ABSTRACT

**BACKGROUND AND PURPOSE:** In MS, it is common to acquire brain and spinal cord MR imaging sequences separately to assess the extent of the disease. The goal of this study was to see how replacing the traditional brain T1-weighted images (brain-T1) with an acquisition that included both the brain and the cervical spinal cord (cns-T1) affected brain- and spinal cord-derived measures.

**MATERIALS AND METHODS:** Thirty-six healthy controls (HC) and 42 patients with MS were included. Of those, 18 HC and 35 patients with MS had baseline and follow-up at 1 year acquired on a 3T magnet. Two 3D T1-weighted images (brain-T1 and cns-T1) were acquired at each time point. Regional cortical thickness and volumes were determined with FastSurfer, and the percentage brain volume change per year was obtained with SIENA. The spinal cord area was estimated with the Spinal Cord Toolbox. Intraclass correlation coefficients (ICC) were calculated to check for consistency of measures obtained from brain-T1 and cns-T1.

**RESULTS:** Cortical thickness measures showed an ICC  $>0.75$  in 94% of regions in healthy controls and 80% in patients with MS. Estimated regional volumes had an ICC  $>0.88$ , and the percentage brain volume change had an ICC  $>0.79$  for both groups. The spinal cord area measures had an ICC of 0.68 in healthy controls and 0.92 in patients with MS.

**CONCLUSIONS:** Brain measurements obtained from 3D cns-T1 are highly equivalent to those obtained from a brain-T1, suggesting that it could be feasible to replace the brain-T1 with cns-T1.

**ABBREVIATIONS:** cns = central nervous system; EDSS = Expanded Disability Status Scale; HC = healthy control; ICC = intraclass correlation coefficient; PBVC = percentage brain volume change; SCA = spinal cord area; SSIM = structural similarity index

The pathologic characterization of MS includes focal and diffuse areas of inflammation, demyelination, neuroaxonal loss, and gliosis in the central nervous system (cns). Lesions in the brain and spinal cord are identified with MR imaging, an essential and fundamental technique in the diagnosis, prediction of disease progression, and monitoring and prediction of the response to disease-modifying treatments.<sup>1</sup> Actually, brain cortical lesions can be identified from routinely acquired T1-weighted

MR imaging in conjunction with FLAIR imaging.<sup>2</sup> Lesions in the spinal cord can be outlined with just T1-weighted MR imaging.<sup>3</sup> Regarding lesion topography and atrophy quantification, both the brain and spinal cord are assessed separately, requiring the acquisition of 2 images,<sup>4</sup> although recent studies have highlighted the relevance of acquiring simultaneous brain and spinal cord MR imaging.<sup>5,6</sup> Several attempts have been made to assess the estimation of spinal cord area (SCA) from brain acquisitions, instead of from spinal cord MR imaging, showing that the estimated SCA values differ.<sup>7,8</sup> Despite SCAs differing, estimation from brain acquisitions is quite common and has been proposed as an alternative in cases in which spinal cord MR imaging has not been acquired, which is a common situation due to the limited availability of the MR imaging scanner. In this context, we propose a study to investigate whether conventional brain T1-weighted MR imaging (brain-T1) can be replaced by an acquisition that encompasses both the brain and the spinal cord (cns-T1). The proposed cns-T1 is a trade-off between having a larger spinal coverage compared with a brain-T1 acquisition, allowing visualization of the presence of lesions, though it is not as complete as conventional spinal cord MR imaging, which covers down to the conus medullaris. The effect on different brain-

Received June 14, 2022; accepted after revision February 1, 2023.

From the Neuroradiology Group (D.P., J.F.C., A.G.-V., C.A., À.R.), Vall d'Hebron Research Institute, Barcelona, Spain; Section of Neuroradiology (D.P., J.F.C., M.A., À.R.), Radiology Department, Vall d'Hebron University Hospital, Barcelona, Spain; and Department of Neurology and Neuroimmunology (J.R., N.M., J.S.-G.), Multiple Sclerosis Centre of Catalonia, Vall d'Hebron University Hospital, Universitat Autònoma de Barcelona, Barcelona, Spain.

This work was funded by the Instituto de Salud Carlos III (PI18/00823).

Please address correspondence to Deborah Pareto, PhD, Section of Neuroradiology, Vall d'Hebron University Hospital Psg. Vall Hebron 119-129, 08035 Barcelona, Spain; e-mail: [deborah.pareto.idi@gencat.cat](mailto:deborah.pareto.idi@gencat.cat)

Indicates open access to non-subscribers at [www.ajnr.org](http://www.ajnr.org)

Indicates article with online supplemental data.

<http://dx.doi.org/10.3174/ajnr.A7843>

derived measures such as cortical thickness, regional volumetry, and changes in the brain volume during a 1-year period has been assessed. The differences in the estimated SCA have also been evaluated.

## MATERIALS AND METHODS

### Cohort

A group of 36 healthy controls (HCs) and 42 patients with MS was included in the study, with baseline MR imaging. From those, 18 HCs and 35 patients with MS had 12-month follow-up MR imaging. The study was approved by the Vall d'Hebron University Hospital ethics committee, and the participating subjects signed their informed consent (PR(AMI)24/2019).

### MR Imaging Acquisition

Images were acquired in a 3T system (Tim Trio; Siemens) with a 12-channel whole-body coil. Acquisition parameters for the 3D T1-weighted images were the following—for brain—T1: TR = 2300 ms, TE = 2.98 ms, TI = 900 ms, 176 slices, FOV = 256 mm, voxel =  $1 \times 1 \times 1 \text{ mm}^3$ , bandwidth = 240 Hz/px, time = 5 minutes 12 seconds; for cns-T1: TR = 2000 ms, TE = 3.21 ms, TI = 100 ms, 192 slices, FOV = 320 mm, voxel =  $1 \times 1 \times 1 \text{ mm}^3$ , bandwidth = 150 Hz/px, time = 4 minutes 52 seconds. The parameters for the brain-plus-spine 3D T1-weighted MR imaging were established according to the protocol suggested by Cohen-Adad et al<sup>9</sup> and include at least the C7 level. The patient table was moved between the 2 acquisitions so that the center of the image was placed in the isocenter.

### MR Image Analysis

Correction for image distortions due to gradient nonlinearity was performed with the Siemens implemented tools on the MR imaging console. The two 3D T1-weighted images were cropped using the `robust_fov` utility in FSL and bias-field-corrected through the N4 algorithm. The aim of this step was to remove the medulla oblongata, which may affect the performance of brain analysis toolboxes. Then, the brain was segmented with FastSurfer (<https://deep-mi.org/research/fastsurfer/>).<sup>10</sup> Cortical thickness was determined in 62 regions, 31 per hemisphere,<sup>11</sup> and global volumes (GM, WM, thalamus, and total intracranial) were also obtained. The thalamus was chosen because it is a structure highly involved in all MS phenotypes with the presence of clinically relevant volume loss.<sup>12</sup> For those subjects with baseline and follow-up MR imaging, the percentage brain volume change (PBVC) was calculated with the SIENA toolbox (<https://fsl.fmrib.ox.ac.uk/fsl/fslwiki/SIENA>).<sup>13</sup>

To ensure that the quality of the baseline and follow-up images was equivalent, we calculated the structural similarity index (SSIM)<sup>14</sup> between them. This task can be accomplished by running SIENA with the `-d` option, which does not delete the baseline and follow-up images coregistered to the halfway point of both studies (which were used to calculate the PBVC). The SSIM is based on the product of 3 terms that account for the contribution of the luminance, contrast, and structure, and it was computed as implemented in Matlab (MathWorks). Finally, the SCA was estimated with the Spinal Cord Toolbox<sup>15</sup> (<https://github.com/spinalcordtoolbox/spinalcordtoolbox>) by manually

labeling the C2-C3 intervertebral level in the 2 acquisitions. Briefly, the spine was segmented with the DeepSeg algorithm and normalized to the multimodal PAM50 atlas to delineate the SCA. The SCA was calculated as the average of 11 sections, centered at the C2-C3 level. The position of the C2-C3 level was defined manually.

### Statistical Analysis

The agreement between the measures obtained from the brain-T1 and cns-T1 was obtained by calculating the intraclass correlation coefficient (ICC). Reproducibility of the cortical thickness, regional brain volumes, and the SCA was assessed by calculating the ICC between the baseline and follow-up measures in the HC group. The Cicchetti criteria<sup>16</sup> were taken as a reference: excellent agreement for  $0.75 < \text{ICC} < 1$ ; good,  $0.60 < \text{ICC} < 0.74$ ; fair,  $0.40 < \text{ICC} < 0.59$ , and poor when  $\text{ICC} < 0.4$ .

For the PBVC, mean cortical thickness, and the SCA, a Bland-Altman plot was used to visualize the agreement between the measures obtained with the 2 sequences for baseline acquisitions. The SSIM values obtained from brain-T1 were compared with those obtained from cns-T1, calculated between baseline and follow-up studies using a paired samples *t* test. The metrics derived (ICC, SSIM) were assessed separately for the 2 groups, HC and patients with MS. Differences in the SCA, GM, and WM fractions between HCs and patients with MS were assessed using a univariate ANOVA with age and sex as covariates and were considered significant at  $P < .05$ . A power analysis was also performed to assess the sample size needed for the SCA and GM and WM fractions with each sequence ( $\alpha = .05$ , power = 0.90). Finally, among the group of patients with MS, the association between the SCA and the Expanded Disability Status Scale (EDSS) was assessed through a nonparametric test (Spearman rank correlation). Statistical analysis was performed with the Statistical Package for Social Sciences (SPSS; IBM).

## RESULTS

Included patients with MS were mainly classified as having progressive MS (64% secondary-progressive, median EDSS = 5.0; range, 3–8.5; 12% primary-progressive, median EDSS = 3.5; range, 3–5.5), while only 24% had a recent diagnosis of relapsing-remitting MS (<1 year, median EDSS = 2.0; range, 1–3). A total of 11 cns-T1 acquisitions were discarded due to movement (8 in HCs, 3 in patients with MS). The segmentation of the SCA from the brain-T1 was not accurate in 5 HC. A representative section of the two 3D T1-weighted sequences can be seen in Fig 1. The acquisition time of the cns-T1 was in the same range as the acquisition time needed for the brain-T1, around 5 minutes. A standard clinical routine sagittal T1-weighted imaging of the spinal cord lasts around 4 minutes. Thus, acquiring the cns-T1 instead of the brain-T1 does not result in any additional acquisition time, and it saves the time needed for an additional spinal cord T1-weighted MR imaging (4 minutes). When cortical thickness measures were compared, 94% of the regions had excellent agreement in HCs and 80% in patients with MS (Online Supplemental Data). The regions that showed an  $\text{ICC} < 0.75$  are represented in



**FIG 1.** Representative sagittal section of the acquired 3D T1-weighted images, brain only (*upper image*) and brain plus spine (*lower image*).

Fig 2. Some of the regions that showed the largest disagreement were common for both groups, like the entorhinal, lateral orbito-frontal, and pericalcarine cortices.

Regarding the agreement in the volumetric measurements, it was excellent for GM, WM, thalamus, and total intracranial volume (Online Supplemental Data). The agreement between the PBVCs obtained from the 2 sequences was fair for the HC group and excellent for the MS group (Fig 3, Online Supplemental Data). The SSIM was significantly higher when comparing images acquired with the *cns-T1* and the *brain-T1* (Online Supplemental Data) for both HCs ( $t = -8.52$ ;  $P < .001$ ) and patients with MS ( $t = -8.33$ ;  $P < .001$ ). The Bland-Altman plot indicated that the mean value of the differences was very close to zero (0.14). Finally, the agreement in the SCA measures was good for HCs and excellent for patients with MS (Fig 3, Online Supplemental Data). When we compared the SCA, GM, WM, and thalamus fractions between HCs and patients with MS, they were significantly smaller in patients with MS ( $P < .003$  for all comparisons). The power analysis indicated that the sample size needed was higher for *cns-T1* when comparing brain-derived measures (GM fraction, 12 subjects per group for *brain-T1* versus 14 for *cns-T1*; WM fraction, 7 versus 12 subjects per group), while it was lower for the SCA (69 subjects per group for *brain-T1* versus 27 for *cns-T1*). The association between the SCA and the EDSS was significant and slightly weaker when assessed from *cns-T1* measures ( $\rho = -0.320$ ;  $P = .044$ ) than from *brain-T1* ( $\rho = -0.368$ ;  $P = .019$ ).

## DISCUSSION

This study assessed whether measures derived from *cns-T1* were equivalent to those obtained from a *brain-T1*. The agreement and reproducibility have been studied for cortical thickness, regional and total intracranial volumes, PBVC between the baseline and follow-up scans, and SCA. To our knowledge, this is the first study that addresses a numeric comparison. Recent studies have compared these 2 acquisitions in voxel-based studies through a Statistical Parametric Mapping (<http://www.fil.ion.ucl.ac.uk/spm/software/spm12>) approach.<sup>5,6</sup>

The agreement in the thickness measured in most of the cortical regions was very high, suggesting that the values obtained from *brain-T1* were very close to the ones obtained with *cns-T1*. This result was not the case for a few regions along the midline in the frontal and occipital lobes. The low agreement in the frontal regions can be explained because this area is more commonly affected by image artifacts due to the presence of the eyes, air-filled cavities, and the optic nerve, which may induce changes in susceptibility. Regarding the low agreement in the occipital lobe, the pericalcarine area is the region with the thinnest cortex; hence, small errors in segmentation may have a larger effect in the measured thickness. In general, it seems that the thickness measured in frontal regions is thinner when derived from *brain-T1* compared with *cns-T1*, while the opposite seems to be true in some regions of the occipital and the temporal cortices. One could argue that because the position of the center of the brain relative to the isocenter was not the same in the 2 acquisitions, the differences may be higher along the dorsal-ventral axis, but this does not seem to be the case here. The additional regions that showed a noticeable disagreement in patients with MS were located adjacent to the area of the eye as well as surrounding the quadrigeminal cistern along the central fissure. A possible explanation might be that the enlargement of the CSF compartment, which includes the quadrigeminal cistern, due to the brain atrophy affects image segmentation and could be a plausible explanation in MS. Another plausible explanation is susceptibility skull base bone artifacts, which may depend on the position regarding the isocenter.

The agreement on the global volumetric measures was very high, supporting again *brain-T1* acquisitions being replaced by *cns-T1*. As expected, patients with MS had lower volume fractions. Actually, the sample size needed to perform a study comparing GM and WM fractions was larger when using measures derived from *cns-T1* compared with *brain-T1*, though the differences were not that large.

Regarding the agreement on the estimated PBVC, it was, unexpectedly, very high for the group of patients with MS and low for HCs. One plausible reason could be that the expected PBVC in HCs is very low, and small differences in the values may have a larger effect on the calculated ICC. Another explanation could be that the sample size of the HCs was smaller compared with that in patients with MS, and the possible outliers may have a larger impact on the calculated ICCs. Regarding the equivalence of the compared images (baseline and follow-up) measured through the SSIM, although they were extremely high in both acquisitions, it was significantly higher for *cns-T1*. Usually, this comparison is performed with measures such as the SNR, though



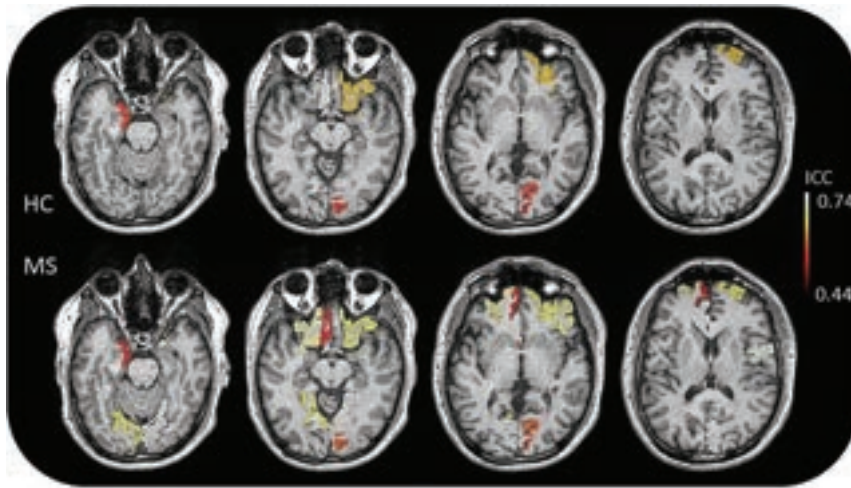


**FIG 2.** Cortical regions segmented with FastSurfer that showed the lowest agreement ( $ICC < 0.75$ ) in HCs (upper row) and patients with MS (lower row).

There are limitations in the proposed study. A single center was analyzed, and patients in an early stage of MS were not included. Thus, the differences between patients with MS in an early stage (relapsing-remitting) and those in a more advanced stage (progressive MS) could not be assessed in this study. The role of the spinal cord lesions in estimating the SCA was not assessed in this study and should be considered because it may be a confounding factor. The acquisition protocols were not identical in terms of TE and TR. Brain-T1 was optimized in-house, and *cns-T1* parameters were collected from the proposed multicenter study by Cohen-Adad et al.<sup>9</sup> The brain volumes were obtained using FastSurfer;

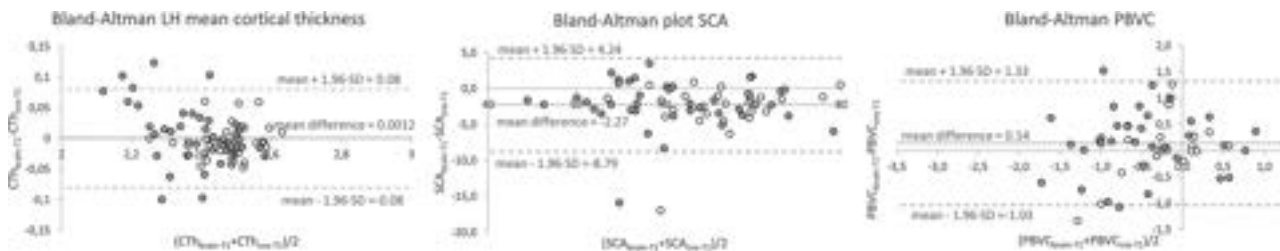


**FIG 3.** Bland-Altman plots for the mean cortical thickness in the left hemisphere, the SCA, and the PBVC. Empty symbols correspond to HCs; filled symbols correspond to patients with MS. CTh indicates cortical thickness; LH, left hemisphere;  $PBVC_{\text{brain-T1}}$ , PBVC derived from brain 3D T1-weighted images;  $PBVC_{\text{cns-T1}}$ , PBVC derived from brain-plus-spine 3D T1-weighted images.

the SSIM takes more factors into account than just the SNR or the contrast. The high SSIM obtained indicates that the 2 images compared to estimate the PBVC were almost identical and that the differences between the 2 acquisitions could not be attributed to this factor.

The agreement in the SCA measures obtained from brain-T1 and *cns-T1* in HCs was unexpectedly low. Segmentations were revised visually, and no artifacts could explain the difference found. Finally, because the size of the SCA is relatively small, small variances in the segmentation make an important difference in the measured area. When we compared the SCA between HCs and patients with MS, the sequence used really seemed to play a role because the sample size needed was more than double when using measures derived from brain-T1 compared with *cns-T1*. The association between the SCA and EDSS in patients with MS revealed by *cns-T1* and brain-T1 measures was highly equivalent.

The main advantage of replacing brain-T1 with *cns-T1* is that the spinal cord can be assessed without acquiring an additional sequence, which is fundamental for clinical routine. Furthermore, if adding an additional spinal cord sequence is not an option, structural information in this segment can be obtained using the proposed *cns-T1*, as recommended in the MAGNIMS-CMSC\_NAIMS consensus.<sup>17</sup>

the results obtained with other tools, such as Statistical Parametric Mapping, were not studied.

## CONCLUSIONS

Taken together, the findings suggest that a brain-T1 acquisition can be replaced by a *cns-T1* acquisition, which provides an enlarged view of the spinal cord with no extra MR imaging acquisition time. Patients with MS may benefit from this approach because a qualitative and quantitative assessment of both the brain and the spinal cord is important for diagnosis and monitoring disease progression and treatment response.

## ACKNOWLEDGMENTS

We thank all subjects participating in the study and the Fundació Esclerosi Múltiple.

Disclosure forms provided by the authors are available with the full text and PDF of this article at [www.ajnr.org](http://www.ajnr.org).

## REFERENCES

- Filippi M, Rocca MA, Ciccarelli O, et al. MRI criteria for the diagnosis of multiple sclerosis: MAGNIMS consensus guidelines. *Lancet Neurol* 2016;15:292–303 CrossRef Medline

2. Mike A, Glanz BI, Hildenbrand P, et al. **Identification and clinical impact of multiple sclerosis cortical lesions as assessed by routine 3T MR imaging.** *AJNR Am J Neuroradiol* 2011;32:515–21 CrossRef Medline
3. Nair G, Absinta M, Reich D. **Optimized T1-MPRAGE sequence for better visualization of spinal cord MS lesions at 3T.** *AJNR Am J Neuroradiol* 2013;34:2215–22 CrossRef Medline
4. Sastre-Garriga J, Pareto D, Battaglini M, et al; on behalf of the MAGNIMS study group. **MAGNIMS consensus recommendations on the use of brain and spinal cord atrophy measures in clinical practice.** *Nat Rev Neurol* 2020;16:171–82 CrossRef Medline
5. Azzarito M, Kyathanahally SP, Balbastre Y, et al. **Simultaneous voxel-wise analysis of brain and spinal cord morphometry and microstructure within the SPM framework.** *Hum Brain Mapp* 2021;42:220–32 CrossRef Medline
6. Freund P, Papinutto N, Bischof A, et al. **Simultaneous assessment of regional distributions of atrophy across the neuraxis in MS patients.** *Neuroimage Clin* 2022;34:102985 CrossRef Medline
7. Papinutto N, Bakshi R, Bischof A, et al; North American Imaging in Multiple Sclerosis Cooperative (NAIMS). **Gradient nonlinearity effects on upper cervical spinal cord area measurement from 3D T1-weighted brain MRI acquisitions.** *Magn Reson Med* 2018;79:1595–1601 CrossRef Medline
8. Lukas C, Bellenberg B, Prados F, et al. **Quantification of cervical cord cross-sectional area: which acquisition, vertebra level, and analysis software? A multicenter repeatability study on a traveling healthy volunteer.** *Front Neurol* 2021;12:693333 CrossRef Medline
9. Cohen-Adad J, Alonso-Ortiz E, Abramovic M, et al. **Generic acquisition protocol for quantitative MRI of the spinal cord.** *Nat Protoc* 2021;16:4611–32 CrossRef Medline
10. Henschel L, Conjeti S, Estrada S, et al. **FastSurfer: a fast and accurate deep learning based neuroimaging pipeline.** *Neuroimage* 2020;219:117012 CrossRef Medline
11. Desikan RS, Ségonne F, Fischl B, et al. **An automated labeling system for subdividing the human cerebral cortex on MRI scans into gyral based regions of interest.** *Neuroimage* 2006;31:968–80 CrossRef Medline
12. Azevedo CJ, Cen SY, Khadka S, et al. **Thalamic atrophy in multiple sclerosis: a magnetic resonance imaging marker of neurodegeneration throughout disease.** *Ann Neurol* 2018;83:223–34 CrossRef Medline
13. Smith SM, Zhang Y, Jenkinson M, et al. **Accurate, robust and automated longitudinal and cross-sectional brain change analysis.** *Neuroimage* 2002;17:479–89 CrossRef Medline
14. Wang Z, Bovik AC, Sheikh HR, et al. **Image quality assessment: from error visibility to structural similarity.** *IEEE Trans on Image Process* 2004;13:600–12 CrossRef Medline
15. De Leener B, Levy S, Dupont SM, et al. **SCT: Spinal Cord Toolbox, an open-source software for processing spinal cord MRI data.** *Neuroimage* 2017;145:24–43 CrossRef Medline
16. Cicchetti DV. **Guidelines, criteria, and rules of thumb for evaluating normed and standardized assessment instruments in psychology.** *Psychological Assessment* 1994;6:284–90 CrossRef
17. Wattjes MP, Ciccarelli O, Reich DS, et al. **2021 MAGNIMS-CMSC-NAIMS consensus recommendations on the use of MRI in patients with multiple sclerosis.** *Lancet Neurol* 2021;20:653–70 CrossRef Medline

# Higher Incidence of Unruptured Intracranial Aneurysms among Black and Hispanic Women on Screening MRA in Large Urban Populations

K. Javed, S. Ahmad, J. Qin, W. Mowrey, D. Kadaba, G. Liriano, A. Fortunel, R. Holland, D. Khatri, N. Haranhalli, and D. Altschul



## ABSTRACT

**BACKGROUND AND PURPOSE:** Intracranial aneurysms have a reported prevalence of 1%–2% in the general population. Currently, only patients with a strong family history or autosomal dominant polycystic kidney disease are screened for intracranial aneurysms using MRA. The purpose of this study was to determine whether there are other specific patient populations at risk that should be offered screening for intracranial aneurysms.

**MATERIALS AND METHODS:** This is a retrospective case-control study of adult patients who underwent a screening MRA of their brain at our comprehensive stroke center from 2011 to 2020. Patients with a history of a known brain aneurysm were excluded. Data were extracted on patient demographics and medical comorbidities. Bivariate analyses were performed, followed by multivariable logistic regression, to identify factors associated with a positive MRA screen for incidental aneurysms.

**RESULTS:** Of 24,397 patients eligible for this study, 2084 screened positive for a possible intracranial aneurysm. On bivariate analysis, significant differences were present in the following categories: age, sex, race and ethnicity, chronic constipation, and hyperlipidemia. On logistic regression analysis, older age (+10 years: OR = 10.01; 95% CI, 10.01–10.02;  $P = .001$ ), female sex (OR = 1.37; 95% CI, 1.24–1.51;  $P = .001$ ), non-Hispanic Black (OR = 1.19; 95% CI, 1.02–1.40;  $P = .031$ ), and Hispanic ethnicity (OR = 1.35; 95% CI, 1.16–1.58;  $P = .001$ ) versus non-Hispanic White remained significant when adjusted for other factors.

**CONCLUSIONS:** Targeted screening for high-risk elderly women of Black or Hispanic descent will yield higher positive findings for brain aneurysms, which may mitigate the risk of rupture. Whether this is a cost-effective approach has yet to be determined.

**ABBREVIATIONS:** ADPKD = autosomal dominant polycystic kidney disease; ICD = International Classification of Diseases

Intracranial aneurysms have a prevalence of 1%–2% in the general population.<sup>1</sup> Most intracranial aneurysms are saccular, a common feature in ruptured aneurysms. Intracranial aneurysms are typically diagnosed in middle-aged or elderly patients. They tend to be asymptomatic, but large aneurysms (>7 mm) may cause symptoms such as headaches, visual disturbances, and cranial nerve palsies due to mass effect.<sup>2</sup> In the event that an intracranial aneurysm ruptures, it causes an SAH, which has disastrous consequences; 30%–50% of patients who experience an SAH die or become permanently disabled.<sup>3</sup> Because most aneurysms are diagnosed as incidental findings on radiographic


imaging, patients may not know that they have an intracranial aneurysm until a serious adverse event occurs. Thus, screening patients at high risk for brain aneurysm formation may offer a protective benefit.

While many studies have been conducted to identify appropriate management strategies for previously diagnosed aneurysms and risk factors predictive of rupture, few studies have addressed the question of which patient populations are at risk of having an undiagnosed intracranial aneurysm.<sup>4,5</sup> As per the American Heart Association guidelines, there are currently only 2 indications for which patients are offered a screening test in the form of a noninvasive MRA scan of the head.<sup>6</sup> Asymptomatic individuals with  $\geq 2$  affected first-degree relatives are offered this test, along with patients with autosomal dominant polycystic kidney disease (ADPKD), due to studies that show these patient populations have a higher incidence of brain aneurysms.<sup>7,8</sup> However, it is imperative to understand which other factors are associated with aneurysm formation for early detection, thus allowing early intervention. To that end, as a first step, we undertook a task to build and analyze a rich 10-year data set at our institution. We defined a

Received September 16, 2022; accepted after revision March 27, 2023.

From the Departments of Neurological Surgery (K.J., S.A., D.K., G.L., A.F., R.H., D.K., N.H., D.A.) and Epidemiology & Population Health (J.Q., W.M.), Montefiore Medical Center, Bronx, New York.

Please address correspondence to David Altschul, MD, Department of Neurological Surgery, Montefiore Medical Center, 3316 Rochambeau Ave, Bronx, NY 10467-2841; e-mail: daltschu@montefiore.org; @DavidAltschulMD

 Indicates article with online supplemental data.

<http://dx.doi.org/10.3174/ajnr.A7856>

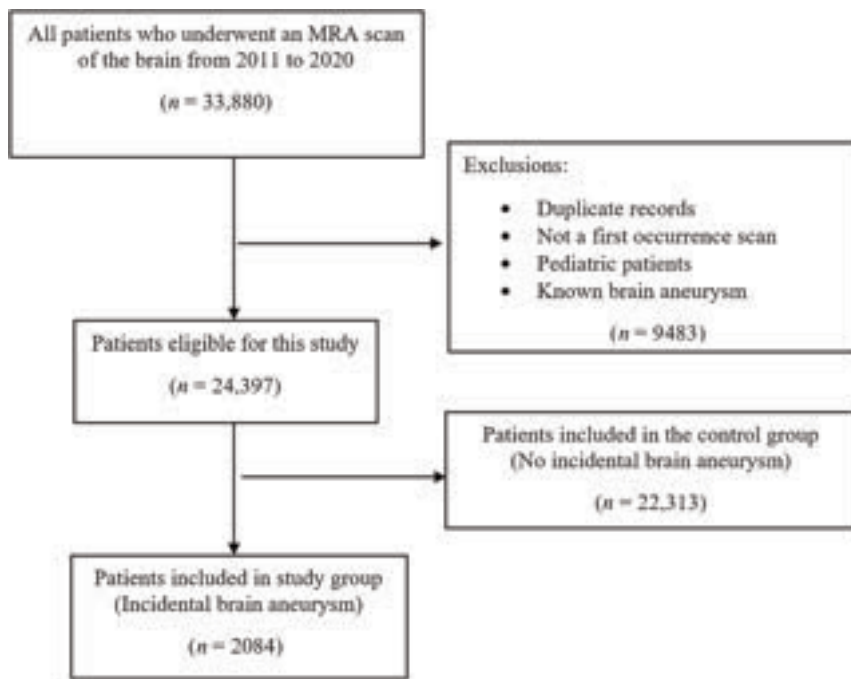


**FIGURE.** Flowchart depicting the cases that were included in our analysis.

sample of patients who were free of aneurysms and underwent MRA for unrelated reasons and then screened positive for a possible intracranial aneurysm. The primary objective of our study was to determine whether there were other patient populations with certain sociodemographic factors or medical comorbidities who should also be offered MRA screening for intracranial aneurysms. Our hypotheses are that patients diagnosed with long-standing hypertension, female sex, and patients with a smoking history are at increased risk for aneurysm formation because hypertension and smoking are known risk factors for aneurysm growth and rupture.<sup>9</sup>

## MATERIALS AND METHODS

### Research Ethics

Approval was obtained from the Albert Einstein College of Medicine/Montefiore Medical Center Institutional Review Board for this study (#2021-13019).

### Patient Sample

This study is a retrospective cohort study. All adult patients (18 years of age and older) who underwent an MRA of the head at a single institution during a 10-year period from 2011 to 2020 were considered for potential enrollment. Patients who had a known history of an intracranial aneurysm that was being followed with routine imaging or patients who presented with an SAH due to aneurysm rupture were excluded. Only patients who were undergoing a screening MRA of the brain for an unrelated reason such as ischemic stroke, head trauma, and headache/dizziness were included. Institutional review board approval was obtained, but individual patient consent was waived, given the minimal risk posed by the study.

### Data Extraction

The following steps were performed to collect data: First, a specialized software program known as mPower (Nuance; <https://www.nuance.com>) was used to identify all patients who underwent an MRA of the head, with or without contrast, at our hospital from 2011 to 2020. These data, including patient medical record number, date of the scan, and official MRA report, were extracted into an Excel file (Microsoft). A search was performed for duplicates, and duplicate entries were removed. If any patient had multiple MRA scans of the head, only the first index scan was included. Patients with known aneurysms undergoing surveillance MRA imaging were excluded from the study because the intention was to determine the incidence of asymptomatic unruptured brain aneurysms. All MRAs were TOF-MRA performed on either 1.5T or 3T machines. The official MRA report, which was read by an independent,

blinded, experienced attending neuroradiologist at the time, was used to determine who had an incidental aneurysm. The MRA report text was searched for the following terms: focal aneurysm, small aneurysm, incidental aneurysm, large aneurysm, likely aneurysm, possible aneurysm, potential aneurysm, presumed aneurysm, probable aneurysm, segmental aneurysm, supraclinoid aneurysm, and suspected aneurysm. All cases that contained any of the aforementioned search terms were transferred to a clean file as the possible case group. All cases whose MRA report had no mention of aneurysms were kept separate as the control group.

All patients in the case group were manually reviewed by the research team. Any patient whose clinical indication for the MRA head scan was to follow-up on a known brain aneurysm was excluded. Any patient who presented with a SAH due to a ruptured aneurysm was excluded. Any patient who had an extradural aneurysm was excluded. Patients who had flow-related aneurysms associated with vascular malformations, possible mycotic aneurysms in the setting of endocarditis, and possible pseudoaneurysms after traumatic injury were excluded. Possible intracranial aneurysms of different sizes, including 1–2 mm, and different types, saccular versus fusiform, were included. If the neuroradiologist's read was unclear as to whether the observed structure was an aneurysm or an infundibulum, the case was included in the study group due to the inability to definitively rule out an intracranial aneurysm. If patients had a strong family history or known ADPKD and were found to have an incidental aneurysm, they were included in the study group (Figure).

For patients in both the study and control groups, data were extracted on sociodemographic factors (age, sex, race and ethnicity), medical comorbidities (hypertension, hyperlipidemia, chronic constipation, and any type of renal disease including ADPKD), and social histories (smoking history, alcohol and



cocaine use). These data were extracted from the Oracle Database called Enterprise Data Warehouse, which is affiliated with the Epic health system, using International Classification of Diseases (ICD) codes. For scans before 2016, ICD-9 codes were used, and for scans in 2016 or after, ICD-10 codes were used. In addition, for each of the previously mentioned independent variables, a number of ICD codes exist. For example, for hypertension, there are ICD codes for essential hypertension, secondary hypertension, renovascular hypertension, and so forth. All of the pertinent ICD codes for each variable were reviewed, and the presence of any of those ICD codes in the patient's chart meant that the patient had that demographic factor or medical comorbidity. For example, the variable hypertension and hyperlipidemia means that the patient was diagnosed with any type of hypertension or hyperlipidemia. Constipation refers to chronic constipation diagnosed at any time in their lives. Renal disease refers to all types of renal disease except ADPKD, which is a separate variable. Alcohol and smoking history refer to any remote history of alcohol or cigarette use. For cocaine use specifically, patients had a history of cocaine use or had a positive urine toxicology result around the date of their MRA scan.

### Statistical Analysis

Patients with incidental intracranial aneurysms in the case group were compared with patients in the control group without intracranial aneurysms on an MRA head scan. Bivariate analyses were performed to examine differences in demographic factors and medical comorbidities. Categorical variables were compared using the Pearson  $\chi^2$  test or Fisher exact test. Continuous variables were compared using Wilcoxon rank-sum tests. All variables that were evaluated on bivariate analysis were then included in the multiple logistic regression model to identify independent predictors of incidental intracranial aneurysms on screening MRA. ORs

**Table 1: Multiple logistic regression model for incidental brain aneurysm on screening MRA**

Independent Predictor	OR	95% CI	P Value
Female sex	1.370	1.240–1.510	<.001
Age	1.010	1.010–1.020	<.001
Non-Hispanic Black	1.190	1.020–1.400	.031
Hispanic	1.350	1.160–1.580	<.001
Other race	1.180	0.980–1.410	.076
Unknown race	1.260	0.930–1.690	.134
Constipation	1.003	0.890–1.130	.956
Renal disease	1.030	0.920–1.140	.612
ADPKD	0.930	0.370–2.340	.883
HTN	1.050	0.930–1.190	.416
Hyperlipidemia	0.970	0.870–1.080	.590
Cocaine use	1.010	0.700–1.450	.954
Alcohol use	1.070	0.820–1.390	.602

Note:—HTN indicates hypertension.

**Table 2: Multiple logistic regression model for incidental brain aneurysm on screening MRA, comparing specific racial and ethnic minorities, sexes, and known risk factors**

Characteristic	OR	95% CI	P Value
Non-His Black woman vs Non-His White man	1.63	1.358–1.956	<.001
Hispanic woman vs Non-His White man	1.851	1.545–2.217	<.001
Non-His Black female smoker with HTN vs Non-His White man without smoking or HTN	1.879	1.478–2.388	<.001
Hispanic female smoker with HTN vs Non-His White man without smoking or HTN	2.134	1.675–2.717	<.001

Note:—Non-His indicates non-Hispanic; HTN, hypertension.

were calculated for specific racial and ethnic groups and sexes to determine which patient was at highest risk of screening positive for a brain aneurysm. All analyses were conducted using R 4.1.2 statistical and computing software (<http://www.r-project.org/>).<sup>10</sup> Statistical significance was set as  $P < .05$ , and all tests were 2-sided.

### RESULTS

A total of 24,397 patients were enrolled in our study. Of them, 2084 patients were found to have an incidental brain aneurysm on MRA, while 22,313 patients did not. This means the incidence of brain aneurysms in our patient population was 0.85% per year. On bivariate analysis (Online Supplemental Data), 67.1% of patients with an incidental brain aneurysm were women compared with 60.3% of patients in the control group ( $P < .001$ ). The mean age of patients with incidental aneurysms was 64 years compared with 60 years in the control group ( $P < .001$ ). A larger percentage of Hispanic patients were found to have an incidental aneurysm than non-Hispanic patients (38.6% versus 35.6%,  $P = .007$ ); 72.1% of patients with incidental aneurysms had a diagnosis of hypertension compared with 66.5% ( $P < .001$ ); 49.9% of patients with incidental aneurysms had hyperlipidemia compared with 45.4% ( $P < .001$ ); and 17.9% of patients had chronic constipation compared with 16.0% ( $P = .023$ ). No statistically significant differences were observed in renal disease or ADPKD. No statistically significant differences were found in alcohol or cocaine use, though there was a trend of difference in smoking history (22.3% versus 20.6%,  $P = .076$ ).

On multiple logistic regression analysis (Table 1), the following variables were found to be independent predictors of incidental aneurysms on MRA: female sex (OR = 1.37; 95% CI, 1.24–1.51;  $P < .001$ ), increasing age (+1 year: OR = 1.01; 95% CI, 1.01–1.02;  $P < .001$ ), Hispanic ethnicity (OR = 1.35; 95% CI, 1.16–1.58;  $P < .001$ ), and Non-Hispanic Black race (OR = 1.19; 95% CI, 1.02–1.40;  $P = .031$ ).

In Table 2, ORs were estimated for specific groups on the basis of race and ethnicity, sex, and known risk factors. Black women had higher odds of having an incidental brain aneurysm compared with White men (OR = 1.63; 95% CI, 1.36–1.96;  $P < .001$ ) and so did Hispanic women (OR = 1.85; 95% CI, 1.55–2.22;  $P < .001$ ). Moreover, Black female smokers with hypertension had higher odds of incidental aneurysms than White men without vascular risk factors (OR = 1.88; 95% CI, 1.48–2.39;  $P < .001$ ); this risk was also true for Hispanic female smokers with hypertension (OR = 2.13; 95% CI, 1.68–2.72;  $P < .001$ ).

### DISCUSSION

The incidence of screening positive for brain aneurysms in our patient population was 0.85% per year. The incidence of

screening positive for brain aneurysms in Black and Hispanic female patients specifically was higher, 0.95% per year. Additionally, Black and Hispanic women had higher odds of screening positive for an incidental brain aneurysm compared with their White male counterparts, and the odds were even higher in Black or Hispanic women with hypertension or a smoking history. These numbers are slightly lower than previously reported expected rates; however, all patients with known aneurysms were excluded in this study.

Our results are consistent with what has previously been published in the literature. Intracranial aneurysms are typically diagnosed in older individuals and have long been considered a disease of aging.<sup>11,12</sup> Increasing age has been shown to be a risk factor for both aneurysm growth and aneurysm rupture. While age is a risk factor for aneurysm formation, increasing age is inversely proportional to the risk of rupture as life expectancy decreases. Similarly, female sex is a previously identified risk factor for multiple intracranial aneurysms.<sup>13</sup> The cause behind sex-based differences seen in aneurysm growth and rupture risk is not fully understood. However, a possible explanation takes into account the differences in sex hormones.<sup>14,15</sup> Older women are thought to be at an increased risk of aneurysms due to decreased estrogen levels after menopause, because estrogen has been linked to reduced aneurysm incidence in mouse models.

Our results suggest racial differences in intracranial aneurysm incidence. There are certain populations, such as certain Asian and European groups, that are reported to have a higher incidence of intracranial aneurysms.<sup>16</sup> This finding has not previously been reported for Hispanic and non-Hispanic Black populations per se. However, there are studies that report that Hispanics and non-Hispanic Black individuals present with SAH due to a ruptured aneurysm more often, while White patients have higher rates of unruptured intracranial aneurysms.<sup>17,18</sup> This phenomenon has always been explained by existing health disparities and barriers in access to health care. Black and Hispanic individuals are less likely to be diagnosed with unruptured intracranial aneurysms and are less likely to be monitored or electively treated, leading to a greater percentage of these patients presenting with a ruptured, aneurysmal SAH. However, our results suggest that perhaps these patient populations have a higher incidence of intracranial aneurysm formation as well. This increased incidence might explain why there has been an observation of increased likelihood to present with rupture.

Two established risk factors for aneurysm growth and rupture are hypertension and smoking history. Our hypothesis was that there would be a higher rate of incidental brain aneurysms in patients with these risk factors. However, they were not found to be independent predictors of incidental brain aneurysms in our study. Given the large body of evidence, our results do not negate them as important risk factors for aneurysm formation, growth, and rupture; rather, there is likely a reason why they did not reach statistical significance in our analysis. Perhaps it is because our data are not granular enough. For example, in regard to our hypertension variable, patients who were diagnosed with any type of hypertension, including newly diagnosed essential hypertension, long-standing chronic hypertension, acute hypertensive emergency, and secondary renovascular hypertension, were

included. However, while some studies have shown that a diagnosis of hypertension is associated with an increased risk of aneurysm destabilization and rupture,<sup>19</sup> other studies have specifically identified acute changes in blood pressure, such as those seen during hypertensive emergency and preeclampsia, as risk factors for rupture.<sup>20</sup>

It is possible that acute changes in blood pressure lead to aneurysm formation as well. Moreover, in a study by Sundström et al<sup>21</sup> that aimed to evaluate risk factors for aneurysm rupture, patients' blood pressure readings were obtained at the time of enrollment. Patients who had persistently elevated blood pressure, suggesting that their hypertension was untreated or not adequately controlled on their current treatment regimen, were found to be at increased risk for SAH, suggesting that persistently elevated blood pressure or untreated chronic hypertension may play a greater role in contributing to aneurysm development and rupture. The role of secondary hypertension in aneurysm pathology is still being explored.<sup>22</sup> Our data set in its current form does not make these distinctions; thus, hypertension reached statistical significance on unadjusted analysis only. Similarly, smoking history is a well-documented risk factor for aneurysm growth and rupture due to its ability to cause vascular endothelium dysfunction and incite an inflammatory response. However, current smokers, as opposed to patients with any smoking history, have higher rates of intracranial aneurysms and present with SAH in larger numbers.<sup>21,23</sup> However, we tested for associations between aneurysm incidence and any remote history of smoking that only reached borderline significance on bivariate analysis. This finding could suggest that smoking has a variable effect on aneurysm formation in relation to other factors such as age, hypertension, race, sex, and ethnicity.

One-time evidence-based screening is recommended for patients with ADPKD, especially those with high-risk features such as a known family history of brain aneurysms.<sup>24</sup> This recommendation is because the prevalence of brain aneurysms in patients with ADPKD is much higher than in the general population, with reports as high as 10%.<sup>25</sup> ADPKD was not found to be significantly associated with incidental aneurysm findings on MRA in our analysis, likely because the number of patients with ADPKD in our study was very small. Of 24,397 patients, only 60 patients had ADPKD, and only 5 of them had incidental brain aneurysms. A much larger subset of patients with ADPKD would be needed to find a statistically significant association.

Hyperlipidemia was another variable that was tested for associations with incidental aneurysms in our analysis. We defined hyperlipidemia in general terms to include both hypertriglyceridemia and hypercholesterolemia. While hyperlipidemia has been linked to abdominal aortic aneurysms, the association between hyperlipidemia and intracranial aneurysms has not been well-studied.<sup>26</sup> Our results suggest that any association between hyperlipidemia and intracranial aneurysms is likely confounded by race, age, or another variable.

Last, chronic constipation was another variable that we considered for possible association with intracranial aneurysm. It has long been theorized that patients with chronic constipation who strain to defecate may have a higher incidence of

intracranial aneurysms because straining can cause a sudden increase in pressure in the arterial wall, leading to breakdown and aneurysm formation. However, constipation was not found to be an independent predictor of incidental brain aneurysm.

One weakness of our study is that we did not assess how many patients in our case group were diagnosed with intracranial aneurysms using DSA. Another weakness is that we evaluated only variables that are known to be possible risk factors for aneurysm formation and growth as mentioned in the literature. One variable that was not assessed was a strong family history of brain aneurysms. However, this is not a variable that can be extracted from the electronic medical record as an ICD code. Additionally, there is an increased level of granularity to some of the independent variables that could be further evaluated. For example, we can investigate different types of hypertension. The ICD codes were intentionally combined into larger groups to assess overarching trends in our analysis. Last, the data-extraction process needs to be verified. All of the reports that were positive for incidental aneurysm were manually reviewed by the research team, but the control group was not due to its large sample size. However, the manual review process for the case group confirmed that our automatic search achieved an accuracy of >85%. Another potential concern is that patients who undergo MRA have a different risk of having an aneurysm than patients who do not undergo MRA. Thus, cross-sectional population studies are integral to further answer this question. However, there was no significant difference in the indication for obtaining the MRA between the aneurysm and no-aneurysm cohort. Therefore, at least in patients with symptoms that prompt vascular imaging, there appear to be specific high-risk groups with a higher likelihood of an incidental unruptured aneurysm being discovered.

## CONCLUSIONS

Our study is the first of its kind to demonstrate that Hispanic ethnicity and Black race in addition to increasing age and female sex are independent predictors of incidental intracranial aneurysms. Targeted screening for high-risk elderly women of Black or Hispanic descent will likely yield higher positive findings. Currently, a strong family history and known ADPKD are the only 2 indications for which asymptomatic individuals are screened for intracranial aneurysms. However, because these patients are historically less likely to be evaluated for unruptured intracranial aneurysms and are more likely to present with ruptured aneurysms that are associated with significant morbidity, it may be reasonable to broaden the preventative screening MRA of Black and Hispanic women after 60 years of age, especially in smokers and women with long-standing hypertension. Future analysis determining whether this approach is cost-effective is still necessary.

Disclosure forms provided by the authors are available with the full text and PDF of this article at [www.ajnr.org](http://www.ajnr.org).

## REFERENCES

1. Brown RD, Broderick JP. **Unruptured intracranial aneurysms: epidemiology, natural history, management options, and familial screening.** *Lancet Neurol* 2014;13:393–404 CrossRef Medline
2. Keedy A. **An overview of intracranial aneurysms.** *Mcgill J Med* 2006;9:141–46 Medline
3. Nieuwkamp DJ, Setz LE, Algra A, et al. **Changes in case fatality of aneurysmal subarachnoid haemorrhage over time, according to age, sex, and region: a meta-analysis.** *Lancet Neurol* 2009;8:635–42 CrossRef Medline
4. Etminan N, de Sousa DA, Tiseo C, et al. **European Stroke Organisation (ESO) guidelines on management of unruptured intracranial aneurysms.** *Eur Stroke J* 2022;7:V CrossRef Medline
5. Morel S, Hostettler IC, Spinner GR, et al; The neurIST Project. **Intracranial aneurysm classifier using phenotypic factors: an international pooled analysis.** *J Pers Med* 2022;12:1410 CrossRef Medline
6. Thompson BG, Brown RD, Amin-Hanjani S, et al; American Stroke Association. **Guidelines for the management of patients with unruptured intracranial aneurysms.** *Stroke* 2015;46:2368–400 CrossRef Medline
7. Chalouhi N, Chitale R, Jabbour P, et al. **The case for family screening for intracranial aneurysms.** *Neurosurg Focus* 2011;31:E8 CrossRef Medline
8. Sanchis IM, Shukoor S, Irazabal MV, et al. **Presymptomatic screening for intracranial aneurysms in patients with autosomal dominant polycystic kidney disease.** *Clin J Am Soc Nephrol* 2019;14:1151–60 CrossRef Medline
9. Backes D, Rinkel GJ, Laban KG, et al. **Patient- and aneurysm-specific risk factors for intracranial aneurysm growth.** *Stroke* 2016;47:951–57 CrossRef Medline
10. R Core Team. **The R Project for Statistical Computing.** R Foundation for Statistical Computing. <https://www.R-project.org>. Accessed June 29, 2022
11. Brinjikji W, Zhu YQ, Lanzino G, et al. **Risk factors for growth of intracranial aneurysms: a systematic review and meta-analysis.** *AJNR Am J Neuroradiol* 2016;37:615–20 CrossRef Medline
12. Greving JP, Wermer MJ, Brown RD, et al. **Development of the PHASES score for prediction of risk of rupture of intracranial aneurysms: a pooled analysis of six prospective cohort studies.** *Lancet Neurol* 2014;13:59–66 CrossRef Medline
13. Rosi Junior J, Gomes dos Santos A, da Silva SA, et al. **Multiple and mirror intracranial aneurysms: study of prevalence and associated risk factors.** *Br J Neurosurg* 2021;35:780–84 CrossRef Medline
14. Fuentes AM, Stone McGuire L, Amin-Hanjani S. **Sex differences in cerebral aneurysms and subarachnoid hemorrhage.** *Stroke* 2022;53:624–33 CrossRef Medline
15. Zuurbier CC, Molenberg R, Mensing LA, et al. **Sex difference and rupture rate of intracranial aneurysms: an individual patient data meta-analysis.** *Stroke* 2022;53:362–69 CrossRef Medline
16. Garcia RM, Yoon S, Potts MB, et al. **Investigating the role of ethnicity and race in patients undergoing treatment for intracerebral aneurysms between 2008 and 2013 from a national database.** *World Neurosurg* 2016;96:230–36 CrossRef Medline
17. Rinaldo L, Rabinstein AA, Cloft HJ, et al. **Racial and economic disparities in the access to treatment of unruptured intracranial aneurysms are persistent problems.** *J Neurointerv Surg* 2019;11:833–36 CrossRef Medline
18. Brinjikji W, Rabinstein AA, Lanzino G, et al. **Racial and ethnic disparities in the treatment of unruptured intracranial aneurysms.** *Stroke* 2012;43:3200–06 CrossRef Medline
19. Karhunen V, Bakker MK, Ruigrok YM, et al. **Modifiable risk factors for intracranial aneurysm and aneurysmal subarachnoid hemorrhage: a Mendelian randomization study.** *J Am Heart Assoc* 2021;10:e022277 CrossRef Medline
20. Kotikoski S, Kurtelius A, Nurmonen HJ, et al. **Pre-eclampsia, gestational diabetes and hypertensive disorders in patients with intracranial aneurysms: a case-control study.** *Eur J Neurol* 2022;29:199–207 CrossRef Medline
21. Sundström J, Söderholm M, Söderberg S, et al. **Risk factors for subarachnoid haemorrhage: a nationwide cohort of 950 000 adults.** *Int J Epidemiol* 2019;48:2018–25 CrossRef Medline

22. Kotikoski S, Huttunen J, Huttunen TJ, et al. **Secondary hypertension in patients with saccular intracranial aneurysm disease: a population-based study.** *PLoS One* 2018;13:e0206432 CrossRef Medline
23. Feigin VL, Rinkel GJ, Lawes CM, et al. **Risk factors for subarachnoid hemorrhage.** *Stroke* 2005;36:2773–80 CrossRef Medline
24. Rinkel GJ, Ruigrok YM. **Preventive screening for intracranial aneurysms.** *Int J Stroke* 2022;17:30–36 CrossRef Medline
25. Zhou Z, Xu Y, Delcourt C, et al. **Is regular screening for intracranial aneurysm necessary in patients with autosomal dominant polycystic kidney disease? A systematic review and meta-analysis.** *Cerebrovasc Dis* 2017;44:75–82 CrossRef Medline
26. Chen Y, Huang M, Xuan Y, et al. **Association between lipid levels and risk for different types of aneurysms: a Mendelian randomization study.** *J PersMed* 2021;11:1171 CrossRef Medline



## Prevalence of Intracranial Aneurysms with Emphasis on Ethnicity and Race

The prevalence of unruptured intracranial aneurysms reaches as high as 3% in the general population.<sup>1-3</sup> As the use of cross-sectional imaging modalities such as CT and MR imaging expands in clinical practice, the detection of intracranial aneurysms has become increasingly more frequent.<sup>3</sup> Moreover, the integration of artificial intelligence tools has improved not only the detection of intracranial aneurysms but also the evaluation of these aneurysms.<sup>4</sup>

Given the risk of rupture and the subsequent devastating consequences on both patient well-being and health care economics, a multitude of studies have attempted to elucidate the natural history of intracranial aneurysms through retrospective analysis and prospective approaches. Those studies aimed to support more informed clinical decision-making. Concurrently, numerous studies have been conducted to identify risk factors that may contribute to the prevalence of intracranial aneurysms and the likelihood of their rupture. Identifying these risk factors could pave the way for targeted screening programs for populations exhibiting these characteristics. Such programs are already debated in the literature.<sup>5-7</sup> The main factors taken into account are a family history of SAH (including the number of affected first-degree relatives), autosomal dominant polycystic disease, age, and various other comorbidities. However, because these risk factors account for only a small percentage of all patients with aneurysmal SAH, there is a need for further research to identify additional high-risk groups. The article by Javed et al,<sup>8</sup> published in the current issue of the *American Journal of Neuroradiology*, represents an effort to identify other specific patient populations at risk for intracranial aneurysm.

The study examined adult patients who underwent screening MRA at a comprehensive stroke center between 2011 and 2020. An analysis of approximately 25,000 patients was conducted following exclusion of patients with known brain aneurysms.

Of 24,397 eligible patients, 2084 screened positive for possible intracranial aneurysms. Bivariate analysis showed significant differences in age, sex, race and ethnicity, chronic constipation, and hyperlipidemia. Logistic regression analysis found that older age, female sex, non-Hispanic Black, and Hispanic ethnicity were significant factors. Targeted screening for high-risk elderly women

of Black or Hispanic descent may yield higher positive findings for brain aneurysms, potentially reducing the risk of rupture. This approach remains uncertain in terms of its cost-effectiveness, suggesting the need for further studies in the future.

A minor criticism of the present work<sup>8</sup> was the data-extraction process: Only positive reports were manually reviewed, while the control group reports were not, owing to the large sample size. A more comprehensive review of these reports could potentially be achieved using natural language-processing tools, and future research may explore the use of such tools to improve the overall robustness of the analysis. Moreover, positive cases were not re-evaluated by a neuroradiologist; instead, only the reports were used, and the data extracted from these positive reports did not encompass aneurysm-specific information, such as size, type, and other relevant characteristics. A subsequent study should delve deeper into these data to assess not only the presence of aneurysms but also the potential risk of rupture.

Despite the aforementioned critiques, some of which the authors acknowledge, the current study<sup>8</sup> is the first to examine the incidence of unruptured intracranial aneurysms among Hispanic and non-Hispanic Black populations. Past research has indicated that Hispanics and non-Hispanic Blacks are more likely to experience SAH from ruptured aneurysms, while White patients exhibit higher rates of unruptured intracranial aneurysms. This outcome is often linked to existing health disparities and barriers to health care access, leading to a larger proportion of these patients presenting with ruptured aneurysmal SAH. The novel findings provided by this study suggest that these patient populations may have a higher incidence of intracranial aneurysms. The use of an exceptionally large cohort further enhances the robustness of the findings.

Finally, the findings presented by Javed et al<sup>8</sup> have the potential to not only impact individual lives but also to shape and inform health policy strategies and contribute to decision-making processes in the broader healthcare landscape.

### REFERENCES

1. Śliwczyński A, Jewczak M, Dorobek M, et al. An analysis of the incidence and cost of intracranial aneurysm and subarachnoid

- haemorrhage treatment between 2013 and 2021.** *Int J Environ Res Public Health* 2023;20:3828 CrossRef Medline
2. Vlak MH, Algra A, Brandenburg R, et al. **Prevalence of unruptured intracranial aneurysms, with emphasis on sex, age, comorbidity, country, and time period: a systematic review and meta-analysis.** *Lancet Neurol* 2011;10:626–36 CrossRef Medline
  3. Brown RD, Broderick JP. **Unruptured intracranial aneurysms: Epidemiology, natural history, management options, and familial screening.** *Lancet Neurol* 2014;13:393–404 CrossRef Medline
  4. Alwalid O, Long X, Xie M, et al. **Artificial intelligence applications in intracranial aneurysm: achievements, challenges and opportunities.** *Acad Radiol* 2022;29:S201–14 CrossRef Medline
  5. Kim B. **Unruptured intracranial aneurysm: screening, prevalence and risk factors.** *Neurointervention* 2021;16:201–203 CrossRef
  6. Van Hoe W, van Loon J, Demeestere J, et al. **Screening for intracranial aneurysms in individuals with a positive first-degree family history: a systematic review.** *World Neurosurg* 2021;151:235–48.e5 CrossRef Medline
  7. Rinkel GJ, Ruigrok YM. **Preventive screening for intracranial aneurysms.** *Int J Stroke* 2022;17:30–36 CrossRef Medline
  8. Javed K, Ahmad S, Qin J, et al. **Higher incidence of unruptured intracranial aneurysms: a among Black and Hispanic women on screening MRA in large urban populations.** *AJNR Am J Neuroradiol* 2023;44:574–79 CrossRef

 **G. Ben-Arie**

Diagnostic Imaging Institute  
Soroka University Medical Center  
Beer-Sheva, Israel

<http://dx.doi.org/10.3174/ajnr.A7869>

# Intensive Blood Pressure Management Preserves Functional Connectivity in Patients with Hypertension from the Systolic Blood Pressure Intervention Randomized Trial

C. Shah, D. Srinivasan, G. Erus, M. Kurella Tamura, M. Habes, J.A. Detre, W.E. Haley, A.J. Lerner, C.B. Wright, J.T. Wright, Jr., S. Oparil, S.B. Kritchevsky, H.A. Punzi, A. Rastogi, R. Malhotra, C.H. Still, J.D. Williamson, R.N. Bryan, Y. Fan, and I.M. Nasrallah



## ABSTRACT

**BACKGROUND AND PURPOSE:** The Systolic Blood Pressure Intervention (SPRINT) randomized trial demonstrated that intensive blood pressure management resulted in slower progression of cerebral white matter hyperintensities, compared with standard therapy. We assessed longitudinal changes in brain functional connectivity to determine whether intensive treatment results in less decline in functional connectivity and how changes in brain functional connectivity relate to changes in brain structure.

**MATERIALS AND METHODS:** Five hundred forty-eight participants completed longitudinal brain MR imaging, including resting-state fMRI, during a median follow-up of 3.84 years. Functional brain networks were identified using independent component analysis, and a mean connectivity score was calculated for each network. Longitudinal changes in mean connectivity score were compared between treatment groups using a 2-sample *t* test, followed by a voxelwise *t* test. In the full cohort, adjusted linear regression analysis was performed between changes in the mean connectivity score and changes in structural MR imaging metrics.

**RESULTS:** Four hundred six participants had longitudinal imaging that passed quality control. The auditory-salience-language network demonstrated a significantly larger decline in the mean connectivity score in the standard treatment group relative to the intensive treatment group ( $P = .014$ ), with regions of significant difference between treatment groups in the cingulate and right temporal/insular regions. There was no treatment group difference in other networks. Longitudinal changes in mean connectivity score of the default mode network but not the auditory-salience-language network demonstrated a significant correlation with longitudinal changes in white matter hyperintensities ( $P = .013$ ).

**CONCLUSIONS:** Intensive treatment was associated with preservation of functional connectivity of the auditory-salience-language network, while mean network connectivity in other networks was not significantly different between intensive and standard therapy. A longitudinal increase in the white matter hyperintensity burden is associated with a decline in mean connectivity of the default mode network.

**ABBREVIATIONS:** ASLN = auditory-salience-language network; BOLD = blood oxygen level–dependent; DMN = default mode network; FC = functional connectivity; MCS = mean connectivity score; rs-fMRI = resting-state fMRI; rTBV = relative total brain volume; SBP = systolic blood pressure; TBV = total brain volume; WMH = white matter hyperintensities

Hypertension is one of the most prevalent diseases and is associated with significant cardiovascular and cerebrovascular complications, including stroke and dementia.<sup>1,2</sup> The Systolic

Blood Pressure Intervention Trial (SPRINT) demonstrated that intensive blood pressure management (systolic blood pressure [SBP] target, <120 mm Hg) improved cardiovascular outcomes

Received May 10, 2022; accepted after revision March 19, 2023.

From the Department of Radiology (C.S.), Imaging Institute, Cleveland Clinic, Cleveland, Ohio; Department of Radiology (D.S., G.E., J.A.D., R.N.B., Y.F., I.M.N.), University of Pennsylvania, Philadelphia, Pennsylvania; Division of Nephrology (M.K.T.), Stanford University, and VA Palo Alto Geriatric Research and Education Clinical Center, Palo Alto, California; Biggs Institute, University of Texas San Antonio (M.H.), San Antonio, Texas; Department of Nephrology and Hypertension (W.E.H.), Mayo Clinic, Jacksonville, Florida; Departments of Neurology (A.J.L.) and Medicine (J.T.W.), Case Western Reserve University, and University Hospitals Cleveland Medical Center, Cleveland, Ohio; National Institute of Neurological Disorders and Stroke (C.B.W.), National Institutes of Health, Bethesda, Maryland; Division of Cardiovascular Disease (S.O.), Department of Medicine, University of Alabama, Birmingham, Alabama; Section of Gerontology and Geriatric Medicine, Department of Internal Medicine (S.B.K., J.D.W.), Wake Forest School of Medicine, Winston-Salem, North Carolina; Punzi Medical Center (H.A.P.), Carrollton, Texas; Division of Nephrology (A.R.), Department of Medicine, University of California Los Angeles, Los Angeles, California; Division of Nephrology (R.M.), University of California San Diego, San Diego, California; Frances Payne Bolton School of Nursing (C.H.S.), Case Western Reserve University, Cleveland, Ohio.

The Systolic Blood Pressure Intervention (SPRINT) randomized trial is funded with Federal funds from the National Institutes of Health, including the National Heart, Lung, and Blood Institute; the National Institute of Diabetes and Digestive and Kidney Diseases; the National Institute on Aging; and the National Institute of Neurological Disorders and Stroke, under contract Nos. HHSN268200900040C, HHSN268200900046C, HHSN268200900047C, HHSN268200900048C, HHSN268200900049C, and Interagency Agreement No. A-HL-13-002-001. It was also supported, in part, by resources and use of facilities through the Department of Veterans Affairs.

The views expressed in this article are those of the authors and do not represent the official position of the National Institutes of Health, the Department of Veterans Affairs, the US Government, or the SPRINT Research Group. This article was not reviewed or approved by the SPRINT Steering Committee.

Please address correspondence to Chintan Shah, MD, MS, Department of Radiology, Imaging Institute, Cleveland Clinic, 9500 Euclid Ave, mail code S3, Cleveland, OH 44195; e-mail: shahc2@ccf.org; @cshahrad

Indicates open access to non-subscribers at [www.ajnr.org](http://www.ajnr.org)

<http://dx.doi.org/10.3174/ajnr.A7852>

compared with standard management (SBP target, <140 mm Hg) during a median follow-up of 3.26 years.<sup>3</sup> SPRINT further showed that intensive therapy was associated with a lower incidence of mild cognitive impairment between treatment groups.<sup>4</sup> A subset of participants underwent brain MR imaging, with the intensive group showing a slower progression of white matter hyperintensities (WMH) compared with the standard group, though also with a slightly greater decline in brain volume.<sup>5</sup> These studies indicate that intensive treatment may provide an overall benefit for cognitive health, though the mechanisms are unclear and remain a key question for further study.<sup>6</sup>

The SPRINT MR imaging protocol included resting-state fMRI (rs-fMRI), a noninvasive tool measuring blood oxygen level-dependent (BOLD) signal and allowing investigation of changes in brain functional connectivity (FC). In a study of SPRINT MR imaging participants at baseline, the burden of WMH was inversely related to FC of the default mode network (DMN) and of the auditory-salience-language network (ASLN).<sup>7</sup> To further determine the impact of hypertension treatment on brain health, we assessed longitudinal changes in brain functional connectivity ( $\Delta$ FC) to determine whether intensive treatment results in less decline in FC and how  $\Delta$ FC relates to changes in brain structure.

## MATERIALS AND METHODS

### Study Cohort

This study is an analysis of SPRINT brain MR imaging data. The trial protocol was approved by the institutional review board at each participating site. All participants provided written informed consent. SPRINT enrolled 9361 adults without diabetes older than 50 years of age with SBP of >130 mm Hg and an elevated cardiovascular risk profile. Exclusion criteria included prior stroke, diabetes, dementia, and a recent cardiovascular event within 3 months. Participants were randomized to intensive or standard SBP management. The main SPRINT outcome publication includes full details on inclusion and exclusion criteria, randomization, locations, and the treatment protocol.<sup>3</sup> The intensive treatment group had antihypertensive medications adjusted during the study duration to target an SBP of 120 mm Hg, whereas the standard treatment group had medications adjusted to target an SBP of 135–139 mm Hg, according to the treatment protocol. The SPRINT MR imaging substudy included a subset of participants within 1.5-hour driving distance of an MR imaging center ( $n = 475$ ) who underwent 2 MR imaging scans: a baseline scan within 3 months of randomization and a follow-up scan approximately 4 years after randomization. Additional participants with chronic kidney disease ( $n = 73$ ) from the SPRINT ancillary study “Mind the Kidneys” scanned using the same brain MR imaging protocol were also included. Exclusion criteria included claustrophobia and a non-MR imaging-compatible device or foreign object.

Of the 548 participants who underwent both MR imaging examinations, 15 were excluded due to the presence of structural brain lesions. An additional 47 participants did not have technically adequate resting-state data at both timepoints (19 resting-state data not acquired, 6 poor-quality raw images, 22 failed processing). Excessive motion resulted in exclusion of 80 additional participants as detailed below. Four hundred six participants had adequate longitudinal resting-state data.

### MR Imaging Data Acquisition

MR images were obtained on 3T scanners at 11 sites (1 Magnetom Skyra VD11B, 3 Magnetom Trio VB17, 2 Magnetom Verio VB17; Siemens; 4 Achieva 3.2; Philips Healthcare; and 1 Discovery MR750W; GE Healthcare) using a multichannel receiver head coil. The structural MR imaging protocol included sagittal 1-mm isotropic T1-weighted 3D MPRAGE, T2-weighted FLAIR, and T2-weighted fast spin-echo sequences, described previously.<sup>5</sup> An rs-fMRI scan was acquired using axial BOLD echo-planar imaging, with TR/TE = 2000/25 ms, isotropic 3.5-mm voxels, and 120 volumes.

### Structural Image Processing

Structural imaging was processed in a manner similar to that of prior SPRINT studies.<sup>5,8,9</sup> Skull stripping was performed,<sup>10</sup> and intracranial tissues were segmented using a multitlas label fusion method.<sup>11</sup> Images were registered into the Montreal Neurological Institute template space. WMH were identified using a deep learning-based segmentation model.<sup>5</sup> Classifications of WMH were assessed for quality by a neuroradiologist.

### Functional Image Processing

Rs-fMRI data were preprocessed in standard fashion, as reported previously.<sup>7</sup> These included removal of the first 6 volumes, section-time correction, motion correction, nuisance variable regression, spatial smoothing (6-mm full width at half maximum), bandpass filtering (0.01–0.1 Hz), and registration via the T1-weighted scan into Montreal Neurological Institute template space, followed by resampling to a 4-mm isotropic resolution. Scans were excluded if any framewise motion exceeded 3.5 mm and if the mean relative displacement was 0.3 mm.<sup>12,13</sup> Twenty independent components<sup>14</sup> were identified at group-level independent component analysis using Melodic (FSL; <https://fsl.fmrib.ox.ac.uk/fsl/fslwiki/MELODIC>).<sup>15</sup> The 20 identified components can be found in previously published work.<sup>7</sup> Canonical networks were identified from these by visual inspection. Subject-level independent components were extracted using group information-guided independent component analysis<sup>16,17</sup> and were used to calculate  $z$  score maps for each network for each study participant.<sup>7</sup>

A mean connectivity score (MCS) was calculated for each network in each participant as the participant's average within-network FC within a 3D mask of the network generated from the group-level independent component analysis.<sup>18</sup> This represents a metric of overall network coherence with greater scores reflecting more integrated dynamics within the network<sup>18</sup> and in this cohort, it was found to be related to baseline volume of WMH for networks of interest as described below. For each network, the longitudinal change in MCS ( $\Delta$ MCS) was calculated by subtracting the participant's baseline MCS from the follow-up MCS, with a positive change with time indicating an overall improvement in within-network connectivity, and a negative change indicating an overall decline. The temporal SD of the resting-state BOLD signal was calculated as the resting-state fluctuation of amplitude to assess neurovascular coupling integrity.<sup>19</sup>

The DMN and ASLN were considered primary networks of interest based on a baseline assessment of this cohort, which demonstrated that the MCS of these networks correlated with the volume



of WMH.<sup>7</sup> The MCS of the DMN at baseline was also significantly related to performance on the Montreal Cognitive Assessment, demonstrating a mediation effect. The MCS of the ASLN demonstrated a nonsignificant inverse relationship with performance on the Digit Symbol Coding Test. Additional secondary networks of interest included the left frontoparietal network, dorsal frontal network, basal ganglia network, and a network including the posterior DMN components, which showed a relationship to WMH but not with cognition.<sup>7</sup>

### Group Level Statistical Analyses

Statistical analyses were performed using Matlab (MathWorks).

**Treatment Group Comparisons.** For the 2 primary networks of interest, the  $\Delta$ MCS was compared between the treatment groups using a *t* test with a Bonferroni correction ( $P < .025$ ). On the basis of the mean and SD of the MCS in the cohort at baseline, we would expect 80% power to detect  $\geq 8\%$  decline in network MCS for the standard compared with the intensive group. To identify regions of the network with significant differences between treatment groups, FC difference maps were calculated from the spatial network maps of each participant at follow-up and baseline, and a voxelwise *t* test was performed on the difference maps. The *t* score map was thresholded at  $t = 2.588$  ( $P < .01$ , uncorrected), and Monte Carlo simulation was then performed to determine the cluster size representative of a threshold of  $P < .0001$ , family-wise error-corrected. Significant clusters represent the regions within the network where  $\Delta$ FC is the difference between treatment groups. Treatment groups were also compared using a *t* test for  $\Delta$ MCS for secondary networks of interest. Resting-state fluctuation of amplitude was also compared between the groups for both the baseline and follow-up scans using a 2-sample *t* test to evaluate evidence that group differences may be affected by differences in neurovascular coupling.

To determine whether significant group differences or significant clusters were influenced by differential rates of network-wide or local atrophy, we performed a post hoc analysis in which cortical volumes were calculated for each participant at each time point within the entire ASLN network, within the significant clusters, as well as cortical volumes within atlas ROIs that corresponded to the significant clusters. The longitudinal change in these cortical volumes was calculated for each participant and compared between the 2 treatment groups using 2-sample *t* tests.

**Subgroup Comparisons.** An exploratory subgroup analysis was conducted on the basis of age, baseline WMH burden, change in WMH, and longitudinal change in relative total brain volume (*r*TBV, defined as the ratio of total brain volume to intracranial volume). Age subgroups were defined as younger than 65 years of age and 65 years or older. Those with high or low baseline burden of WMH were dichotomized by the median value of 1536 mm<sup>3</sup> for WMH burden within supratentorial regions of the brain at baseline. Longitudinal change in WMH subgroups were defined as those with minimal or no substantial change ( $\Delta$ WMH of  $< 250$  mm<sup>3</sup>) or those with some change ( $\Delta$ WMH of  $\geq 250$  mm<sup>3</sup>). Subgroups for longitudinal change in *r*TBV were defined on the basis of the median value as those with minimal or no substantial decrease across

time ( $\Delta$ *r*TBV  $> -0.019$ ) or those with a larger decrease with time ( $\Delta$ *r*TBV  $\leq -0.019$ ). The  $\Delta$ MCS was compared between treatment groups using a 2-sample *t* test within each subgroup.

**Longitudinal Changes in FC across the Entire Longitudinal Cohort.** To determine how longitudinal changes in FC were related to changes in brain structure with time, we created multiple, variable, linear regression models for  $\Delta$ MCS across the entire SPRINT longitudinal fMRI cohort within primary networks of interest. Models were created using the  $\Delta$ MCS as the outcome variable,  $\Delta$ WMH and  $\Delta$ *r*TBV as predictors, adjusting for age, sex, and race. Because none of these covariates were significant, these variables were removed from the final models.

## RESULTS

### Study Cohort

The study cohort included 406 participants: 226 in the intensive arm and 180 in the standard arm (Fig 1). Baseline characteristics are shown in Table 1. Participant demographics, clinical variables, and structural brain volumes were similar between treatment groups at baseline. Hispanic ethnicity and Black race were underrepresented relative to the overall SPRINT cohort. Women made up a slightly larger proportion of the intensive group and a smaller proportion of the standard group relative to the overall SPRINT trial. There was a greater proportion of participants with chronic kidney disease in the current cohort relative to the main SPRINT trial but no difference in the estimated glomerular filtration rate between the treatment groups.

### Treatment Group Comparisons

In the ASLN, there was a significant difference between groups in  $\Delta$ MCS ( $P = .014$ ), with the intensive treatment group demonstrating a slightly positive change with time (mean, 0.22 [SD, 1.65]) versus a slightly negative change with time in the standard treatment group (mean,  $-0.19$  [SD, 1.64]). In the DMN, there was no significant difference in  $\Delta$ MCS between groups ( $P = .24$ ).

Voxelwise analysis of the longitudinal change in FC ( $\Delta$ FC) in the ASLN is demonstrated in Fig 2. In the standard treatment group, the  $\Delta$ FC map shows areas of negative change with time in the bilateral posterior temporal lobes, right insula, and anterior and midcingulate region and some smaller areas of mild positive change across time in the anterior right insula and left parietal lobe. In the intensive treatment group, there is a small region of positive change with time in the anterior cingulate region and no areas of decline with time. The comparison *t* map demonstrates the results of the voxelwise *t* test on  $\Delta$ FC. The standard group shows a significantly larger decrease in FC in the right posterior temporal/insular and cingulate regions, relative to the intensive group. A post hoc comparison of longitudinal change in gray matter volumes in the ASLN network and in cortical regions corresponding to these clusters found no significant difference between the 2 treatment groups ( $P > .05$ ).

Additional secondary networks of interest demonstrated no significant difference in  $\Delta$ MCS between treatment groups (all,  $P > .05$ ). There was no difference between treatment groups in resting-state fluctuation of amplitude to suggest systematic differences in neurovascular coupling.

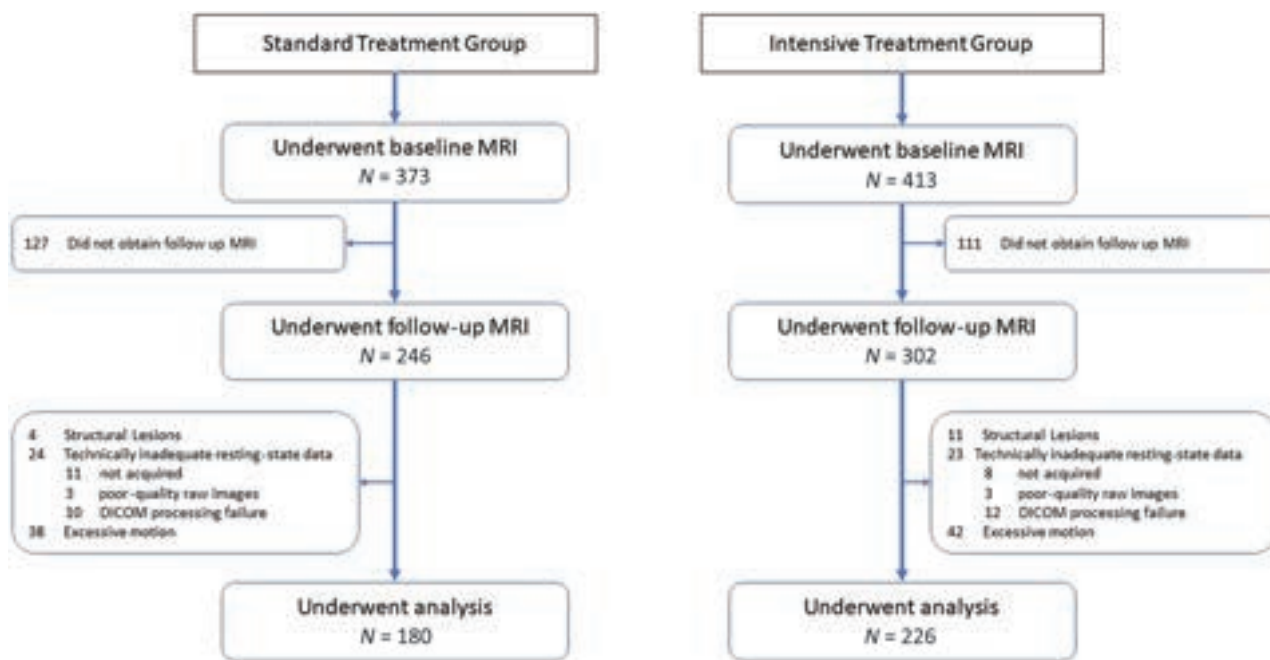


FIG 1. Flow diagram for SPRINT participants undergoing fMRI.

Table 1: Characteristics of study cohort at baseline<sup>a</sup>

	Standard Treatment Group (n = 180)	Intensive Treatment Group (n = 226)
Follow-up period (median) (yr)	3.86	3.82
Age (yr)	67.5 (SD, 8.4)	68.4 (SD, 8.4)
Female sex (No.) (%)	60 (33.3%)	89 (39.4%)
Race (No.) (%)		
White	117 (65.0%)	156 (69.0%)
Black	51 (28.3%)	59 (26.1%)
Hispanic	9 (5.0%)	7 (3.1%)
Other	3 (1.7%)	4 (1.8%)
SBP (mm Hg)	139.6 (SD, 18.4)	136.2 (SD, 18.2)
DBP (mm Hg)	82.2 (SD, 13.2)	80.2 (SD, 11.2)
eGFR (mL/min/1.73 m <sup>2</sup> )	69.1 (SD, 21.3)	65.2 (SD, 19.0)
Serum creatinine level (mg/dL)	1.1 (SD, 0.4)	1.1 (SD, 0.4)
Chronic kidney disease (eGFR < 60 mL/min/1.73 m <sup>2</sup> ) (No.) (%)	61 (33.9)	88 (38.9)
Framingham 10-year cardiovascular disease risk score (%)	24.3 (SD, 12.4)	23.5 (SD, 12.6)
TBV (cm <sup>3</sup> )	1150.9 (SD, 117.0)	1139.3 (SD, 117.3)
rTBV/ICV	0.82 (SD, 0.04)	0.82 (SD, 0.04)
White matter lesion volume (median) (IQR) (cm <sup>3</sup> )	1.6 (0.9–3.8)	1.4 (0.6–3.6)

Note:—DBP indicates diastolic blood pressure; IQR, interquartile range; eGFR, estimated glomerular rate; ICV, intracranial volume.

<sup>a</sup> All values provided as means unless otherwise specified.

### Subgroup Comparisons

Table 2 shows the results of the subgroup analyses. In those with greater longitudinal decline in rTBV, the standard group demonstrated greater decline in the MCS of the DMN relative to the intensive group ( $P = .024$ , uncorrected). For the  $\Delta$ MCS in the ASLN, there were differences between treatment groups in the subgroups with greater baseline WMH volume ( $P = .044$ ), older age ( $P = .037$ ), and smaller longitudinal change in rTBV ( $P = .0058$ ), with the intensive group demonstrating less longitudinal decline.

### Longitudinal Changes in FC across the Entire MR Imaging Cohort

In the multiple variable regression model for  $\Delta$ MCS of the DMN,  $\Delta$ WMH demonstrated a negative relationship ( $P = .013$ ) and  $\Delta$ rTBV demonstrated a positive relationship ( $P = .03$ ); however, only  $\Delta$ WMH was statistically significant after Bonferroni correction for the 2 models. Model parameters are listed in Table 3. Neither  $\Delta$ WMH nor  $\Delta$ rTBV were significant predictors in the model for  $\Delta$ MCS of the ASLN.

fMRI findings from the SPRINT randomized clinical trial indicated that intensive blood pressure management results in preservation of FC as measured by MCS in the ASLN, while other networks were not significantly different relative to standard therapy in our sample. Furthermore, we observed that worsening of WMH volume is associated with decreased FC in the DMN.

In the ASLN, FC was preserved in the intensive group compared with the standard group, primarily in the insula and cingulate regions, which correspond primarily to the salience component of the network.<sup>20</sup> The salience network has been posited to modulate redirecting attention between internal and external stimuli.<sup>20</sup> In the baseline study of this cohort, ASLN FC was also related to WMH burden and demonstrated a nonsignificant inverse relationship with performance on the Digit Symbol Coding Test, which assesses processing speed and working memory.<sup>21</sup> However, in the current study, there was no significant

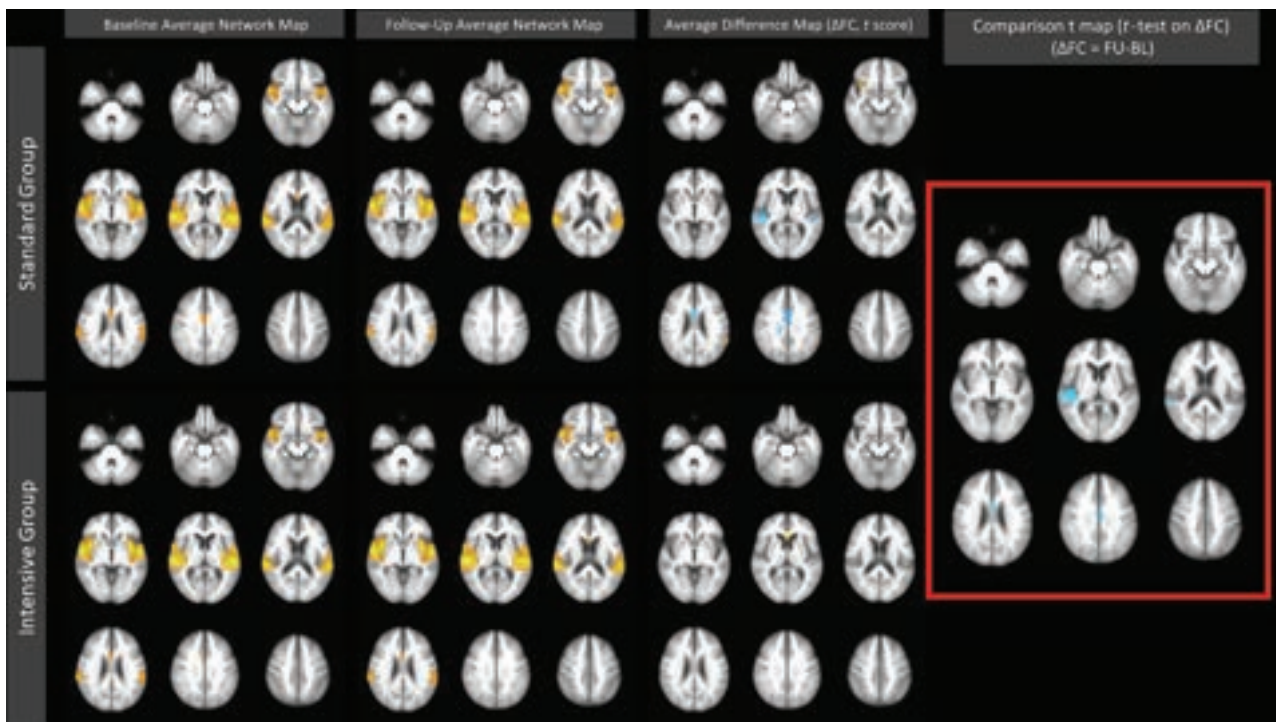


**FIG 2.** Voxelwise *t* test comparing the longitudinal change of the ASLN between treatment groups. Comparison *t* map on the right (red box) demonstrates regions of significantly more negative change with time in the standard group compared with the intensive group in the cingulate region and right posterior insula and temporal lobe. Clusters are significant to  $P < .0001$  family-wise error–corrected. BL indicates baseline; FU, Follow-up.

**Table 2: Subgroup comparisons between treatment groups in longitudinal  $\Delta$ MCS**

	Standard Group	Intensive Group	Default Mode Network			ASLN		
			Effect Size (Cohen d)	<i>t</i>	<i>P</i> Value	Effect Size (Cohen d)	<i>t</i>	<i>P</i> Value
Overall	180	226	−0.12	−1.17	.24	−0.24	−2.46	.014 <sup>a</sup>
Subgroups								
High baseline WMH	94	108	−0.14	−0.97	.33	−0.28	−2.03	.044 <sup>b</sup>
Low baseline WMH	85	118	−0.09	−0.66	.51	−0.21	−1.47	.144
High $\Delta$ WMH	101	96	−0.08	−0.55	.59	−0.24	−1.67	.097
Low $\Delta$ WMH	77	127	−0.12	−0.86	.39	−0.27	−1.86	.064
Older age	97	131	−0.12	−0.90	.37	−0.28	−2.10	.037 <sup>b</sup>
Younger age	83	95	−0.11	−0.73	.47	−0.19	−.28	.20
Larger rTBV decline	87	117	−0.32	−2.27	.024 <sup>b</sup>	−0.09	−0.64	.52
Smaller rTBV decline	93	109	0.09	0.66	.51	−0.39	−2.79	.0058 <sup>b</sup>

<sup>a</sup>  $P < .05$ , Bonferroni-corrected.

<sup>b</sup>  $P < .05$ , uncorrected.

**Table 3: Multiple variable linear regression parameters for models of longitudinal  $\Delta$ MCS**

Predictors	$\Delta$ MCS Model Parameters			
	Default Mode Network Model		ASLN Model	
	$\beta$	<i>P</i> Value	$\beta$	<i>P</i> Value
$\Delta$ WMH	$-7.86 \times 10^{-7}$	.013	$7.21 \times 10^{-7}$	.067
$\Delta$ rTBV	0.14	.030	0.1106	.17

relationship between longitudinal change in ASLN FC and change in WMH or rTBV. These results suggest that intensive therapy may impact ASLN FC independent of the effects on global WMH or rTBV. This possibility may perhaps be through more local or

regional changes or through other mechanisms related directly to the hypertensive treatments.

The longitudinal changes in ASLN FC were small in magnitude, as were the differences between the treatment groups. This finding is likely related to the short study duration of 4 years relative to the typical duration of hypertension, both study arms being treated with a relatively small difference in achieved blood pressure, and the small impact seen on cognitive function in other SPRINT studies.<sup>4,22</sup> The small effect size suggests that there may be a slow impact at the functional network level, which may take years of treatment to manifest as a larger effect or clinically apparent cognitive changes. The treatment group differences in the ASLN FC were more prominent in the older age subgroup and in those with greater WMH burden



at baseline. Prior studies have noted that higher blood pressure is associated with poorer processing speed, particularly in older individuals.<sup>23</sup> Overall, the neurocognitive significance of our findings in the ASLN is uncertain. Future study on long-term changes in processing speed and working memory would be of interest, particularly in the elderly or in those with greater WMH. However, in a separate SPRINT substudy assessing domain-specific cognitive changes, no significant difference was found in memory scores between groups, and there was a small decline in the processing speed domain score in the intensive treatment group.<sup>22</sup>

The DMN is disrupted in disease states such as Alzheimer disease,<sup>24</sup> including those individuals with hypertension.<sup>25</sup> While SPRINT also demonstrated slower progression of WMH with intensive compared with standard therapy,<sup>5</sup> no treatment group difference was seen in DMN FC. This result may be because of the opposing effects of the observed changes in WMH and rTBV in SPRINT on DMN FC. We observed an association of higher DMN FC with both lower WMH burden and larger brain volume, and in the prior SPRINT imaging study, intensive therapy resulted in both lower progression of WMH volume and slightly lower brain volumes,<sup>5</sup> which would predict opposing effects on DMN connectivity. In fact, in the subgroup of participants who all had a greater decline in rTBV, intensive therapy was associated with less decline in FC in the DMN relative to standard treatment. Changes in FC resulting from structural changes in WMH volume or rTBV may also be less sensitive, either due to resiliency in FC or our ability to quantify small changes. Furthermore, the apparent difference in FC decline between treatment groups was small, and the study may have had insufficient power to detect such a small change. It is possible that studies across a longer time interval or in a larger sample may provide different results. Despite the lack of a beneficial effect of intensive therapy on DMN FC, these results provide some reassurance that intensive lowering of blood pressure does not result in an accelerated decline in connectivity within this network.

Limitations of this study include the longitudinal fMRI cohort being slightly different from the overall SPRINT study, including having less cardiovascular disease but a higher proportion of chronic kidney disease, potentially affecting generalizability. Although hypertension may theoretically impact neurovascular coupling, there was no group difference in resting-state fluctuation of amplitude; thus, group differences in neurovascular coupling are unlikely to have systematically affected the treatment group comparison.

There was a greater rate of loss to follow-up imaging in the standard group and a greater number of exclusions in the intensive group, which could introduce bias. Such bias is difficult to predict; however, if participant losses were due to poorer cognitive function, effects would likely be of small magnitude given the small cognitive differences detected in other SPRINT studies. SPRINT observed little change in domain-specific cognitive score measures<sup>22</sup> and adjudicated cases of dementia and mild cognitive impairment in the MR imaging group,<sup>4</sup> reducing the power to evaluate associations between cognitive and imaging measures. Finally, because the trial intervention was stopped early due to a significant cardiovascular benefit, this decision likely reduced the magnitude of longitudinal changes in FC, given the shorter time interval, and may have reduced the power to detect group differences.

This last point emphasizes a notable gap in the literature: Despite the well-established role of hypertension as a risk factor for

cognitive impairment, cognitive outcomes have primarily been investigated only as a secondary end point in studies of hypertension. Our results are in accord with the results of prior cognitive studies from SPRINT, which found no clinically relevant differences between treatment groups in memory or processing speed,<sup>22</sup> no significant difference in incident dementia, and only a small difference in mild cognitive impairment.<sup>4</sup> Combined with the results from additional trials, there is mounting evidence that intensive blood pressure management is not harmful and may be beneficial for cognition, even in the elderly.<sup>26</sup> However, there remains uncertainty regarding the optimal treatment thresholds with regard to cognitive outcomes, whether those goals may change across the life span, and optimal strategies specific to patients with pre-existing cognitive impairment, who were largely excluded from these trials.<sup>27</sup> A recent trial designed with executive function as the primary outcome found that in older adults with mild cognitive impairment, treatment with candesartan was superior to lisinopril.<sup>28</sup> There remains a need for additional long-term trials designed and powered to assess the role of blood pressure management in preventing cognitive decline, particularly given the increasing worldwide prevalence of hypertension and the aging population.

## CONCLUSIONS

In patients with hypertension, intensive lowering of blood pressure results in preservation of FC in the ASLN, particularly in older subjects and those with greater WMH at baseline. Greater accumulation of WMH is related to a greater decline in the MCS of the DMN; however, intensive blood pressure lowering did not significantly impact longitudinal change in the DMN MCS compared with standard treatment.

## ACKNOWLEDGMENTS

The SPRINT investigators acknowledge the contribution of study medications (azilsartan and azilsartan combined with chlorthalidone) from Takeda Pharmaceuticals International, Inc. All components of the SPRINT study protocol were designed and implemented by the investigators. The investigative team collected, analyzed, and interpreted the data. All aspects of manuscript writing and revision were carried out by the coauthors. For a full list of contributors to SPRINT, please see the supplementary acknowledgement list (<https://www.sprintrial.org/public/dspScience.cfm>).

Disclosure forms provided by the authors are available with the full text and PDF of this article at [www.ajnr.org](http://www.ajnr.org).

## REFERENCES

1. Mozaffarian D, Benjamin EJ, Go AS, et al; American Heart Association Statistics Committee; Stroke Statistics Subcommittee. **Heart Disease and Stroke Statistics-2016 Update: a report from the American Heart Association.** *Circulation* 2016;133:e38–360 CrossRef Medline
2. Law MR, Morris JK, Wald NJ. **Use of blood pressure lowering drugs in the prevention of cardiovascular disease: meta-analysis of 147 randomised trials in the context of expectations from prospective epidemiological studies.** *BMJ* 2009;338:b1665 CrossRef Medline
3. Wright JT, Williamson JD, Whelton PK, et al; SPRINT Research Group. **A randomized trial of intensive versus standard blood-pressure control.** *N Engl J Med* 2015;373:2103–16 CrossRef Medline



4. Williamson JD, Pajewski NM, Auchus AP, et al; SPRINT MIND Investigators for the SPRINT Research Group. **Effect of Intensive vs Standard Blood Pressure Control on Probable Dementia: a randomized clinical trial.** *JAMA* 2019;321:553–61 CrossRef Medline
5. Nasrallah IM, Pajewski NM, Auchus AP, et al; SPRINT MIND Investigators for the SPRINT Research Group. **Association of intensive vs standard blood pressure control with cerebral white matter lesions.** *JAMA* 2019;322:524–34 CrossRef Medline
6. Iadecola C, Yaffe K, Biller J, et al; American Heart Association Council on Hypertension; Council on Clinical Cardiology; Council on Cardiovascular Disease in the Young; Council on Cardiovascular and Stroke Nursing; Council on Quality of Care and Outcomes Research; and Stroke Council. **Impact of hypertension on cognitive function: a scientific statement from the American Heart Association.** *Hypertension* 2016;68:e67–94 CrossRef Medline
7. Shah C, Srinivasan D, Erus G, et al. **Changes in brain functional connectivity and cognition related to white matter lesion burden in hypertensive patients from SPRINT.** *Neuroradiology* 2021;63:913–24 CrossRef Medline
8. Tamura MK, Pajewski NM, Bryan RN, et al; SPRINT Study Research Group. **Chronic kidney disease, cerebral blood flow, and white matter volume in hypertensive adults.** *Neurology* 2016;86:1208–16 CrossRef Medline
9. Freedman BI, Gadegbeku CA, Bryan RN, et al. **APOL1 renal-risk variants associate with reduced cerebral white matter lesion volume and increased gray matter volume.** *Kidney Int* 2016;90:440–49 CrossRef Medline
10. Doshi J, Erus G, Ou Y, et al. **Multi-atlas skull-stripping.** *Acad Radiol* 2013;20:1566–76 CrossRef Medline
11. Doshi J, Erus G, Ou Y, et al; Alzheimer's Neuroimaging Initiative. **MUSE: MUlti-atlas region Segmentation utilizing Ensembles of registration algorithms and parameters, and locally optimal atlas selection.** *Neuroimage* 2016;127:186–95 CrossRef Medline
12. Satterthwaite TD, Wolf DH, Loughead J, et al. **Impact of in-scanner head motion on multiple measures of functional connectivity: relevance for studies of neurodevelopment in youth.** *Neuroimage* 2012;60:623–32 CrossRef Medline
13. Power JD, Mitra A, Laumann TO, et al. **Methods to detect, characterize, and remove motion artifact in resting state fMRI.** *Neuroimage* 2014;84:320–41 CrossRef Medline
14. Ray KL, McKay DR, Fox PM, et al. **ICA model order selection of task co-activation networks.** *Front Neurosci* 2013;7:237 CrossRef Medline
15. Beckmann CF, Smith SM. **Probabilistic independent component analysis for functional magnetic resonance imaging.** *IEEE Trans Med Imaging* 2004;23:137–52 CrossRef Medline
16. Du Y, Fan Y. **Group information guided ICA for fMRI data analysis.** *Neuroimage* 2013;69:157–97 CrossRef Medline
17. Du Y, Allen EA, He H, et al. **Artifact removal in the context of group ICA: a comparison of single-subject and group approaches.** *Hum Brain Mapp* 2016;37:1005–25 CrossRef Medline
18. Wisner KM, Patzelt EH, Lim KO, et al. **An intrinsic connectivity network approach to insula-derived dysfunctions among cocaine users.** *Am J Drug Alcohol Abuse* 2013;39:403–13 CrossRef Medline
19. Kannurpatti SS, Motes MA, Biswal BB, et al. **Assessment of unconstrained cerebrovascular reactivity marker for large age-range fMRI studies.** *PLoS One* 2014;9:e88751 CrossRef Medline
20. Menon V. **Saliency Network.** In: Toga AW, ed. *Brain Mapping: An Encyclopedic Reference*. 2nd ed. Academic Press: Elsevier; 2015:597–611
21. Jaeger J. **Digit symbol substitution test.** *J Clin Psychopharmacol* 2018;38:513–19 CrossRef Medline
22. Rapp SR, Gausoin SA, Sachs BC, et al; SPRINT Research Group. **Effects of intensive versus standard blood pressure control on domain-specific cognitive function: a substudy of the SPRINT randomised controlled trial.** *Lancet Neurol* 2020;19:899–907 CrossRef Medline
23. Forte G, Pascalis VD, Favieri F, et al. **Effects of blood pressure on cognitive performance: a systematic review.** *J Clin Med* 2019;9:34 CrossRef Medline
24. Hafkemeijer A, van der Grond J, Rombouts SA. **Imaging the default mode network in aging and dementia.** *Biochim Biophys Acta* 2012;1822:431–41 CrossRef Medline
25. Son SJ, Kim J, Lee E, et al. **Effect of hypertension on the resting-state functional connectivity in patients with Alzheimer's disease (AD).** *Arch Gerontol Geriatr* 2015;60:210–16 CrossRef Medline
26. Peters R, Warwick J, Anstey KJ, et al. **Blood pressure and dementia: what the SPRINT-MIND trial adds and what we still need to know.** *Neurology* 2019;92:1017–18 CrossRef Medline
27. Gorelick PB, Sorond F. **Cognitive function in SPRINT: where do we go next?** *Lancet Neurol* 2020;19:880–81 CrossRef Medline
28. Hajjar I, Okafor M, McDaniel D, et al. **Effects of Candesartan vs Lisinopril on Neurocognitive Function in Older Adults with Executive Mild Cognitive Impairment: a randomized clinical trial.** *JAMA Netw Open* 2020;3:e2012252 CrossRef Medline

# Imaging the Tight Orbit: Radiologic Manifestations of Orbital Compartment Syndrome

C. Maier, N. Thieme, B. Beck-Broichsitter, N.L. Beetz, T.C. Walter-Rittel, K. Rubarth, M. Heiland, K. Kreutzer, S. Koerdt, and J.O. Voss



## ABSTRACT

**BACKGROUND AND PURPOSE:** Orbital compartment syndrome is a sight-threatening emergency caused by rising pressure inside the orbit. It is usually diagnosed clinically, but imaging might help when clinical findings are inconclusive. This study aimed to systematically evaluate imaging features of orbital compartment syndrome.

**MATERIALS AND METHODS:** This retrospective study included patients from 2 trauma centers. Proptosis, optic nerve length, posterior globe angle, morphology of the extraocular muscles, fracture patterns, active bleeding, and superior ophthalmic vein caliber were assessed on pretreatment CT. Etiology, clinical findings, and visual outcome were obtained from patient records.

**RESULTS:** Twenty-nine cases of orbital compartment syndrome were included; most were secondary to traumatic hematoma. Pathologies occurred in the extraconal space in all patients, whereas intraconal abnormalities occurred in 59% (17/29), and subperiosteal hematoma in 34% (10/29). We observed proptosis (affected orbit: mean, 24.4 [SD, 3.1] mm versus contralateral: 17.7 [SD, 3.1] mm;  $P < .01$ ) as well as stretching of the optic nerve (mean, 32.0 [SD, 2.5] mm versus 25.8 [SD, 3.4] mm;  $P < .01$ ). The posterior globe angle was decreased (mean, 128.7° [SD, 18.9°] versus 146.9° [SD, 6.4°];  $P < .01$ ). In 69% (20/29), the superior ophthalmic vein was smaller in the affected orbit. No significant differences were detected regarding the size and shape of extraocular muscles.

**CONCLUSIONS:** Orbital compartment syndrome is characterized by proptosis and optic nerve stretching. In some cases, the posterior globe is deformed. Orbital compartment syndrome can be caused by an expanding pathology anywhere within the orbit with or without direct contact to the optic nerve, confirming the pathophysiologic concept of a compartment mechanism.

**ABBREVIATIONS:** EOM = extraocular muscles; OCS = orbital compartment syndrome

The orbital compartment syndrome (OCS) is a sight-threatening emergency caused by increasing pressure inside the orbital cavity. The tissues in the orbital pyramid are bound by 4 osseous walls and anteriorly by the orbital septum, canthal ligaments, and tarsal plates of the eyelids. There is only limited capacity for volume expansion through protrusion of the eye bulb. Therefore, rapidly expanding orbital lesions can increase

intraorbital pressure precipitously, compromising intraorbital structures. Common space-occupying pathologies underlying the volume expansion are traumatic or iatrogenic intraorbital/retrobulbar bleeding, emphysema, and infection.<sup>1</sup> The pathophysiology of the resulting neuropathy is still unclear. Different theories exist including direct compression of vulnerable neurosensory orbital tissues and ischemia. Ischemia may be attributed to arterial occlusion or compression of venous outflow channels in the context of increased intraorbital pressure.<sup>1-4</sup>

The key symptom of a fulminant OCS is progressive vision impairment with the risk of permanent vision loss. Early signs on the ophthalmologic examination include a relative afferent pupillary defect, deficient pupillary light reflex, increased intraocular pressure, or impaired motility.<sup>1,5</sup> Clinical symptoms can be missing initially, but when the rising intraorbital pressure exceeds the mean arterial pressure, a critical reduction in tissue perfusion and oxygen supply results. The pathophysiology is considered to be similar to that of compartment syndrome in the extremities.<sup>6-8</sup> Progressively tense and painful proptosis with a hard eyeball reflects an orbit under pressure also known as a tight orbit.<sup>9</sup>

Received November 27, 2022; accepted after revision March 4, 2023.

From the Departments of Radiology (C.M., N.T., N.L.B., T.C.W.-R.) and Oral and Maxillofacial Surgery (B.B.-B., M.H., K.K., S.K., J.O.V.), and Institute of Biometry and Clinical Epidemiology (K.R.), Charité—Universitätsmedizin Berlin, corporate member of Freie Universität Berlin, Humboldt-Universität zu Berlin, Berlin, Germany; Department of Radiology (C.M.), Center for Advanced Imaging Innovation and Research, New York University School of Medicine, New York, New York; Department of Oral and Maxillofacial Surgery (B.B.-B.), Katharinenhospital Stuttgart, Stuttgart, Germany; and Berlin Institute of Health (K.R., J.O.V.), Berlin, Germany.

C. Maier and N. Thieme contributed equally to this work.

Please address correspondence to Christoph Maier, MD, Department of Radiology, Charité—Universitätsmedizin Berlin, corporate member of Freie Universität Berlin, Humboldt-Universität zu Berlin, and Berlin Institute of Health, Augustenburger Platz 1, 13353 Berlin, Germany; e-mail: christoph.maier@charite.de

Indicates article with online supplemental data.

<http://dx.doi.org/10.3174/ajnr.A7840>

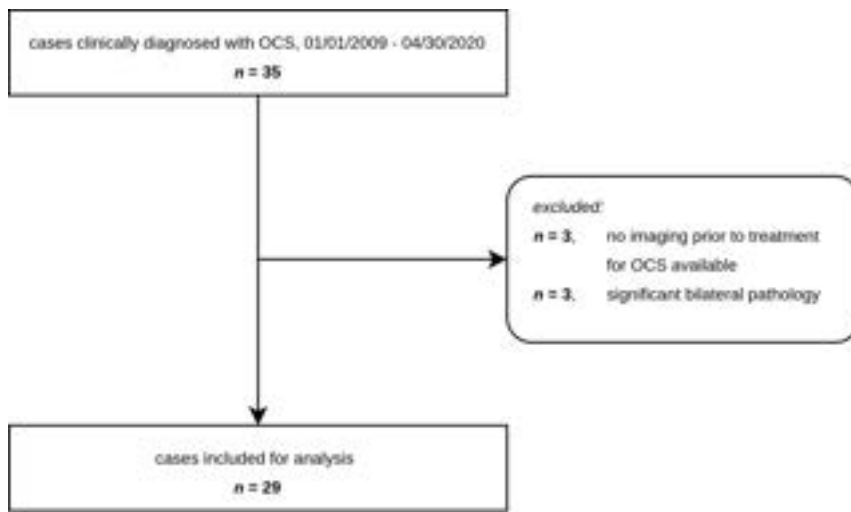


**FIG 1.** Patient flow chart.

Rapid recognition of the condition and initiation of surgical decompression is paramount to avert permanent vision loss. OCS is considered a clinical diagnosis characterized by proptosis and a firm globe, reduced visual acuity, and impaired ocular motility. However, clinical examination can be impeded in patients who are unconscious or who have received opioids (impairing pupillary reflexes), in children, and in the presence of profuse periorbital hematoma, which limits palpation of the globe. Various case series have proposed imaging features that may aid the diagnosis in clinically ambiguous cases.<sup>10,11</sup> The purpose of this study was to systematically evaluate radiologic signs in a patient cohort with posttraumatic OCS.

## MATERIALS AND METHODS

### Study Design and Patient Collective

Ethics approval was granted by our institution's ethical review board (file number EA4/098/20, Charité-Universitätsmedizin Berlin). For this retrospective study, all patients clinically diagnosed with OCS at the Department of Maxillofacial Surgery of 2 academic level I trauma centers between January 1, 2009, and April 30, 2020, were retrieved from the electronic medical system. A subset of these patients had been included in a previously published study on clinical parameters of OCS (16 cases; timeframe, January 1, 2012, to May 31, 2015).<sup>12</sup> Three patients were excluded because no CT imaging covering the orbits had been performed before the initiation of surgical or medical treatment for OCS. Three further patients were excluded because the bony landmarks required for image analysis were obscured or shifted by severe, bilateral, midfacial injuries. A flow chart of included patients is shown in Fig 1.

### Clinical Data

Clinical information was extracted from electronic and paper medical records, including the etiology, initial clinical findings, ophthalmologic status, therapeutic procedures (surgical and/or medical), long-term anticoagulant or antiplatelet medication, and final outcome.

### Image Acquisition

Due to the retrospective nature of our study, imaging protocols were heterogeneous with regard to parameters such as scanner hardware, acquisition mode (incremental-versus-helical), IV contrast agent administration, radiation dose, and reconstruction kernels. In all cases included in the analysis, the orbits were completely depicted and image quality was sufficient. When available, the soft-tissue kernel was used for the analysis (in 4/29 cases, only bone kernel images were available for analysis). Section thickness ranged from 0.5 to 1.25 mm. IV contrast had been administered in 14/29 cases.

### Image Analysis

All images were analyzed using Visage 7.1.15 (Visage Imaging). Type and localization of the orbital pathology, possible concomitant craniofacial fractures, active intraorbital bleeding (if contrast-enhanced imaging was available), and the caliber of the superior ophthalmic vein were qualitatively assessed (C.M., 6 years of experience in head and neck imaging).

Proptosis, optic nerve length, and posterior globe angle were quantified. Each patient's unaffected orbit served as an intraindividual control. Globe displacement or motility disorders in the affected orbit often made it impossible to assess the relevant anatomy on both sides in 1 imaging plane. Therefore, we modified established methods for these parameters<sup>10,13</sup> as follows, with measurements being obtained in a plane reformatted respective to the pertinent anatomy, separately for each side. Proptosis is the distance between the interzygomatic line and the corneal apex; optic nerve length, the distance between the orbital aperture of the optic canal and the scleral contour at the optic nerve head; and posterior globe angle, the angle between the tangents at the scleral contours, measured in a plane bisecting the optic nerve head, and the center of the lens. The size and shape of the extraocular muscles (EOM) were assessed on the plane perpendicular to the axis of the optic nerve, where the EOM size is maximal. Size was defined as cross-sectional area, assuming an elliptical shape:

$$A = \pi \times \frac{\text{Long Axis} \times \text{Short Axis}}{2}$$

Muscle shape was analyzed by determining the eccentricity of the elliptical cross-section, in which a value of zero represents a perfect circle and higher values indicate more oblong shapes:

$$e = \sqrt{1 - \left(\frac{\text{Short Axis}}{\text{Long Axis}}\right)^2}$$

Because the superior rectus muscle cannot be reliably discriminated from the levator palpebrae superioris muscle on CT, these 2 muscles were measured together (termed "superior group"). In a few cases, EOM size and superior ophthalmic vein caliber could not be determined because these structures were obscured by

### Clinical data<sup>a</sup>

Variable	All Patients (n = 29)
Age (yr) <sup>b</sup>	62 [SD, 23] (22–102)
Sex	
Female	14/29 (48)
Male	15/29 (51)
Initial trauma mechanism	
Stumbling/fall	16/29 (55)
Assault	7/29 (24)
Motor vehicle crash	3/29 (10)
Fall from great height	2/29 (7)
Unknown	1/29 (3)
Affected eye	
Left	22/29 (76)
Right	7/29 (24)
Antithrombotic medication	
None	11/29 (38)
Antiplatelet	7/29 (24)
Anticoagulation	5/29 (17)
Antiplatelet + anticoagulation	2/29 (7)
Unknown	4/29 (14)

<sup>a</sup> Unless indicated, data are number of patients, and data in parentheses are percentages.

<sup>b</sup> Data are means, and range is given in parentheses.

surrounding hematoma or because of excessive image noise. In addition to analyzing the pretherapeutic CT studies, follow-up MR imaging was evaluated for potential causes of vision loss in the globe, optic nerve, and brain parenchyma when available.

### Statistical Analysis

Data are reported as means, and the 95% confidence intervals were computed. To test for statistical significance, we used the *t* test or paired *t* test. Statistical analysis was performed using R statistical and computing software, Version 3.5.2 (<http://www.r-project.org/>).

## RESULTS

### Clinical Parameters

A total of 29 patients were included in the study. Clinical parameters are summarized in the Table. All patients had been initially admitted to the hospital for craniofacial trauma involving the orbits. Of note, however, in 3 cases, OCS was diagnosed only after orbital fractures had already been treated surgically.

Initial visual examination results in the emergency department varied, ranging from relative afferent pupillary defect, impaired pupillary light reflex, anisocoria, or even blindness of the patient. Other clinical findings included a tense, painful hard eyeball; proptosis; impaired ocular motility; monocular hematoma; and hyposphagma or chemosis.

The OCS was treated by surgical intervention in most cases (27/29 patients). Conservative treatment was pursued in 1 patient without substantial visual impairment and in 1 moribund patient for whom the legal guardian declined a surgical intervention. Surgical decompression was achieved by different approaches, mainly lateral canthotomy and cantholysis or in combination with a transseptal orbital incision. In 2 patients, additional bony wall decompression was performed. Adjuvant treatment in patients undergoing surgery included antibiotics, mainly  $\beta$ -lactam compounds, and steroids.

Conservative treatment included systemic mannitol, carbonic anhydrase inhibitors, as well as local travoprost and timolol.

Vision could be preserved or restored in 20 patients. Visual acuity ranged from hand movement and counting fingers to full vision and was also influenced by pre-existing conditions. In 6 patients, loss of vision persisted at discharge (of note, the ophthalmic artery had been sacrificed by catheter embolization in 1 patient due to surgically uncontrollable hemorrhage). In 3 patients, visual outcome could not be fully evaluated because of the death of the patient or dementia.

### Qualitative Imaging Results

Various space-occupying lesions were found in the affected orbits. While intraorbital hematoma was observed in all patients, intraorbital emphysema occurred in 31% (9/29) of patients, and intraorbitally displaced bone fragments, in 17% (5/29). Regarding the sublocalizations of these intraorbital lesions, the extraconal space was affected in all patients, whereas the intraconal space was affected in 59% (17/29), and the subperiosteal space, in 34% (10/29).

In total,  $\geq 1$  concomitant craniofacial fracture was detected in 86% of patients (25/29). The most frequent fracture patterns were in the orbital floor ( $n = 11$ ), zygoma ( $n = 9$ ), and medial orbital wall ( $n = 6$ ), but more serious injuries involving the anterior skull base or complex midfacial fractures at various Le Fort levels were also observed.

Active bleeding was observed in 50% (7/14) of patients who had been examined with contrast-enhanced CT. The superior ophthalmic vein in the affected orbit was smaller than in the contralateral side in 20 cases, larger in 1 case, equivalent in 7 cases, and could not be assessed in 1 case.

Follow-up MR imaging performed after treatment for OCS was available in 4/29 patients. Notably, diffusion restriction in the optic nerve was observed in 1 patient with permanent vision loss (Online Supplemental Data).

### Quantitative Imaging Results

Figure 2 summarizes the quantitative imaging findings in a typical case of OCS; see the Online Supplemental Data for additional illustrative figures. OCS resulted in marked proptosis (Fig 3A, affected orbit: mean, 24.4 [SD, 3.1] mm [95% CI, 23–26 mm] versus the contralateral orbit: 17.7 [SD, 3.1] mm [95% CI, 17–19 mm];  $P < .01$ ) as well as stretching of the optic nerve (Fig 3B, affected orbit: mean, 32.0 [SD, 2.5] mm [95% CI, 31–33 mm] versus the contralateral orbit: 25.8 [SD, 3.4] mm [95% CI, 25–27 mm];  $P < .01$ ). We also observed a decrease of the posterior globe angle, though variability was higher for this parameter (Fig 3C, affected orbit: mean, 128.7° [SD, 18.9°] [95% CI, 121°–136°] versus the contralateral orbit: 146.9° [SD, 6.4°] [95% CI, 144°–149°];  $P < .01$ ).

To characterize the size and shape of the EOM, we determined the cross-sectional area and eccentricity, respectively. Eccentricity is a measure of the “roundness” of such shapes with a value of zero representing a perfect circle and higher values indicating more oblong shapes. We did not find significant differences in the muscle cross-sectional area between the affected orbit and the contralateral control (Online Supplemental Data) (affected orbit: mean, 98.7 [SD, 40.3] mm<sup>2</sup> [95% CI, 82–115 mm<sup>2</sup>] versus the contralateral orbit: 102.3 [SD, 23.0] mm<sup>2</sup> [95% CI, 93–111 mm<sup>2</sup>] for





**FIG 2.** Representative case with traumatic left-sided OCS due to intraorbital hematoma in the extraconal space (white arrow) and in the subperiosteal space (black arrow). Imaging is helpful to differentiate intraorbital hematoma from periorbital hematoma (dashed white arrow), which is anterior to the orbital septum and therefore does not lead to compartment syndrome. Intraorbital hematoma in this case results in increased proptosis (A and B), optic nerve stretching (C and D), and a decreased posterior globe angle (E and F). Besides stretching of the optic nerve, subtle thinning of the nerve and loss of normal undulation can be observed. Note that the angulation is slightly different for each side because the planes of measurement were reconstructed separately relative to the respective anatomic landmarks.

the medial rectus; 86.7 [SD, 25.9] mm<sup>2</sup> [95% CI, 76–98 mm<sup>2</sup>] versus 82.8 [SD, 20.0] mm<sup>2</sup> [95% CI, 75–91 mm<sup>2</sup>] for the inferior rectus; 88.1 [SD, 40.0] mm<sup>2</sup> [95% CI, 72–104 mm<sup>2</sup>] versus 85.1 [SD, 22.9] mm<sup>2</sup> [95% CI, 76–94 mm<sup>2</sup>] for the lateral rectus; 84.9 [SD, 22.8] mm<sup>2</sup> [95% CI, 76–94 mm<sup>2</sup>] versus 90.4 [SD, 23.2] mm<sup>2</sup> [95% CI, 81–100 mm<sup>2</sup>] for the superior group). Likewise, no significant differences were detected in the eccentricity of any of the muscles (Online Supplemental Data) (affected orbit: mean, 0.92 [SD, 0.05] [95% CI, 0.91–0.94] versus the contralateral orbit: 0.95 [SD, 0.02] [95% CI, 0.94–0.95] for the medial rectus; 0.93 [SD, 0.04] [95% CI, 0.91–0.94] versus 0.94 [SD, 0.03] [95% CI, 0.93–

0.95] for the inferior rectus; 0.93 [SD, 0.04] [95% CI, 0.91–0.95] versus 0.95 [SD, 0.04] [95% CI, 0.93–0.96] for the lateral rectus; and 0.93 [SD, 0.03] [95% CI, 0.92–0.95] versus 0.94 [SD, 0.01] [95% CI, 0.93–0.94] for the superior group).

### Visual Outcome

To evaluate whether imaging findings can help predict clinical outcome, we correlated the differences in quantitative parameters between the affected orbit and the contralateral orbit with visual outcome (Fig 4). The difference in proptosis was similar in both groups (lost vision: mean, 5.95 [SD, 2.92] mm versus preserved vision: 6.64 [SD, 2.63] mm;  $P = .6$ ). Likewise, no significant differences were detected in optic nerve length difference (lost vision: mean, 6.55 [SD, 2.33] mm versus preserved vision: 5.82 [SD, 2.67] mm;  $P = .5$ ) or posterior globe angle difference (lost vision: mean, 20.9° [SD, 23.7°] versus preserved vision: 16.8° [SD, 17.4°];  $P = .7$ ).

### DISCUSSION

In this retrospective study, we systematically evaluated the radiologic signs of OCS, which is a rare-but-vision-threatening emergency, requiring prompt recognition and treatment. To our knowledge, this retrospective data set comprising 29 patients with trauma represents the largest systematic study on OCS reported to date. We observed that OCS invariably led to marked proptosis and optic nerve stretching in the affected orbit, and a reduced posterior globe angle occurred in some cases.

In this study, intraorbital volume expansion was mostly due to hematoma and emphysema, occurring in intraconal, extraconal, and/or subperiosteal locations. In a substantial number of the cases, the space-occupying lesions were not in direct contact with the optic nerve, which is in keeping with a compartment hypothesis. Along this line, previous experimental cadaver studies have demonstrated that volume expansion inside the orbital cavity causes a rapid rise in intraorbital and intraocular pressure.<sup>14,15</sup> It seems reasonable that this increase in pressure damages the delicate neuronal structures in the retina and/or optic nerve. In one of our patients who coincidentally underwent MR imaging after emergency decompression for OCS, we observed marked diffusion restriction in the optic nerve, consistent with infarction. However, the exact pathophysiology of neuronal damage in OCS is still not fully understood because direct pressure damage, arterial occlusion, and/or venous congestion may be implicated. We observed that the diameter of the superior ophthalmic vein in the affected orbit was overwhelmingly reduced, probably representing venous collapse secondary to increased intraorbital pressure. Venous collapse might serve as a clue that compromised venous drainage plays a role in optic nerve damage in OCS, which can occur at lower pressures than frank arterial infarction. In the setting of sudden vision loss following facial trauma, other mechanisms of visual compromise such as direct injury of the globe, traumatic optic neuropathy, or orbital apex syndrome also have to be considered.<sup>16–18</sup> It is crucial to differentiate these conditions by ophthalmologic examination and/or imaging studies because the treatment approach depends on the underlying pathophysiology.

Because our collective was recruited from patients under the care of maxillofacial surgeons, all patients had craniofacial trauma involving the orbit. OCS was accompanied by fractured orbital

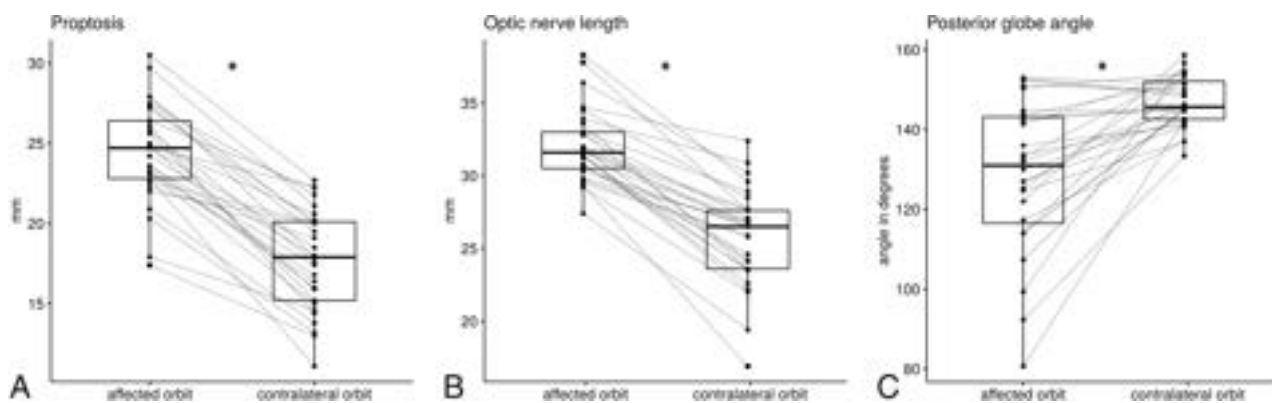


**FIG 3.** Quantitative imaging data. Boxplots show the distribution of proptosis, defined as the distance between the interzygomatic line and the corneal apex (A); optic nerve length, defined as the distance between the orbital aperture of the optic canal and the scleral contour at the optic nerve head (B); and posterior globe angle, as measured by drawing tangents on the scleral contours at the optic nerve head (C). Each affected orbit is connected to its contralateral control by a *thin line*. The *asterisk* indicates  $P < .05$ .

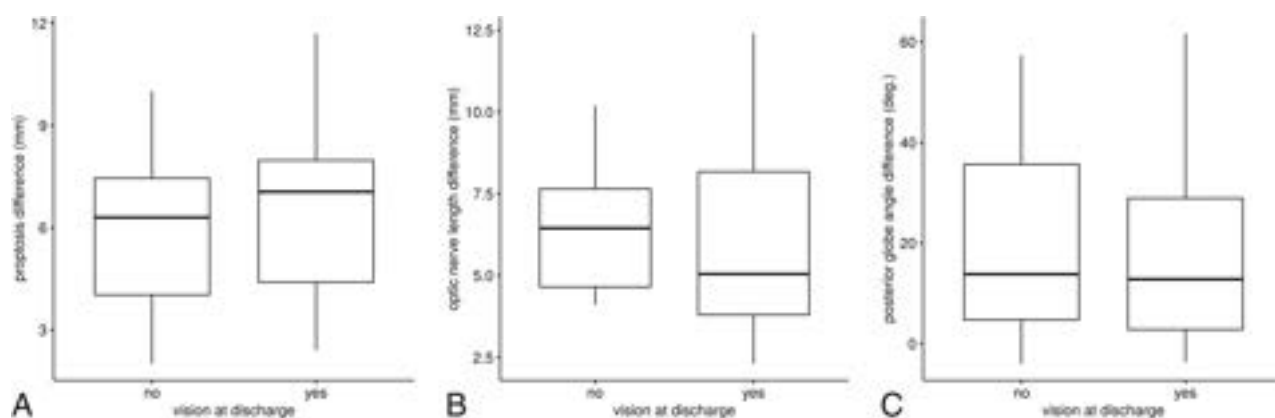


**FIG 4.** Differences between the affected orbit and the contralateral orbit in patients with vision loss at discharge ( $n = 6$ ) and in patients with preserved vision ( $n = 20$ ) regarding proptosis (A), optic nerve length (B), and posterior globe angle (C). No significant differences were detected. For 3 patients, data on visual outcome were unavailable.

walls in the overwhelming majority of patients. In only 3 cases was OCS diagnosed after fractures involving the orbital walls had already been surgically addressed. Whether OCS in these 3 cases was due to the primary trauma or occurred as a complication of surgery or a combination of both cannot be determined with certainty in this retrospective study. OCS occurred even in the presence of fracture patterns that expand the bony orbit, eg, dislocated fractures of the orbital floor. This finding may be explained by the periosteal sleeve and/or intraorbital fibrous septa remaining intact, thereby precluding a decompressive effect of the fracture. Alternatively, the amount of hematoma and emphysema may exceed the volume gained through expansion of the osseous wall. Similarly, Zogheib et al<sup>19</sup> recently reviewed 18 cases of OCS with concomitant displaced orbital fractures. OCS can also result from a range of nontraumatic lesions.<sup>1</sup> While we only investigated a trauma collective, we assume that nontraumatic OCS leads to a similar imaging phenotype as described here.

Various measurements based on orbital CT have been proposed in the literature to stratify the severity of OCS and to predict possible clinical outcomes. In a series of 10 patients, Dalley et al<sup>10</sup> reported that the severity of posterior globe tenting correlated with visual impairment, with a posterior globe angle of  $<120^\circ$  indicating severe proptosis and unfavorable outcomes. A posterior

globe angle of  $120^\circ$ – $130^\circ$  was reported to correlate with mild visual impairment and good clinical recovery.<sup>10</sup> Using a different angle of measurement between the medial rectus insertion and the optic nerve, Oester et al<sup>11</sup> also found that deformity of the posterior globe was more pronounced in patients who lost their vision. In our data, we found no significant differences in the quantitative imaging parameters between patients who lost vision in the affected orbit and patients with preserved vision.

These results must be interpreted with caution, however, because it can be expected that the elapsed time between the initial trauma (or symptom onset) and intervention is a decisive factor on visual outcome. Moreover, interindividual differences in the anatomy (size of the orbital cavity), time point of imaging, as well as the extent and timeframe of volume expansion might affect and influence the visual outcome or impairment. We performed extensive chart reviews trying to establish this timeframe. Unfortunately, this data point could not be determined with the necessary accuracy because the documented clinical histories were terse, owing to the emergency nature of the condition and because the initial time course was unclear in some patients transferred from other hospitals. Furthermore, the level of detail of the visual examinations at discharge was heterogeneous due to the retrospective nature of our study. While some patients received

consults from the ophthalmologic service, not all patients did (especially when subjective vision was satisfactory).

One of the limitations of our study is that the specificity of these imaging findings cannot be derived from our data. In clinical practice, it is not unusual to observe some amount of intraorbital hematoma on CT after facial trauma. However, only a small minority develops compartment syndrome.<sup>20</sup> Determining the specificity of the proposed triad retrospectively is challenging because a “fair control group” would need to be matched not only for the volume of the space-occupying pathology but also for clinical parameters. Because the diagnosis of OCS still remains clinical, a prospective evaluation based on imaging diagnosis is limited.

Further research is necessary to clarify which patients require urgent decompression. Due to the time delay inherently associated with imaging studies, radiologic evaluation should be reserved for ambiguous cases.<sup>21</sup>

In summary, the proposed imaging phenotype should not be understood as diagnostic of OCS but as an indication that OCS might be present, implying that urgent clinical attention is warranted. In this context, we have to bear in mind that CT can detect only structural abnormalities. By contrast, the clinical examination can also reveal visual impairment or other functional deficits. Principally, OCS remains a clinical diagnosis, and imaging procedures must not delay emergency decompression if the diagnosis has already been established on clinical grounds. However, CT can be a decisive factor in decision-making when the clinical examination is limited, eg, in children, in patients who are unconscious or who have received opioids (impairing pupillary reflexes), and in the presence of profuse periorbital hematoma, which impairs palpation of the globe.

## CONCLUSIONS

Proptosis and optic nerve stretching are signs of vision-threatening OCS, which may require urgent surgical decompression. In more severe cases, the posterior globe may be tented. In this collective of traumatic OCS, we have found that the expanding pathology can be located anywhere in the orbit, with or without direct contact with the optic nerve. Coexisting “decompressing” fractures do not exclude OCS. Clinicians who are not specialized in maxillofacial surgery or ophthalmology may be unaware of the condition. Radiologists can play a key role in patient management by raising the suspicion of OCS and initiating an urgent referral to a specialist.

## ACKNOWLEDGMENTS

Dr Jan Voss is a participant in the Berlin Institute of Health Charité Clinician Scientist Program funded by the Charité-Universitätsmedizin Berlin and the Berlin Institute of Health.

Disclosure forms provided by the authors are available with the full text and PDF of this article at [www.ajnr.org](http://www.ajnr.org).

## REFERENCES

1. Lima V, Burt B, Leibovitch I, et al. **Orbital compartment syndrome: the ophthalmic surgical emergency.** *Surv Ophthalmol* 2009;54:441–49 CrossRef Medline
2. Bailey WK, Kuo PC, Evans LS. **Diagnosis and treatment of retrobulbar hemorrhage.** *J Oral Maxillofac Surg* 1993;51:780–82 CrossRef Medline
3. Hargaden M, Goldberg SH, Cunningham D, et al. **Optic neuropathy following simulation of orbital hemorrhage in the nonhuman primate.** *Ophthalmic Plast Reconstr Surg* 1996;12:264–72 CrossRef Medline
4. Vassallo S, Hartstein M, Howard D, et al. **Traumatic retrobulbar hemorrhage: emergent decompression by lateral canthotomy and cantholysis.** *J Emerg Med* 2002;22:251–56 CrossRef Medline
5. Ballard SR, Enzenauer RW, O'Donnell T, et al. **Emergency lateral canthotomy and cantholysis: a simple procedure to preserve vision from sight threatening orbital hemorrhage.** *J Spec Oper Med* 2009;9:26–32 CrossRef Medline
6. Oestern HJ. **Compartment syndrome: definition, etiology, pathophysiology** [in German]. *Unfallchirurg* 1991;94:210–15 Medline
7. Reszel PA, Janes JM, Spittell JA. **Ischemic necrosis of the peroneal musculature: a lateral compartment syndrome.** *Proc Staff Meet Mayo Clin* 1963;38:130–36 Medline
8. Von Volkmann R. **Ischämische Muskellähmungen und kontrakturen (Ischemic muscle paralysis and contractures).** *Zentralbl Chir* 1881;8:801–03
9. Alford EL, Soparkar CN. **Management of the ‘tight orbit’ and associated visual loss.** *Curr Opin Otolaryngol Head Neck Surg* 2013;21:417–22 CrossRef Medline
10. Dalley RW, Robertson WD, Rootman J. **Globe tenting: a sign of increased orbital tension.** *AJNR Am J Neuroradiol* 1989;10:181–86 Medline
11. Oester AE, Sahu P, Fowler B, et al. **Radiographic predictors of visual outcome in orbital compartment syndrome.** *Ophthalmic Plast Reconstr Surg* 2012;28:7–10 CrossRef Medline
12. Voss JO, Hartwig S, Doll C, et al. **The “tight orbit”: incidence and management of the orbital compartment syndrome.** *J Craniomaxillofac Surg* 2016;44:1008–14 CrossRef Medline
13. Gibson RD. **Measurement of proptosis (exophthalmos) by computerised tomography.** *Australas Radiol* 1984;28:9–11 CrossRef Medline
14. Stanley RJ, McCaffrey TV, Offord KP, et al. **Space-occupying orbital lesions: can laryngeal increases in intraorbital pressure be predicted clinically?** *Laryngoscope* 1989;99:19–22 CrossRef Medline
15. Zoumalan CI, Bullock JD, Warwar RE, et al. **Evaluation of intraocular and orbital pressure in the management of orbital hemorrhage: an experimental model.** *Arch Ophthalmol* 2008;126:1257–60 CrossRef Medline
16. Badakere A, Patil-Chhablani P. **Orbital apex syndrome: a review.** *Eye Brain* 2019;11:63–72 CrossRef Medline
17. Pery M. **Acute proptosis in trauma: retrobulbar hemorrhage or orbital compartment syndrome—does it really matter?** *J Oral Maxillofac Surg* 2008;66:1913–20 CrossRef Medline
18. Rocca F, Boffano P, Guglielmi V, et al. **Role of the maxillofacial surgeon in the management of severe ocular injuries after maxillofacial fractures.** *J Emerg Trauma Shock* 2011;4:188–93 CrossRef Medline
19. Zogheib S, Sukkarieh G, Mjaess G, et al. **Displaced orbital fractures with concurrent orbital compartment syndrome: a case-based systematic review.** *Facial Plast Surg* 2022;38:274–78 CrossRef Medline
20. Kondoff M, Nassrallah G, Ross M, et al. **Incidence and outcomes of retrobulbar hematoma diagnosed by computed tomography in cases of orbital fracture.** *Can J Ophthalmol* 2019;54:606–10 CrossRef Medline
21. Erickson BP, Garcia GA. **Evidence-based algorithm for the management of acute traumatic retrobulbar haemorrhage.** *Br J Oral Maxillofac Surg* 2020;58:1091–96 CrossRef Medline

# A Novel MR Imaging Sequence of 3D-ZOOMit Real Inversion-Recovery Imaging Improves Endolymphatic Hydrops Detection in Patients with Ménière Disease

J. Li, L. Sun, N. Hu, L. Li, G. Song, H. Xu, T. Xu, Y. Cheng, L. Xiao, L. Wang, R. Gong, and C. Li



## ABSTRACT

**BACKGROUND AND PURPOSE:** The detection rate of pre-mortem MR imaging endolymphatic hydrops is lower than that of post-mortem endolymphatic hydrops in Ménière disease, indicating that current MR imaging techniques may underestimate endolymphatic hydrops. Therefore, we prospectively investigated whether a novel high-resolution MR imaging technique, the 3D zoomed imaging technique with parallel transmission real inversion-recovery (3D-ZOOMit real IR), would improve the detection of endolymphatic hydrops compared with conventional 3D TSE inversion-recovery with real reconstruction.

**MATERIALS AND METHODS:** Fifty patients with definite unilateral Ménière disease were enrolled and underwent 3D-ZOOMit real IR and 3D TSE inversion-recovery with real reconstruction 6 hours after IV gadolinium injection. The endo- and perilymph spaces were scored separately. The contrast-to-noise ratio, SNR, and signal intensity ratio of the 2 sequences were respectively calculated and compared. The presence of endolymphatic hydrops was evaluated.

**RESULTS:** The endolymphatic space in the cochlea and vestibule was better visualized with 3D-ZOOMit real IR than with conventional 3D TSE inversion-recovery with real reconstruction ( $P < .001$ ). There were differences between the 2 sequences in the evaluation of no cochlear hydrops and cochlear hydrops (both,  $P < .017$ ). All contrast-to-noise ratio, SNR, and signal intensity ratio values of 3D-ZOOMit real IR images were statistically higher than those of conventional 3D TSE inversion-recovery with real reconstruction (all,  $P < .001$ ).

**CONCLUSIONS:** The 3D-ZOOMit real IR sequences are superior to conventional 3D TSE inversion-recovery with real reconstruction sequences in visualizing the endolymphatic space, detecting endolymphatic hydrops, and discovering contrast permeability.

**ABBREVIATIONS:** CNR = contrast-to-noise ratio; 3D real IR = 3D inversion-recovery with real reconstruction; EH = endolymphatic hydrops; FOV = field of view; MD = Ménière disease; SI = signal intensity; SPACE = sampling perfection with application-optimized contrasts by using different flip angle evolution; SIR = signal-intensity ratio; t-3D real IR = 3D TSE inversion-recovery with real reconstruction; ZOOMit = zoomed imaging technique with parallel transmission; zs-3D real IR = 3D ZOOMit SPACE real inversion-recovery

Ménière disease (MD) is a chronic disease characterized by spontaneous attacks of vertigo, fluctuating hearing loss, tinnitus, and aural fullness.<sup>1</sup> However, the clinical symptoms are assessed by the patients themselves with poor objectivity, and consequently, MD is often misinterpreted and confused with other pathologies mimicking MD clinically, such as vestibular

migraine.<sup>2</sup> Accordingly, it is difficult and unreliable to diagnose MD solely on the basis of the clinical symptoms, especially when the symptoms are unusual. Additionally, endolymphatic hydrops (EH) is a pathologic manifestation of MD.<sup>3</sup> A 100% correlation between MD and EH has been reported in the literature on the basis of histopathologic analysis of human temporal bones. Therefore, the 2020 revised diagnostic criteria of Japan<sup>4</sup> emphasized the importance of MR imaging for identifying EH for the differential diagnosis between certain MD and definite MD.<sup>5-7</sup>

The current standards for EH MR imaging are either 3D inversion-recovery with real reconstruction (3D real IR) or 3D FLAIR. Naganawa et al<sup>8</sup> reported that 3D TSE inversion-recovery with real reconstruction (t-3D real IR) was superior to 3D FLAIR for the assessment of EH; 3D FLAIR can only differentiate endolymph from perilymph, but not from the surrounding bone, while 3D real IR can better separate them (producing a negative signal for endolymphatic space, a near-zero signal for surrounding

Received December 6, 2022; accepted after revision March 8, 2023.

From the Departments of Radiology (J.L., L.S., N.H., T.X., L.W., R.G.) and Medical Service (L.L.), Shandong Provincial ENT Hospital, Shandong University, Jinan, China; Department of Radiology (G.S.), Shandong Province Qianfoshan Hospital, Jinan, China; Department of Radiology (H.X., R.G., C.L.) and Gong Ruozhen Innovation Studio (R.G.), Shandong Provincial Hospital, Shandong University, Jinan, China; Siemens Healthineers Digital Technology (Shanghai) Co. Ltd (Y.C.), Shanghai, China; and MR Scientific Marketing (L.X.), Diagnostic Imaging, Siemens Healthineers Ltd, Shanghai, China.

Please address correspondence to Chuanting Li, MD, Department of Radiology, Shandong Provincial Hospital, Shandong University, 324 Jing wu wei-qj Rd, Jinan, China; e-mail: lichuantingl@126.com



Indicates article with online supplemental data.

<http://dx.doi.org/10.3174/ajnr.A7842>



bone, and a high signal for perilymphatic space). Unfortunately, conventional t-3D real IR imaging after IV gadolinium-based contrast media occasionally results in an insufficient contrast-to-noise ratio (CNR) to separately visualize the endolymph, perilymph, and surrounding bony structures when evaluating EH in the cochlea.<sup>9,10</sup> Consequently, >90% but not 100% of patients with MD showed EH by pre-mortem MR imaging in at least 1 ear,<sup>11,12</sup> indicating that the current MR imaging technique may underestimate EH. Additionally, detecting slight hydrops at early stages is important to investigate longitudinal changes of EH in MD and understand their relationship. Therefore, a more sensitive and accurate MR image in identifying EH is needed.

An improved 3D real IR imaging technique called 3D zoomed imaging with parallel transmission technique (ZOOMit) sampling perfection with application-optimized contrasts by using different flip angle evolution (SPACE; Siemens) real IR (zs-3D real IR), which allows localized excitation using parallel transmission, was proposed with a higher CNR. The ZOOMit technique powered by parallel transmission architecture can create a zoom effect during MR imaging to shape images, which can be faster compared with the t-3D real IR sequence, and the image quality in the selected zoom area is considerably improved.<sup>13</sup> The SPACE sequence can avoid the blurring effect caused by the long echo chain and can be modified and optimized according to the T2 value of the tissue to be examined.<sup>14</sup> The zs-3D real IR technique, a combination of ZOOMit and the SPACE sequence, can minimize the negative effects of folding artifacts and provide high image quality, decreasing distortion and blurring, and increasing spatial resolution, resulting in faster screening.<sup>13-16</sup> This use leads to the detection and evaluation of smaller lesions, especially in areas prone to susceptibility artifacts, such as the temporal bone,<sup>17,18</sup> for increased diagnostic confidence.

However, the usefulness of this sequence for evaluating EH in MD has not yet been reported. We, therefore, propose the hypothesis that zs-3D real IR is superior to t-3D real IR for the evaluation of EH in MD. To achieve this goal, we compared the differences between these 2 sequences in the CNR, SNR, and signal-intensity ratio (SIR); the scores of endo- and perilymph space; and EH in patients with MD.

## MATERIALS AND METHODS

### Patients

Fifty patients with definite unilateral MD (according to the 2015 revised diagnostic criteria of the Balance Society<sup>3</sup>) who visited our outpatient department (Shandong Provincial ENT Hospital) from December 2020 to October 2021 were recruited consecutively. The exclusion criteria were as follows: 1) trauma or neoplasm of the temporal bone; 2) prior ear surgery or treatment with chemotherapeutic agents or other immunosuppressive drugs; and 3) MR imaging-related contraindications. This prospective study was approved by the ethics committee of our institution, and all patients provided informed consent.

### MR Imaging Experiments

All scans were performed on a 3T MR imaging system (Magnetom Prisma; Siemens) with parallel transmission technology (TimTX TrueShape; Siemens) and a 64-channel array head and neck coil.

**Table 1: Pulse sequence parameters**

Parameter	ZOOMit SPACE Real IR	TSE Real IR
TR (ms)	8000	5300
TE (ms)	491	191
TI (ms)	2250	1850
Turbo factor	192	33
BW (Hz/pixel)	305	213
Voxel (mm)	0.6 × 0.6 × 1.0	0.6 × 0.6 × 0.6
Average	4	1
iPAT	2	2
Scan time	15 min 12 sec	16 min 47 sec
Flip angle mode	Constant	180
FOV (mm)	160 × 80	220 × 220
Matrix size	256 × 128	384 × 384
Reconstruction mode	Real	Real

**Note:**—BW indicates bandwidth; iPAT, integrated parallel acquisition techniques.

We used 2 MR images: conventional t-3D real IR image and zs-3D real IR. All patients had an IV injection of a double dose (0.4 mL/kg body weight) of gadoteridol (ProHance; Bracco Diagnostics).<sup>19,20</sup> All 50 patients with unilateral definite MD underwent conventional t-3D real IR and zs-3D real IR 6 hours after the IV administration of gadolinium.<sup>21</sup> The order of zs-3D real IR and t-3D real IR image acquisitions was randomized. Referring to the previous study,<sup>22</sup> we obtained the optimal scanning parameters on the basis of the initial experimental scanning in some volunteers who were not included in the study. Details of the optimal parameters on 3D real IR are listed in Table 1.

### Data Collection and Analysis

All data were processed at the ADW 4.7 workstation (GE Healthcare). MR images were evaluated by 2 independent radiologists with 10 and 15 years of working experience, respectively, who were blinded to the clinical data in different sessions. The interval between reading sessions for t-3D real IR and zs-3D real IR was >1 week. To avoid reading and measuring bias, we enlarged the display field of view (FOV) for both the conventional t-3D real IR and zs-3D real IR images to 50 × 50 mm.

### Qualitative Analysis

Two radiologists independently reviewed the images, scored the separation of endo- and perilymph, and graded the degree of cochlea and vestibule hydrops on zs-3D real IR and t-3D real IR in the same session.

Scores for the separate visualization of the cochlear and vestibular endolymph were as follows: 1, impossible to recognize; 2, some can be recognized; 3, most can be recognized; and 4, all can be recognized.<sup>23</sup> The corresponding specific scoring for cochlear and vestibular endolymph is demonstrated in Fig 1.

The grading of vestibular and cochlear hydrops was assessed separately. The degree of cochlear hydrops was graded as none, grade I, or grade II according to the criteria previously proposed by Baráth et al.<sup>11</sup> To determine the degree of vestibular hydrops, we used a modified 4-stage grading system (Fig 2) based on Bernaerts et al.<sup>24</sup> In this modified 4-stage grading system, we redefined vestibular EH (II) as the confluence of the saccule and utricle with a continuous peripheral rim enhancement and vestibular EH (III) as the confluence in which the perilymphatic

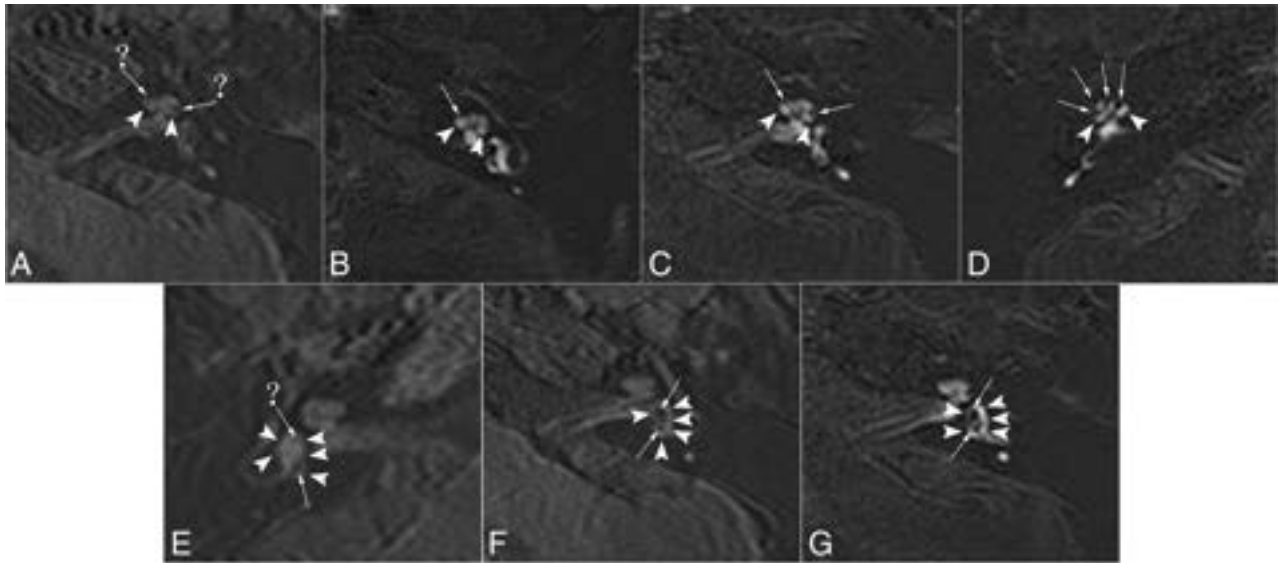


**FIG 1.** The images of different scores for the separate visualization of the cochlear and vestibular endolymph in patients with MD. A, E, and F, 3D TSE real IR images. The perilymph is slightly enhanced (arrowheads). B, C, D, and G, ZOOMit SPACE real IR images. The perilymph is markedly enhanced (arrowheads). A, Score 1 for the cochlea. It is impossible to recognize the cochlear duct (endolymph, arrows and question marks). B, Score 2 for the cochlea. The cochlear duct (endolymph, arrow) was recognized only in the basal turn of the cochlea. C, Score 3 for the cochlea. The cochlear duct (endolymph, arrows) was recognized in the basal and middle turns of the cochlea. D, Score 4 for the cochlea. The cochlear duct (endolymph, arrows) was recognized in the basal, middle, and apical turns of the cochlea. E, Score 2 for the vestibule. A small part of the boundary for the utricle (arrow) was clearly displayed ( $\leq$  one-half of vestibular endolymph), and the edge could be clearly delineated, while the rest of the boundary was blurred (saccule, arrow and question mark). F, Score 3 for the vestibule. Most of the boundary of the saccule and the whole utricle (arrows) was clearly displayed ( $>$  one-half and  $<$  1 of vestibular endolymph), and the edge could be clearly delineated. G, Score 4 for the vestibule. The boundary of the saccule and utricle (endolymph, arrows) was clearly displayed (the whole vestibular endolymph).

enhancement is no longer continuous (Fig 2). In our experience, some patients with vestibular EH (II) were categorized as having serious EH according to the grading criteria for EH reported by Nakashima et al.<sup>25</sup>

Next, the evaluation results of the 2 radiologists were collected. If there were any discrepancies between the 2, those images were evaluated again by a third radiologist with 20 years of experience and the results were regarded as the final results. All radiologists graded the degree of cochlea and vestibule hydrops according to the criteria previously proposed by Baráth et al<sup>11</sup> and the modified 4-stage grading system based on Bernaerts et al.<sup>24</sup>

### Quantitative Analysis

Referring to method of Naganawa et al,<sup>23</sup> the signal intensity (SI) in all patients with MD was measured. The method (Fig 3) was as follows: We set a 1-mm<sup>2</sup> circular ROI on the center of the scala tympani of the cochlear basal turn ( $SI_{\text{peri}}$ ) at the best-enhanced section (Fig 3A).<sup>23</sup> For the SI of the endolymph ( $SI_{\text{endo}}$ ), we set a 1-mm<sup>2</sup> circular ROI on the utricle (Fig 3B), where a larger ROI can usually be drawn than in other endolymphatic spaces and the utricle is most consistently recognized even in subjects without EH. Two oblique sagittal reference slices were obtained using multiplanar reconstructions from coronal and axial slices in the cochlear basal turn and vestibular plane, respectively. When we combined the 2 reference slices, the ROIs in the scala tympani and utricle were accurately delineated on axial images. A 10-mm<sup>2</sup> circular ROI was set in the left middle cerebellar peduncle of the image ( $SI_{\text{mcp}}$ ) (Fig 3C).<sup>12</sup> Noise was defined as the SD of the ROI with 6 mm<sup>2</sup> in the artifact-free air area ( $SD_{\text{noise}}$ ) of the ipsilateral external auditory canal (Fig 3D).

The ROI was first drawn on the zs-3D real IR image for the right side and then copied to the left side. It was then drawn on the corresponding t-3D real IR image. In the case of any misregistration between the zs-3D real IR and t-3D real IR images, the ROI placement was manually adjusted. The average SI or SD values of the ROI automatically generated by the workstation were recorded. Blinding to the 2 sequences performed in the present study was not feasible because their FOVs were different. Two radiologists determined each ROI twice for each patient and averaged the SI of the 2 measurements for analysis. Finally, the CNR, SNR, and SIR values were dependent on the average value and were calculated using the following equations:

$$\text{CNR} = (SI_{\text{peri}} - SI_{\text{endo}}) / SD_{\text{noise}},$$

$$\text{SNR} = SI_{\text{peri}} / SD_{\text{noise}},$$

$$\text{SIR} = SI_{\text{peri}} / SI_{\text{mcp}}.$$

We then compared the CNR, SNR, and SIR values of zs-3D real IR and t-3D real IR and further compared the SIR values in the affected and asymptomatic sides by zs-3D real IR or t-3D real IR.

### Statistical Analyses

Statistical analyses were performed using SPSS (Version 25.0; IBM). Interobserver agreement between the first 2 radiologists was tested using  $\kappa$  statistics. For quantitative and qualitative analyses, we used the paired samples *t* test or the Wilcoxon signed-ranked test. Statistical significance was set at  $P < .05$ .

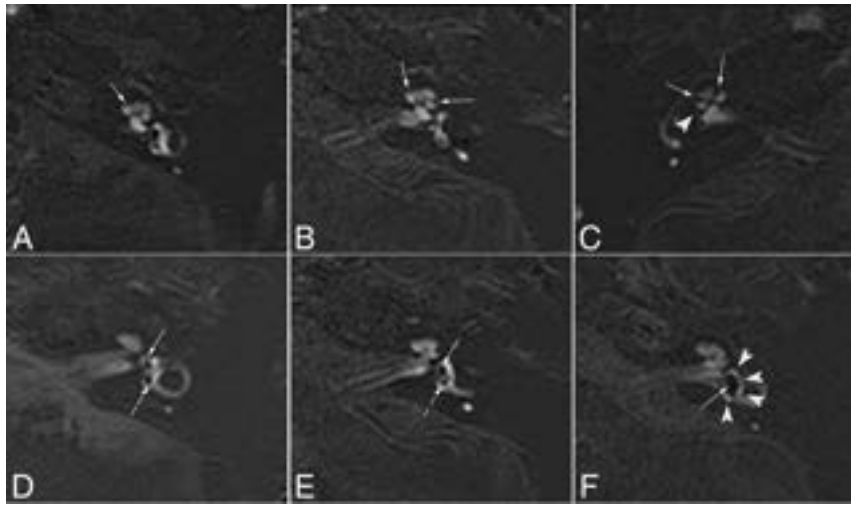


**FIG 2.** ZOOMit SPACE real IR images of different degrees of cochlear and vestibular EH in patients with MD. *A*, Normal cochlea (none). The scala media is minimally visible (*solid arrow*). *B*, Cochlear EH (I). The scala media becomes indirectly visible (*solid arrows*) as a nodular black cutout of the scala vestibuli, which was partially obstructed. *C*, Cochlear EH (II) and vestibular EH (III). The scala vestibuli is fully obliterated owing to the distended scala media (*solid arrows*). There is major or full obliteration of the bony vestibule; occasionally, only a few vestibular perilymphatic spaces near the cochlea remained (*arrowhead*). *D*, Normal vestibule. The saccule (*solid arrow*) and utricle (*dotted arrow*) are visibly separated and take less than one-half of the area of the vestibule. *E*, Vestibular EH (I). The saccule (*solid arrow*), normally smaller than the utricle, has become equal or larger than the utricle but is not yet confluent with the utricle (*dotted arrow*). *F*, Vestibular EH (II). There is a confluence of the saccule and utricle (*solid arrow*), with a continuous peripheral rim enhancement of the perilymphatic space (*arrowheads*).

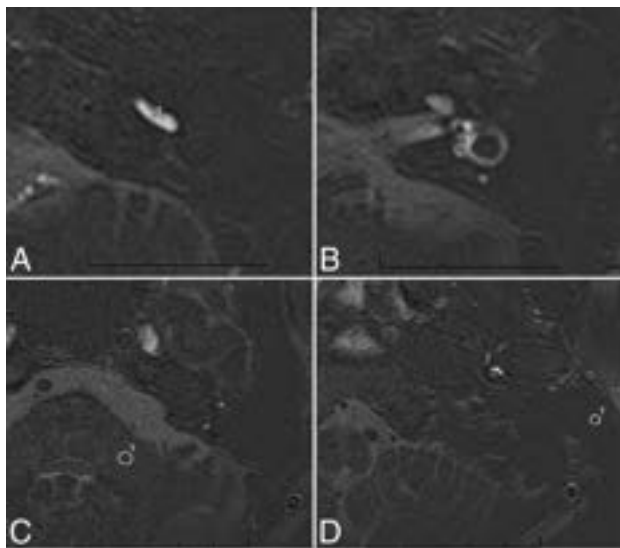


**FIG 3.** *A*, ROI image of zs-3D real IR at the level of the lower cochlear basal turn. *Circle 1* of 1 mm<sup>2</sup> indicates the ROI for the perilymph in the scala tympani in the basal turn of the cochlea. *B*, Zs-3D real IR image at the middle level of the vestibule. *Circle 1* of 1 mm<sup>2</sup> indicates the ROI for the endolymph in the utricle. *C*, The zs-3D real IR image at the level of the left middle cerebellar peduncle. *Circle 1* of 10 mm<sup>2</sup> indicates the ROI for SI in the left middle cerebellar peduncle. *D*, The zs-3D real IR image at the level of the artifact-free air area of the ipsilateral external auditory canal. *Circle 1* of 6 mm<sup>2</sup> indicates the ROI for the SD in the artifact-free air area of the ipsilateral external ear.

## RESULTS

### Population

Fifty consecutive patients with definite unilateral MD (right side = 21 and left side = 29) were included in our study. Additionally, there were 22 men and 28 women with a mean age of 53.06 (SD, 13.28) years (ranging from 16 to 81 years of age).

### Qualitative Analysis

The 2 radiologists completely agreed on the final grading and scoring of all evaluated cochleae and vestibules.  $\kappa$  values evaluating interobserver agreement for cochlear endolymph recognition and cochlear hydrops were 0.58 and 0.56 for t-3D real IR and 0.97 and 0.96 for zs-3D real IR. Moreover, those for the vestibule were 0.98 and 0.97 for t-3D real IR and 1.0 and 1.0 for zs-3D real IR.

Separate visualization of the endolymphatic space in the cochlea and vestibule of 50 patients with MD was evaluated using zs-3D real IR and t-3D real IR images, and the scores are listed in Table 2. For recognition of endolymphatic space in the cochlea, none of the 50 ears scored 1 on the affected side on zs-3D real IR, but 2 of the 50 ears scored

1 on t-3D real IR. None of the asymptomatic ears scored 1 on the zs-3D real IR, while 3 asymptomatic ears scored 1 on the t-3D real IR. Meanwhile, for the recognition of the endolymphatic space in the vestibule, 9 ears scored 3 on the affected side on zs-3D real IR, but 22 ears scored 3 on t-3D real IR; similarly, one of the asymptomatic ears scored 3 on the zs-3D real IR, while 23 asymptomatic ears scored 3 on the t-3D real IR. Obviously, among all patients, we recognized the endolymphatic space for both the cochlea and vestibule better on zs-3D real IR than on t-3D real IR on both affected and asymptomatic sides (all  $P < .001$ ).

The percentages of inner ear EH on zs-3D and t-3D real IR in the 50 affected ears were 98.0% and 96.0%, respectively. Consequently, there was no difference between the 2 sequences in the evaluation of the inner ear EH ( $P = 1.000$ ). Furthermore, the grading of vestibular and cochlear hydrops of 50 patients with MD by the 2 sequences is detailed in Table 3. The percentages of no cochlear EH, cochlear EH (I), and cochlear EH (II) on affected side were 14.0%, 24.0%, and 62.0% in zs-3D images and 30.0%, 8.0%, and 62.0% in t-3D real IR images, respectively (Table 3). Consequently, there were differences between the 2 sequences in evaluating cochlear EH of the affected sides ( $Z = -2.83, P = .005$ ), but not in vestibular EH ( $Z = 0.00, P = 1.000$ ). By means of the  $\alpha$ -segmentation method post hoc test, significant differences were observed between the 2 sequences in evaluating no cochlear EH and cochlear EH (I) ( $P < .017$ ). There were no differences between the 2 sequences in evaluating cochlear or vestibular EH of asymptomatic sides.

### Quantitative Analysis

The mean CNR, SNR, and SIR values of the affected side on zs-3D real IR were 1.51, 1.56, and 8.19 times higher than those of t-3D real IR (Online Supplemental Data). Obviously, the CNR, SNR, and SIR values of zs-3D real IR images were statistically higher than those of t-3D real IR images on both the affected and asymptomatic sides (all,  $P < .001$ ) (Fig 4). Additionally, there was a significant interaural difference in SIR in patients with definite unilateral MD by zs-3D real IR ( $Z = -5.266$ ,  $P < .001$ ) and t-3D real IR ( $Z = -5.063$ ,  $P < .001$ ).

**Table 2: Scores for separate visualization of endolymphatic space in the cochlea and vestibule by 2 pulse sequences in 50 patients with MD**

Visualization	Sequence	Score			
Affected side		4	3	2	1
Cochlea	3D ZOOMit SPACE real IR	37	13	0	0
	3D TSE real IR	17	28	3	2
Vestibule	3D ZOOMit SPACE real IR	40	9	1	0
	3D TSE real IR	27	22	1	0
Asymptomatic side					
Cochlea	3D ZOOMit SPACE real IR	3	45	2	0
	3D TSE real IR	1	28	18	3
Vestibule	3D ZOOMit SPACE real IR	49	1	0	0
	3D TSE real IR	27	23	0	0

**Table 3: Number and percentage distribution of cochlear and vestibular EH grading by 2 pulse sequences in 50 patients with MD**

	3D ZOOMit SPACE Real IR (No.) (%)	3D TSE Real IR (No.) (%)	Wilcoxon Signed-Rank Test	
			Z Value	P Value
Affected side				
No cochlear EH	7 (14.0) <sup>a</sup>	15 (30.0)	-2.83	.005
Cochlear EH (I)	12 (24.0) <sup>a</sup>	4 (8.0)		
Cochlear EH (II)	31 (62.0)	31 (62.0)		
No vestibular EH	3 (6.0)	3 (6.0)	0.00	1.000
Vestibular EH (I)	13 (26.0)	13 (26.0)		
Vestibular EH (II)	18 (36.0)	18 (36.0)		
Vestibular EH (III)	16 (32.0)	16 (32.0)		
Asymptomatic side				
No cochlear EH	46 (92.0)	48 (96.0)	-1.41	.157
Cochlear EH (I)	3 (6.0)	1 (2.0)		
Cochlear EH (II)	1 (2.0)	1 (2.0)		
No vestibular EH	48 (96.0)	48 (96.0)	0.00	1.000
Vestibular EH (I)	0 (0.0)	0 (0.0)		
Vestibular EH (II)	2 (4.0)	2 (4.0)		
Vestibular EH (III)	0 (0.0)	0 (0.0)		

<sup>a</sup> Compared with the 3D TSE real IR sequence,  $P < .017$ .

### DISCUSSION

In our study, CNR, SNR, and SIR values; endo- and perilymph scores; and EH grading by zs-3D real IR were higher than those by t-3D real IR.

Our results suggest that visualization of the endolymphatic space by IV gadolinium-based contrast media might be higher by zs-3D real IR compared with t-3D real IR, especially in the cochlea. The possible reasons might be as follows: 1) Owing to the morphologic differences in the utricle, saccule, and cochlear duct, the cochlear endolymph was smaller than the vestibular endolymph on axial MR images. 2) The ZOOMit SPACE with an independent parallel transmission (pTX; Siemens Healthcare) system prevents the appearance of folds over artifacts and uses dynamic excitation pulses to achieve selective FOV (zoomed) imaging, thus reducing the acquisition time without introducing aliasing artifacts.<sup>26,27</sup> Reduced FOV images negated the need to increase the number of phase-encoding steps and the penalty of an increased minimum measurement time,<sup>14</sup> which leads to further improvement in image quality in terms of markedly reduced susceptibility artifacts. Less image blur and artifacts, higher spatial resolution, and faster screening were observed with zs-3D real IR compared with t-3D real IR. Thus, the zs-3D real IR images provided better separation of endo- and perilymph space in most cases.

The improved image quality with zs-3D real IR could potentially help more precisely identify mild EH in MD, especially for detecting cochlear EH (I). There were differences between zs-3D and t-3D real IR sequences in evaluating cochlear EH in MD. In a previous animal study, 1 of the 14 guinea pigs with apical turns of the cochlea EH was not found using t-3D real IR images.<sup>9</sup> Similar to findings in this study, 7 patients with MD showed no evident cochlear EH by conventional t-3D real IR, but an exact cochlear EH (I) was found by zs-3D real IR. The better sensitivity shown by the zs-3D real IR sequence makes it preferable to the t-3D real IR for the detection of mild cochlear EH. This preference is of particular interest in early disease, when symptoms

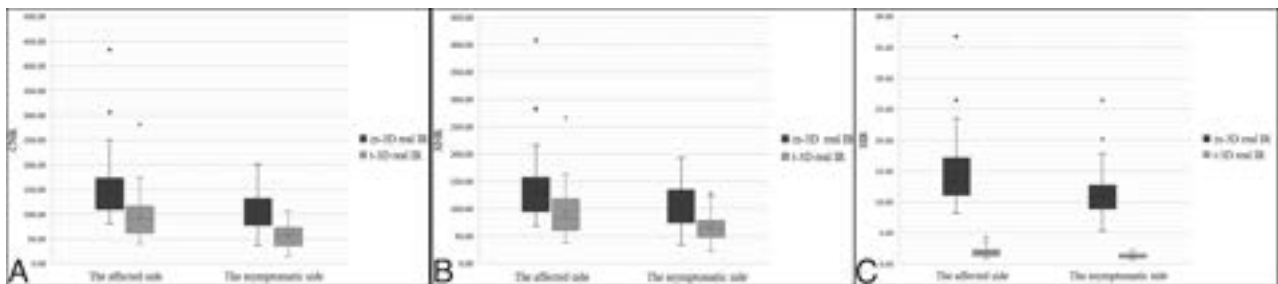


**FIG 4.** Differences in the CNRs (A), SNRs (B), and SIRs (C) of the affected and asymptomatic sides are found between the 2 sequences ( $P < .001$ ).



and signs normalize after a crisis stops. Moreover, the 2020 revised diagnostic criteria of Japan<sup>4</sup> emphasized the importance of MR imaging for identifying EH to differentially distinguish certain MD and definite MD. Therefore, for suspicious MD with atypical clinical manifestations, the presence or absence of EH determined by MR imaging is very helpful for clinical diagnosis and treatment.

Furthermore, the present study found that the CNRs on both sides using the zs-3D real IR sequence were higher than those using the t-3D real IR sequence. The former sequence was more beneficial for visualizing EHs because it primarily reflected the differences in signals between the endo- and perilymphatic spaces. Similar to the CNR values, the SNR and SIR values of both sides were significantly higher on zs-3D real IR than on t-3D real IR because the zs-3D real IR sequence used a reduced FOV and more average times. The cochlea, endo- and perilymphatic spaces, and surrounding bone were differentiated well in images of the zs-3D real IR sequence compared with images of the t-3D real IR sequence.

Most interesting, the affected ears of 50 patients with MD showed higher perilymphatic enhancement compared with asymptomatic ears, consistent with the results of previously published studies.<sup>28-32</sup> SIR was a good indicator for the quantitative evaluation of contrast permeability, which can give hints about blood-labyrinth barrier damage.<sup>29</sup> Meanwhile, the blood-labyrinth barrier may play a role in the process of EH in MD.<sup>33</sup> Moreover, the progression of MD may be monitored using SIR. In this study, the perilymph in the images obtained by the zs-3D real IR sequence demonstrated an obviously higher signal compared with the images obtained by the t-3D real IR sequence. A previous study revealed that in 1 case with faint enhancement of the cochlea, the image quality was inadequate with t-3D real IR.<sup>10</sup> Therefore, compared with t-3D real IR imaging, zs-3D real IR imaging may be more sensitive to contrast permeability, indicating possible blood-labyrinth barrier damage, which may be of great significance for the treatment choice of patients with MD.

This study has some limitations. The ROIs for the endolymph and perilymph were small. To ensure the reliability of the SI measured in the small ROI of the endolymph and perilymph and to diminish the measurement error, 2 radiologists determined every ROI twice for each patient and averaged the SIs of the 2 measurements for analysis. In addition, the oblique sagittal reference slices were obtained to enable the ROIs in the scala tympani and utricle to be accurately delineated on axial images.

## CONCLUSIONS

The zs-3D real IR sequence provides higher CNR, SNR, and SIR values and is superior to conventional t-3D real IR sequences in reliably visualizing the endolymphatic space, precisely detecting EH, and sensitively revealing contrast permeability. The zs-3D real IR sequence may potentially replace conventional t-3D real IR sequences for the diagnosis of MD in the future.

Disclosure forms provided by the authors are available with the full text and PDF of this article at [www.ajnr.org](http://www.ajnr.org).

## REFERENCES

1. Committee on Hearing and Equilibrium guidelines for the diagnosis and evaluation of therapy in Ménière's disease: American Academy of Otolaryngology-Head and Neck Foundation, Inc. *Otolaryngol Head Neck Surg* 1995;113:181-85 CrossRef Medline
2. Shephard NT. Differentiation of Ménière's disease and migraine-associated dizziness: a review. *J Am Acad Audiol* 2006;17:69-80 CrossRef Medline
3. Lopez-Escamez JA, Carey J, Chung WH, et al; Classification Committee of the Barany Society; Japan Society for Equilibrium Research; European Academy of Otolology and Neurotology (EAONO); Equilibrium Committee of the American Academy of Otolaryngology-Head and Neck Surgery (AAO-HNS), Korean Balance Society. Diagnostic criteria for Meniere's disease. *J Vestib Res* 2015;25:1-7 CrossRef Medline
4. Iwasaki S, Shojaku H, Murofushi T, et al; Committee for Clinical Practice Guidelines of Japan Society for Equilibrium Research. Diagnostic and therapeutic strategies for Meniere's disease of the Japan Society for Equilibrium Research. *Auris Nasus Larynx* 2021;48:15-22 CrossRef Medline
5. Merchant SA, Adams JC, Nadol JB Jr. Pathophysiology of Meniere's syndrome: are symptoms caused by endolymphatic hydrops? *Otol Neurotol* 2005;26:74-81 CrossRef Medline
6. Rauch SD, Merchant SN, Thedinger BA. Meniere's syndrome and endolymphatic hydrops: double-blind temporal bone study. *Ann Otol Rhinol Laryngol* 1989;98:873-83 CrossRef Medline
7. Foster CA, Breeze RE. Endolymphatic hydrops in Ménière's disease: cause, consequence, or epiphenomenon? *Otol Neurotol* 2013;34:1210-14 CrossRef Medline
8. Naganawa S, Satake H, Kawamura M, et al. Separate visualization of endolymphatic space, perilymphatic space and bone by a single pulse sequence: 3D-inversion recovery imaging utilizing real reconstruction after intratympanic Gd-DTPA administration at 3 Tesla. *Eur Radiol* 2008;18:920-24 CrossRef Medline
9. Wang F, Lyu H, Zhao M, et al. Assessment of cochlea endolymphatic hydrops using 3-D FLAIR and 3-D Real IR sequence in guinea pigs via 3T MRI after intratympanic gadolinium: a histopathological comparison. *Otol Neurotol* 2017;38:585-90 CrossRef Medline
10. Naganawa S, Sone M, Yamazaki M, et al. Visualization of endolymphatic hydrops after intratympanic injection of Gd-DTPA: comparison of 2D and 3D real inversion recovery imaging. *Magn Reson Med Sci* 2011;10:101-06 CrossRef Medline
11. Baráth K, Schuknecht B, Naldi AM, et al. Detection and grading of endolymphatic hydrops in Meniere disease using MR imaging. *AJNR Am J Neuroradiol* 2014;35:1387-92 CrossRef Medline
12. van Steekelenburg JM, van Weijnen A, de Pont LM, et al. Value of endolymphatic hydrops and perilymph signal intensity in suspected Meniere disease. *AJNR Am J Neuroradiol* 2020;41:529-34 CrossRef Medline
13. Blasche MR, Riffel P, Lichy M. TimTX TrueShape and syngo ZOOMit technical and practical aspects. *Magnetom Flash* 2012;1:74-84
14. Naganawa SK, Fukatsu H, Ishigaki T, et al. High-speed imaging at 3 Tesla: a technical and clinical review with an emphasis on whole-brain 3D imaging. *Magn Reson Med Sci* 2004;3:177-87 CrossRef Medline
15. Riffel PM, Michaely HJ. Improved echo planar diffusion-weighted imaging of the head and neck using syngo ZOOMit. *Magnetom Flash* 2013;2:68-71
16. Riffel P, Michaely HJ, Morelli JN, et al. Zoomed EPI-DWI of the pancreas using two-dimensional spatially-selective radiofrequency excitation pulses. *PLoS One* 2014;9:e89468 CrossRef Medline
17. Schulze M, Seeger A, Reimann K, et al. Parallel-transmit-accelerated 2D selective RF excitation MR of the temporal bone: enhanced resolution of labyrinthine and IAC structures. *Otol Neurotol* 2016;37:408-14 CrossRef Medline
18. Schulze M, Reimann K, Seeger A, et al. Improvement in imaging common temporal bone pathologies at 3 T MRI: small structures benefit from a small field of view. *Clin Radiol* 2017;72:e261e1-67e21 CrossRef Medline

19. Xie J, Zhang W, Zhu J, et al. **Comparison of inner ear MRI enhancement in patients with Meniere's disease after intravenous injection of gadobutrol, gadoterate meglumine, or gadodiamide.** *Eur J Radiol* 2021;139:109682 CrossRef Medline
20. Eliezer M, Poillon G, Gillibert A, et al. **Comparison of enhancement of the vestibular perilymph between gadoterate meglumine and gadobutrol at 3-Tesla in Meniere's disease.** *Diagn Interv Imaging* 2018;99:271–77 CrossRef Medline
21. Li J, Sun L, Wang L, et al. **Contrast-enhanced three-dimensional fluid-attenuated inversion recovery imaging with an optimal scan interval and angulation to visualize endolymphatic hydrops.** *Iran J Radiol* 2022;19:e122424 CrossRef
22. Ohashi T, Naganawa S, Takeuchi A, et al. **Quantification of endolymphatic space volume after intravenous administration of a single dose of gadolinium-based contrast agent: 3D-real inversion recovery versus HYDROPS-Mi2.** *Magn Reson Med Sci* 2020;19:119–24 CrossRef Medline
23. Naganawa S, Kawai H, Sone M, et al. **Increased sensitivity to low concentration gadolinium contrast by optimized heavily T2-weighted 3D-FLAIR to visualize endolymphatic space.** *Magn Reson Med Sci* 2010;9:73–80 CrossRef Medline
24. Bernaerts A, Vanspauwen R, Blaivie C, et al. **The value of four stage vestibular hydrops grading and asymmetric perilymphatic enhancement in the diagnosis of Meniere's disease on MRI.** *Neuroradiology* 2019;61:421–29 CrossRef Medline
25. Nakashima T, Naganawa S, Pyykko I, et al. **Grading of endolymphatic hydrops using magnetic resonance imaging.** *Acta Otolaryngol Suppl* 2009;5–8 CrossRef Medline
26. Seeger A, Schulze M, Schuettauf F, et al. **Advanced diffusion-weighted imaging in patients with optic neuritis deficit: value of reduced field of view DWI and readout-segmented DWI.** *Neuroradiol J* 2018;31:126–32 CrossRef Medline
27. Morimoto K, Yoshida T, Sugiura S, et al. **Endolymphatic hydrops in patients with unilateral and bilateral Meniere's disease.** *Acta Otolaryngol* 2017;137:23–28 CrossRef Medline
28. Shi S, Guo P, Wang W. **Magnetic resonance imaging of Meniere's disease after intravenous administration of gadolinium.** *Ann Otol Rhinol Laryngol* 2018;127:777–82 CrossRef Medline
29. Chen W, Geng Y, Niu Y, et al. **Inner ear MRI enhancement based on three dimensional-real IR sequence in patients with Meniere's disease after intravenous gadolinium injection: comparison of different doses used and exploration of an appropriate dose.** *Clin Otolaryngol* 2022;47:717–23 CrossRef Medline
30. Tagaya M, Yamazaki M, Teranishi M, et al. **Endolymphatic hydrops and blood-labyrinth barrier in Meniere's disease.** *Acta Otolaryngol* 2011;131:474–79 CrossRef Medline
31. Yamazaki M, Naganawa S, Tagaya M, et al. **Comparison of contrast effect on the cochlear perilymph after intratympanic and intravenous gadolinium injection.** *AJNR Am J Neuroradiol* 2012;33:773–78 CrossRef Medline
32. Suzuki H, Teranishi M, Sone M, et al. **Contrast enhancement of the inner ear after intravenous administration of a standard or double dose of gadolinium contrast agents.** *Acta Otolaryngol* 2011;131:1025–31 CrossRef Medline
33. Zhang W, Xie J, Hui L, et al. **The correlation between endolymphatic hydrops and blood-labyrinth barrier permeability of Meniere disease.** *Ann Otol Rhinol Laryngol* 2021;130:578–84 CrossRef Medline

# MELAS: Phenotype Classification into Classic-versus-Atypical Presentations

C.A.P.F. Alves, A. Zandifar, J.T. Peterson, S.Z. Tara, R. Ganetzky, A.N. Viaene, S. Andronikou, M.J. Falk, A. Vossough, and A.C. Goldstein



## ABSTRACT

**BACKGROUND AND PURPOSE:** An increased number of pathogenic variants have been described in mitochondrial encephalomyopathy lactic acidosis and strokelike episodes (MELAS). Different imaging presentations have emerged in parallel with a growing recognition of clinical and outcome variability, which pose a diagnostic challenge to neurologists and radiologists and may impact an individual patient's response to therapeutic interventions. By evaluating clinical, neuroimaging, laboratory, and genetic findings, we sought to improve our understanding of the sources of potential phenotype variability in patients with MELAS.

**MATERIALS AND METHODS:** This retrospective single-center study included individuals who had confirmed mitochondrial DNA pathogenic variants and a diagnosis of MELAS and whose data were reviewed from January 2000 through November 2021. The approach included a review of clinical, neuroimaging, laboratory, and genetic data, followed by an unsupervised hierarchical cluster analysis looking for sources of phenotype variability in MELAS. Subsequently, experts identified "victory-variables" that best differentiated MELAS cohort clusters.

**RESULTS:** Thirty-five patients with a diagnosis of mitochondrial DNA-based MELAS (median age, 12 years; interquartile range, 7–24 years; 24 female) were eligible for this study. Fifty-three discrete variables were evaluated by an unsupervised cluster analysis, which revealed that two distinct phenotypes exist among patients with MELAS. After experts reviewed the variables, they selected 8 victory-variables with the greatest impact in determining the MELAS subgroups: developmental delay, sensorineural hearing loss, vision loss in the first strokelike episode, Leigh syndrome overlap, age at the first strokelike episode, cortical lesion size, regional brain distribution of lesions, and genetic groups. Ultimately, 2-step differentiating criteria were defined to classify atypical MELAS.

**CONCLUSIONS:** We identified 2 distinct patterns of MELAS: classic MELAS and atypical MELAS. Recognizing different patterns in MELAS presentations will enable clinical and research care teams to better understand the natural history and prognosis of MELAS and identify the best candidates for specific therapeutic interventions.

**ABBREVIATIONS:** CSLL = cortical strokelike lesion; LS = Leigh syndrome; MELAS = mitochondrial encephalomyopathy lactic acidosis and strokelike episodes; mtDNA = mitochondrial DNA; mt-tRNA = mitochondrial tRNA; SLE = strokelike episode; SNHL = sensorineural hearing loss

Mitochondrial encephalomyopathy lactic acidosis and strokelike episodes (MELAS) is considered a canonical mitochondrial disorder,<sup>1,2</sup> primarily caused by pathogenic variants

in mitochondrial DNA (mtDNA), though few nuclear genes have been considered.<sup>3-5</sup>

A 2012 study updated the clinical criteria for MELAS diagnosis from the previous ones, described in 1992.<sup>6,7</sup> The current criteria include at least 2 category A and at least two category B criteria. Category A is based on clinical symptoms and neuroimaging findings, including headaches with vomiting, seizures, hemiplegia, cortical blindness, and acute focal lesions involving the brain cortex.<sup>7,8</sup> Category B is based on laboratory results showing increased plasma or CSF lactate, mitochondrial abnormalities on muscle biopsy, and a MELAS-related pathogenic variant on genetic testing. Although these well-defined MELAS diagnostic criteria have been established, there is still large clinical, imaging, and outcome variability among patients with a diagnosis of MELAS.<sup>9</sup>

The *MT-TL1* m.3243A>G is considered the most common pathogenic variant identified with MELAS.<sup>10,11</sup> However, reports

Received December 22, 2022; accepted after revision February 24, 2023.

From the Division of Neuroradiology (C.A.P.F.A., A.Z., S.A., A.V.), Department of Radiology; Mitochondrial Medicine Frontier Program (J.T.P., S.Z.T., R.G., M.J.F., A.C.G.), Division of Human Genetics, Department of Pediatrics; and Department of Pathology and Laboratory Medicine (A.N.V.), The Children's Hospital of Philadelphia, Philadelphia, Pennsylvania; and Departments of Pediatrics (R.G., M.J.F., A.C.G.), Pathology and Laboratory Medicine (A.N.V.), and Radiology (S.A., A.V.), Perelman School of Medicine, University of Pennsylvania Perelman School of Medicine, Philadelphia, Pennsylvania.

C.A.P.F. Alves and A. Zandifar contributed equally to this work.

A. Vossough and A.C. Goldstein shared the last authorship.

Please address correspondence to Cesar Augusto Alves, MD, PhD, Division of Neuroradiology, Department of Radiology, Children's Hospital of Philadelphia, 324 South 34th St, Philadelphia, PA 19104; e-mail: alvesc@chop.edu; @cesaralvesneuro

Indicates article with online supplemental data.

<http://dx.doi.org/10.3174/ajnr.A7837>

show that the phenotype has a more diverse and heterogeneous clinical spectrum, even within families.<sup>12-15</sup> Moreover, other mtDNA causes of MELAS include but are not limited to variants such as m.3271T>C and m.3252A>G in *MT-TL1*. Recently, MELAS has been described with other mtDNA genes, particularly those linked to the mitochondrial respiratory chain complex subunits involved with oxidative phosphorylation.<sup>9,16,17</sup> In parallel with the clinical and genetic variability, new imaging manifestations are being recognized. Mitochondrial experts believe these advances warrant a better, more granular delineation of this disorder and a revision of the current diagnostic criteria, which may have direct implications for appropriate management and formulation of clinical trials. Therefore, we sought to investigate the variations in clinical features, brain MR imaging, laboratory and genetic findings, and outcome differences in a mtDNA-based MELAS cohort to provide an updated and comprehensive classification of this disorder.

## MATERIALS AND METHODS

### Setting and Participants

We designed this retrospective study according to the Strengthening the Reporting of Observational Studies in Epidemiology statement.<sup>18</sup> The institutional review board (The Children's Hospital of Philadelphia) approved this study, and informed consent was obtained. Brain MRIs were retrieved from January 2000 to November 2021. We identified clinical cases from the Mitochondrial Medicine Frontier Program. All individuals with a diagnosis followed and treated as MELAS at our institution who had an available MR imaging were included. All included individuals had a genetically confirmed primary mitochondrial disorder due to any pathogenic mtDNA variant with a heteroplasmy level of >30% in at least 1 tested tissue.<sup>19</sup> Individuals with nuclear DNA etiologies were excluded.

### Clinical and Outcome Data

Symptoms presenting from the onset of the disorder until the last visit were recorded. One pediatric neurologist (A.C.G.) specializing in mitochondrial disorders with 20 years of experience reviewed the medical records to confirm the diagnosis and the accuracy of the collected clinical data.

### Genetic, Laboratory, and Histopathology Data

A genetic counselor (J.T.P.) reviewed genetic analyses performed to confirm the pathogenic variants. Patients with nuclear DNA etiologies causing stroke-like episodes were not included in this MELAS cohort because they likely have distinct pathogenesis and may represent a better clinically-defined entity such as *POLG*-related disorders.<sup>20,21</sup> Comprehensive mtDNA genome sequencing was completed via next-generation sequencing for most of the cohort (31/35). Four of 35 individuals had only historical results available and had either Sanger sequencing, real-time amplification refractory mutation system polymerase chain reaction, or *HaeIII* restriction digest testing for m.3243A>G. The maternal inheritance pattern was confirmed when parental samples were available and the proband had clinical and MR imaging findings supporting a diagnosis of MELAS. Laboratory data (highest lifetime plasma, CSF lactate, and plasma alanine) were noted when available. A

pediatric neuropathologist (A.N.V.) reviewed any available pathology specimen results.

### MR Imaging

MR imaging was performed on a variety of 1.5T and 3T scanners (Siemens, GE Healthcare, Philips Healthcare). Detailed imaging protocol and parameters can be found in a previous article published by our group.<sup>9</sup> Additional sequences including single-voxel <sup>1</sup>H-MR spectroscopy, postcontrast axial T1-weighted imaging, arterial spin-labeling, SWI, and DTI were assessed when available.

Brain MR imaging, previously performed for clinical purposes, was independently reviewed by 2 neuroradiologists (C.A.P.F.A. and A.V.). MR imaging examinations were reviewed on clinical-grade viewing software, and data were collected using a standardized form. Reviewers were blinded to patients' genetic and clinical features, but not to the primary diagnosis. MR imaging findings were described according to their signal-intensity characteristics and location in the brain. For cortical lesions, in addition to the overall description, further classification was based on the presence of small (<30 mm) and/or large (≥30 mm) cortical stroke-like lesions (CSLLs) and number, symmetry, anatomic and regional distribution of the lesions (frontal and anterior parietal lobes were considered the anterior region, and posterior parietal, insula, occipital, and temporal lobes, were considered posterolateral regions), and the presence of subcortical white matter extension. CSLLs were measured in their largest anterior-posterior extension in the axial plane using FLAIR and/or DWI sequences.

### Unsupervised Clustering Analysis

All potential variables, including clinical, laboratory, and imaging data, were pooled. We performed an unsupervised hierarchical cluster analysis to expose any potential phenotype patterns across cases of MELAS. To evaluate differences in variable frequencies among the clusters, we compared all included variables using appropriate statistical tests. In the second step, we calculated the agglomerative coefficient of our clustering before and after removing each variable to find its contribution size. According to agglomerative coefficient changes, we selected the strongest variables to differentiate the subgroups. On the basis of the modified variable list, the final agglomerative coefficient was calculated to confirm the optimization of our cluster analysis. The association between the assigned clusters and the genetic data was assessed at this step. To ensure the quality of clustering, we used the average silhouette method to confirm the optimal number of clusters.

### Expert Panel

A team of mitochondrial medicine specialists was invited to the expert panel. They were provided with a summary of unidentified patient data and were asked to categorize patients into classic MELAS or an atypical phenotype based on the modified variable list. The experts were blinded to the results of unsupervised clustering during categorization. Furthermore, they indicated which modified variables played an important role in categorization and could be considered "victory-variables" to differentiate the clusters. Finally, the expert clustering was compared with the results of the unsupervised cluster analysis. To define the differentiating



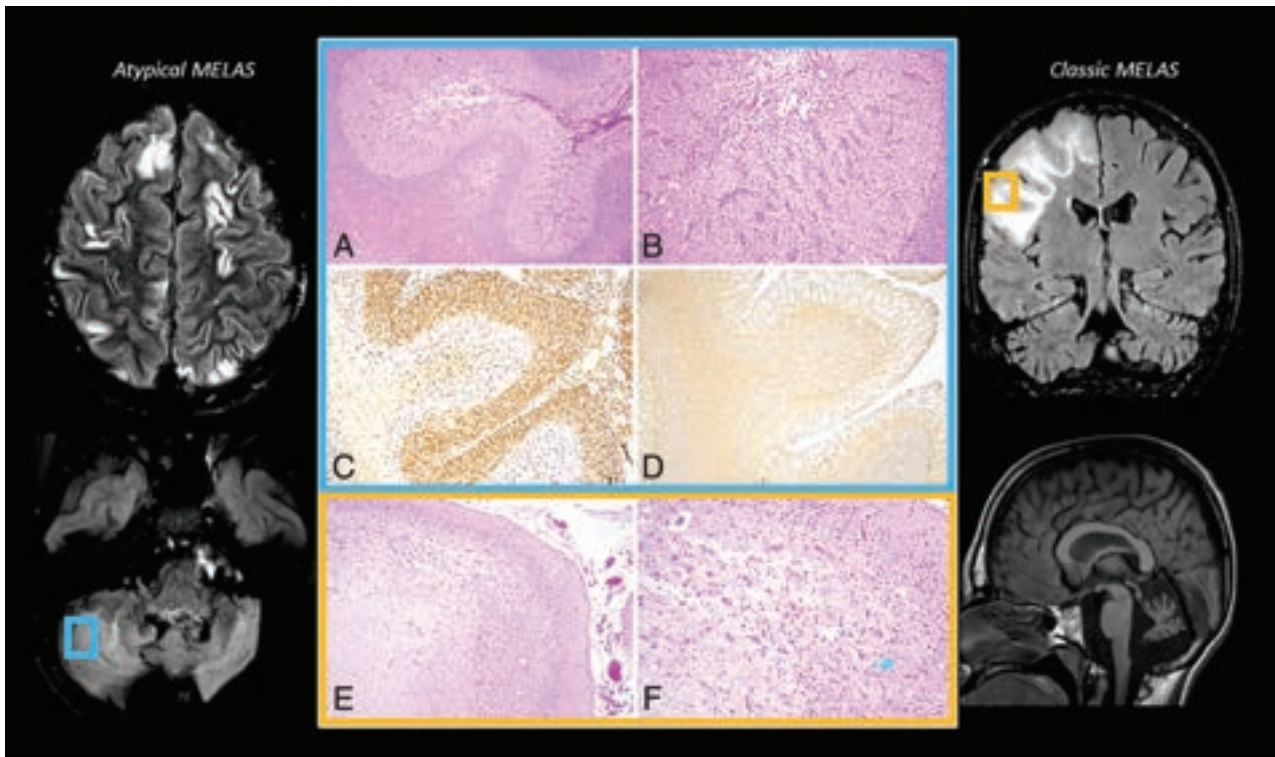


**FIG 1.** A, Biopsy of the cerebellum showing a subacute infarct involving the folia (H&E stain, original magnification  $\times 40$ ). B, Higher magnification of the subacute infarct. There is rarefaction, marked vascular proliferation, and macrophage collections within the molecular layer as well as loss of Purkinje neurons (H&E stain, original magnification  $\times 100$ ). C, CD68 immunostain demonstrates numerous macrophages within the molecular layer (CD68 immunostain, original magnification  $\times 40$ ). D, Glial fibrillary acidic protein (GFAP) highlights reactive gliosis (GFAP immunostain, original magnification  $\times 40$ ). E, Postmortem tissue from a second, classic MELAS patient demonstrates the cortex with an infarct involving the gyral crest (H&E stain, original magnification  $\times 40$ ). F, Higher magnification image of the infarct shows neuronal loss, tissue rarefaction, and gliosis (H&E stain, original magnification  $\times 200$ ).

criteria, we weighted victory-variables according to their specificity, and score cutoffs were determined to differentiate classic MELAS from atypical MELAS.

### Longitudinal Evaluation

Individuals were evaluated longitudinally to determine their clinical course and prognosis based on medical complications and the pattern of progression of the neuroimaging findings. Poor clinical prognosis was defined as respiratory failure and bulbar dysfunction. Survival at last evaluation or age at death or both were determined. For the neuroimaging pattern of progression, the interval appearance of new lesions, increased size of previously detected lesions, and extensive volume loss from baseline MR imaging to the last MR imaging study were defined as poor outcomes.

### Statistical Data

Data were analyzed using R statistical and computing software (Version 3.5.1; <http://www.r-project.org/>), SPSS Statistics for Windows (Version 26.0; IBM), and MedCalc Software odds ratio calculator (Version 20.106; [https://www.medcalc.org/calc/odds\\_ratio.php](https://www.medcalc.org/calc/odds_ratio.php)). Numeric variables were described according to their distribution with median and interquartile range and were compared using the Mann-Whitney *U* test. Categorical variables were expressed as percentages and frequency and were compared using the Fisher exact test and an OR with a 95% CI. Two-sided

*P* values  $< .01$  were considered statistically significant. Kaplan-Meier curves and log-rank tests were used to determine the differences in the occurrence of respiratory failure and bulbar dysfunction between different types of MELAS.

### RESULTS

One hundred twenty-one of 237 patients with a confirmed mitochondrial disorder had brain MRIs available for review. Thirty-five of these 121 individuals had a diagnosis of MELAS and pathogenic mtDNA variants.<sup>6</sup> Our cohort had a median age at symptom onset of 10 years (interquartile range = 4–19 years) and a male/female ratio of 2.2:1. A total of 79 brain MRIs (baseline and follow-up studies) were available. Follow-up MRIs were accessed for 26 of 35 (74%) individuals. Longitudinal clinical data were available for all patients. At the time of this analysis, 3 of 35 patients were deceased with the ages of death at 0.1, 1.8, and 7 years. Two had brain pathology specimens (1 surgical biopsy and 1 postmortem) available that showed indistinguishable infarctions consistent with vasculonecrotic lesions and vascular mitochondrial dysfunction (Fig 1). Demographic, clinical, laboratory, and genetic data are summarized in the Online Supplemental Data.

The schematic workflow of the successive steps is shown in Fig 2. Fifty-three variables were evaluated by unsupervised cluster analysis and visualized through a heatmap, which revealed 2

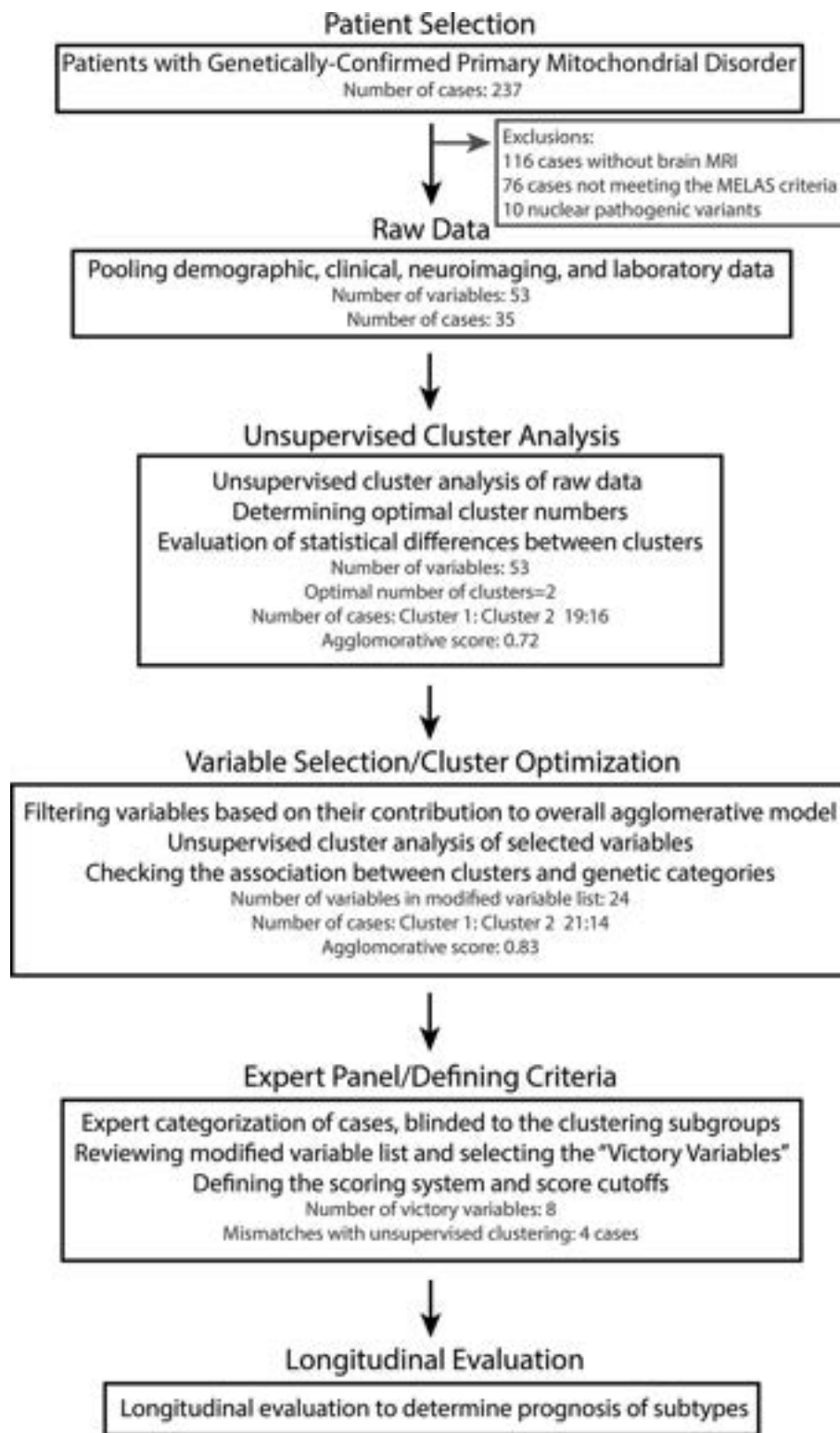


**FIG 2.** Work flow diagram. yo indicates years of age.

phenotype patterns among the mtDNA-based MELAS cohort (Online Supplemental Data). The average silhouette confirmed 2 to be the optimal number of cohort subgroups (Online Supplemental Data). When comparing the frequency of included variables between the 2 clusters, we found differences in 18 of 53 variables (all with  $P$  value  $< .01$ ) (Online Supplemental Data). In the

second step, agglomerative scores of the clusters were calculated before and after removing each variable, and 24 variables with a positive contribution were selected to optimize the clusters. The overall agglomerative score of the clustering changed from 0.72 to 0.83, with more distinct patterns of the variables evident in the visual heatmap (Fig 3). Comparing the results of unsupervised

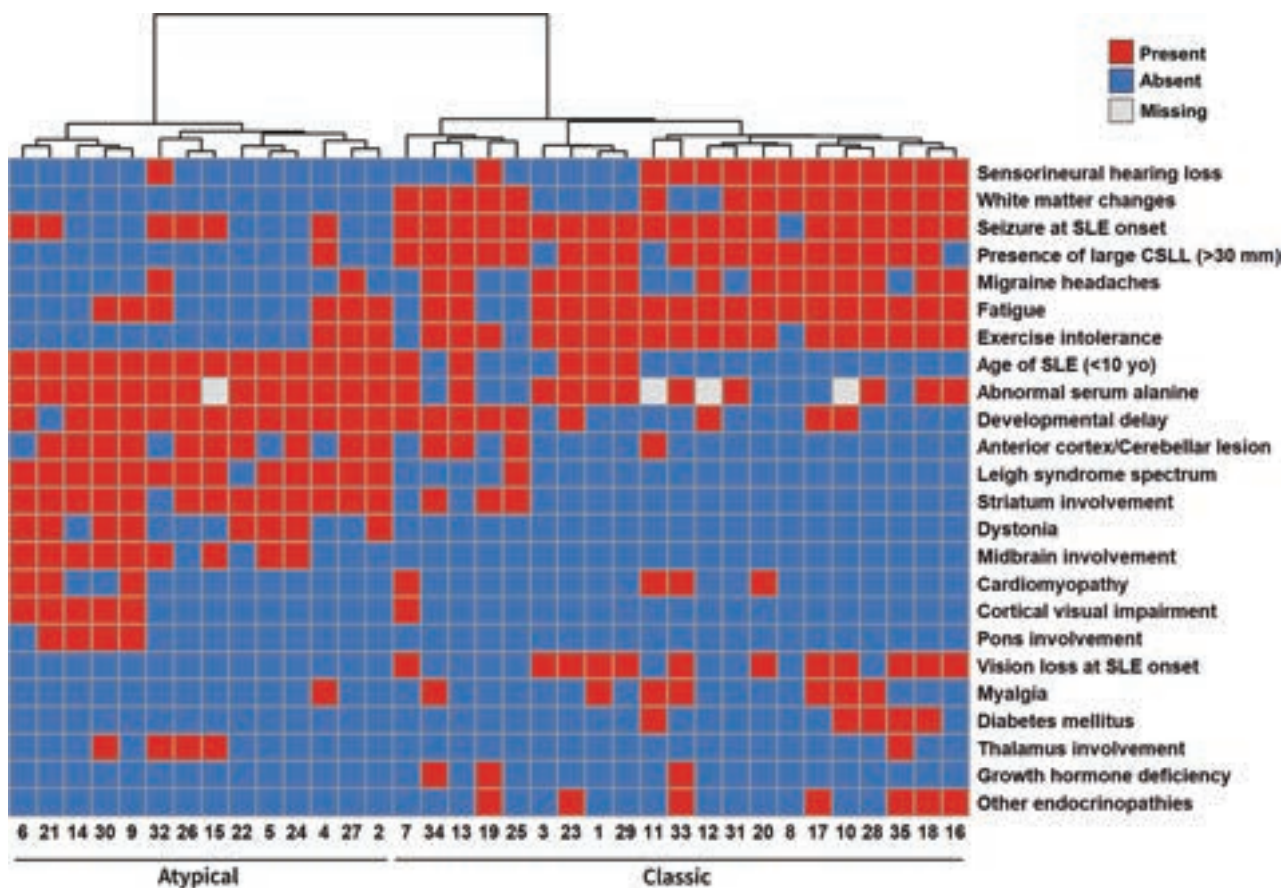


**FIG 3.** Unsupervised cluster analysis of the binary data based on the modified variable list (y-axis) using the Ward hierarchic clustering method. Each column represents 1 patient (x-axis). Red and blue squares show the presence and absence of the findings in each patient, respectively. At the top of the heatmap, the height of the dendrogram for main clusters demonstrates the high distance between clusters, which confirms the 2 distinct patterns of disease.

cluster analysis with the genetic data demonstrated that the mitochondrial tRNA (mt-tRNA) variants were more associated with one of the clusters while respiratory chain subunit genes were associated with the other cluster (OR = 26; 95% CI, 2.8–241; *P* value = .001).

Subsequently, the experts, blinded to the distribution of cases, were asked to categorize the patients into 2 subtypes using the 24 variables and the genetic data. The expert categorization results were then compared with the cluster subgroups, which showed 31 agreements and 4 discrepancies in assigning the individuals into 2 categories.

To enrich the clustering with clinical judgment, the experts reviewed the 24 variables and selected the most discriminating to differentiate MELAS subgroups from clinical, neuroimaging, and genetic perspectives, noteworthy all with *P* value < .01. Eight variables were selected as victory-variables. These victory-variables included the following: A) 5 clinical and demographic findings: 1) developmental delay, 2) sensorineural hearing loss (SNHL), 3) vision loss at stroke-like episode (SLE) onset, 4) overlap with Leigh syndrome (LS) as defined by additional symptoms of dystonia and brain lesions in the basal ganglia and/or brainstem, and 5) age at first SLE (10 years or younger versus older than 10 years of age); B) 2 neuroimaging variables: 1) the presence of large CSLLs ( $\geq 30$  mm), and 2) regional lesion distribution (anterior

and/or cerebellar versus posterolateral involvement, as previously defined); and C) 1 pathogenic variant category: gene categories involving the mt-tRNA variants or respiratory chain subunit genes. According to these variables, 2 subgroups of MELAS were defined.

Classic MELAS was associated with SNHL, vision loss at the onset of SLE, the first SLE occurring at older than 10 years of age, the presence of large CSLLs ( $\geq 30$  mm), and the mt-tRNA variant gene group. Atypical MELAS was associated with developmental delay, LS overlap, the first SLE at 10 years of age or younger, small CSLLs, cortical lesions predominantly located in anterior regions of the brain (frontal and anterior parietal lobes) and cerebellar cortex (the latter particularly in the context of *MT-ATP6* variants), and belonging to the respiratory chain subunit gene group (Fig 4). There were no differences among the subgroups based on other imaging features, including other cortical changes,<sup>22</sup> number of areas with hyper- or hypoperfusion on arterial spin-labeling, MR spectroscopy, iron deposition, or cerebellar atrophy.

Ultimately, using the victory-variables, we defined a 2-step criterion to differentiate the subtypes generated by the cluster analysis. The first step was to calculate a score on the basis of 5 clinical and 2 neuroimaging findings. The second step involved using genetic data for equivocal cases. On the basis of the specificity of victory-variables, LS overlap and SNHL were weighted



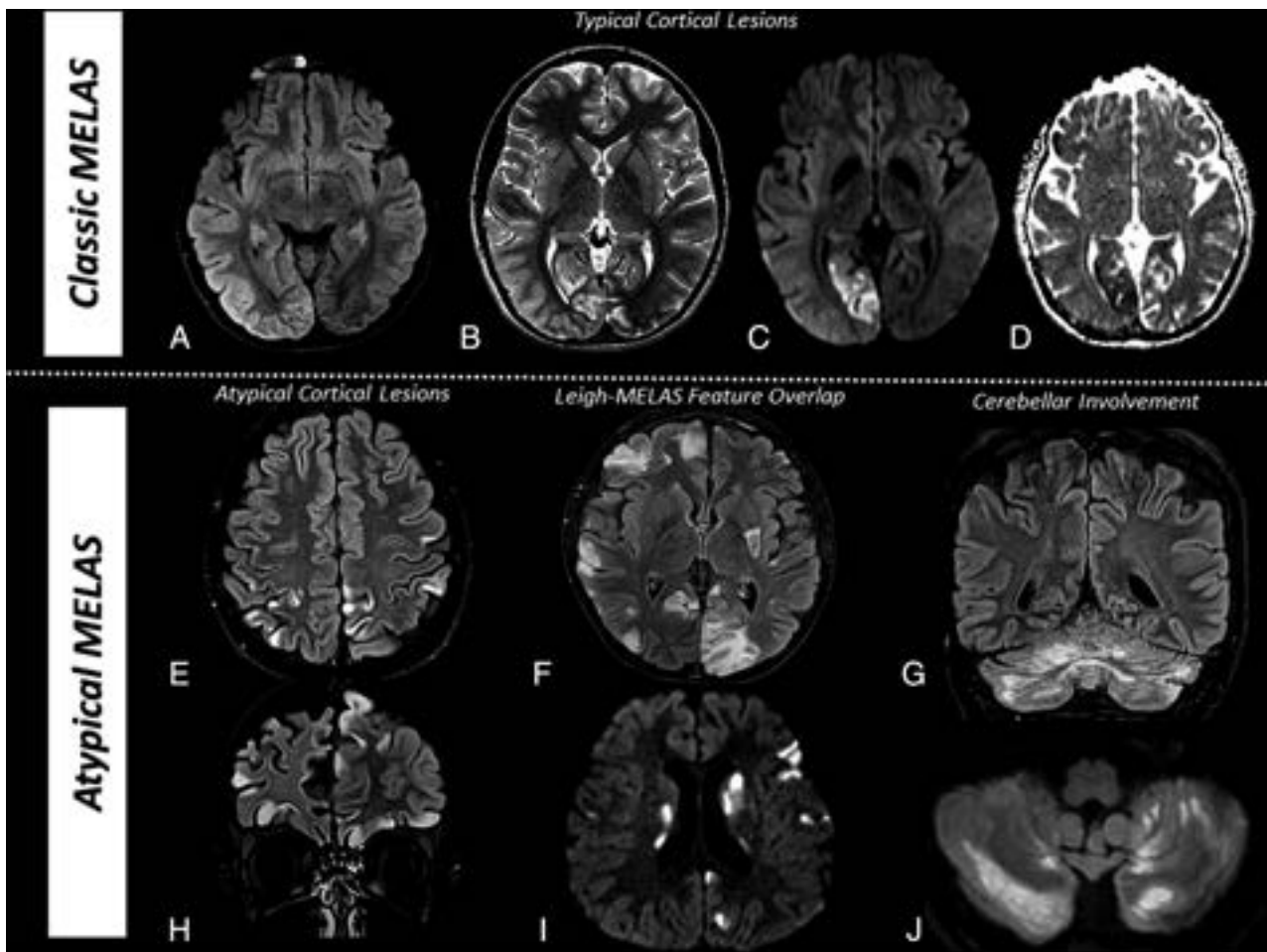


**FIG 4.** Classic MELAS. A large unique cortical lesion involves the right occipital and temporal lobes (posterolateral region of the brain) with FLAIR and T2 hyperintensity (A and B) and components of restricted diffusion in the medial occipital lobe confirmed in the ADC MAP (C and D). Atypical MELAS. Scattered, multiple, small cortical lesions involving both frontal and parietal lobes with FLAIR hyperintensity (E–H). Atypical MELAS with LS overlap. Multiple scattered cortical lesions with subcortical extension in association with basal ganglia involvement, configuring LS overlap, with FLAIR hyperintensity (F) and some areas of restricted diffusion (I) confirmed in the ADC MAP, not shown. Atypical MELAS with predominant cerebellar involvement. Cerebellar FLAIR hyperintensity (G) and components of restricted diffusion (J) were confirmed in the ADC MAP, not shown.

twice (high accuracy variables for cluster differentiation) relative to the other variables. The overall score (range from  $-4$  to  $+5$ ) was calculated for each case, and score cutoffs were defined to differentiate classic MELAS from atypical MELAS. The calculated score of  $\leq -2$  was defined as classic MELAS and  $\geq +2$  was defined as atypical MELAS. Scores between  $-1$  and  $+1$  were considered equivocal, which included cases in which the expert opinion and the cluster data were incompatible. In these cases, the genetic data were used as a confirmatory method to define the final subtype of mtDNA-based MELAS (Table 1).

Longitudinal evaluation showed that patients diagnosed with atypical MELAS based on the defined criteria had a higher chance of experiencing respiratory failure [ $\chi^2(1) = 4.686, P = .03$ ] and bulbar dysfunction [ $\chi^2(1) = 10.885, P = .001$ ] during the course of their disease (Fig 5). Among 3 deceased individuals, 2 had atypical and 1 had classic MELAS. Neuroimaging follow-up studies showed that atypical MELAS was more often associated with an increasing number of CSLs during the disease course (OR = 24; 95% CI, 1.04–559;  $P = .006$ ).

## DISCUSSION

While MELAS is a well-established mitochondrial disorder with a generally recognizable clinical phenotype, the clinical, imaging, genetic, and outcome variability of this complex syndrome remains underrecognized. In this study, 2 subgroups of MELAS were defined in a cohort of patients with MELAS on the basis of key clinical, neuroimaging, and genetic categories. The constellation of multiple variables from these 3 categories was evaluated, and 8 victory-variables were selected. The 8 victory-variables encompassed the following: A) 5 clinical/demographic variables: age of the first SLE, SNHL, developmental delay, vision loss occurring at onset of SLE, and overlap with LS; B) 2 neuroimaging variables: an anterior scattered region (frontal and anterior parietal lobes) and/or cerebellar-versus-posterolateral (temporo-occipital lobes) involvement, and cortical lesion size on the baseline MR imaging; and C) 1 genetic variable: gene categories involving the mt-tRNA variants or respiratory chain subunit genes.

Atypical MELAS was associated with symptoms occurring at a younger age (SLE at younger than 10 years of age) and



**Two-step differentiating criteria for distinguishing atypical MELAS from classic MELAS<sup>a</sup>**

Finding Category	Findings	Score
Step 1		
Demographic	First strokelike episode at younger than 10 years of age	+1
Clinical	Vision loss at strokelike episode onset	-1
Clinical	Overlap with LS spectrum	+2
Clinical	SNHL	-2
Clinical	Developmental delay	+1
Neuroimaging	Scattered, anterior/cerebellar lesions	+1
Neuroimaging	Presence of large CSLLs (>30 mm) <sup>b</sup>	-1
Step 2 (If -1 ≤ score ≤ 1)		
Genetic	Respiratory chain subunit gene group is most likely associated with atypical MELAS; mt-tRNA genes group is most likely associated with classic MELAS	

<sup>a</sup>Score ≥2: atypical MELAS, score ≤ -2: classic MELAS. If -1 ≤ score ≤ 1: equivocal (genetic study should be considered) → Step 2.

<sup>b</sup>CSLLs measured in their largest anterior-posterior extension in the axial plane using FLAIR and/or DWI sequences.

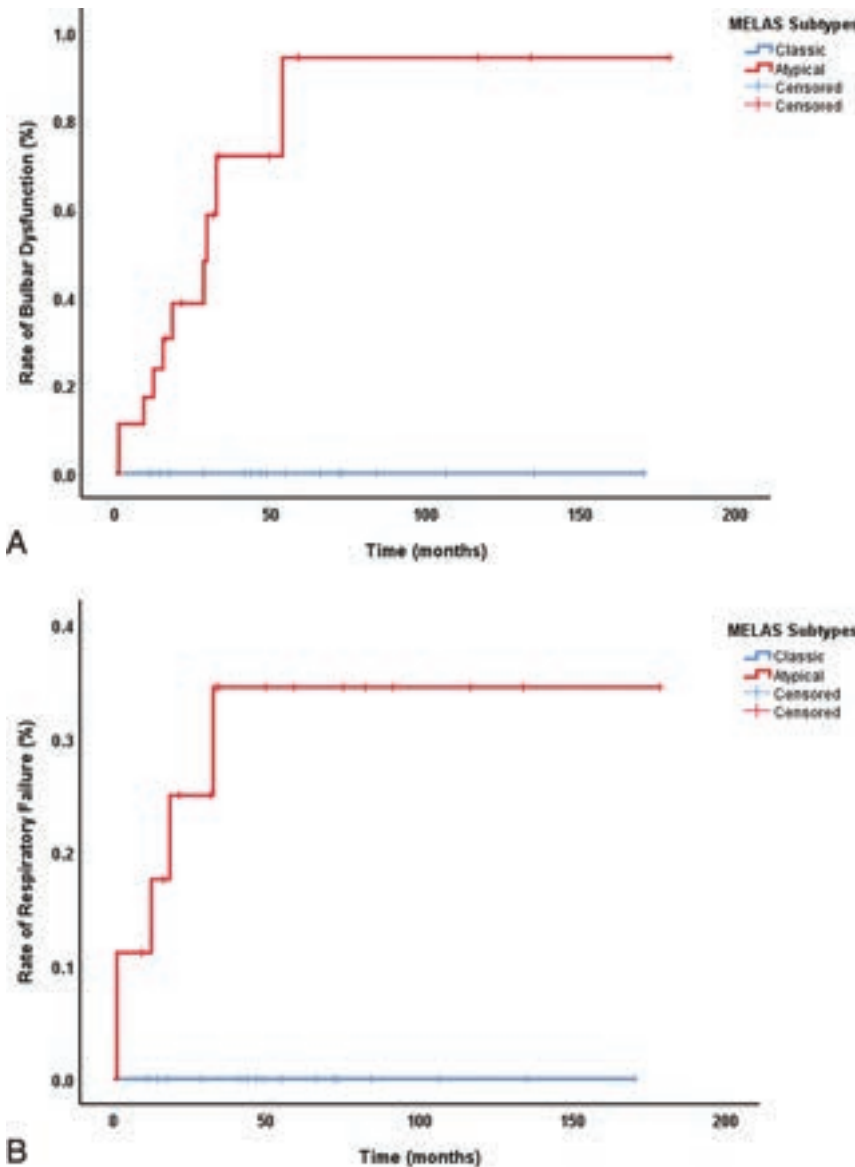


**FIG 5.** A, Clinical outcome (rates of bulbar dysfunction between MELAS subgroups). B, Clinical outcome (rates of respiratory failure between MELAS subgroups).

developmental delay, while classic MELAS was associated with SNHL and vision loss occurring at the first SLE.<sup>6,23</sup> Although not part of the victory-variables, other important clinical differences should be considered to distinguish between subtypes of MELAS, including diabetes mellitus and migraine, which demonstrated significant differences in this study and are associated with classic MELAS.<sup>24-26</sup> Conditions of individuals with the classic form of MELAS were rarely associated with LS (6%), while this overlap was frequent in the atypical MELAS subgroup (80%). Following a complex clinical variability, LS/MELAS overlap included mostly individuals presenting with additional symptoms of dystonia and the neuroimaging criteria for LS, including lesions in the basal ganglia and/or brainstem.<sup>9</sup>

Consistent with reported literature, the genetic category analysis showed that mt-tRNA variants, particularly *MT-TL1* m.3243 A > G, were observed in classic MELAS.<sup>13,14</sup> In contrast, respiratory chain subunit genes were associated with atypical MELAS, specifically variants in complex I (*MT-ND1*, *MT-ND3*, *MT-ND5*) and complex V (*MT-ATP6*, *MT-ATP8*) subunits. Even though genes involving the respiratory chain subunits have been established in association with MELAS,<sup>9</sup> most of these genes are known to be causally related to LS.<sup>27</sup> In our cohort, the genetic results were predictive of clinical and radiologic phenotypes. However, there were exceptions seen, including 1 patient with the *MT-TL1* variant presenting with atypical MELAS and 2 patients with subunit genetic variants (*MT-CYB*, *MT-ND5*) presenting with classic MELAS.

Neuroimaging findings with corresponding imaging symptoms play a critical role in the definition of MELAS, often revealing a characteristic pattern of disappearing and relapsing large CSLLs in the brain.<sup>28</sup> These lesions are characteristically located in the occipital, posterior parietal, or temporal lobes, not respecting vascular territories.<sup>28,29</sup> We observed that large lesions mainly involving the occipital and temporal lobes were associated with classic MELAS, similar to findings in the literature.<sup>28,29</sup> Atypical patterns of CSLL,

including smaller size, lower frequency of posterolateral distribution, and higher frequency of cerebellar involvement were noted in atypical MELAS. Additional association was noted between cerebellar lesions (with or without supratentorial cortical involvement) and *MT-ATP6* variants in the context of atypical MELAS. Surveillance MR imaging studies were also helpful in distinguishing subgroups; although not part of the variable criteria to differentiate MELAS subgroups, patients with atypical MELAS showed new lesions and more severe progression of the atrophy in short follow-up studies, supporting the more severe clinical outcome noted in this group.

Although there were several key differences distinguishing the 2 groups, all 35 individuals with MELAS in our cohort met the MELAS diagnostic criteria. In addition, 2 individuals, 1 from each group (classic and atypical), showed similar findings from histologic analysis, further supporting the groups having shared similar pathophysiology.<sup>29</sup> The underlying pathophysiology of acute SLE of MELAS has been elucidated during the past few decades, with a major role related to altered nitric oxide metabolism causing vascular endothelium dysfunction.<sup>24,30</sup> Overall, less nitric oxide is present in patients with MELAS due to excess cytochrome c oxidase in smooth-muscle binding to nitric oxide.<sup>24,30</sup> Therefore, MELAS places the individual at risk of SLE, especially during periods of increased metabolic demand due to physiologic stressors.

The lesions may respond to specific therapy management, particularly in the context of drugs implicated in the nitric oxide pathway, such as arginine. These drugs have been considered as a treatment for these patients, but there are currently no FDA-approved medications for MELAS treatment, primarily because there is a large outcome variability without a predictable response to the drugs. Using homogeneous subgroups in clinical trials, classic MELAS versus atypical MELAS, will likely be an important factor contributing to drug development and in predicting a response to therapeutic interventions. For promising future results, the patient population must be carefully phenotyped; the natural history of the disease, well understood; and the patient's health, optimized for trial readiness.<sup>31</sup>

The main limitation of this study is the potential bias from the challenge of clinically diagnosing mitochondrial disorders. To avoid the inclusion of patients without MELAS, a neurologist performed a clinical chart review to confirm that each patient fulfilled the established MELAS criteria, despite the presence of other symptoms or clinical overlap syndromes. Because the MELAS diagnosis is also based on radiologic appearance, our study meets a crucial need by expanding the radiologic-phenotype spectrum of this disorder beyond that of existing literature. Another limitation is that the sample size is relatively small. This small size was due to our preference for using rigorous inclusion criteria, recruiting only those patients with a definitive diagnosis of MELAS; a full set of clinical, genetic, laboratory, and MR imaging data available for review; and mtDNA pathogenic variants, because the pathophysiology of the mtDNA replication defect should be considered distinct from nuclear DNA disorders.

## CONCLUSIONS

Overall, we have identified a composite set of parameters that collectively serve as a clinical biomarker for distinguishing classic

and atypical subgroups of MELAS. These subgroups should be prospectively validated in future natural history studies and may be used in interventional clinical trials for defining clinical and neuroimaging phenotypes and correlating these with underlying gene etiologies and, ultimately, candidate treatment outcomes.

## ACKNOWLEDGMENTS

We thank the patients and their families for their involvement. We also thank Victoria A. Ramirez (PSM, Medical Science Writer at the Department of Radiology, Children's Hospital of Philadelphia) for providing editorial support for this article.

Disclosure forms provided by the authors are available with the full text and PDF of this article at [www.ajnr.org](http://www.ajnr.org).

## REFERENCES

1. Finsterer J. **Mitochondrial metabolic stroke: phenotype and genetics of stroke-like episodes.** *J Neurol Sci* 2019;400:135–41 CrossRef Medline
2. Lu JQ, Tarnopolsky MA. **Mitochondrial neuropathy and neurogenic features in mitochondrial myopathy.** *Mitochondrion* 2021;56:52–61 CrossRef Medline
3. Chakrabarty S, Govindaraj P, Sankaran BP, et al. **Contribution of nuclear and mitochondrial gene mutations in mitochondrial encephalopathy, lactic acidosis, and stroke-like episodes (MELAS) syndrome.** *J Neurol* 2021;268:2192–207 CrossRef Medline
4. Wei X, Du M, Li D, et al. **Mutations in FASTKD2 are associated with mitochondrial disease with multi-OXPHOS deficiency.** *Hum Mutat* 2020;41:961–72 CrossRef Medline
5. Yoo DH, Choi YC, Nam DE, et al. **Identification of FASTKD2 compound heterozygous mutations as the underlying cause of autosomal recessive MELAS-like syndrome.** *Mitochondrion* 2017;35:54–58 CrossRef Medline
6. Yatsuga S, Povalko N, Nishioka J, et al; Taro Matsuoka for MELAS Study Group in Japan. **MELAS: a nationwide prospective cohort study of 96 patients in Japan.** *Biochim Biophys Acta* 2012;1820:619–24 CrossRef Medline
7. Hirano M, Ricci E, Koenigsberger MR, et al. **Melas: an original case and clinical criteria for diagnosis.** *Neuromuscul Disord* 1992;2:125–35 CrossRef Medline
8. Sproule DM, Kaufmann P. **Mitochondrial encephalopathy, lactic acidosis, and strokelike episodes: basic concepts, clinical phenotype, and therapeutic management of MELAS syndrome.** *Ann N Y Acad Sci* 2008;1142:133–58 CrossRef Medline
9. Alves CA, Teixeira SR, Martin-Saavedra JS, et al. **Pediatric Leigh syndrome: neuroimaging features and genetic correlations.** *Ann Neurol* 2020;88:218–32 CrossRef Medline
10. Goto Y, Nonaka I, Horai S. **A mutation in the tRNA(Leu)(UUR) gene associated with the MELAS subgroup of mitochondrial encephalomyopathies.** *Nature* 1990;348:651–53 CrossRef Medline
11. Karicheva OZ, Kolesnikova OA, Schirtz T, et al. **Correction of the consequences of mitochondrial 3243A>G mutation in the MT-TL1 gene causing the MELAS syndrome by tRNA import into mitochondria.** *Nucleic Acids Res* 2011;39:8173–86 CrossRef Medline
12. Chin J, Marotta R, Chiotis M, et al. **Detection rates and phenotypic spectrum of m. 3243A>G in the MT-TL1 gene: a molecular diagnostic laboratory perspective.** *Mitochondrion* 2014;17:34–41 CrossRef Medline
13. Pickett SJ, Grady JP, Ng YS, et al. **Phenotypic heterogeneity in m.3243A>G mitochondrial disease: the role of nuclear factors.** *Ann Clin Transl Neurol* 2018;5:333–45 CrossRef Medline
14. Nesbitt V, Pitceathly RD, Turnbull DM, et al. **The UK MRC Mitochondrial Disease Patient Cohort Study: clinical phenotypes associated with the m.3243A>G mutation—implications for diagnosis**

- and management.** *J Neurol Neurosurg Psychiatry* 2013;84:936–38 CrossRef Medline
15. Miyahara H, Matsumoto S, Mokuno K, et al. **Autopsied case with MERRF/MELAS overlap syndrome accompanied by stroke-like episodes localized to the precentral gyrus.** *Neuropathology* 2019;39:212–17 CrossRef Medline
  16. Malfatti E, Bugiani M, Invernizzi F, et al. **Novel mutations of ND genes in complex I deficiency associated with mitochondrial encephalopathy.** *Brain* 2007;130:1894–904 CrossRef Medline
  17. Mezuki S, Fukuda K, Matsushita T, et al. **Isolated and repeated stroke-like episodes in a middle-aged man with a mitochondrial ND3 T10158C mutation: a case report.** *BMC Neurol* 2017;17:217 CrossRef Medline
  18. von Elm E, Altman DG, Egger M, et al; STROBE Initiative. **The Strengthening the Reporting of Observational Studies in Epidemiology (STROBE) statement: guidelines for reporting observational studies.** *Lancet* 2007;20:1453–7 CrossRef Medline
  19. Rahman S, Poulton J, Marchington D, et al. **Decrease of 3243 A→G mtDNA mutation from blood in MELAS syndrome: a longitudinal study.** *Am J Hum Genet* 2001;68:238–40 CrossRef Medline
  20. Ng YS, Lax NZ, Blain AP, et al. **Forecasting stroke-like episodes and outcomes in mitochondrial disease.** *Brain* 2022;145:542–54 CrossRef Medline
  21. Rahman S, Copeland WC. **POLG-related disorders and their neurological manifestations.** *Nat Rev Neurol* 2019;15:40–52 CrossRef Medline
  22. Ishigaki H, Sato N, Kimura Y, et al. **Linear cortical cystic lesions: characteristic MR findings in MELAS patients.** *Brain Dev* 2021;43:931–38 CrossRef Medline
  23. Di Stadio A, Pegoraro V, Giaretta L, et al. **Hearing impairment in MELAS: new prospective in clinical use of microRNA, a systematic review.** *Orphanet J Rare Dis* 2018;13:35 CrossRef Medline
  24. El-Hattab AW, Adesina AM, Jones J, et al. **MELAS syndrome: clinical manifestations, pathogenesis, and treatment options.** *Mol Genet Metab* 2015;116:4–12 CrossRef Medline
  25. Chae HW, Na JH, Kim HS, et al. **Mitochondrial diabetes and mitochondrial DNA mutation load in MELAS syndrome.** *Eur J Endocrinol* 2020;183:505–12 CrossRef Medline
  26. Cho JH, Kim JH, Choi JH, et al. **Endocrine dysfunctions in patients with mitochondrial diseases.** *Int J Pediatr Endocrinol* 2015;2015:O23 CrossRef
  27. Rahman J, Rahman S. **Mitochondrial medicine in the omics era.** *Lancet* 2018;391:2560–74 CrossRef Medline
  28. Bhatia KD, Krishnan P, Kortman H, et al. **Acute cortical lesions in MELAS syndrome: Anatomic distribution, symmetry, and evolution.** *AJNR Am J Neuroradiol* 2020;41:167–73 CrossRef Medline
  29. Betts J, Jaros E, Perry RH, et al. **Molecular neuropathology of MELAS: level of heteroplasmy in individual neurones and evidence of extensive vascular involvement.** *Neuropathol Appl Neurobiol* 2006;32:359–73 CrossRef Medline
  30. El-Hattab AW, Jahoor F. **Assessment of nitric oxide production in mitochondrial encephalomyopathy, lactic acidosis, and stroke-like episodes syndrome with the use of a stable isotope tracer infusion technique.** *J Nutr* 2017;147:1251–57 CrossRef Medline
  31. Goldstein A, Rahman S. **Seeking impact: global perspectives on outcome measure selection for translational and clinical research for primary mitochondrial disorders.** *J Inher Metab Dis* 2021;44:343–57 CrossRef Medline

# Brain Activation Evoked by Motor Imagery in Pediatric Patients with Complete Spinal Cord Injury

L. Wang, W.M. Zheng, T.F. Liang, Y.H. Yang, B.N. Yang, X. Chen, Q. Chen, X.J. Li, J. Lu, B.W. Li, and N. Chen



## ABSTRACT

**BACKGROUND AND PURPOSE:** Currently, there is no effective treatment for pediatric patients with complete spinal cord injury. Motor imagery has been proposed as an alternative to physical training for patients who are unable to move voluntarily. Our aim was to reveal the potential mechanism of motor imagery in the rehabilitation of pediatric complete spinal cord injury.

**MATERIALS AND METHODS:** Twenty-six pediatric patients with complete spinal cord injury and 26 age- and sex-matched healthy children as healthy controls were recruited. All participants underwent the motor imagery task-related fMRI scans, and additional motor execution scans were performed only on healthy controls. First, we compared the brain-activation patterns between motor imagery and motor execution in healthy controls. Then, we compared the brain activation of motor imagery between the 2 groups and compared the brain activation of motor imagery in pediatric patients with complete spinal cord injury and that of motor execution in healthy controls.

**RESULTS:** In healthy controls, compared with motor execution, motor imagery showed increased activation in the left inferior parietal lobule and decreased activation in the left supplementary motor area, paracentral lobule, middle cingulate cortex, and right insula. In addition, our results revealed that the 2 groups both activated the bilateral supplementary motor area, middle cingulate cortex and left inferior parietal lobule, and supramarginal gyrus during motor imagery. Compared with healthy controls, higher activation in the bilateral paracentral lobule, supplementary motor area, putamen, and cerebellar lobules III–V was detected in pediatric complete spinal cord injury during motor imagery, and the activation of these regions was even higher than that of healthy controls during motor execution.

**CONCLUSIONS:** Our study demonstrated that part of the motor imagery network was functionally preserved in pediatric complete spinal cord injury and could be activated through motor imagery. In addition, higher-level activation in sensorimotor-related regions was also found in pediatric complete spinal cord injury during motor imagery. Our findings may provide a theoretic basis for the application of motor imagery training in pediatric complete spinal cord injury.

**ABBREVIATIONS:** CSCI = complete spinal cord injury; FWE = family-wise error; HC = healthy control; KVIQ-10 = Kinesthetic and Visual Imagery Questionnaire; IPL = inferior parietal lobule; ME = motor execution; MI = motor imagery; PCL = paracentral lobule; SMA = supplementary motor area

Traumatic spinal cord injury is a sudden and unpredictable incident that can destroy the spinal cord, leading to sensory and motor dysfunction.<sup>1</sup> It can occur at any age, including childhood, not only causing a heavy burden on the families but

also having serious consequences for children's physical and mental well-being.<sup>2</sup> The most common rehabilitation strategy used in patients with incomplete spinal cord injury is physical training, which is intended to promote cortical plasticity by driving motor neural networks and facilitating functionally relevant muscle activity below the injury level.<sup>3</sup> However, due to the complete disruption of afferent and efferent pathways,<sup>4</sup> pediatric patients with complete spinal cord injury (CSCI) are not able to execute physical movement. At present, there is no effective treatment for pediatric CSCI. Currently, motor imagery (MI) is

Received November 26, 2022; accepted after revision March 16, 2023.

From the Department of Radiology and Nuclear Medicine (L.W., W.M.Z., Y.H.Y., B.N.Y., X.C., J.L., N.C.), Xuanwu Hospital, Capital Medical University, Beijing, China; Beijing Key Laboratory of Magnetic Resonance Imaging and Brain Informatics (L.W., W.M.Z., Y.H.Y., B.N.Y., X.C., J.L., N.C.), Beijing, China; Department of Medical Imaging (T.F.L., B.W.L.), Affiliated Hospital of Hebei Engineering University, Handan, Hebei Province, China; Department of Radiology (Q.C.), Beijing Friendship Hospital, Capital Medical University, Beijing, China; and Department of Radiology (X.J.L.), China Rehabilitation Research Center, Beijing, China.

Ling Wang and Weimin Zheng contributed equally to this work and share first authorship.

This study was supported by the National Natural Science Foundation of China (Nos. 81871339 and 81271556), the Beijing Municipal Natural Science Foundation (No.7113155), and the Science Foundation of Beijing Municipal Commission of Education (No. KM201210025013).

Please address correspondence to Nan Chen, MD, Department of Radiology and Nuclear Medicine, Xuanwu Hospital, Capital Medical University, Beijing Key Laboratory of Magnetic Resonance Imaging and Brain Informatics, No. 45 Changchun St, Xicheng District, Beijing, China; e-mail: chenzen8057@sina.com

Indicates open access to non-subscribers at [www.ajnr.org](http://www.ajnr.org)

Indicates article with online supplemental data.

<http://dx.doi.org/10.3174/ajnr.A7847>



being studied as a potential treatment for the functional recovery of motor dysfunction diseases<sup>5,6</sup> because it can activate sensorimotor networks and can be performed by injured patients who are unable to move voluntarily.<sup>7-9</sup>

MI is the mental simulation of a movement in the absence of obvious motor output.<sup>10</sup> The link between MI and motor execution (ME) has been empirically demonstrated in adult studies.<sup>11,12</sup> A number of neuroimaging studies have repeatedly revealed overlapping neural activity during MI and ME,<sup>12</sup> including the premotor cortices, supplementary motor area (SMA), basal ganglia, and cerebellum.<sup>10</sup> MI may reinforce these crucial motor networks and improve the motor skills of healthy individuals, including athletes<sup>13</sup> and musicians.<sup>14</sup> Additionally, MI may be an alternative to physical training in cases where movement is severely impaired or not possible, such as when patients have CNS injuries including stroke,<sup>7,8</sup> Parkinson's syndrome,<sup>9</sup> MS,<sup>15</sup> and spinal cord injury.<sup>16</sup>

Compared with adult patients, children have a greater possibility of developing neuroplasticity because their brains are undergoing rapid growth and development;<sup>17</sup> therefore, effective therapies may lead to satisfactory rehabilitation in children.<sup>18</sup> According to previous studies,<sup>19,20</sup> children 5–6 years of age have already demonstrated MI abilities, and it has been reported that MI training can also improve the motor function of children with cerebral palsy,<sup>18,21</sup> developmental coordination disorder,<sup>22,23</sup> and perinatal stroke.<sup>5</sup> The application of MI training in the motor rehabilitation of adults with CNS injury and children with cerebral palsy, developmental coordination disorder, or perinatal stroke suggests that it may also be helpful for the rehabilitation of pediatric patients with CSCI. However, there is no research on the application of MI in pediatric patients with CSCI, and the neural mechanism of MI in the rehabilitation of pediatric patients with CSCI is unclear.

In this study, we intended to apply task-based fMRI to study the alterations in brain activation in pediatric patients with CSCI during MI and to reveal its potential mechanisms for motor rehabilitation, which may provide insights into the potential applications of MI training in pediatric patients with CSCI.

## MATERIALS AND METHODS

### Participants

After obtaining approval from the Medical Research Ethics Committee of Xuanwu Hospital, all participants were enrolled, and informed consent was obtained from the parents or guardians of the children. On admission to the hospital, all patients were evaluated by 2 experienced physicians, using the Glasgow Coma Scale, Posttraumatic Amnesia Scale, and loss of consciousness assessment. Then, the American Spinal Injury Association scale was administered to evaluate the sensory and motor functions of the pediatric patients with CSCI. After that, the Kinesthetic and Visual Imagery Questionnaire (KVIQ-10)<sup>24</sup> was conducted to evaluate the MI abilities of all participants. To be included in this study, all patients had to meet following requirements: 1) history of traumatic CSCI; 2) between 6 and 12 years of age; 3) time since injury  $\geq 2$  months; 4) KVIQ-10 score  $\geq 25$ ;<sup>25</sup> 5) no associated traumatic brain injury confirmed by conventional MR imaging; 6) no history of mental disorder, mental illness, epilepsy, or cognitive disorder; and 7) no

contraindication for MR imaging. The inclusion criteria of healthy controls (HCs) were as follows: 1) age, sex, and education matched those of pediatric patients with CSCI; 2) KVIQ-10 score  $\geq 25$ ; 3) no history of mental disorder, mental illness, epilepsy, or cognitive disorder; and 4) no contraindication to MR imaging.

### Experimental Tasks

In this study, the HCs underwent both MI and ME task-based fMRI scans, and the pediatric patients with CSCI underwent only the MI task. HCs performed the ME task with right-ankle dorsiflexion, and all participants performed the MI task using a kinesthetic MI of right-ankle dorsiflexion. During the experiment, each participant conducted a prescan practice, underwent task-based fMRI scans, and was asked to complete a questionnaire after the fMRI scans. All processes were completed with the aid of the parents or guardians of the recruited children.

During the prescan practice, all participants familiarized themselves with the procedure of the tasks to ensure proper execution. Our rehabilitation physicians conducted the intensive ME simulation training for all HCs. ME training used a recording of ME produced by our rehabilitation medicine department. In the beginning, the HCs relaxed for 3 minutes, then a rehabilitation physician explained and demonstrated the ME of right-ankle dorsiflexion, and the HCs followed. Then following the guidance of the ME recording, all HCs conducted the ME of ankle dorsiflexion step by step. MI training used an MI therapy recording produced by our rehabilitation medicine department. First, the participants relaxed for 3 minutes, then a rehabilitation physician explained and demonstrated the MI of the right ankle dorsiflexion, and the participants followed. To ensure that all participants could understand and accurately perform the MI of ankle dorsiflexion, the participants repeated this process 3 times. After that, following the guidance of the MI recording, participants performed the MI of ankle dorsiflexion step-by-step. All processes were conducted in a quiet environment.

In the design of the task experiment, for the first 10 scans, no task was given so that participants could adjust and adapt themselves. Then, 4 repetitions were completed, which alternated between 10 scan task blocks and 10 scan rest blocks (task block first, rest block last). The ME task required HCs to conduct active ankle dorsiflexion (from dorsiflexion 20° to plantarflexion 30°) using their own pace (an approximate frequency of 0.5–1.0 Hz). A small pillow was placed under each participant's popliteal fossa to make ankle movement easier. While the patient performed the tasks, foam pads were used to minimize head motion. In MI tasks, both HCs and pediatric patients with CSCI were asked to imagine themselves performing the same movements as the right ankle dorsiflexion, rather than actually performing them. For the MI tasks to be performed successfully, an operator must visually observe the entire task procedure to ensure that no overt movement occurred during either the MI or rest blocks.

As reported in questionnaire interviews after the fMRI scan, all participants in this study were able to complete the MI tasks, and they did not perform any imagery during the rest blocks.

**MR Imaging.** Imaging scans were acquired on a 3T MR imaging scanner (Siemens) using 12-channel phased array head coils. To avoid

visual input, participants were asked to lie supine and close their eyes. The conventional brain axial FLAIR sequence was acquired first to rule out cerebral abnormalities. The images were collected with a single-shot gradient-echo-planar imaging sequence. The acquisition parameters for the scans were as follows: Each volume consisted of 35 axial slices (section thickness = 3 mm and interslice gap = 1 mm), TR = 2000 ms, TE = 30 ms, flip angle = 90°, matrix = 64 × 64, field of view = 220 × 220 mm<sup>2</sup>, readout bandwidth = 2004 Hz/px, and final voxel size = 3.4 × 3.4 × 4.2 mm<sup>3</sup>.

### Data Preprocessing

Data preprocessing was performed using Statistical Parametric Mapping, Version 12 (SPM12; <http://www.fil.ion.ucl.ac.uk/spm>) based on Matlab 2013b (MathWorks). The first 10 time point images were discarded to ensure stabilization of the signal. Then, the remaining images were slice-timing-corrected using the middle slice as a reference, and all volumes were spatially realigned to correct for head movements. Realignment of the volumes was followed by checking the head-movement parameters, and the data sets with more than 3 mm maximum translation or 3° maximum rotation were discarded. For spatial normalization of the realigned volumes, the data were then spatially normalized to a pediatric brain template from the 6- to 12-year age group in Montreal Neurological Institute space (<https://www.nitrc.org/projects/chnpd>). Then, the images were resampled to 3 × 3 × 3 mm<sup>3</sup> voxel size. In the final step, a Gaussian kernel with an 8-mm full width at half maximum was applied to smooth the data.

### Statistical Analysis

The statistical analyses were performed with SPM 12 implemented in Matlab 2013b. In the first level of analyses, brain activations during tasks were estimated using a general linear model. The blood oxygen level–dependent signal time courses were convolved with a canonical hemodynamic response function. A 6-parameter rigid body transformation (3 translations, 3 rotations) derived from the head-motion correction was added in the general linear model as covariates of no interest. A standard high-pass filter (128-second cutoff) was used to eliminate low-frequency signal drift. After the model estimation, by comparing experimental conditions with respective control conditions, the contrast within each task was defined to obtain task-related activations. Second-level analyses were then performed using the contrast images.

In the second-level group analyses, one-sample *t* tests were conducted to identify brain regions significantly activated by MI in both groups or ME in HCs. Statistical significance was determined on the basis of cluster-level family-wise error (FWE) correction ( $P < .05$ , 2-tailed). A paired *t* test was used for the comparison of brain activation during MI and ME tasks in HCs (cluster-level FWE correction with  $P < .05$ ). With age and sex as nuisance covariates, two-sample *t* tests were conducted to compare the activation of the brain between pediatric patients with CSCI and HCs during MI and the activation of the brain between pediatric patients with CSCI during the MI task and HCs during the ME task (cluster-level FWE correction with  $P < .05$ ).

Spearman analyses were performed to explore any possible correlation between the activation intensity of the regions with significant group differences during MI and the clinical variables

of pediatric patients with CSCI (including injury duration, sensory scores, motor scores, and KVIQ-10 scores).

## RESULTS

### Demographic Information

Twenty-six pediatric patients with CSCI (23 girls and 3 boys, with a mean age of 8.04 [SD, 1.89] years and a range from 6 to 12 years) and 26 HCs (23 girls and 3 boys with a mean age of 8.65 [SD, 1.96] years and a range from 6 to 12 years) were enrolled in this study. Pediatric patients with CSCI had the disease for a duration ranging from 2 to 108 months, with a mean of 24.73 (SD, 24.15) months. All patients were classified as grade A according to the American Spinal Injury Association Impairment Scale 2012 ([https://www.physio-pedia.com/American\\_Spinal\\_Cord\\_Injury\\_Association\\_\(ASIA\)\\_Impairment\\_Scale](https://www.physio-pedia.com/American_Spinal_Cord_Injury_Association_(ASIA)_Impairment_Scale)). The detailed information of pediatric patients with CSCI was provided by Online Supplemental Data. No differences were found in age (Mann-Whitney *U* test,  $P = .23$ ) or sex ( $\chi^2$ ,  $P = 1.00$ ) between pediatric patients with CSCI and HCs.

### Brain Activation

**Brain Activation Patterns of HCs during ME and MI.** Figure 1A, -B shows significant activation of HCs during ME and MI. The ME and MI tasks of HCs evoked several similar brain regions, mainly including the bilateral SMA and left middle cingulate cortex.

In a direct comparison of maps between the ME and MI of HCs, the MI task showed significantly increased activation in the left inferior parietal lobule (IPL) and significantly decreased activation in the left SMA, paracentral lobule (PCL), middle cingulate cortex, and right insula (Fig 2 and Table 1).

### Comparison of MI-Evoked Brain Activation Patterns between Pediatric Patients with CSCI and HCs

During the MI task, pediatric patients with CSCI and HCs showed similar activated brain areas, mainly including the bilateral SMA, middle cingulate cortex and left IPL, supramarginal gyrus (Fig 1B, -C). However, compared with HCs, pediatric patients with CSCI showed significantly increased activation in the bilateral PCL, SMA, putamen, and cerebellar lobules III–V during MI (Fig 3 and Table 2).

### Comparison between MI-Evoked Brain Activation Patterns in Pediatric Patients with CSCI and ME-Evoked Brain Activation Patterns in HCs

Additionally, we observed that the MI task in pediatric patients with CSCI activated brain structures similar to those in the ME task in HCs. In comparison with the ME task in HCs, the MI task in pediatric patients with CSCI showed significantly increased activation in the right PCL, bilateral putamen, and left cerebellar lobules III–V (Online Supplemental Data).

### Correlation Analyses between the Brain Activation and Clinical Variables in Pediatric Patients with CSCI

According to the Spearman correlation analyses, there were no correlations between the activation of brain regions with significant group differences during MI and the clinical variables (including injury duration, sensory scores, motor scores, and KVIQ-10 scores) in pediatric patients with CSCI ( $P > .05$ ).

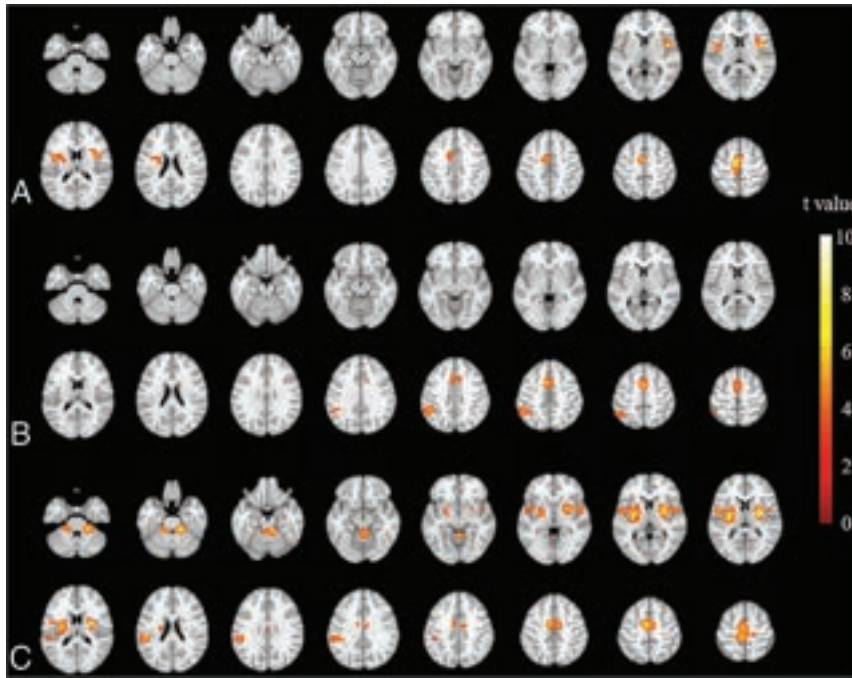


**FIG 1.** Brain activation of HCs during ME and MI and the activation of pediatric patients with CSCI during MI. Typical brain regions with activation in HCs during ME are shown in *A*, mainly including the left PCL, PSMC, middle cingulate cortex, precuneus, and bilateral insula, SMA (uncorrected voxelwise  $P < .001$ , FWE-corrected cluster-level  $P < .05$  and cluster  $\geq 172$ ). Typical brain regions with activation in HCs during MI in *B*, mainly including the left IPL and the bilateral SMA, middle cingulate cortex (uncorrected voxelwise  $P < .001$ , FWE-corrected cluster-level  $P < .05$  and cluster  $\geq 248$ ). Typical brain regions with activation in pediatric patients with CSCI during MI are shown in *C*, mainly including the bilateral SMA, PCL, PSMC, putamen, pallidum, insula, superior temporal gyrus, middle cingulate cortex, cerebellar lobules III–V, and the left IPL, precuneus, and supramarginal gyrus (uncorrected voxelwise  $P < .001$ , FWE-corrected cluster-level  $P < .05$  and cluster  $\geq 199$ ). PSMC indicates primary sensory and motor cortex.

## DISCUSSION

The present study explores the potential neural mechanism of MI in the rehabilitation of pediatric patients with CSCI. Our study included 2 major findings: First, motor-related areas (the bilateral SMA and left middle cingulate cortex) and cognitive-related regions (the left IPL and supramarginal gyrus) were functionally preserved in the MI of pediatric patients with CSCI. Second, the MI of pediatric patients with CSCI evoked higher activation in sensorimotor-related regions (bilateral PCL, SMA, putamen, and cerebellar lobules III–V) than that of HCs, and the activation of some of these regions that of pediatric patients with CSCI during MI was even higher than that of HCs during ME.

### MI and ME in Healthy Children

Our findings showed that MI shares some neural substrates with ME in healthy children, including the bilateral SMA and left middle cingulate cortex, consistent with findings in previous studies in adults.<sup>12</sup> MI may improve the motor skills of healthy children by activating brain areas shared with ME.<sup>26,27</sup>

In addition, compared with ME, MI in healthy children showed reduced

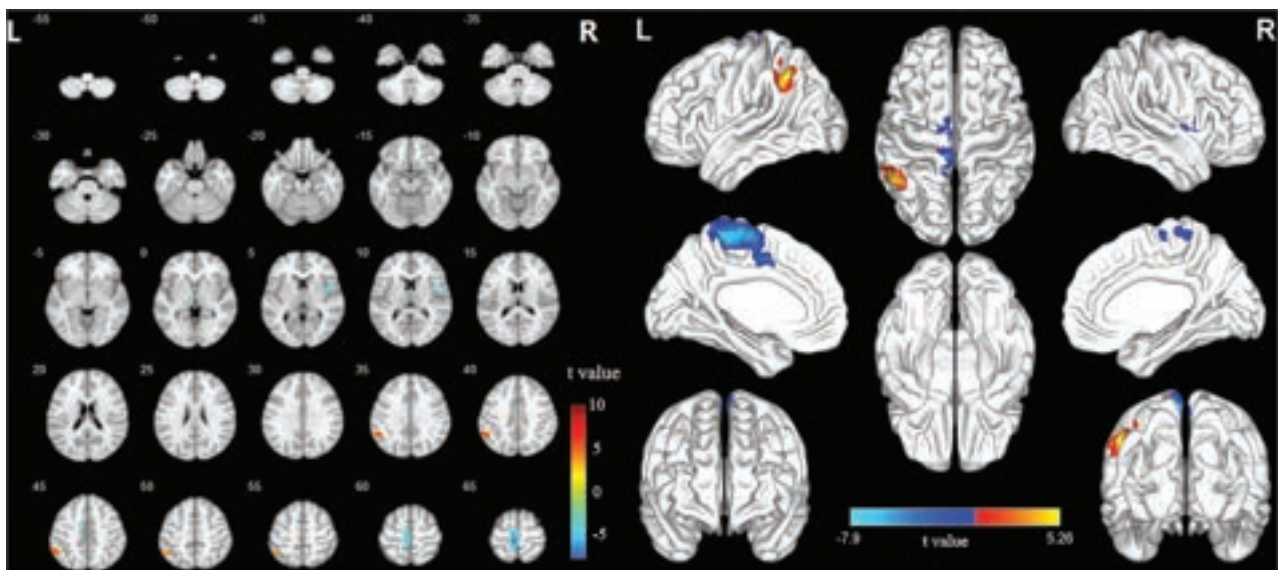


**FIG 2.** Brain regions with significant differences between MI and ME in HCs. Compared with ME, MI of HCs shows increased activation in the left IPL (uncorrected voxelwise  $P < .001$ , FWE-corrected cluster-level  $P < .05$  and cluster  $\geq 113$ , red) as well as decreased activation in the left SMA, PCL, middle cingulate cortex, and right insula (uncorrected voxelwise  $P < .001$ , FWE-corrected cluster-level  $P < .05$  and cluster  $\geq 24$ ; blue). R indicates right; L, left.



activation in the left SMA, PCL, middle cingulate cortex, and right insula, which are thought to be involved in motor preparation, execution, and modulation.<sup>12</sup> MI is an internal representation of movement in the absence of any obvious motor output,<sup>10</sup> which may be responsible for the reduced activation of motor-related brain areas. Conversely, compared with ME, MI in healthy children showed increased activation in the left IPL, which plays a key role in higher cognitive functions.<sup>10,28</sup> As proposed in a recent motor-cognitive model of MI, action simulation is more dependent on consciously controlled cognitive processes.<sup>26,29</sup> This model can be further supported by the increased activation of the IPL in our results.

### Brain Preservation and Reorganization during the MI Task in Pediatric Patients with CSCI

When performing MI, both groups activated not only motor-related areas (the bilateral SMA and middle cingulate cortex)<sup>12</sup> but also cognitive-related regions (the left IPL and supramarginal gyrus).<sup>11</sup> Our results revealed that many features of MI-evoked

brain activation in pediatric patients with CSCI were consistent with those observed in healthy children. After CSCI, the functions of these brain regions may be preserved and can be activated by MI,<sup>10</sup> possibly aiding pediatric patients in improving their sensory and motor functions, just as MI can assist healthy children in improving their motor skills.<sup>27</sup>

Additionally, during the MI task, pediatric patients with CSCI showed higher-level activation in a sensorimotor network that included the bilateral PCL, SMA, putamen, and cerebellar lobules III–V than HCs, and the activation in some of these brain regions in pediatric patients with CSCI during MI was even higher than that of HCs during ME. According to a previous study, task-related activation of the motor cortex is closely associated with motor recovery after subcortical stroke,<sup>30</sup> indicating that overactivation of these regions is likely to reflect neural reorganization.<sup>11</sup>

The PCL, SMA, and putamen are all located in the corticostriatal sensorimotor circuit, which is a pathway from the motor areas of the frontal cortex (including the primary motor cortex, SMA, pre-SMA, and premotor cortex) to the putamen located in the striatum.<sup>31</sup> The corticostriatal sensorimotor circuit is involved in motor control via glutamatergic projections.<sup>32</sup> As part of the primary motor cortex, the PCL is not only involved in the cortical control of micturition and defecation but also responsible for the motor and sensory innervations of the lower extremities.<sup>33</sup> The SMA is a cortical region located in the premotor cortex

**Table 1: Brain regions with significant differences between MI and ME in HCs**

Brain Regions	MNI Coordinate			Cluster Size (Voxels)	Peak T Value
	X	Y	Z		
MI-ME					
Left IPL	-54	-51	39	113	5.2647
ME-MI					
Right insula	45	0	6	44	-5.782
Left middle cingulate cortex	-9	0	42	24	-4.1211
Left PCL/SMA	-6	-30	66	266	-7.9027

**Note:**—MNI indicates Montreal Neurological Institute; PCL/SMA, paracentral lobule (extending to the left SMA).

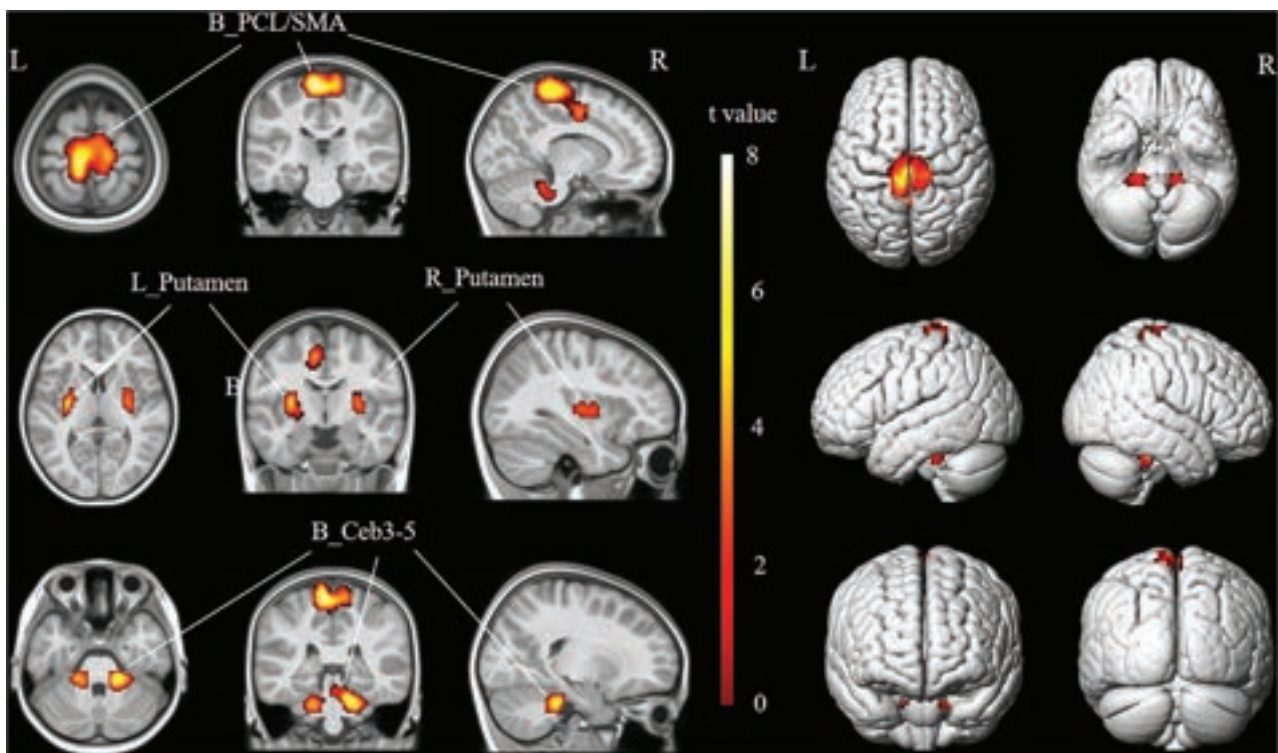


**FIG 3.** Brain regions with increased activation in pediatric patients with CSCI during MI. Compared with HCs, pediatric patients with CSCI show increased activation in bilateral PCL, SMA, putamen, and cerebellar lobules III–V (uncorrected voxelwise  $P < .001$ , FWE-corrected cluster-level  $P < .05$  and cluster  $\geq 91$ ). R indicates right; L, left; Ceb3–5, cerebellar lobules III–V.



**Table 2: Brain regions with increased activation in pediatric patients with CSCI during MI**

Brain Regions	MNI Coordinate			Cluster Size (Voxels)	Peak T Value
	X	Y	Z		
Bilateral PCL/SMA	-6	-27	66	687	8.1397
Left putamen	-30	-9	9	123	6.2061
Right putamen	30	-6	6	91	4.8388
Bilateral cerebellum lobules III-V	15	-36	-27	360	7.3477

**Note:**—MNI indicates Montreal Neurological institute; PCL/SMA paracentral lobule (extending to the left SMA).

that plays important roles in the planning, preparation, and initiation of motor acts.<sup>34</sup> At the level of the striatum, the sensorimotor circuit is largely centered on the putamen, which receives projections from the motor and sensory cortices,<sup>35</sup> including the PCL and SMA. The putamen has been reported to be involved in reinforcement learning as well as motor control,<sup>36</sup> and its activity correlates with the speed and extent of motor execution.<sup>37</sup> Abnormal sensorimotor functions in pediatric patients with CSCI may be linked to changes in the corticostriatal sensorimotor circuit, and our results may suggest that MI can improve sensory and motor functions by activating the corticostriatal sensorimotor circuit.

In addition to the reorganization of the corticostriatal circuit, MI of pediatric patients with CSCI also showed higher-level activation in cerebellar lobules III-V, which are located in the anterior cerebellum and play a key role in sensory and motor functions.<sup>38</sup> Previous scholars have revealed that increased activation in the anterior cerebellum is related to the spatial accuracy demands of imagining the pointing movement.<sup>39</sup> In addition, the cerebellum is known to store internal forward models that can predict movement outcomes, thereby providing precise timing information for predictions.<sup>40</sup> The higher-level activation of cerebellar lobules III-V in our results may suggest that MI in pediatric patients with CSCI involves more spatial and temporal accuracy demands after the loss of sensorimotor function.

**Limitations.** There are 2 major limitations in our study. First, pediatric patients with CSCI in the current study had varying disease durations. Second, this study was a cross-sectional study, and a future longitudinal study is required to confirm the effect of MI on pediatric patients with CSCI.

## CONCLUSIONS

Our study demonstrated that several motor- and cognitive-related areas in the MI network can be functionally preserved in pediatric patients after CSCI. In addition, higher-level activation in sensorimotor-related regions, which reflects functional reorganization, was also detected in pediatric patients with CSCI. The functional preservation and reorganization in the MI network may provide a theoretic basis for the application of MI training in pediatric CSCI.

## ACKNOWLEDGMENTS

The authors thank the patients and healthy volunteers who participated in this study.

**Disclosure forms** provided by the authors are available with the full text and PDF of this article at [www.ajnr.org](http://www.ajnr.org).

## REFERENCES

1. Benedetti B, Weidenhammer A, Reisinger M, et al. **Spinal cord injury and loss of cortical inhibition.** *Int J Mol Sci* 2022;23:5622 CrossRef Medline
2. McIntyre A, Sadowsky C, Behrman A, et al; the SCIRE Project Research Group. **A systematic review of the scientific literature for rehabilitation/habilitation among individuals with pediatric-onset spinal cord injury.** *Top Spinal Cord Inj Rehabil* 2022;28:13–90 CrossRef Medline
3. Knikou M. **Neural control of locomotion and training-induced plasticity after spinal and cerebral lesions.** *Clin Neurophysiol* 2010;121:1655–68 CrossRef Medline
4. Park E, Cha H, Kim E, et al. **Alterations in power spectral density in motor- and pain-related networks on neuropathic pain after spinal cord injury.** *Neuroimage Clin* 2020;28:102342 CrossRef Medline
5. Adams I, Smits-Engelsman B, Lust JM, et al. **Feasibility of motor imagery training for children with developmental coordination disorder: a pilot study.** *Front Psychol* 2017;8:1271 CrossRef Medline
6. Wang H, Xiong X, Zhang K, et al. **Motor network reorganization after motor imagery training in stroke patients with moderate to severe upper limb impairment.** *CNS Neurosci Ther* 2023;29:619–32 CrossRef Medline
7. Guerra ZF, Lucchetti ALG, Lucchetti G. **Motor imagery training after stroke: a systematic review and meta-analysis of randomized controlled trials.** *J Neurol Phys Ther* 2017;41:205–14 CrossRef Medline
8. Li F, Zhang T, Li BJ, et al. **Motor imagery training induces changes in brain neural networks in stroke patients.** *Neural Regen Res* 2018;13:1771–81 CrossRef Medline
9. Tinaz S, Kamel S, Aravala SS, et al. **Neurofeedback-guided kinesthetic motor imagery training in Parkinson's disease: randomized trial.** *Neuroimage Clin* 2022;34:102980 CrossRef Medline
10. Hetu S, Gregoire M, Saimpont A, et al. **The neural network of motor imagery: an ALE meta-analysis.** *Neurosci Biobehav Rev* 2013;37:930–49 CrossRef Medline
11. Chen X, Wan L, Qin W, et al. **Functional preservation and reorganization of brain during motor imagery in patients with incomplete spinal cord injury: a pilot fMRI study.** *Front Hum Neurosci* 2016;10:46 CrossRef Medline
12. Hardwick RM, Caspers S, Eickhoff SB, et al. **Neural correlates of action: comparing meta-analyses of imagery, observation, and execution.** *Neurosci Biobehav Rev* 2018;94:31–44 CrossRef Medline
13. Cederstrom N, Graner S, Nilsson G, et al. **Effect of motor imagery on enjoyment in knee-injury prevention and rehabilitation training: a randomized crossover study.** *J Sci Med Sport* 2021;24:258–63 CrossRef Medline
14. Regev M, Halpern AR, Owen AM, et al. **Mapping specific mental content during musical imagery.** *Cereb Cortex* 2021;31:3622–40 CrossRef Medline
15. Kahraman T, Savci S, Ozdogar AT, et al. **Physical, cognitive and psychosocial effects of telerehabilitation-based motor imagery training in people with multiple sclerosis: a randomized controlled pilot trial.** *J Telemed Telecare* 2020;26:251–60 CrossRef Medline
16. Sharp KG, Gramer R, Butler L, et al. **Effect of overground training augmented by mental practice on gait velocity in chronic, incomplete spinal cord injury.** *Arch Phys Med Rehabil* 2014;95:615–21 CrossRef Medline
17. Pindus DM, Drollette ES, Raine LB, et al. **Moving fast, thinking fast: the relations of physical activity levels and bouts to neuroelectric indices of inhibitory control in preadolescents.** *J Sport Health Sci* 2019;8:301–14 CrossRef Medline
18. Xie J, Jiang L, Li Y, et al. **Rehabilitation of motor function in children with cerebral palsy based on motor imagery.** *Cogn Neurodyn* 2021;15:939–48 CrossRef Medline

19. Funk M, Brugger P, Wilkening F. **Motor processes in children's imagery: the case of mental rotation of hands.** *Dev Sci* 2005;8:402–08 CrossRef Medline
20. Spruijt S, Jongsma ML, van der Kamp J, et al. **Predictive models to determine imagery strategies employed by children to judge hand laterality.** *PLoS One* 2015;10:e126568 CrossRef Medline
21. Souto DO, Cruz T, Coutinho K, et al. **Effect of motor imagery combined with physical practice on upper limb rehabilitation in children with hemiplegic cerebral palsy.** *NRE* 2020;46:53–63 CrossRef Medline
22. Marshall B, Wright DJ, Holmes PS, et al. **Combined action observation and motor imagery facilitates visuomotor adaptation in children with developmental coordination disorder.** *Res Dev Disabil* 2020;98:103570 CrossRef Medline
23. Scott MW, Wood G, Holmes PS, et al. **Combined action observation and motor imagery: an intervention to combat the neural and behavioural deficits associated with developmental coordination disorder.** *Neurosci Biobehav Rev* 2021;127:638–46 CrossRef Medline
24. Malouin F, Richards CL, Jackson PL, et al. **The Kinesthetic and Visual Imagery Questionnaire (KVIQ) for assessing motor imagery in persons with physical disabilities: a reliability and construct validity study.** *J Neurol Phys Ther* 2007;31:20–29 CrossRef Medline
25. Butler AJ, Cazeaux J, Fidler A, et al. **The Movement Imagery Questionnaire-Revised, Second Edition (MIQ-RS) is a reliable and valid tool for evaluating motor imagery in stroke populations.** *Evid Based Complement Alternat Med* 2012;2012:1–11 CrossRef Medline
26. Fan L, Li H, Zhuo J, et al. **The Human Brainnetome Atlas: a new brain atlas based on connectonal architecture.** *Cereb Cortex* 2016;26:3508–26 CrossRef Medline
27. Behrendt F, Zumbrennen V, Brem L, et al. **Effect of motor imagery training on motor learning in children and adolescents: a systematic review and meta-analysis.** *Int J Environ Res Public Health* 2021;18:9467 CrossRef Medline
28. Wang X, Wang H, Xiong X, et al. **Motor imagery training after stroke increases slow-5 oscillations and functional connectivity in the ipsilesional inferior parietal lobule.** *Neurorehabil Neural Repair* 2020;34:321–32 CrossRef Medline
29. Glover S, Bibby E, Tuomi E. **Executive functions in motor imagery: support for the motor-cognitive model over the functional equivalence model.** *Exp Brain Res* 2020;238:931–44 CrossRef Medline
30. Ward NS, Brown MM, Thompson AJ, et al. **Neural correlates of motor recovery after stroke: a longitudinal fMRI study.** *Brain* 2003;126:2476–96 CrossRef Medline
31. Romanelli P, Esposito V, Schaal DW, et al. **Somatotopy in the basal ganglia: experimental and clinical evidence for segregated sensorimotor channels.** *Brain Res Brain Res Rev* 2005;48:112–28 CrossRef Medline
32. Gittis AH, Kreitzer AC. **Striatal microcircuitry and movement disorders.** *Trends Neurosci* 2012;35:557–64 CrossRef Medline
33. Patra A, Kaur H, Chaudhary P, et al. **Morphology and morphology of human paracentral lobule: an anatomical study with its application in neurosurgery.** *Asian J Neurosurg* 2021;16:349–54 CrossRef Medline
34. Si L, Cui B, Li Z, et al. **Altered resting-state intranetwork and inter-network functional connectivity in patients with chronic unilateral vestibulopathy.** *J Magn Reson Imaging* 2022;56:291–300 CrossRef Medline
35. Zhu Y, Song X, Xu M, et al. **Impaired interhemispheric synchrony in Parkinson's disease with depression.** *Sci Rep* 2016;6:27477 CrossRef Medline
36. Kunimatsu J, Maeda K, Hikosaka O. **The caudal part of putamen represents the historical object value information.** *J Neurosci* 2019;39:1709–19 CrossRef Medline
37. Turner RS, Desmurget M, Grethe J, et al. **Motor subcircuits mediating the control of movement extent and speed.** *J Neurophysiol* 2003;90:3958–66 CrossRef Medline
38. Stoodley CJ, Schmahmann JD. **Evidence for topographic organization in the cerebellum of motor control versus cognitive and affective processing.** *Cortex* 2010;46:831–44 CrossRef Medline
39. Lorey B, Pilgramm S, Walter B, et al. **Your mind's hand: motor imagery of pointing movements with different accuracy.** *Neuroimage* 2010;49:3239–47 CrossRef Medline
40. Brooks JX, Carriot J, Cullen KE. **Learning to expect the unexpected: rapid updating in primate cerebellum during voluntary self-motion.** *Nat Neurosci* 2015;18:1310–17 CrossRef Medline

# Fluoroscopy- and CT-Guided Gold Fiducial Marker Placement for Intraoperative Localization during Spinal Surgery: Review of 179 Cases at a Single Institution—Technique and Safety Profile

C.P. Siminski, C.M. Carr, D.F. Kallmes, M.P. Oien, J.L.D. Atkinson, J.C. Benson, F.E. Diehn, D.K. Kim, G.B. Liebo, V.T. Lehman, A.A. Madhavan, I.T. Mark, P.P. Morris, D.P. Shlapak, J.T. Verdoorn, and J.M. Morris

## ABSTRACT

**BACKGROUND AND PURPOSE:** Wrong-level spinal surgery, especially in the thoracic spine, remains a challenge for a variety of reasons related to visualization, such as osteopenia, large body habitus, severe kyphosis, radiographic misinterpretation, or anatomic variation. Preoperative fiducial marker placement performed in a dedicated imaging suite has been proposed to facilitate identification of thoracic spine vertebral levels. In this current study, we report our experience using image-guided percutaneous gold fiducial marker placement to enhance the accuracy and safety of thoracic spinal surgical procedures.

**MATERIALS AND METHODS:** A retrospective review was performed of all fluoroscopy- or CT-guided gold fiducial markers placed at our institution between January 3, 2019, and March 16, 2022. A chart review of 179 patients was performed detailing the procedural approach and clinical information. In addition, the method of gold fiducial marker placement (fluoroscopy/CT), procedure duration, spinal level of the gold fiducial marker, radiation dose, fluoroscopy time, surgery date, and complications (including whether wrong-level surgery occurred) were recorded.

**RESULTS:** A total of 179 patients (104 female) underwent gold fiducial marker placement. The mean age was 57 years (range, 12–96 years). Fiducial marker placement was performed by 13 different neuroradiologists. All placements were technically successful without complications. All 179 (100%) operations were performed at the correct level. Most fiducial markers (143) were placed with fluoroscopy with the most common location at T6–T8. The most common location for placement in CT was at T3 and T4.

**CONCLUSIONS:** All operations guided with gold fiducial markers were performed at the correct level. There were no complications of fiducial marker placement.

**ABBREVIATION:** FL = fluoroscopy

Wrong-level spinal surgery occurs for various reasons, including misinterpreting radiographs, miscounting vertebrae, scapular shadowing, large body habitus, and osteoporosis.<sup>1,2</sup> Additionally, anatomic variations such as thoracolumbar transitional vertebrae, rib variants, hemivertebrae, and block vertebrae can contribute to wrong-level surgery.<sup>3</sup> Human error, such as poor communication and fatigue in the operating room, is also a major risk factor for wrong-level spinal surgery.<sup>4</sup> Furthermore, standard operating room fluoroscopy (FL) equipment is often less robust than interventional imaging techniques, generally

lacking the biplane capability that allows accurate interrogation of the anatomy.<sup>5</sup> Spinal surgery is the most common neurosurgical malpractice claim, and surveys of neurosurgeons indicate that 50% may perform surgery at the wrong vertebral level at least once during their careers.<sup>6,7</sup> Approximately 8% of wrong-level spinal surgeries occur in the thoracic region.<sup>7</sup>

Wrong-level surgical errors can be prevented with preoperative localization techniques.<sup>8–10</sup> A variety of techniques have been put forward to improve localization of thoracic spine surgeries. Several key features of a technique are needed to prevent wrong-level surgery. The technique needs to be safe, reasonably inexpensive, and not overly invasive. Most important, it needs to be accurate, with the marker remaining in place regardless of patient positioning, movement, anatomy, or body habitus. Use of skin markers, soft-tissue markers, and spinous process injection with methylene blue and percutaneous polymethylmethacrylate have all been reported.<sup>2,10–12</sup> In addition, there are a few small retrospective studies that have shown gold fiducial markers to be useful

Received December 1, 2022; accepted after revision March 16, 2023.

From the Mayo Clinic Alix School of Medicine (C.P.S.), Department of Neuroradiology (J.L.D.A., J.C.B.), and Department of Radiology (C.M.C., D.F.K., M.P.O., F.E.D., D.K.K., G.B.L., V.T.L., A.A.M., I.T.M., P.P.M., D.P.S., J.T.V., J.M.M.), Mayo Clinic, Rochester, Minnesota.

Please address correspondence to Clayton Printz Siminski, MD, Mayo Clinic, Mayo Clinic Alix School of Medicine, 200 1st St SW, Rochester, Minnesota 55905; e-mail: siminski.clayton@mayo.edu, siminskic@gmail.com

<https://dx.doi.org/10.3174/ajnr.A7854>

in localizing the correct spinal level.<sup>13,14</sup> Gold fiducial markers are relatively inexpensive, costing approximately US \$50 at our institution, which is comparable and typically less expensive compared with a microcoil. Nonetheless, there is a lack of literature describing routine placement of preoperative gold fiducial markers in a large cohort with multiple interventionalists.

The purpose of this retrospective study was to review and describe our institution's experience with routine FL- and CT-guided preoperative percutaneous spinal gold fiducial marker placement by multiple neuroradiologists in a large cohort of patients with varied pathologies. We will discuss the technique, safety profile, and complications.

## MATERIALS AND METHODS

### Imaging Review

This was a Health Insurance Portability and Accountability Act-compliant retrospective study, approved by the institutional review board of Mayo Clinic. A retrospective search of our radiology data base from January 1, 2019, through March 16, 2022, was performed to identify patients who had FL- or CT-guided spinal gold fiducial marker placement. Inclusion criteria were gold fiducial marker placement in the spine via FL or CT guidance and subsequent spine surgery. The search yielded 183 patients, with 4 patients excluded due to inability to obtain information on  $\geq 1$  variable such as radiation dose or procedure duration. Ultimately, 179 patients were included in the final study cohort.

The electronic medical record was reviewed for patient demographics (sex, age, race, body mass index, osteoporosis diagnosis [yes/no], a trainee being present during the gold fiducial marker placement, method of gold fiducial marker placement [FL/CT], procedure duration, spinal level of gold fiducial marker, radiation dose, FL time, surgery date, and complications [including whether wrong-level surgery occurred]). The safety of gold seed placement was also assessed (eg, bleeding, wrong level, fiducial marker migration).

### Gold Fiducial Marker Placement Technique

The desired location of the gold fiducial marker was specified in the procedural request and neurosurgery notes. Gold fiducial marker placement typically occurs on an outpatient basis the day before surgery, though on occasion, it is done the morning of the operation. Moderate sedation is typically used with IV midazolam and fentanyl, with continuous hemodynamic monitoring by a nurse under supervision of a spine interventional neuroradiologist. Local anesthetic, typically with 1% lidocaine, at the skin surface and 0.25% bupivacaine along the deeper soft tissues and posterior cortex of the targeted vertebra, was used in each procedure.

Most gold fiducial markers were placed with biplane FL guidance (Figs 1 and 2). Alternatively, CT-guided placement performed on a standard CT scanner was used on the basis of the availability of equipment as well as the preference of the proceduralist. Potentially more challenging FL cases would include patients with osteoporosis or severe thoracic kyphosis, particularly when the intended surgical level is within the upper thoracic spine. An advantage of using a standard CT scanner is being able to review the initial focused CT localizer images, including the

axial as well as the coronal and sagittal reformats, allowing the proceduralist to confidently confirm the intended surgical level.

Patients are positioned prone on the table. After the usual sterile technique and before starting the procedure, the spine interventional neuroradiologist carefully determines the location. Identifying the intended surgical pathology via FL or CT guidance alone was unreliable in most cases. Therefore, before the procedure, the interventionalist must perform a complete review of the spine imaging to evaluate any anomalous anatomy (eg, absent ribs, transitional lumbosacral anatomy) and count the vertebral bodies with reference to the cervicothoracic, thoracolumbar, or lumbosacral junctions. In cases with an anomalous vertebral count, especially in those with varying or incorrect counting methods, clear communication of the vertebral counting method is required and should be communicated with the operating surgeon directly and documented in the radiology report.

An 11- or 13-ga bone access needle is used to gain access into the pedicle and is typically positioned near the junction of the pedicle and the vertebral body. In younger patients with extremely dense bone, placement at this location may be impractical and the needle may be placed only into the superficial aspect of the pedicle. Ultimately, the bone access needle must breach the periosteum and be well-seated in the posterior elements to ensure that the gold fiducial marker is not deposited in the overlying soft-tissues where it could be at risk of migration. A gold fiducial marker is placed coaxially through the needle, and the stylet is used to push it into the bone. The needle is removed, and the presence and location of the gold fiducial marker are confirmed with either biplane spot films for FL-guided procedures or a series of postprocedural CT images for CT-guided procedures. Sterile dressing is applied to the site after hemostasis is achieved. The images are labeled, and the interventionalist dictates the side and level of the fiducial marker. Patients are discharged when they met the criteria for recovery from sedation.

## RESULTS

There were 179 patients who had gold fiducial marker placement from January 3, 2019, through March 16, 2022. The mean patient age at the time of gold fiducial marker placement was 57 years (range, 12–96 years), and 104 were female (58%). Fluoroscopy was used to place the gold fiducial marker in 143 patients (80%), with CT used in 36 (20%). All procedures were performed by a group of 13 board-certified and fellowship-trained neuroradiologists. See Table 1 for cohort and procedural demographics.

Gold fiducial marker placement occurred at every level of the thoracic spine with single cases of marker placement at C7, L3, and L4. The most common vertebral levels for placement in our cohort were T6–T8, with T7 being the most common. Four patients each received 2 distinct fiducial marker placements during the same procedure (T4/T10, T2/T10, T8/T11, and T6/T10).

The mean radiation dose was 183.43 mGy (range, 13–805 mGy), and the mean FL time was 3.92 minutes (range, 0.4–15.2 minutes). The average radiation dose for CT-guided placement (258.92 mGy) was higher than the average radiation dose for FL-guided placement (164.43 mGy), though the average procedural time was similar (51.19 minutes for CT and 52.09 minutes



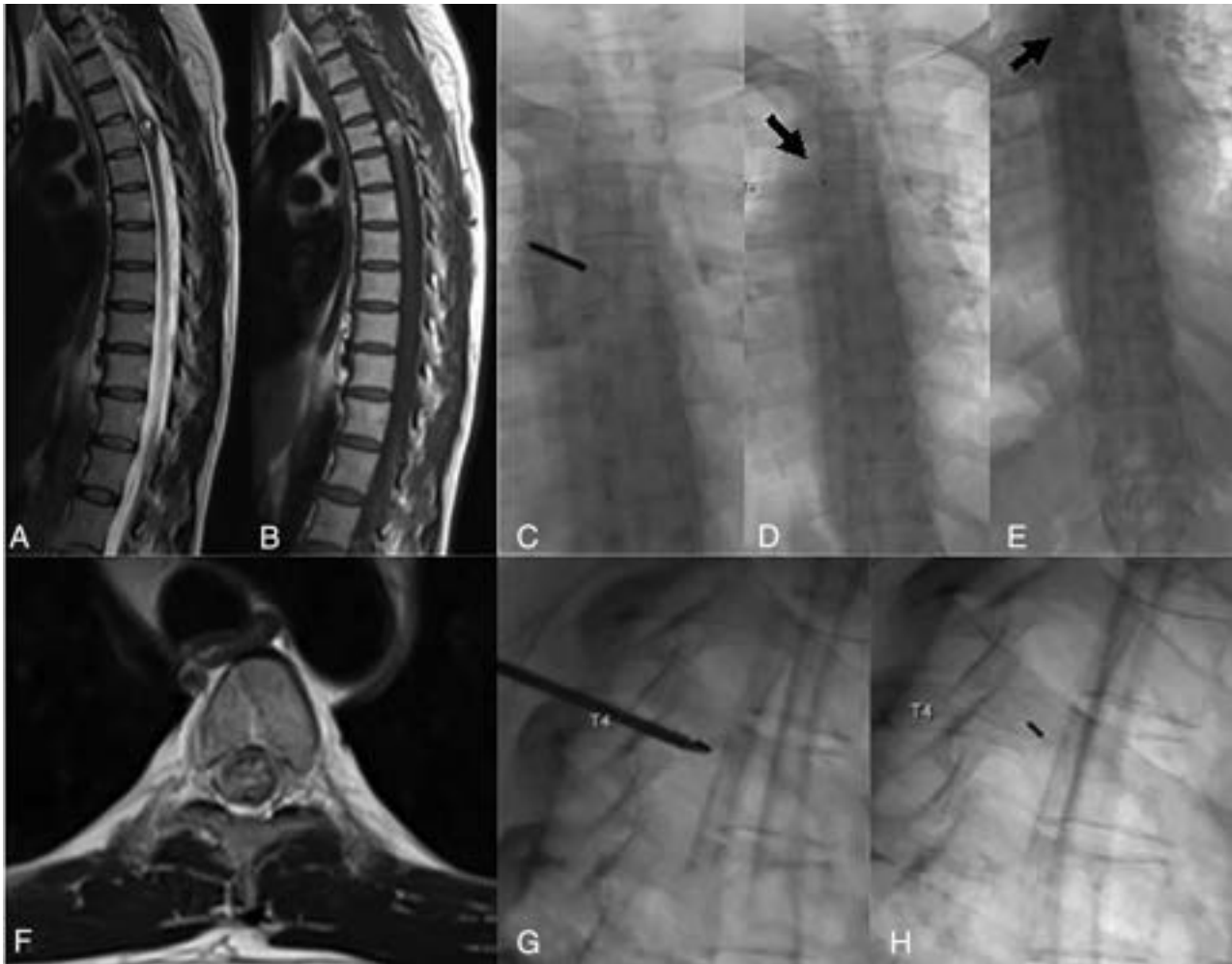


**FIG 1.** Biplane FL was used to place a gold fiducial marker at T4. Sagittal T2WI (A), sagittal T1WI pregadolinium (B), and axial T2WI (F) demonstrate a multilobulated T1-hyperintense, intramedullary mass with fluid-fluid levels and peripheral T2 hypointensity, which was resected and pathologically proved to be a cavernous malformation. C, Anterior-posterior FL image demonstrates the bone access needle traversing the left pedicle of T4. D and E, Postprocedural images for counting purposes show the first and last ribs, respectively, with the fiducial marker in place (arrow). G, Intraoperative image demonstrates the coaxial bone access needle with the stylet in place and the gold fiducial at the tip of the needle. H, Subsequently, the needle has been removed, and the gold fiducial remains in place at the junction of the pedicle and vertebral body.

for FL). See Table 2 for the comparison between CT- and FL-guided gold fiducial marker placement. The most common vertebral levels for CT-guided placement were T3 and T4; for FL-guided placement, the most common levels were T6–T8.

The subsequent operations that relied on gold fiducial marker placement for localization all occurred at the correct spinal level. These were performed by 14 different spine surgeons. No complications related to gold fiducial marker placement were reported.

## DISCUSSION

The purpose of this study was to review and describe our institution's experience with routine FL- and CT-guided preoperative percutaneous gold fiducial marker placement in the spine in a large cohort of patients with multiple interventionalists. Our results demonstrate that the procedure is safe, and no wrong-level surgeries occurred following gold fiducial marker placement in 179 consecutive cases. Moreover, 13 different radiologists performed this same technique, suggesting that this can be a routine

procedure that can be readily learned and performed by procedurally trained radiologists. This outcome provides evidence of the safety and efficacy of this relatively rarely reported technique.

The primary benefit of gold fiducial marker placement is to allow the surgeon to quickly and safely localize the correct vertebral level to mitigate the risk of wrong-level surgery. Additionally, although not directly assessed in our review, fiducial marker placement has been shown to greatly reduce intraoperative FL time and ultimately operative time.<sup>2</sup> In spinal surgery cases performed without a localizing technique, typically the operating surgeon uses a similar method of meticulous counting but often on inferior imaging equipment compared with the radiology suite.

When gold fiducial markers are placed in the spine, the interventionalist must verify the correct level for placement. This verification occurs through carefully reviewing the relevant imaging, noting any anatomic variations, and subsequently verifying the level of gold fiducial marker placement. Assessment for a few common anatomic variations should be performed. Occasionally, C7 will have an elongated transverse process, so-called "cervical



**FIG 2.** CT-guided gold fiducial marker placement. *A* and *B*, Sagittal T2WI and fat-saturated postcontrast T1WI demonstrate an intradural extramedullary, lobulated, homogeneously intensely enhancing mass that was resected and found to be a schwannoma on pathology. *D*, Intraprocedural axial CT bone windows at T12 demonstrate a coaxial bone access needle located within the left pedicle of T12. *C* and *E*, Postprocedural CT MIP and sagittal reconstructions confirm the gold fiducial marker placement in the left T12 pedicle. Arrow points toward gold fiducial marker.

ribs.” At imaging they tend to be much more gracile than the usual first ribs. Close correlation with prior chest x-rays or CTs in conjunction with counting from C2 can ensure correct identification. The absence of ribs at T12 as well as the presence of riblets at L1 are another common anatomic variation that occurs at the thoracolumbar junction. Careful review of the number of ribs on prior imaging and counting not only from C2 inferiorly but also from the sacrum superiorly will assist in verification of the numbering. Finally, it is common to have transitional vertebrae at L5 or S1 with partial sacralization or lumbarization, respectively, of those levels. As with other anatomic variations, correlation with all imaging to determine the total number of presacral segments will allow successful enumeration of the spine. In addition, review of imaging relating to the lesion of surgical interest will help confirm the desired fiducial marker placement for surgery.

This procedure is safe when the appropriate technique is followed because no adverse events occurred in our cohort. Review of the literature would support this outcome, with rare case reports discussing complications. One case report detailed a complication related to fiducial marker placement at C7 from which the patient endured lower extremity pain and vibrations postoperatively, which subsided with a course of steroids.<sup>15</sup> The suspected cause was excessive forceful hyperextension of the neck from anteriorly directed thrusting during needle insertion. This issue highlights the importance of patient positioning for stability during the procedure. In addition, in younger patients

**Table 1: Cohort and procedural demographics**

Demographics	
Mean age (range)	57 (12–96)
Sex	Male = 75 Female = 104
Level of gold fiducial marker placement	C7 = 1 T1 = 5 T2 = 5 T3 = 14 T4 = 14 T5 = 18 T6 = 21 T7 = 26 T8 = 21 T9 = 15 T10 = 19 T11 = 15 T12 = 7 L3 = 1 L4 = 1
Method	CT = 36 FL = 143
Mean radiation dose (range) (mGy)	183.43 (13–805)
Mean FL time (range) (min)	3.92 (0.4–15.2)
No. of wrong-level surgeries	0
No. of different radiologists who performed a gold fiducial marker placement	13
Mean BMI (range)	28.9 (16.1–55.8)
Osteoporosis diagnosis	No = 159 Yes = 20
Trainee present?	No = 107 Yes = 72
Mean procedure duration (range) (min) <sup>a</sup>	51.9 (20–114)
Mean No. of days when operation was performed after placement (range)	3.6 days (0–92)

**Note:**—BMI indicates body mass index.

<sup>a</sup>Entry of the room by physician to room exit time.

without osteoporosis, the bone can be extremely dense, making needle placement very challenging. We recommend consideration of other tools such as a drill, which can be helpful in these situations.

Past research has described fiducial marker placement as a preventative technique to mitigate the risk of wrong-level surgery.<sup>8–10</sup> Additionally, other research has described gold fiducial marker placement to be an advantageous choice because it is relatively inexpensive and can be visualized on several forms of imaging.<sup>13</sup> Moreover, gold fiducial markers have already been used in other specialties such as urology and colorectal surgery.<sup>16,17</sup> Ishak et al<sup>14</sup> also performed a similar review in a smaller sample size ( $n = 57$ ) demonstrating gold fiducial marker placement to be safe and accurate in marking vertebral levels. Past research has described fiducial marker placement as an accurate, relatively inexpensive, and preventative technique to mitigate the risk of wrong-level surgery, and the literature reports its use in multiple specialties such as urology and colorectal surgery.<sup>8–10,13,14,16,17</sup> Increasing awareness and availability of this safe and routine procedure at other institutions could be beneficial in eliminating serious, preventable, and costly medical errors associated with wrong-level spinal surgery.

Limitations of this study include the retrospective nature of the review without a control group. Another limitation is that our study only reviewed procedures that occurred at a single

**Table 2: Comparison between CT- and FL-guided gold fiducial marker placements**

	CT	FL
Total cases	36	143
Level of gold fiducial marker placement	C7 = 1 T1 = 4 T2 = 3 T3 = 6 T4 = 6 T5 = 2 T6 = 2 T7 = 2 T8 = 2 T9 = 1 T10 = 4 T11 = 1 T12 = 2 L3 = 0 L4 = 0	C7 = 0 T1 = 1 T2 = 2 T3 = 8 T4 = 8 T5 = 16 T6 = 19 T7 = 24 T8 = 19 T9 = 14 T10 = 15 T11 = 14 T12 = 5 L3 = 1 L4 = 1
Average radiation dose (range) (mGy)	258.92 (80.69–563.56)	164.43 (13–805)
Average procedural time (range) (min)	51.19 (31–114)	52.09 (20–89)

institution and results could differ when analyzed across multiple institutions.

## CONCLUSIONS

Our largest-to-date single-center retrospective study of 179 spinal gold fiducial marker placements supports these procedures being performed safely by neuroradiologists. No wrong-level surgery occurred in these 179 consecutive cases, of which 176 were at the thoracic levels.

Disclosure forms provided by the authors are available with the full text and PDF of this article at [www.ajnr.org](http://www.ajnr.org).

## REFERENCES

- James MA, Seiler JG 3rd, Harrast JJ, et al. **The occurrence of wrong-site surgery self-reported by candidates for certification by the American Board of Orthopaedic Surgery.** *J Bone Joint Surg Am* 2012;94:e2 CrossRef Medline
- Upadhyaya CD, Wu JC, Chin CT, et al. **Avoidance of wrong-level thoracic spine surgery: intraoperative localization with preoperative percutaneous fiducial screw placement: clinical article.** *J Neurosurg Spine* 2012;16:280–84 CrossRef Medline

- Shah M, Halalmeh DR, Sandio A, et al. **Anatomical variations that can lead to spine surgery at the wrong level, Part II: thoracic spine.** *Cureus* 2020;12:e8684 CrossRef Medline
- Epstein N. **A perspective on wrong level, wrong side, and wrong site spine surgery.** *Surg Neurol Int* 2021;12:286 CrossRef Medline
- Nguyen A, Lyon K, Robinson T, et al. **Biplane fluoroscopic-guided percutaneous thoracic instrumentation: a technical note.** *Cureus* 2020;12:e11939 CrossRef Medline
- Fager CA. **Malpractice issues in neurological surgery.** *Surg Neurol* 2006;65:416–21 CrossRef Medline
- Mody MG, Nourbakhsh A, Stahl DL, et al. **The prevalence of wrong level surgery among spine surgeons.** *Spine (Phila Pa 1976)* 2008;33:194–98 CrossRef Medline
- Strong MJ, Santarosa J, Sullivan TP, et al. **Pre- and intraoperative thoracic spine localization techniques: a systematic review.** *J Neurosurg Spine* 2021 Nov 19. [Epub ahead of print] CrossRef Medline
- Anaizi AN, Kalhorn C, McCullough M, et al. **Thoracic spine localization using preoperative placement of fiducial markers and subsequent CT: a technical report.** *J Neurol Surg A Cent Eur Neurosurg* 2015;76:66–71 CrossRef Medline
- Binning MJ, Schmidt MH. **Percutaneous placement of radiopaque markers at the pedicle of interest for preoperative localization of thoracic spine level.** *Spine (Phila Pa 1976)* 2010;35:1821–25 CrossRef Medline
- Hsu W, Sciubba DM, Sasson AD, et al. **Intraoperative localization of thoracic spine level with preoperative percutaneous placement of intravertebral polymethylmethacrylate.** *J Spinal Disord Tech* 2008;21:72–75 CrossRef Medline
- Paolini S, Ciappetta P, Missori P, et al. **Spinous process marking: a reliable method for preoperative surface localization of intradural lesions of the high thoracic spine.** *Br J Neurosurg* 2005;19:74–76 CrossRef Medline
- Dhahri PA, McCreary R, George KJ. **A novel gold marker to aid intraoperative localisation during spinal surgery!** *Br J Neurosurg* 2020;34:305–07 CrossRef Medline
- Ishak B, Abdul-Jabbar A, Tawfik T, et al. **Prevention of wrong-level surgery in the thoracic spine: preoperative computer tomography fluoroscopy-guided percutaneous gold fiducial marker placement in 57 patients.** *Spine (Phila Pa 1976)* 2020;45:1720–24 CrossRef Medline
- Stevens QE, Dickerman RD, Kattner KA, et al. **Nonhemorrhagic cord contusion after percutaneous fiducial placement: case report and surgical recommendations.** *J Spinal Cord Med* 2006;29:425–29 CrossRef Medline
- van den Ende RP, Rigter LS, Kerkhof EM, et al. **MRI visibility of gold fiducial markers for image-guided radiotherapy of rectal cancer.** *Radiother Oncol* 2019;132:93–99 CrossRef Medline
- Gustafsson C, Korhonen J, Persson E, et al. **Registration free automatic identification of gold fiducial markers in MRI target delineation images for prostate radiotherapy.** *Med Phys* 2017;44:5563–74 CrossRef Medline

# Celebrating 35 Years of the AJNR

May 1988 edition

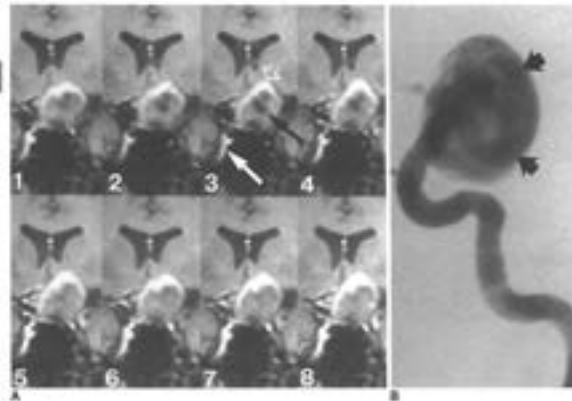
## MR Evaluation of Large Intracranial Aneurysms Using Cine Low Flip Angle Gradient-Refocused Imaging

Jay S. Tarullo<sup>1\*</sup>  
 Greg V. Krishnan<sup>1</sup>  
 Harold T. Hargrave<sup>1</sup>  
 Alexander S. Marks<sup>1</sup>  
 Grant D. Huxford<sup>1</sup>  
 David Norman<sup>1</sup>

MR imaging has proved to be useful in evaluating large intracranial aneurysms. The aneurysm and parent vessel can be identified on flow voids and distended flow. However, in the presence of slow flow, even-echo refocusing, and motion artifact, flow void intraluminal signal may be present, which may be difficult to distinguish from thrombus. Anomalous flow that originates from the aneurysm may affect an adjacent structure. Further definition of aneurysm position and anatomy may aid in treatment planning and assessment. Cine MR is a new technique using a movie loop of sequential 30- to 60-degree gradient-echo images in the steady state. Images obtained during various points in the cardiac cycle. The combination of 30- to 60-degree images and cine flow voids show oblique display of aneurysm structure. A comparison of the method with routine T1- and T2-weighted MR imaging and angiography was made in a group of 13 patients with intracranial aneurysms greater than 1.0 cm in diameter. Eight of these patients underwent transcranial Doppler flow studies before MR imaging. Cine MR imaging showed low flow intensity that is less resistant to even-echo refocusing and high-velocity flow can be recognized on the basis of signal loss, which occurs during systole. Thrombus demonstrated variable signal intensity, which remained unchanged during the cardiac cycle. Compared with routine MR imaging, flow voids were more conspicuous than phase-contrast artifacts and improved visualization of the neck of the aneurysm. Flow voids were also more conspicuously demonstrated after transcranial Doppler flow studies. Cine MR demonstrated improved conspicuity of aneurysm flow and higher contrast between flowing blood and the aneurysm lumen when compared with routine MR. Cine MR is a new technique that provides additional information and may be useful in the evaluation and assessment of large intracranial aneurysms. Cine MR is not available with other routine MR or angiography. The inherent limitations of this new technique include patient motion artifacts, flow that originates from distal aneurysms or smaller aneurysms, and poor flow acquisition due to cardiac arrhythmias.

This article appears in the November 1988 issue of AJNR and the July 1989 issue of AJNR. Received September 15, 1987; accepted after revision December 15, 1987. Received for consideration of the American Society of Neuroradiology, New York, May 1987. <sup>1</sup> Division of Neuroradiology, Department of Radiology, University of California, San Francisco, San Francisco, California. Reprint requests to Jay S. Tarullo, MD, Department of Radiology, University of California, San Francisco, 1601 Divisadero Street, San Francisco, CA 94115.

The evaluation of intracranial aneurysms by MR has been described. MR has several known advantages over both angiography and contrast-enhanced CT. These advantages include identification of signal voids within the parent lumen (1-3), laminated thrombus (2), adjacent parenchymal edema, and hemorrhage (2, 4) and parent vessel (4), as well as the definition of an aneurysm location with mass effect (2). For these reasons MR may be more specific in characterizing these lesions (5). The parent lumen of the aneurysm can be identified on routine MR sequences for high-velocity signal loss resulting from flow void effects or by subtraction. However, in the presence of slow flow and/or even-echo refocusing (2, 3), distinguishing flowing blood from thrombus may be difficult. On the other hand, calcium in the aneurysm wall may be identified with flow void. If the aneurysm is mural or is aneurysmally treated with associated thrombus, a parent artery may be mistaken for an aneurysmal malformation (2). Good aneurysm flow is a variable indicator of associated subarachnoid hemorrhage and air emboli.



## Posterior Pituitary Ectopia: An MR Feature of Pituitary Dwarfism

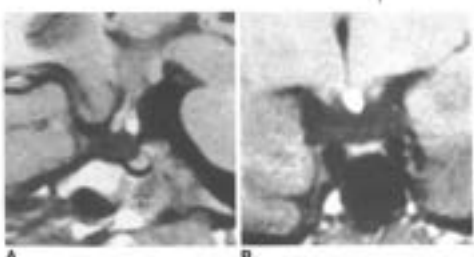
William M. Kelly<sup>1\*</sup>  
 Walter Kucharsky<sup>1</sup>  
 John Kucharsky<sup>1</sup>  
 Gerald Kipin<sup>1</sup>  
 Wallace W. Frank<sup>1</sup>  
 David Norman<sup>1</sup>  
 T. H. Newton<sup>1</sup>

Using high-field strength, 1.0 T, high-resolution MR, we identified the following examples of neurohypophysial abnormalities in each of the pituitary dwarfs (7) whose hypoplasia or total absence of the neurohypophysis (2) absence of the posterior pituitary bright spot on the superior sagittal section (3-6) and basal nuclear cisterns of the posterior aneurysmal enhancing/hypointense signal on T1-weighted images (in the basis of the signal reduction and the absence of distal extension) in these patients. The median anterior median cisterns appeared to represent an enlarged and functional posterior pituitary gland.

We propose that this anatomic abnormality is the end result of a localized defect of developmental origin, possibly congenital in nature, and involving primarily the infundibular stem. These lesions probably represent a form of isolated posterior pituitary gland hypoplasia through degeneration of stem defects of neural hypophysial-releasing factors. Finally, we suggest that the magnetic resonance contrast mechanism of the median anterior median cisterns proliferation of stem cell phenotype is a process that reduces formation of an anterior and functional posterior pituitary gland, compatible with the anatomic origin.

Although the underlying cause of congenital pituitary dwarfism remains unknown, the current consensus of opinion is that a primary hypophysial lesion probably accounts for the neuroendocrine disorder. An increased incidence of brain delivery and birth asphyxia among newborns who later develop pituitary dwarfism has prompted researchers to invoke an ischemic mechanism of injury that impairs hypophysial function in the perinatal period (1, 2). However, pathologic proof of hypoxic damage to the hypophysial stem and craniochordal imaging techniques have thus far failed to identify an abnormality of hypophysial tissue. Furthermore, pituitary dwarfs have not been reported to exhibit an increased incidence of motor deficits or basal ganglia disturbances, which might be expected from injury to descending sensory tracts that share a common vascular territory with the hypophysium.

High-resolution (7) is a well-established and widely accepted method of evaluating the posterior region. However, more recent techniques indicate that studies of the MR in currently the imaging techniques of choice for investigating patients with suspected pituitary-related endocrine disease (3-6). Relative to MR, CT provides complementary near null-tissue contrast-resolution, and diagnostic results are often obscured by beam-hardening artifacts projected through the sella turcica. Despite these technical limitations, a recent report (8) involving CT evidence of both pituitary gland and stalk hypoplasia in pituitary dwarfs (2). The improved spatial detail provided by high-resolution MR enables more thorough evaluation and tissue characterization of descending structures in and about the sella turcica. These diagnostic advantages provide more consistent post-natal documentation of the recently described pattern of hypoplasia encountered in pituitary dwarfs and disclose additional findings that might help to elucidate the underlying cause of the disease. The inherently superior contrast provided by MR



Received August 15, 1987; accepted after revision December 15, 1987. Presented at the 1988 annual meeting of the American Society of Neuroradiology, New York, May 1988. <sup>1</sup> Division of Neuroradiology, Department of Radiology, University of California, San Francisco, San Francisco, California. Reprint requests to Jay S. Tarullo, MD, Department of Radiology, University of California, San Francisco, 1601 Divisadero Street, San Francisco, CA 94115.



# Critical Appraisal of Artificial Intelligence–Enabled Imaging Tools Using the Levels of Evidence System

N. Pham, V. Hill, A. Rauschecker, Y. Lui, S. Niogi, C.G. Fillipi, P. Chang, G. Zaharchuk, and M. Wintermark

## ABSTRACT

**SUMMARY:** Clinical adoption of an artificial intelligence–enabled imaging tool requires critical appraisal of its life cycle from development to implementation by using a systematic, standardized, and objective approach that can verify both its technical and clinical efficacy. Toward this concerted effort, the ASFNR/ASNR Artificial Intelligence Workshop Technology Working Group is proposing a hierarchal evaluation system based on the quality, type, and amount of scientific evidence that the artificial intelligence–enabled tool can demonstrate for each component of its life cycle. The current proposal is modeled after the levels of evidence in medicine, with the uppermost level of the hierarchy showing the strongest evidence for potential impact on patient care and health care outcomes. The intended goal of establishing an evidence-based evaluation system is to encourage transparency, foster an understanding of the creation of artificial intelligence tools and the artificial intelligence decision-making process, and to report the relevant data on the efficacy of artificial intelligence tools that are developed. The proposed system is an essential step in working toward a more formalized, clinically validated, and regulated framework for the safe and effective deployment of artificial intelligence imaging applications that will be used in clinical practice.

**ABBREVIATIONS:** AI = artificial intelligence; HIPPA = Health Insurance Portability and Accountability Act

As artificial intelligence (AI) reimagines many facets of health care, radiology will be a leading force for developing and leveraging AI-based imaging technologies.<sup>1–3</sup> This past decade saw a dramatic rise in the number of commercially available AI products receiving US FDA approval for clinical use in imaging.<sup>4</sup> As of October 2022, there are 521 FDA-authorized AI-enabled medical devices, of which 75.2% are for radiology use.<sup>5</sup> Of these, neuroimaging applications comprise a large share, with estimates of up to 40% of products on the market.<sup>6</sup> With the increasing availability of AI software, a systematic method of integrating these tools into a clinically validated and regulated framework is necessary for the safe and effective deployment of medical imaging AI applications in routine clinical patient care. Unlike AI in other

industries, such as entertainment and advertising, which can afford to be tolerant of errors, errors in medicine can be fatal.

Adoption of an AI-enabled tool requires critical appraisal of its life cycle from development to implementation, with careful consideration of the existing scientific evidence supporting its clinical utility. However, standardized objective metrics to quantify AI quality and clinical utility are currently lacking, limiting the fair and accurate evaluation and comparison of different AI-enabled tools, especially when multiple products exist for the same clinical task.<sup>7</sup>

These are not new issues as they also affect other medical imaging software products, but the number and diversity of AI-enabled tools suddenly now hitting the market makes it a timely moment to consider practical and unbiased ways of assessing such tools. Thus, the ASFNR/ASNR has created an AI workshop technology working group with the goal of providing a practical approach for evaluating the potential effectiveness of AI technology in clinical practice.

Toward this goal, here we introduce an evaluation system using hierarchal levels of evidence that reflect the rigor of scientific data (Figure). Demonstration of clinical efficacy and value, at the pinnacle of this evaluation system, is the most important factor for clinical adoption.

Different points in the imaging workflow can be augmented by AI-enabled tools, with a range of clinical applications including

Received December 16, 2022; accepted after revision March 16, 2023.

From the Department of Radiology (N.P., G.Z.), Stanford School of Medicine, Palo Alto, California; Department of Radiology (V.H.), Northwestern University Feinberg School of Medicine, Chicago, Illinois; Department of Radiology (A.R.), University of California, San Francisco, San Francisco, California; Department of Radiology (Y.L.), NYU Grossman School of Medicine, New York, New York; Department of Radiology (S.N.), Weill Cornell Medicine, New York, New York; Department of Radiology (C.G.F.), Tufts University School of Medicine, Boston, Massachusetts; Department of Radiology (P.C.), University of California, Irvine, California; and Department of Neuroradiology (M.W.), The University of Texas MD Anderson Cancer Center, Houston, Texas.

Please address correspondence to Nancy Pham, MD, Stanford School of Medicine, Department of Radiology, 453 Quarry Rd, 322.11, Palo Alto, CA 94304; e-mail: pham.nancy@gmail.com; @stanfordneuroil

<http://dx.doi.org/10.3174/ajnr.A7850>

but not limited to administrative, operational, patient, and image centered tasks.<sup>8-10</sup> For the purposes of this white paper, the hierarchical levels of evidence system is most useful for imaging and patient-related AI applications. However, the main principles can be generalized to other applications.

Finally, the radiologist continues to be an instrumental gatekeeper of patient care quality and safety, particularly now as we enter the era of AI. As clinical domain experts, radiologists provide important oversight on the effective use of AI software in the clinical setting.<sup>11</sup> To better position the radiologist in this role, this white paper presents a structured method of guidance on the critical appraisal of AI software using the levels of evidence system.

### Levels of Evidence

To date, there are no agreed upon levels of evidence needed for the evaluation of AI-enabled tools; thus, the already established medicine model provides a practical starting point for the development of such a systematic process.<sup>12</sup> We propose a hierarchy of levels of evidence reflecting the critical elements of an AI product's life cycle from development to the clinical implementation phase (Figure).

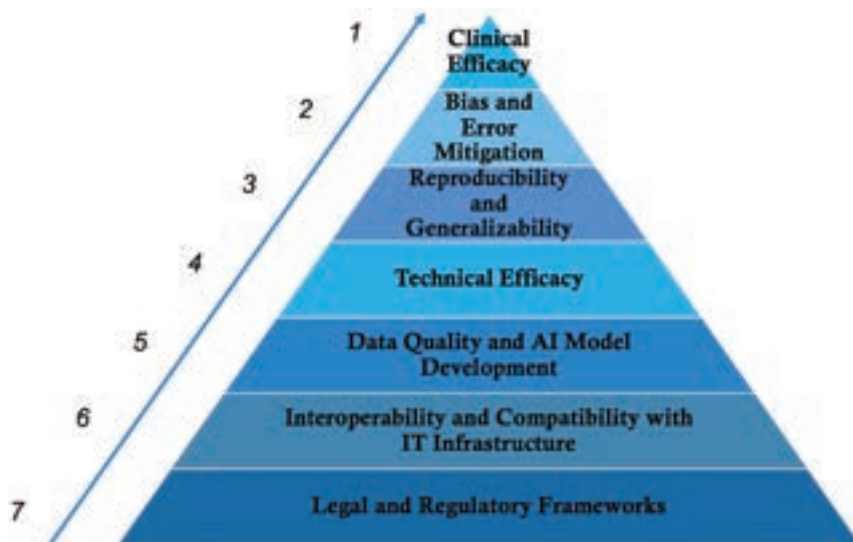


**FIGURE.** Levels of evidence. Proposed 7 levels of evidence for the systematic evaluation of an AI product's quality and effectiveness in the clinical setting.

The two levels at the base of the hierarchy, levels 6 and 7, are considered fundamental requirements that an AI product must meet before further consideration for implementation in the clinical workflow. For example, an AI product must comply with current legal and regulatory requirements (level 7) such as Health Insurance Portability and Accountability Act (HIPAA) and FDA clearance. Thereafter, it must be compatible with the information technology infrastructure (level 6) at the site where it will be deployed, before proceeding with other requirements listed in the hierarchy.

Further description of the levels of evidence from 1 to 7 is detailed below, with level 1 denoting the highest quality and strongest evidence for potential impact on patient care and health care outcomes. In addition, Table 1 provides an abbreviated summary, while Table 2 provides an expanded summary of each component of the evaluation system.

### Data Quality and AI Model Development

AI models should be developed from data that are large, diverse, and reflective of the intended population. However, in practice, access to comprehensive and “big” data is challenging, and training is often performed on limited data.<sup>13</sup> This introduces bias that can affect reproducibility, generalizability, and performance outside the data range on which the model was trained. Thus, peer-reviewed publications including information on the source and characteristics of the data used to train, validate, and test the AI model can help end-users determine overall compatibility with the target patient population of interest.<sup>14-16</sup>

AI companies and developers do not typically publicly report detailed information on data used to develop or validate algorithms, despite having undergone the necessary FDA clearance process, limiting the ability of end-users to make informed decisions

**Table 1: Summary of levels of evidence**

Levels of Evidence	Element	Types of Evidence
Level 1	Clinical efficacy	One prospective or randomized clinical trial or meta-analysis
Level 2	Bias and error mitigation	At least 2 independent retrospective studies separate from original institution
Level 3	Reproducibility and generalizability	At least 2 retrospective studies with at least 1 from an institution independent of the original institution
Level 4	Technical efficacy	Two retrospective studies from the same institution
Level 5A	Data quality and AI model development with external testing	One retrospective study with internal and external data used for final performance reporting
Level 5B	Data quality and AI model development with internal testing	One retrospective study with only internal data used for final performance reporting
Level 6	Interoperability and integration into the IT infrastructure	AI company can provide a plan including interoperability standards for integration into the existing radiology and hospital digital information systems
Level 7	Legal and regulatory frameworks	AI-enabled tool is compliant with current patient data protection, security, privacy, HIPAA, and government regulations

**Note:**—IT indicates information technology.

**Table 2: Detailed summary of levels of evidence<sup>a</sup>**

Levels of Evidence	Element	Description	Types of Evidence	Significance
Level 1	Clinical efficacy	Clinical efficacy is the assessment of how the AI tool impacts patient care and health care outcomes	AI tool has been used in at least 1 prospective study, randomized clinical trial, or meta-analysis demonstrating potential for improved patient care and health care outcomes, including improved mortality, quality of life, morbidity, or reduced health care cost	Although measuring clinical efficacy and added value for an early AI technology is challenging, it remains the single most important feature for clinical success and adoption
Level 2	Bias and error mitigation	Biases of different types invariably exist in all data and can lead to AI modeling errors when applied to patients in different clinical settings	AI model can adapt to at least 2 separate institutions different from where it was initially developed (2 independent retrospective studies) AND Peer-reviewed results from those retrospective studies from above are available describing the various populations used to test the AI model, including age ranges, sex, and types of scanners AND AI company has a process to continuously incorporate feedback and improve their model (postdeployment monitoring)	AI related errors in clinical practice may be harmful to patients; thus, the AI tool should be tested at multiple different sites, with differing patient demographics, disease prevalence, and imaging vendors to determine operational characteristics, generalizability, and potential pitfalls  As clinical and patient care standards are constantly evolving, AI models may need routine surveillance and updates for performance and data drift
Level 3	Reproducibility and generalizability	AI-enabled tool can be applied to different clinical settings, while demonstrating consistent high-quality results	At least 2 retrospective studies showing that the AI tool has performance characteristics similar to or alternative methods in the literature AND At least 1 independent study different from where the AI tool was developed to demonstrate that the AI tool can adapt to at least 1 different institution	A multi-institution approach supports reproducibility and generalizability of the AI tool
Level 4	Technical efficacy	Technical efficacy is the assessment that the AI model correctly performs the task that it was trained to do	AI model performance has been shown in 2 retrospective studies to have potential clinical impact compared with similar or alternative methods in the literature AND These retrospective studies can be from the same institution	Recent investigations suggest that less than 40% of AI models have peer-reviewed evidence available on their efficacy <sup>6</sup>
Level 5A	Data quality and AI model development with external testing	AI models are prone to overfitting and an external test data set during development should be used to report final performance metrics	Level 5B evidence as described with an external test set used for performance validation	Inclusion of an external data set during the development phase supports the generalizability of the AI tool
Level 5B	Data quality and AI model development with internal testing	AI company should provide peer-reviewed information about the characteristics of the data used to develop the AI model  AI company can explain how the AI model	One retrospective study showing the following: Peer-reviewed results detailing the inclusion/exclusion criteria, source, and type of data used to train, validate, and test the AI model  AND	Data characteristics will influence the suitability and applicability of the AI model to the target patient population of interest

*Continued on next page*

**Table 2: Continued**

Levels of Evidence	Element	Description	Types of Evidence	Significance
		makes decisions that are relevant to patient care	Peer-reviewed results describing how the AI model was developed, including use of a standard of reference that is widely accepted for the intended clinical task AND No final external test set was used for final performance reporting	Selection of a high-quality standard of reference is important for accurately comparing the peak performance of the AI model to that of current clinical practice
Level 6	Interoperability and integration into the IT infrastructure	AI software should integrate seamlessly into the hospital information system, radiology information system, and PACS to be clinically useful	AI company can provide a plan including interoperability standards for integration into the existing radiology and hospital digital information systems  AI company can provide on-site demonstration of clinical integration and potential impact on workflow before full deployment	Successful clinical implementation of an AI tool requires close collaboration between the AI company and site experts, including radiologists, referring physicians, data scientists, and information technologists Real time demonstration is an important mechanism for identifying potential site-specific problems
Level 7	Legal and regulatory frameworks	Patient consent, privacy, and confidentiality laws will vary depending on state, local, and institutional regulations	AI-enabled tool is compliant with current patient data protection, security, privacy, HIPAA, and government regulations	AI companies, health care systems, and radiologists are key gatekeepers of patient autonomy, privacy, and safety

<sup>a</sup> Appropriate reporting of AI model performance will depend on the task; however, examples of relevant statistical measures include ROC, sensitivity, specificity, and positive and negative predictive values, among others.

about these products. Thus, the emphasis on more than 1 peer-reviewed publication in this white paper encourages some level of independent, critical, and structured analysis to provide scientific evidence for verifying the intended use and clinical impact of the AI product.

At the very least, even if a product does not meet this level of evidence expectation, it is most responsible for a company to provide information about their patient population, including demographic characteristics, model development and validation methods, and indicators of statistical efficacy. Purchasers and end-users should expect and require statistical evidence and, preferably, consider these levels of evidence as indicators for the strength of a tool’s methodological quality of design, validity, and applicability to patient care.

Barriers to improving AI transparency include competing financial incentives among developers, data privacy and sharing restrictions, and some degree of acceptance of the “black box” nature of AI-based solutions. To overcome these limitations, initiatives have been proposed to establish minimum data reporting standards for AI in health care including but not limited to MINIMAR (MINimum Information for Medical AI Reporting), CONSORT-AI (Consolidated Standard of Reporting Trials-Artificial Intelligence), and CLAIM (Checklist for Artificial Intelligence in Medical Imaging).<sup>17-19</sup> Others have also introduced checklists, recommendations, and guidelines toward assessing the suitability of AI-based tools in the health care environment.<sup>11,20-22</sup> Our proposal utilizing the levels of evidence builds on these ongoing initiatives, with a greater focus on the availability of peer-reviewed evidence and publications, to improve confidence and trust for all stakeholders using AI-based tools.

Selection of a quality standard of reference during the development phase is critical for an accurate and fair comparison of the AI model’s performance against the current standard of practice.<sup>23,24</sup> After all, the adoption of any clinical tool relies on scientific evidence that it imparts some advantage over an already existing approach to the problem. Using subpar proxies for the intended clinical task may overestimate the actual performance of the AI model in the clinical setting. For example, assessment of an AI-enabled tool for the detection of intracranial hemorrhage might utilize turnaround time in outpatients with unexpected bleeds as a metric rather than reporting the overall accuracy of the tool.<sup>15,25</sup>

To evaluate potential real-world clinical efficacy and generalizability, it is important to gauge an AI tool’s performance on an external data set. Selection bias and reliance on retrospective data can lead to an AI model that too closely aligns with the original data and lacks the ability to generalize to new and unseen data. A recent study of deep learning algorithms for image-based radiologic diagnosis suggests that most will demonstrate diminished algorithm performance on the external data set, with some reporting a substantial performance decrease.<sup>25</sup>

External validation is increasingly recognized as a critical step for evaluating model performance but has been employed in relatively few published studies.<sup>26</sup> The latter may be attributed to the challenges of obtaining an appropriate external data set. However, nonetheless, it remains important to use an external testing data set, separate from the original data used to develop the model, to calculate final performance metrics.<sup>15,25</sup> This criterion is used to differentiate level 5A and level 5B. Potential sources of external



data includes information from a different institution or public data bases. Further rigorous external verification of performance, generalization, and reproducibility can be tested through a multi-institution approach.

To provide appropriate oversight on how AI decisions will impact patients, radiologists must encourage AI vendors to explain steps in the AI product's life cycle, in a manner that would allow for greater understandability and interpretability of its results. Of particular interest are details of the steps taken to reduce bias and ensure quality during the development process.<sup>27</sup> Detecting and mitigating bias in a machine learning model can be one of the most effort-intensive steps in the development process, as bias may be introduced at any point in the product's life cycle. Various approaches to reducing bias include emphasis on data transparency, mathematical approaches to de-biasing, interpretability/explainability of the decision-making process, and post-deployment surveillance strategies.<sup>28</sup>

### **Technical Efficacy versus Clinical Efficacy**

There is a need to verify both the technical and clinical efficacy of any AI-enabled tool before clinical implementation.<sup>29,30</sup> Interestingly, a study in 2020 found that fewer than 40% of commercially available AI products had published, peer-reviewed evidence available demonstrating their efficacy.<sup>4</sup> Receiving FDA clearance for clinical use in radiology in no way guarantees clinical utility or clinical efficacy of the product.

Technical efficacy is defined by the ability of the AI model to correctly perform the task for which it was trained (level 4).<sup>31</sup> Scientific evidence that supports technical efficacy is often in the form of retrospective studies and includes peer-reviewed information about the AI model's data quality, development, and performance metrics, benchmarked against similar or alternatively accepted methods in the literature. For example, an automated brain tumor segmentation task may require initial published results on the Dice coefficient or Jaccard index score to demonstrate technical efficacy. Subsequently, it would be important to provide scientific evidence that performance is reproducible and generalizable across different clinical institutions, patient populations, MR imaging field strengths, and imaging vendors.<sup>25</sup>

Clinical efficacy is defined by the ability of the AI model to change patient care and health care outcomes (level 1). Therefore, this requires a higher level of evidence, often in the form of prospective and randomized clinical trials to prove that the AI-enabled tool can lead to results that are better than standard level of care. It is important to note that technical efficacy does not equate to clinical efficacy.<sup>29-32</sup> For example, performance metrics such as reproducibility, sensitivity, specificity, positive and negative predictive values, and area under the curve are able to summarize AI model performance well but provide little information on how it could change patient outcome. Thus, despite impressive and exciting AI research, we continue to see relatively slow adoption of this technology to the health care setting. This is partly attributed to the paucity of scientific evidence supporting clinical efficacy.<sup>33</sup>

### **Bias and Error Mitigation**

AI clinical errors often reflect the interplay of different types of biases introduced by the imperfect process of collecting, training,

and applying data (level 2).<sup>16,34,35</sup> Additionally AI-enabled tools can project societal and historical biases that may further exacerbate existing inequities related to sex, age, and socioeconomic differences, among others. Thus, it is important to have a systematic approach for monitoring performance variances in different patient populations.<sup>36,37</sup> Other mechanisms that can be used to mitigate errors include ensuring data quality, as described above; verifying generalizability and reproducibility across different clinical sites (level 3); and careful consideration of epidemiological and statistical factors, such as disease prevalence, that can impact AI performance on a specific population.<sup>25,31</sup> A major goal of this white paper is to emphasize the importance of peer-reviewed publications, including robust internal and external validation during model development and subsequent validation at other sites. Differing feature distribution among clinical sites and patient populations such as sex, ethnicity, age, socioeconomic condition, geographic distribution, disease risk factors, imaging equipment, and image quality can lead to unexpected model performance errors.

Health care is a fluid and dynamic landscape, with new and evolving clinical practice standards that will require routine re-evaluation of the performance of the AI-enabled tool. This is further compounded by the yet to be defined process of how AI models continuously learn and evolve over time with new data. Thus, defining a practical mechanism for postdeployment monitoring including incorporating an iterative feedback loop between the radiologist, AI-enabled tool, and AI company during the implementation phase will be critical for adapting to these changes and achieving long-term consistent effectiveness.<sup>11,29,30,32</sup>

### **Legal and Regulatory Frameworks**

Policies pertaining to patient consent, data collection, and data usage will vary on a state, local, and institutional level. However, AI companies and health care systems should have standard operating procedures to maintain HIPAA compliance, patient data safety, confidentiality, and privacy (level 7).<sup>36,38,39</sup>

AI-enabled tools can be subjected to different regulatory requirements, depending on the proposed clinical setting and intended use. For example, for medically oriented AI-based tools, the FDA has 3 levels of clearance: the 510(k), premarket approval, and de novo pathways, each with its own specific criteria, which have been thoroughly explained elsewhere.<sup>40</sup>

Additionally, many other innovative and experimental AI research tools are being developed in-house under institutional internal review board approval outside the purview of government oversight.

Of the AI-enabled tools that have gone through FDA review, most have received FDA 510(k) clearance, which does not require safety or effectiveness data from clinical trials. Instead, the manufacturer can demonstrate that it is substantively equivalent to a predicate (another FDA-cleared or approved product). Thus, the emphasis on AI-enabled tools having more than 1 peer-reviewed publication is necessary in this white paper to encourage an independent, critical, and structured analysis of the AI-product. In contrast, substantially fewer products have gone through the FDA's more rigorous premarket approval or, alternatively, the de novo pathway, which is designed for AI-enabled medical devices that are not deemed high risk but do not have a predicate.

Currently, any major changes to an AI-enabled tool will require resubmission for FDA approval; thus, most AI algorithms may remain “static” or “locked” after they are introduced into the market. However, periodic surveillance and refinement of AI algorithms may be needed to adapt to the evolving health care environment,<sup>41</sup> without going through the full FDA review process again. This has prompted the FDA to consider more efficient and streamlined regulatory pathways to evaluate continuously learning AI through proposals such as the digital health precertification program and predetermined change control plan, which are currently under discussions. Unfortunately, as of now, no official process exists for major amendments to an existing AI algorithm.

The proposed hierarchy levels of evidence can be used to support an AI product’s life cycle in both the static and continuously learning environment. For continuous learning AI, there is mobility between the levels of the hierarchy. As an example, once an AI-enabled tool has established its baseline technical and clinical efficacy, modifications to the AI algorithm requiring FDA approval may allow it to move between level 7 and any other upper levels by providing additional scientific data, since the other levels have been supported by scientific evidence during its development phase.

### **Interoperability and Integration into the IT Infrastructure**

AI software should integrate seamlessly into the hospital information system, radiology information system, and PACS to be clinically and functionally useful.<sup>30,32</sup> A recent white paper on AI interoperability in imaging has explored the problems and challenges that must be addressed to achieve an ecosystem of interoperable AI products.<sup>42</sup> Until such harmonized standards are adopted, AI companies will need to provide a clear plan with defined interoperability standards for integration into the existing digital infrastructure (level 6).<sup>43</sup> The AI vendor should also be able to provide an on-site demonstration of the clinical tool in action in real time before full deployment. This will be an important opportunity to observe the AI model’s performance on the target population, impact on workflow, and potential errors in clinical practice.

### **Added Clinical Value**

It can take decades for health care innovations to become fully implemented into clinical practice.<sup>44</sup> Thus, the full clinical impact of AI on the health care system is likely to still mature and may not be completely apparent at the present time. Although challenging, defining and measuring the added value of an early technology remains the single most important factor for achieving clinical success and adoption.<sup>2</sup> No current consensus exists on how to measure the added value of an AI-enabled tool in clinical practice. However, one approach is to consider the tool’s potential to improve patient outcomes compared with the cost of achieving that improvement in a value-based health care system:<sup>45-47</sup> Value = Patient Outcome/Cost. As emphasized previously, AI performance accuracy alone does not necessarily lead to improved patient outcomes; future prospective investigations, clinical trials, or meta-analyses (level 1 evidence) are needed to establish such a link. Similarly, AI-enabled tools may reduce cost

to the patient and health care system by guiding clinical decision-making through a much more evidenced-based approach (ie, early detection of cerebral ischemia); however, more long-term investigations are still needed to understand the cost-benefit ratio. Randomized clinical trials are considered the gold standard for determining an intervention’s impact on clinical care. Several recent failures to implement AI-based tools in the clinical setting have suggested their relevance for selecting AI products with meaningful clinical benefit, especially given some inherent opacity and incomplete understanding of the mechanistic basis for how AI models actually make predictions.<sup>48,49</sup> Toward establishing scientific evidence for clinical efficacy, several AI-enabled tools have successfully demonstrated a positive impact on patient-centered related outcomes in clinical trials (level 1 evidence).<sup>50</sup> The proposed hierarchy levels of evidence can be used to support an AI product’s potential effectiveness and added value in the context of its available scientific data.

### **User Cases**

To understand how the levels of evidence can be utilized, the following user cases derive from selected real-world applications of AI-enabled tools in the literature. Employing the levels of evidence can facilitate communication and understanding among stakeholders regarding the strength of peer-reviewed evidence available to support that tool’s reported goal and potential clinical impact.

**Level 1 Evidence.** Strong scientific evidence exists for the positive clinical impact of AI-based tools used to guide clinical decision-making in stroke care.<sup>51</sup> Specifically, AI-based ischemic stroke triage and management have been shown to decrease patient morbidity and mortality while improving patient functionality through multiple practice-defining clinical trials.<sup>52,53</sup> There is also emerging evidence that these tools have the potential to reduce overall health care costs.<sup>54</sup>

**Level 3 Evidence.** AI-based tools can be used to augment aneurysm detection and analysis. In this example, the AI-based tool has at least 2 retrospective peer-reviewed publications inclusive of 2 or more different institutions.<sup>55,56</sup> However, there are currently no prospective data to assess the clinical impact of such a tool.

**Level 5B Evidence.** An AI-based tool designed to segment brain tumors with 1 retrospective study describing model development and performance without use of an external data set.

In summary, the levels of evidence are an important component of evidence-based medicine, and the adoption of such a classification system can help end-users prioritize information on the quality of AI products. Most importantly, AI-enabled tools exist on a spectrum with regard to their scientific rigor, with some products lacking peer-reviewed publications altogether to those that have been well-validated through multiple randomized clinical trials. The level of evidence that an AI-enabled tool will need, of course, will depend on its intended task, as illustrated above. As with all classification systems, level 1 evidence does not necessarily mean that these data should be accepted as fact while level 5B data should be disregarded. Our goal is to introduce a method

of scientific scrutiny to address the disconnect between expectations and reality.

## CONCLUSIONS

Barriers to the clinical implementation of AI-enabled tools include factors related to the lack of understandability of the AI development and decision-making process, standardized criteria for comparing product quality and effectiveness, and rigorous scientific evidence supporting meaningful impact on patient care and health care outcomes. To overcome some of these challenges, the ASFN/ASNR AI Workshop Technology Working Group has proposed hierarchical levels of evidence to objectively evaluate the scientific merit and potential effectiveness of AI technologies in clinical practice.

Disclosure forms provided by the authors are available with the full text and PDF of this article at [www.ajnr.org](http://www.ajnr.org).

## REFERENCES

- Zaharchuk G, Gong E, Wintermark M, et al. **Deep learning in neuro-radiology.** *AJNR Am J Neuroradiol* 2018;39:1776–84 CrossRef Medline
- Lui YW, Chang PD, Zaharchuk G, et al. **Artificial intelligence in neuroradiology: current status and future directions.** *AJNR Am J Neuroradiol* 2020;41:E52–59 CrossRef Medline
- Bohr A, Memarzadeh K. **The rise of artificial intelligence in healthcare applications.** *Artificial Intelligence in Healthcare.* Cambridge, Massachusetts; Academic Press; 2020:25–60
- van Leeuwen KG, de Rooij M, Schalekamp S, et al. **How does artificial intelligence in radiology improve efficiency and health outcomes?** *Pediatr Radiol* 2022;52:2087–93 CrossRef Medline
- Artificial intelligence and machine learning (AI/ML)-enabled medical devices.** October 5, 2022. <https://www.fda.gov/medical-devices/software-medical-device-samd/artificial-intelligence-and-machine-learning-aiml-enabled-medical-devices>. Accessed March 5, 2023
- van Leeuwen KG, Schalekamp S, Rutten MJ, et al. **Artificial intelligence in radiology: 100 commercially available products and their scientific evidence.** *Eur Radiol* 2021;31:3 797–804 CrossRef Medline
- Goergen SK, Frazer HM, Reddy S. **Quality use of artificial intelligence in medical imaging: what do radiologists need to know?** *J Med Imaging Radiat Oncol* 2022;66:225–32 CrossRef Medline
- Letourneau-Guillon L, Camirand D, Guilbert F, et al. **Artificial intelligence applications for workflow, process optimization and predictive analytics.** *Neuroimaging Clin N Am* 2020;30:e1–15 CrossRef Medline
- Kitamura FC, Pan I, Ferraciolli SF, et al. **Clinical artificial intelligence applications in radiology: Neuro.** *Radiol Clin North Am* 2021;59:1003–12 CrossRef Medline
- Kaka H, Zhang E, Khan N. **Artificial intelligence and deep learning in neuroradiology: exploring the new frontier.** *Can Assoc Radiol J* 2021;72:35–44 CrossRef Medline
- Scott I, Carter S, Coiera E. **Clinician checklist for assessing suitability of machine learning applications in healthcare.** *BMJ Health Care Inform* 2021;28:e100251 CrossRef Medline
- Burns PB, Rohrich RJ, Chung KC. **The levels of evidence and their role in evidence-based medicine.** *Plast Reconstr Surg* 2011;128:305–10 CrossRef Medline
- Willeminck MJ, Koszek WA, Hardell C, et al. **Preparing medical imaging data for machine learning.** *Radiology* 2020;295:4–15 CrossRef Medline
- Mongan J, Moy L, Kahn CE. **Checklist for artificial intelligence in medical imaging (CLAIM): a guide for authors and reviewers.** *Radiol Artif Intell* 2020;2:e200029 CrossRef Medline
- Bluemke DA, Moy L, Bredella MA, et al. **Assessing radiology research on artificial intelligence: a brief guide for authors, reviewers, and readers-from the radiology editorial board.** *Radiology* 2020;294:487–89 CrossRef Medline
- Yu AC, Eng J. **One algorithm may not fit all: how selection bias affects machine learning performance.** *Radiographics* 2020;40:1932–39 CrossRef Medline
- Hernandez-Boussard T, Bozkurt S, Ioannidis JP, et al. **MINIMAR (MINimum information for medical AI reporting): developing reporting standards for artificial intelligence in health care.** *J Am Med Inform Assoc* 2020;27:2011–15 CrossRef Medline
- Radiology: Artificial intelligence. **Checklist for Artificial Intelligence in Medical Imaging (CLAIM).** <https://pubs.rsna.org/page/ai/claim?doi=10.1148%2Fryai&publicationCode=ai>. Accessed March 2, 2023
- Liu X, Rivera SC, Moher D, et al. **Reporting guidelines for clinical trial reports for interventions involving artificial intelligence: the CONSORT-AI extension.** *BMJ (Online)* 2020;370:m3164 CrossRef
- Park Y, Jackson GP, Foreman MA, et al. **Evaluating artificial intelligence in medicine: phases of clinical research.** *JAMIA Open* 2020;3:326–31 CrossRef Medline
- Jha A, Bradshaw T, Buvat I, et al. **Best practices for evaluation of artificial intelligence-based algorithms for nuclear medicine: the RELIANCE guidelines.** *J Nucl Med* 2022;63(Suppl 2):1725
- Filice RW, Mongan J, Kohli MD. **Evaluating artificial intelligence systems to guide purchasing decisions.** *J Am Coll Radiol* 2020;17:1405–09 CrossRef Medline
- Krause J, Gulshan V, Rahimy E, et al. **Grader variability and the importance of reference standards for evaluating machine learning models for diabetic retinopathy.** *Ophthalmology* 2018;125:1264–72 CrossRef Medline
- Duggan GE, Reicher JJ, Liu Y, et al. **Improving reference standards for validation of AI-based radiography.** *Br J Radiol* 2021;94:20210435 CrossRef Medline
- Yu AC, Mohajer B, Eng J. **External validation of deep learning algorithms for radiologic diagnosis: a systematic review.** *Radiol Artif Intell* 2022;4:e210064 CrossRef Medline
- Kim DW, Jang HY, Kim KW, et al. **Design characteristics of studies reporting the performance of artificial intelligence algorithms for diagnostic analysis of medical images: results from recently published papers.** *Korean J Radiol* 2019;20:405–10 CrossRef Medline
- Dunnmon J. **Separating hope from hype: artificial intelligence pitfalls and challenges in radiology.** *Radiol Clin North Am* 2021;59:1063–74 CrossRef Medline
- Vokinger KN, Feuerriegel S, Kesselheim AS. **Mitigating bias in machine learning for medicine.** *Commun Med (Lond)* 2021;1:25 CrossRef Medline
- Kelly CJ, Karthikesalingam A, Suleyman M, et al. **Key challenges for delivering clinical impact with artificial intelligence.** *BMC Med* 2019;17:195 CrossRef Medline
- He J, Baxter SL, Xu J, et al. **The practical implementation of artificial intelligence technologies in medicine.** *Nat Med* 2019;25:30–36 CrossRef Medline
- Park SH, Han K. **Methodologic guide for evaluating clinical performance and effect of artificial intelligence technology for medical diagnosis and prediction.** *Radiology* 2018;286:800–09 CrossRef Medline
- Wolff J, Pauling J, Keck A, et al. **Success factors of artificial intelligence implementation in healthcare.** *Front Digit Health* 2021;3:594971 CrossRef Medline
- Omoumi P, Ducarouge A, Tournier A, et al. **To buy or not to buy: evaluating commercial AI solutions in radiology (the ECLAIR guidelines).** *Eur Radiol* 2021;31:3786–96 CrossRef Medline
- DeCamp M, Lindvall C. **Latent bias and the implementation of artificial intelligence in medicine.** *J Am Med Inform Asso.* 2020;27:2020–23 CrossRef Medline
- Finlayson SG, Subbaswamy A, Singh K, et al. **The clinician and dataset shift in artificial intelligence.** *N Engl J Med* 2021;385:283–86 CrossRef Medline

36. Geis JR, Brady AP, Wu CC, et al. **Ethics of artificial intelligence in radiology: summary of the Joint European and North American Multisociety Statement.** *Radiology* 2019;293:436–40 CrossRef
37. Liu X, Glocker B, McCradden MM, et al. **The medical algorithmic audit.** *Lancet Digit Health* .2022;4:e384–97 CrossRef Medline
38. Vollmer S, Mateen BA, Bohner G, et al. **Machine learning and artificial intelligence research for patient benefit: 20 critical questions on transparency, replicability, ethics, and effectiveness.** *BMJ* 2020;368:l6927 CrossRef Medline
39. Spilseth B, McKnight CD, Li MD, et al. **AUR-RRA review: logistics of academic-industry partnerships in artificial intelligence.** *Acad Radiol* 2022;29:119–28 CrossRef Medline
40. **FDA-regulated AI algorithms: trends, strengths, and gaps of validation studies.** *Acad Radiol* 2022;29:559–66 CrossRef Medline
41. Pianykh OS, Langs G, Dewey M, et al. **Continuous learning AI in radiology: implementation principles and early applications.** *Radiology* 2020;297:6–14 CrossRef Medline
42. Genereaux B, O'Donnell K, Bialecki B, et al. **IHE radiology white paper: AI interoperability in imaging.** *Integrating the Healthcare Enterprise* 2021;1:????? [https://www.ihe.net/uploadedFiles/Documents/Radiology/IHE\\_RAD\\_White\\_Paper\\_AI\\_Interoperability\\_in\\_Imaging.pdf](https://www.ihe.net/uploadedFiles/Documents/Radiology/IHE_RAD_White_Paper_AI_Interoperability_in_Imaging.pdf). Accessed March 3, 2023
43. Wiggins WF, Magudia K, Schmidt TMS, et al. **Imaging AI in practice: a demonstration of future workflow using integration standards.** *Radiol Artif Intell* 2021;3:e210152 CrossRef Medline
44. Kirchner JE, Smith JL, Powell BJ, et al. **Getting a clinical innovation into practice: an introduction to implementation strategies.** *Psychiatry Res* 2020;283:112467 CrossRef Medline
45. Porter ME. **What is value in health care?** *N Engl J Med* 2010;363:2477–81 CrossRef
46. Brady AP, Visser J, Frija G, et al. **Value-based radiology: what is the ESR doing, and what should we do in the future?** *Insights Imaging* 2021;12:108 CrossRef
47. Teisberg E, Wallace S, O'Hara S. **Defining and implementing value-based health care: a strategic framework.** *Acad Med* 2020;95:682–85 CrossRef Medline
48. Plana D, Shung DL, Grimshaw AA, et al. **Randomized clinical trials of machine learning interventions in health care: a systematic review.** *JAMA Netw Open* 2022;5:e2233946 CrossRef Medline
49. Wilkinson J, Arnold KF, Murray EJ, et al. **Time to reality check the promises of machine learning-powered precision medicine.** *Lancet Digit Health* 2020;2:e677–80 CrossRef Medline
50. Campbell BC, Mitchell PJ, Kleinig TJ, et al; EXTEND-IA Investigators. **Endovascular therapy for ischemic stroke with perfusion-imaging selection.** *N Engl J Med* 2015;372:1009–18 CrossRef Medline
51. Soun JE, Chow DS, Nagamine M, et al. **Artificial intelligence and acute stroke imaging.** *AJNR Am J Neuroradiol* 2021;42:2–11 CrossRef Medline
52. Albers GW, Marks MP, Kemp S, et al; DEFUSE 3 Investigators. **Thrombectomy for stroke at 6 to 16 hours with selection by perfusion imaging.** *N Engl J Med* 2018;378:708–18 CrossRef Medline
53. Ma H, Campbell BC, Parsons MW, et al; EXTEND Investigators. **Thrombolysis guided by perfusion imaging up to 9 hours after onset of stroke.** *N Engl J Med* 2019;380:1795–803 CrossRef Medline
54. van Leeuwen KG, Meijer FJ, Schalekamp S, et al. **Cost-effectiveness of artificial intelligence aided vessel occlusion detection in acute stroke: an early health technology assessment.** *Insights Imaging* 2021;12:133 CrossRef Medline
55. Heit JJ, Honce JM, Yedavalli VS, et al. **RAPID aneurysm: artificial intelligence for unruptured cerebral aneurysm detection on CT angiography.** *J Stroke Cerebrovasc Dis* 2022;31:106690 CrossRef Medline
56. Sahlein DH, Gibson D, Scott JA, et al. **Artificial intelligence aneurysm measurement tool finds growth in all aneurysms that ruptured during conservative management.** *J Neurointerv Surg* 2022 Sep 30. [Epub ahead of print] CrossRef Medline



## Pituitary MRI to Evaluate Extraocular Muscles: Is That Possible with a Routine Scanning Protocol?

**W**ith great interest, we read the article, “Extraocular Muscle Enlargement in Growth Hormone-Secreting Pituitary Adenomas,” recently published by Coutu et al in the *American Journal of Neuroradiology*.<sup>1</sup> We have 3 important concerns about the methodology that need to be clarified.

First, in a routine pituitary MR imaging protocol, it is interesting to evaluate the 4 extraocular muscles (EOMs) that were analyzed in your study, namely, the superior, lateral, medial, and inferior rectus muscles. In our experience, producing a pituitary MR imaging with optimal quality to detect tiny adenomas depends on a trade-off between the small FOV and various scanning parameters. Expanding the FOV to the orbital structures is not common in a dedicated high-quality pituitary MR imaging protocol.

Second, the methodology for EOM measurement was not systematically described. However, the authors cited a related article for measurements.<sup>2</sup> Certain details are crucial to evaluate the appropriateness of the measurements and should be given as the cited article did. For instance, the planes for superior-inferior and lateral-medial muscle groups should be described separately.

Third, despite the article being published in one of the most prestigious neuroradiology journals, no single MR imaging figure

was presented. We also wonder how the reviewers and the Editor were convinced about the EOM measurement on routine pituitary MR imaging. Our purpose is not to devalue this research article but to improve the transparency of its methodology, guiding future research. Therefore, presenting MR imaging figures showing the measurement technique in routine pituitary MR imaging seems crucial to externally validate the findings presented in the article.

We look forward to reading the authors' and editors' comments, which would clarify the methodology of the article.

Disclosure forms provided by the authors are available with the full text and PDF of this article at [www.ajnr.org](http://www.ajnr.org).

### REFERENCES

1. Coutu B, Alvarez DA, Ciurej A, et al. **Extraocular muscle enlargement in growth hormone-secreting pituitary adenomas.** *AJNR Am J Neuroradiol* 2022;43:597–602 CrossRef Medline
2. Ozgen A, Aydingöz U. **Normative measurements of orbital structures using MRI.** *J Comput Assist Tomogr* 2000;24:493–96 CrossRef Medline

● **B. Kocak**

Department of Radiology  
Basaksehir Cam and Sakura City Hospital  
Istanbul, Turkey

<http://dx.doi.org/10.3174/ajnr.A7681>

**REPLY:**

**W**e appreciate the interest demonstrated in our article, “Extraocular Muscle Enlargement in Growth Hormone-Secreting Pituitary Adenomas.” *AJNR Am J Neuroradiol* 2022;43:597–602. It is correct that dedicated orbital imaging was not performed in this series of patients secondary to the retrospective nature of the study. That would be an excellent next step in the further analysis of

the changes in extraocular muscles in this clinical scenario. The images analyzed were not all from dedicated pituitary imaging. Many of the images analyzed were from the preoperative MRIs and from MRIs used for radiation planning. The measurement of the extraocular muscles was the greatest short axis diameter of the muscle (Figure).

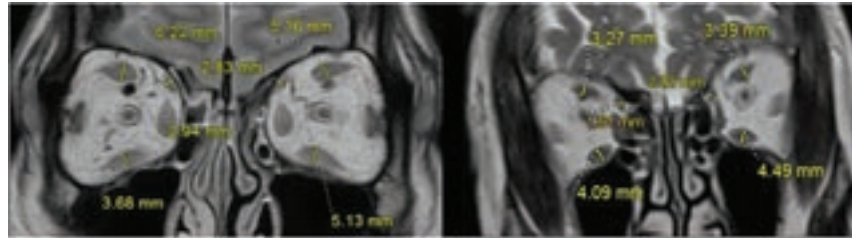


**FIGURE.** The example of measurement of extraocular muscles.

● M. White  
● C. Zhang  
● A. Drincic

University of Nebraska Medical Center  
Omaha, Nebraska

<http://dx.doi.org/10.3174/ajnr.A7857>